

Sea ice Thermodynamic and Dynamic Processes in the
Ocean-sea ice-Atmosphere System of the Canadian Arctic

by

Ryan James Galley

A Thesis submitted to the Faculty of Graduate Studies of
The University of Manitoba
in partial fulfillment of the requirements for the degree of

DOCTOR OF PHILOSOPHY

Department of Environment and Geography
University of Manitoba
Winnipeg, Manitoba, Canada

Copyright © 2009 by Ryan James Galley

THE UNIVERSITY OF MANITOBA
FACULTY OF GRADUATE STUDIES

COPYRIGHT PERMISSION

**Sea Ice Thermodynamic and Dynamic Processes in the
Ocean-Sea Ice-Atmosphere System of the Canadian Arctic**

By

Ryan James Galley

A Thesis/Practicum submitted to the Faculty of Graduate Studies of The University of
Manitoba in partial fulfillment of the requirement of the degree

Of

Doctor of Philosophy

Ryan James Galley©2009

Permission has been granted to the University of Manitoba Libraries to lend a copy of this thesis/practicum, to Library and Archives Canada (LAC) to lend a copy of this thesis/practicum, and to LAC's agent (UMI/ProQuest) to microfilm, sell copies and to publish an abstract of this thesis/practicum.

This reproduction or copy of this thesis has been made available by authority of the copyright owner solely for the purpose of private study and research, and may only be reproduced and copied as permitted by copyright laws or with express written authorization from the copyright owner.

ABSTRACT

Sea ice, by its presence or absence, controls the transfer of energy, mass and momentum between the ocean and atmosphere in the Arctic playing a vital role in the modulation of earth's climate systems. Polynyas are of particular importance in to ocean-atmosphere exchange in the Arctic because they are integral components of the physical and biological nature of the Arctic climate. The aim of this thesis is to investigate snow-covered sea ice volumes from the local to regional scale in the context of thermodynamic and dynamic processes that create them and cause their interaction. Measurement of separate snow and sea ice thickness has in the past been of some difficulty, especially when attempting to obtain spatially distributed samples. Using snow and sea ice physical *in situ* sampling, a method for remotely sensing separate snow and sea ice thickness using ground penetrating radar has been created to allow for high frequency sampling in time and space. The effect of a melting sea ice volume on ocean stratification is then examined in a Canadian Arctic polynya, where it is determined that the onset of ponding over landfast sea ice surrounding the polynya coincides with the summer stratification of the upper ocean mixed layer. Increasing in scale from local to regional study, the interaction of different sea ice volumes in time and space are examined, including the spatial and temporal evolution and trends of sea ice concentration. Break-up and freeze-up in the Cape Bathurst polynya region are examined to elucidate the variability of break-up and freeze-up in Amundsen Gulf in terms of regional dynamics and the evolving seasonal ice cover in the area. This work leads to an explanation of the thermodynamic and dynamic processes that cause the interaction of volumes in the

region over an annual cycle; physical mechanisms that pre-condition, form and maintain the Cape Bathurst polynya. This is an important step in understanding the nature of atmosphere-ocean interaction in an ecologically important transition zone between the Arctic multi-year pack and seasonal sea ice of the Canadian Arctic Archipelago.

ACKNOWLEDGEMENTS

I would like to thank my supervisor, Dr. David Barber, and my graduate committee members, Drs. Simon Prinsenber, Tim Papakyriakou and Steve Ferguson. Without your support this would not have been possible.

I would like to thank Drs. Brenda Hann (zoology) and Gary Johnson (agriculture) of the University of Manitoba for being great teachers and stimulating me to pursue process-based research.

I would like to extend my thanks and appreciation to Jens Ehn, Byong Jun Hwang, Steve Howell, Alexandre Langlois, and Michael Trachtenberg for their friendship, collaboration and assistance. I would especially like to thank Erica Key for her friendship and collaboration which has made this a much more enjoyable process.

I would also like to thank the following organizations for their support in this endeavor: the Canadian Arctic Shelf Exchange Study, the ArcticNet program of the Network of Centres of Excellence, the Canadian Ice Service and the Northern Science Training Program.

To my wife Lianne, and my parents Terry and Jim, thank you very much for all your support and encouragement.

"The important thing in science is not so much to obtain new facts as to discover new ways of thinking about them."

- Sir William Bragg (1862 - 1942)

TABLE OF CONTENTS

<u>ABSTRACT.....</u>	<u>II</u>
<u>ACKNOWLEDGEMENTS.....</u>	<u>IV</u>
<u>TABLE OF CONTENTS.....</u>	<u>V</u>
<u>LIST OF TABLES.....</u>	<u>VIII</u>
<u>LIST OF FIGURES.....</u>	<u>IX</u>
<u>CHAPTER ONE: INTRODUCTION.....</u>	<u>14</u>
1. RATIONALE AND CONTEXT.....	14
2. SCIENCE OBJECTIVES.....	15
3. RESEARCH STRUCTURE.....	16
LITERATURE CITED.....	19
<u>CHAPTER TWO: BACKGROUND AND LITERATURE REVIEW.....</u>	<u>20</u>
1. SEA ICE THERMODYNAMICS.....	20
<i>FREEZING SEAWATER.....</i>	<i>20</i>
<i>ICE CRYSTAL STRUCTURE.....</i>	<i>20</i>
<i>SEA ICE GROWTH, STRUCTURE AND PROPERTIES.....</i>	<i>22</i>
<i>FRAZIL ICE.....</i>	<i>22</i>
<i>FRAZIL-PANCAKE CYCLE.....</i>	<i>23</i>
<i>CONGELATION ICE.....</i>	<i>24</i>
<i>CONSTITUTIONAL SUPER-COOLING IN THE SKELETAL LAYER.....</i>	<i>26</i>
<i>MULTI-YEAR SEA ICE.....</i>	<i>27</i>
<i>SEA ICE SALINITY AND TEMPERATURE.....</i>	<i>27</i>
<i>BRINE CELL FORMATION AND DYNAMICS.....</i>	<i>29</i>
<i>SOLID SALTS IN SEA ICE.....</i>	<i>32</i>
<i>SEA ICE PHASE RELATIONSHIPS.....</i>	<i>32</i>
<i>SNOW COVER ON SEA ICE - FORMATION, PHYSICAL AND THERMAL PROPERTIES AND DISTRIBUTION.....</i>	<i>34</i>
<i>THERMAL PROPERTIES AND THE SURFACE ENERGY BALANCE OF SNOW-COVERED SEA ICE.....</i>	<i>37</i>
<i>RADIATIVE FLUXES.....</i>	<i>39</i>
<i>INFLUENCE OF CLOUDS.....</i>	<i>44</i>
<i>TURBULENT FLUXES.....</i>	<i>45</i>
<i>CONDUCTIVE FLUX.....</i>	<i>48</i>
<i>INFLUENCE OF SNOW COVER ON THERMODYNAMIC PROCESSES IN SEA ICE.....</i>	<i>51</i>
<i>OCEAN HEAT FLUX.....</i>	<i>52</i>
<i>THERMODYNAMIC GROWTH AND DECAY OF SEA ICE.....</i>	<i>55</i>
2. SEA ICE DYNAMICS.....	60
<i>MOMENTUM BALANCE.....</i>	<i>61</i>
<i>SEA ICE MOTION IN FREE DRIFT.....</i>	<i>64</i>
<i>SEA ICE STRENGTH AND RHEOLOGY.....</i>	<i>66</i>
3. SEA ICE MORPHOLOGY AND THICKNESS DISTRIBUTION: THERMODYNAMICS AND DYNAMICS.....	68
<i>THE PROBABILITY DISTRIBUTION FUNCTION OF SEA ICE THICKNESS.....</i>	<i>69</i>
4. LARGE-SCALE PROCESSES AND CHANGING CLIMATE.....	73

<i>CIRCULATION</i>	73
<i>SEA ICE EXTENT AND THICKNESS</i>	77
5. CONCLUSIONS.....	86
LITERATURE CITED	88
<u>CHAPTER THREE: OBSERVATIONS OF GEOPHYSICAL AND DIELECTRIC PROPERTIES AND GROUND PENETRATING RADAR SIGNATURES FOR DISCRIMINATION OF SNOW, SEA ICE AND FRESHWATER ICE THICKNESS</u>	98
INTRODUCTION.....	98
METHODS	101
SNOW AND ICE PHYSICAL PROPERTIES.....	102
SNOW AND ICE DIELECTRIC PROPERTIES.....	103
GROUND PENETRATING RADAR.....	105
RESULTS AND DISCUSSION	108
CHURCHILL RIVER ESTUARY ICE AND SNOW - PHYSICAL AND DIELECTRIC PROPERTIES.....	108
CHURCHILL RIVER ESTUARY GPR RETURNS.....	110
BUTTON BAY ICE AND SNOW - PHYSICAL AND DIELECTRIC PROPERTIES ON 4 MARCH 2006	117
BUTTON BAY GPR RETURNS - 4 MARCH 2006.....	121
BUTTON BAY ICE AND SNOW - PHYSICAL AND DIELECTRIC PROPERTIES ON 7 MARCH 2006	123
BUTTON BAY GPR RETURNS - 7 MARCH 2006.....	127
CONCLUSION	128
LITERATURE CITED	130
<u>CHAPTER FOUR: ON THE LINK BETWEEN SAR-DERIVED SEA ICE MELT AND DEVELOPMENT OF THE SUMMER UPPER OCEAN MIXED LAYER IN THE NORTH OPEN WATER POLYNYA</u>	134
1. INTRODUCTION AND BACKGROUND.....	134
2. OBJECTIVE.....	138
3. METHODS.....	138
4. RESULTS AND DISCUSSION – LOCAL SCALE.....	141
5. RESULTS AND DISCUSSION – REGIONAL SCALE.....	148
6. CONCLUSIONS.....	154
LITERATURE CITED	156
<u>CHAPTER FIVE: SPATIAL AND TEMPORAL VARIABILITY OF SEA ICE IN THE SOUTHERN BEAUFORT SEA AND AMUNDSEN GULF: 1980 – 2004</u>	158
1. INTRODUCTION	158
2. STUDY AREA, DATA AND METHODS	164
2.1. AMUNDSEN GULF AND THE SOUTHERN BEAUFORT SEA	164
2.2. SEA ICE CONCENTRATION DATA.....	165
3. SEA ICE CLIMATOLOGY AND TRENDS.....	168
3.1. SEA ICE IN THE SOUTHERN BEAUFORT SEA AND AMUNDSEN GULF.....	168
3.2. SEA ICE CONCENTRATION TRENDS	181
3.3. DISCUSSION – SEA ICE CONCENTRATION TRENDS	185
4. BREAK-UP AND FREEZE-UP WITHIN THE SOUTHERN BEAUFORT SEA AND AMUNDSEN GULF	188
4.1. AVERAGE BREAK UP	188
4.2. AVERAGE FREEZE UP	190
5. BREAK-UP AND FREEZE-UP TIMING AND DURATION IN AMUNDSEN GULF.....	192
5.1. BREAK-UP VARIABILITY.....	193

5.2. OPEN WATER.....	196
5.3. FREEZE-UP VARIABILITY.....	197
6. CONCLUSIONS.....	198
LITERATURE CITED	201
<u>CHAPTER SIX: A PHYSICAL EXPLANATION OF THE FORMATION OF THE CAPE BATHURST POLYNYA, NWT, CANADA</u>	<u>205</u>
1. INTRODUCTION	205
2. DATA AND METHODS.....	210
2.1. CANADIAN ICE SERVICE DIGITAL ARCHIVE AND RADARSAT-1.....	210
2.2. THE SEA ICE THICKNESS DISTRIBUTION OF WESTERN AMUNDSEN GULF	211
2.3. MODELED THERMODYNAMIC SEA ICE GROWTH IN WESTERN AMUNDSEN GULF.....	213
2.4. SEA ICE MOTION IN THE SOUTHERN BEAUFORT SEA AND WESTERN AMUNDSEN GULF.....	214
3. RESULTS.....	215
3.1. EVOLUTION OF THE CAPE BATHURST FLAW LEAD POLYNYA COMPLEX 2003-2004	215
3.2. SEA ICE MOTION IN THE SOUTHERN BEAUFORT SEA AND WESTERN AMUNDSEN GULF.....	219
3.3. THERMODYNAMIC SEA ICE GROWTH IN WESTERN AMUNDSEN GULF.....	223
3.4. SPRING SEA ICE THICKNESS DISTRIBUTION IN WESTERN AMUNDSEN GULF	226
3.5. SPRING FORMATION OF THE CAPE BATHURST POLYNYA.....	232
4. CONCLUSIONS.....	237
LITERATURE CITED	240
<u>CHAPTER SEVEN: CONCLUSIONS AND RECOMMENDATIONS.....</u>	<u>244</u>
SUMMARY AND CONTRIBUTIONS	244
FUTURE DIRECTION.....	245
CONCLUSIONS	247
<u>APPENDIX A: CONTRIBUTIONS OF COLLABORATING AUTHORS.....</u>	<u>250</u>
<u>APPENDIX B: ADDITIONAL CONTRIBUTIONS TO THE PEER-REVIEWED LITERATURE</u>	<u>251</u>

LIST OF TABLES

Table 3.1. Summary snow and ice thickness and observed radar velocities calculated from GPR returns compared against those calculated using dielectric information for the Churchill River estuary (fresh ice).	116
Table 3.2. Summary snow and ice thickness and observed radar velocities calculated from GPR returns compared against those calculated using dielectric information over snow-covered sea ice in Button Bay on 4 March 2006.	122
Table 3.3. Summary snow and ice thickness and observed radar velocities calculated from GPR returns compared against those calculated using dielectric information over snow-covered sea ice in Button Bay on 7 March 2006.	127
Table 4.1. Melt onset and pond onset date for each scanSAR sample location (after <i>Yackel et al.</i> , 2001).	139
Table 5.1. Year week in each year where the average total sea ice concentration in Amundsen Gulf reaches spring break-up, the open water (OW) season and fall freeze-up. The slopes of the total concentration curves (Figure 15) are shown for break-up and freeze-up.	195
Table 6.1. Summary statistics for sea ice thickness (Z_i) sections 1-12 in the map in Figure 6.7.	229

LIST OF FIGURES

- Figure 2.1. The crystal structure of ice Ih, indicating the basal (0001) plane, the c-axis and prism face (1100). From Weeks and Ackley (1986). 21
- Figure 2.2. The evolution of sea ice salinity with depth over time as determined by Malmgren (1927). 28
- Figure 2.3. Sea ice phase diagram indicating the (top) mass fraction of ice (middle) solid salts and (bottom) liquid brine with respect to temperature in a closed volume of standard seawater. From Assur (1958). 33
- Figure 2.4. Fluxes in a uniform snow-covered ice sheet. Redrawn after Maykut and Untersteiner, (1971). 56
- Figure 2.5. A one-dimensional comparison of sea ice rheologies. The viscous-plastic rheology is considered a nonlinear viscous fluid with the inclusion of a minimum pressure term (P^*). From Hibler (1979). 67
- Figure 2.6. A probability distribution function of sea ice thickness (top) shown with the processes which may alter it over the course of an annual cycle (bottom). Modified from Thorndike et al. (1992). 71
- Figure 2.7. Arctic Ocean circulation showing the average position of the Beaufort Gyre and the Transpolar Drift stream. From AMAP (1998: figure 3.29). 74
- Figure 2.8. Yearly and seasonal sea ice extents from 1979-2006. The winter (W), spring (Sp), summer (Su) and autumn (A) values cover JFM, AMJ, JAS, and OND respectively. Modified from Parkinson and Cavalieri (2008). 78
- Figure 2.9. Monthly ice extent (a) and ice area (b) anomalies from November 1978 to September 2007 (green and blue) with 12-month running average (red) and linear trend lines for three periods (full record: black; 1978-1996: green; 1996-2007: blue). From Comiso et al. (2008). 79
- Figure 2.10. Arctic sea ice concentration and extent on 14 September 2007. The gold contour represents the average sea ice cover edge from 1979-2006 and the red contour represents the previous record minimum sea ice cover in 2005. From Comiso et al. (2008). 81
- Figure 2.11. Mean draft changes between 1958-1976 and 1993-1997 at regions in the Arctic Ocean derived from submarine surveys. From Rothrock et al. (1999). 84

Figure 3.1. (top) Map of Canada showing the Churchill River estuary and Button bay (black box) and (bottom) Radarsat-1 scanSAR image of Button Bay and the Churchill River estuary in southwestern Hudson Bay, Canada. 101

Figure 3.2. Salinity and temperature profiles of river ice in the Churchill River estuary (left), permittivity (ϵ') profiles of river ice (middle) and dielectric loss (ϵ'') profiles of river ice (right) on 6 March 2006 ($z_i = 135\text{cm}$). 108

Figure 3.3. Snow temperature and density (left), permittivity (ϵ') at 1GHz (middle) and dielectric loss (ϵ'') at 1GHz (right) profiles on the Churchill River estuary ($z_s = 44\text{cm}$). 109

Figure 3.4. Trace plot returns over bare ice at 250MHz and 1GHz on 6 March 2006 in the Churchill River estuary ($z_i = 1.38\text{m}$). 111

Figure 3.5. Trace plot returns on 6 March 2006 over snow-covered river ice in the Churchill river estuary at 250 MHz (left column) and 1GHz (right column) where (a) $z_s = 0.65\text{m}$ and $z_i = 1.12\text{m}$, (b) $z_s = 0.44\text{m}$ and $z_i = 1.12\text{m}$ and (c) $z_s = 0.15\text{m}$ and $z_i = 1.20\text{m}$. 114

Figure 3.6. (a) Snow temperature, salinity, density, and water-by-volume (Wv) (left), permittivity (ϵ') at 1GHz (middle) and dielectric loss (ϵ'') at 1GHz (right) profiles on 4 March 2006 in Button Bay ($z_s = 0.12\text{m}$), (b) Salinity, temperature and brine volume profiles of sea ice (left) and calculated permittivity (ϵ') profiles (middle) and dielectric loss (ϵ'') profiles (right) within Button Bay 4 March 2006 ($z_i = 1.05\text{m}$), (c) Trace plots over snow-covered ice at 250 MHz (left) and 1 GHz (right) on 04 March 2006 in Button Bay, $z_s = 0.12\text{m}$ and $z_i = 1.05\text{m}$. 120

Figure 3.7. (a) Snow temperature, salinity and density (left), permittivity (ϵ') at 1GHz (middle) and dielectric loss (ϵ'') at 1GHz (right) profiles on 7 March 2006 in Button Bay ($z_s = 0.12\text{m}$), (b) Salinity, temperature and brine volume profiles of sea ice (left) and calculated permittivity (ϵ') profiles (middle) and dielectric loss (ϵ'') profiles (right) within Button Bay 7 March 2006, $z_i = 1.01\text{m}$, (c) Trace plots over snow-covered ice at 250MHz (left) and 1GHz (right) on 7 March 2006 in Button Bay $z_s = 0.12\text{m}$ and $z_i = 1.01\text{m}$. 126

Figure 4.1. The seasonal evolution of σ° from the ERS-1 SAR for thick first-year and multi-year sea ice over the annual sea ice cycle (after Barber *et al.*, 1998). 136

Figure 4.2. RADARSAT-1 ScanSAR sample site locations over landfast first-year sea ice surrounding the North Water Polynya (after Yackel *et al.*, 2001). 140

Figure 4.3. (a) Location of CTD profiles in April (x) and May (+), and (b) in June (x) and July (+). 141

- Figure 4.4. Local scale study area on the west side of Smith Sound, including CTD station 2, Rosse Bay (RB) and Goding Bay (GB) RADARSAT-1 ScanSAR sites. 142
- Figure 4.5. (a) Temperature (b) salinity and (c) potential density profiles at CTD station 2, and (d) mixed layer depth at CTD station 2. 145
- Figure 4.6. Canadian Ice Service digital ice charts showing ice concentration and relative extent. (top) YD 121 (May 01), (middle) YD 135 (May 15), and (bottom) YD 152 (June 01). 149
- Figure 4.7. Time series evolution of (a) near surface salinity (b) near surface potential density and (c) mixed layer depth in the North Water. 151
- Figure 4.8. SAR-derived pond onset date interpolated over the polynya, overlaid by all CTD profiles conducted in 1998. ScanSAR sample sites denoted by gray triangles. 152
- Figure 4.9. Mixed layer depth time-referenced against pond onset date at the same location within the North Water. 153
- Figure 5.1. The southern Beaufort Sea and Amundsen Gulf, western Canadian Arctic. Black lines delineate the study area used in Section 5. The area normally occupied by the flaw lead system is shown in grey. 162
- Figure 5.2. Average winter sea ice concentration by type between 1980 and 2004 (a) total sea ice, (b) old sea ice, (c) first year, (d) thick first year, (e) young and new sea ice. 169
- Figure 5.3. Average winter old sea ice concentration by year from 1980 to 2004. 170
- Figure 5.4. Average winter first year sea ice concentration by year from 1980 to 2004. 171
- Figure 5.5. Average winter thin first year sea ice concentration by year from 1980 to 2004. 173
- Figure 5.6. Average winter young and new sea ice concentration by year from 1980 to 2004. 174
- Figure 5.7. Average summer sea ice concentration by type between 1980 and 2004 (a) total sea ice, (b) old sea ice and (c) first year sea ice. 175
- Figure 5.8. Average summer total sea ice concentration by year from 1980 to 2004. 177

Figure 5.9. Average summer old sea ice concentration by year from 1980 to 2004. 179

Figure 5.10. Average summer first year sea ice concentration by year from 1980 to 2004. 180

Figure 5.11. Winter sea ice concentration trend (%/year) in the left column and statistical significance in the right column for (a, b) old sea ice, (c, d) first year, (e, f) thick first year, (g, h) young sea ice. Black areas in the right column indicate statistical significance at the 99% level, dark grey areas indicate statistical significance at the 95% level and light grey areas indicate statistical significance at the 90% level. 182

Figure 5.12. Summer sea ice concentration trend (%/year) in the left column and statistical significance in the right column for (a, b) old sea ice and (c, d) first year sea ice. Black areas in the right column indicate statistical significance at the 99% level, dark grey areas indicate statistical significance at the 95% level and light grey areas indicate statistical significance at the 90% level. 185

Figure 5.13. Mean break-up (a) start year-week (b) start occurrence (%), (c) start mean standard deviation (weeks), (d) end year-week (e) end occurrence (%) and (f) end mean standard deviation (weeks) for each grid cell between 1980 and 2004. Occurrence is defined as the amount of times each grid cell began to break up or finished breaking up in 25 years, expressed as a percent. 189

Figure 5.14. Mean freeze-up (a) start year-week (b) start occurrence (%), (c) start mean standard deviation (weeks), (d) end year-week (e) end occurrence (%) and (f) end mean standard deviation (weeks) for each grid cell between 1980 and 2004. Occurrence is defined as the amount of times each grid cell began to freeze up or finished freezing up in 25 years, expressed as a percent. 191

Figure 5.15. Sea ice concentration in Amundsen Gulf averaged over all grid cells for each year studied by year-week. Total (black), old (blue), first year (green), new & young (red). 192

Figure 6.1. The southern Beaufort Sea and Amundsen Gulf study area, (Inset) Amundsen Gulf's location in the Canadian Arctic. 206

Figure 6.2. Sea ice concentration (tenths) over the study area: (a) median total sea ice concentration for September 2003, (b) median old sea ice concentration for September 2003 and (c) median new-and-young sea ice (<30cm thick) concentration for October 2003. 216

Figure 6.3. The monthly evolution of the interface between mobile very close pack ice in the southern Beaufort Sea and western Amundsen Gulf and the landfast sea

ice of Amundsen Gulf. Note the consist shape of the mobile sea ice tongue in western Amundsen Gulf beginning in February. 218

Figure 6.4. (Left) Study area map with RGPS grid position (black dots) bisected into the southern Beaufort Sea and Amundsen Gulf by black line. (Right) Mean sea ice speed and direction the ice *is moving* in the SBS and AG (black, dotted lines) overlaid with mean wind speed and direction the wind *is going towards* (blue lines) in the study area. 220

Figure 6.5. Modeled year-day of freeze-up in fall 2003 (YD306 = 2 Nov, YD326 = 22 Nov). 224

Figure 6.6. Modeled monthly sea ice thickness in the study area in winter 2004. 225

Figure 6.7. Map of western Amundsen Gulf (center panel) showing sea ice thickness sections flown by the IcePic system on May 8 2004 surrounded by semi-log probability distribution functions for sea ice thickness of each each section in the map. 227

Figure 6.8. Percentage of level sea ice, leads and ridged/rubbed sea ice in each ice thickness section mapped in Figure 6.7. 228

Figure 6.9. (Center) Modeled sea ice thickness on 8 May 2004 overlaid by the position of sea ice thickness sections on the same day. (Left and right panels) Ice thickness sections corresponding to the section positions at center (in blue). 230

Figure 6.10. Modeled break-up (YD 175 = 23 Jun, YD183 = 1 Jul) in spring 2004. 234

Figure 6.11. Radarsat-1 ScanSAR (σ^0) images of the advection of the mobile very close pack ice out of western Amundsen Gulf between May 24 and June 6 2004. 236

CHAPTER ONE: INTRODUCTION

1. Rationale and Context

The Arctic has undergone profound change in the last thirty years as a result of the earth's warming climate. Sea ice controls the transfer of energy, mass and momentum between the ocean and atmosphere in the Arctic, playing a vital role in the modulation of the earth's climate systems. Arctic multi-year sea ice extent in particular continues to be a casualty of global climate change, having undergone near continual reduction in minimum extent since the beginning of the satellite record in 1979, and especially since 1996 (*Parkinson and Cavalieri, 2008; Comiso et al., 2008*).

Arctic multi-year sea ice thickness has also undergone substantial change in the past fifty years, thinning variably in different areas of the Arctic Ocean by as much as 42% between the 1960's and 1990's (*Rothrock et al., 1999; Hilmer and Lemke, 2000*). However, what we know of Arctic sea ice volume is limited; it has been explored by only a small relative number of researchers, using field data that is sparse in space and time due to constraints on collecting it. Therefore, it is often modeled without confirmation of the model's accuracy. While that multi-year sea ice extent and volume have been decreasing, the role of first-year sea ice in the Arctic ecological and climate system has been growing because the relative portion of Arctic sea ice winter extent that is seasonal has increased (*Parkinson and Cavalieri, 2008*). So, it follows that a study of the interaction of first-year sea ice with the ocean and atmosphere, as well as its interaction with multi-year sea ice are important steps in understanding how the Arctic ocean-sea ice-atmosphere system

might operate in an icescape dominated by seasonal sea ice. It also follows that the study of Arctic sea ice should include the interaction of multi-year and seasonal sea ice, and should be expanded to studies of volume in addition to extent. Polynyas are natural laboratories for this type of study due to the occurrence of many different sea ice types at any time during the annual cycle.

The thesis first examines the best way to accurately obtain measurements of snow and sea ice volume. Second, it examines the effect that a thermodynamically melting snow and sea ice volume has on the summer upper ocean mixed layer in the adjacent water column. Third, the thesis explains how different sea ice volumes interact spatially and temporally at the regional scale in a physically and biologically significant area of the Canadian Arctic. Finally, the thesis determines how thermodynamic and dynamic processes contribute to the interaction of different sea ice volumes over an annual cycle.

2. Science Objectives

Recognizing that thermodynamic and dynamic sea ice processes are concomitant in nature, the overall goal of this research is to enhance the understanding of thermodynamic and dynamic processes in snow-covered sea ice across the ocean-sea ice-atmosphere interface by teasing apart these processes so as to understand them. In order to achieve this goal, the following science objectives have been satisfied, in large part by studying the North Water and Cape Bathurst Polynyas of the Canadian Arctic where the interaction of the ocean, sea ice and atmosphere are highlighted throughout the annual cycle:

- 1) Determine the physical and dielectric properties of a snow-covered sea ice volume.
- 2) Using the properties obtained in (1), develop a new method for the accurate characterization of separate snow and sea ice thickness at the same location that enables these data to be collected at high frequency in both time and space enabling high quality sea ice and snow volume data to be collected in the future.
- 3) Evaluate the interaction of a volume of melting first-year sea ice with the adjacent ocean column in producing the biologically significant upper ocean mixed layer in a region of the Canadian Arctic.
- 4) Assess the historical sea ice mass balance by type for the Cape Bathurst Polynya which recurs each year, determine how that sea ice mass balance has changed, and discern the variability of break-up, freeze-up and the evolving sea ice cover in the area.
- 5) Describe in detail the interaction of thermodynamic and dynamic processes at the ocean-sea ice interface that give rise to the operation of the Cape Bathurst Polynya annually, given context by the historical information obtained as a result of (4).

3. Research Structure

This thesis is composed of seven chapters. Chapter two consists of a literature review describing the physical nature of dynamic and thermodynamic processes in snow covered sea ice and assesses the relative contributions of oceanic

and atmospheric forcing in these processes across the ocean-sea ice-atmosphere interface. It describes how climate change may affect the timing and rate of these processes. This chapter also establishes the nomenclature used in the subsequent chapters. Chapters three to six address the science objectives.

Chapter three describes the physical and dielectric properties of sea ice, river ice and the snow cover that resides atop each. It presents collocated physical measurements of the three media and their ground penetrating radar signatures at two frequencies (250MHz and 1GHz) in order to investigate the accurate characterization of snow, river ice, and sea ice thickness prior to spring melt. The material in chapter three appears in this thesis as it has been published in the peer-reviewed literature in the journal *Cold Regions Science and Technology*:

Galley, R.J., M. Tractenberg, A. Langlois, D.G. Barber, 2009. Observations of geophysical and dielectric properties and ground penetrating radar signatures for discrimination of snow, sea ice, and freshwater ice thickness. *Cold Regions Science and Technology*, 57: 29-38.

Chapter four investigates the relationship between the time-dependent thermo-physical state of landfast first-year sea ice and its relationship to the development of the upper ocean mixed layer in the adjacent water column during the spring and summer melt season. The material in chapter four appears in this thesis as it has been published in the peer-reviewed literature in the *International Journal of Remote Sensing*:

Galley, R.J., D.G. Barber and J.J. Yackel, 2007. On the link between SAR-derived sea ice melt and the development of the summer ocean mixed layer in the North Open Water Polynya. *International Journal of Remote Sensing*, 28(18): 3979-3994.

Chapter five describes the spatial and temporal evolution of sea ice in several pertinent thickness/age classes in the Cape Bathurst Polynya in the southern

Beaufort Sea and Amundsen Gulf. It investigates trends in sea ice concentration by sea ice type in both the summer and winter and discusses in detail the spatial and temporal variability of sea ice freeze-up and break-up in the region. Further, the material present in Chapter five gives historical context to much of the material presented in Chapter six. The material in chapter five appears in this thesis as it has been published in the peer-reviewed literature in the *Journal of Geophysical Research – Oceans*:

Galley, R.J. E. Key, D.G. Barber, B.J. Hwang, and J. Ehn, 2008. Spatial and temporal variability of sea ice in the southern Beaufort Sea and Amundsen Gulf: 1980-2004. *Journal of Geophysical Research*, 113, C05S95, doi: 10.1029/2007JC004553.

Chapter six presents a detailed explanation of the physical processes at the ocean–sea ice–atmosphere interface that contribute to the operation of the Cape Bathurst Polynya over an annual cycle. The material in chapter six has been peer-reviewed by the *Journal of Geophysical Research – Oceans*. The suggestions provided by an associate editor and two anonymous reviewers have been addressed and are included in this thesis in the form in which it has been resubmitted to the *Journal of Geophysical Research – Oceans*.

Chapter seven summarizes the results of chapters three through six and presents concluding remarks, including recommendations for future work.

Appendix A describes the contributions of collaborating authors to the work presented in chapters three to six.

Appendix B contains a list of contributions made as co-author during my time as a Ph.D. student at the University of Manitoba.

Literature Cited

Comiso, J. C., C.L. Parkinson, R. Gersten and L. Stock, 2008. Accelerated decline in the Arctic sea ice cover. *Geophys. Res. Lett.*, 35, doi: 10.1029/2007GL031972.

Hilmer, M. and P. Lemke, 2000. On the decrease of Arctic sea ice volume. *Geophys. Res. Lett.*, 27(2): 3751-3754.

Parkinson, C.L. and D. J. Cavalieri, 2008. Arctic sea ice variability and trends, 1979-2006. *J. Geophys. Res.*, 113, doi: 10.1029/2007JC004558.

Rothrock, D.A., Y. Yu and G.A. Maykut, 1999. Thinning of the Arctic sea-ice cover. *Geophys. Res. Lett.*, 26(23): 3469-3472.

CHAPTER TWO: BACKGROUND AND LITERATURE REVIEW

1. Sea ice thermodynamics

Freezing seawater

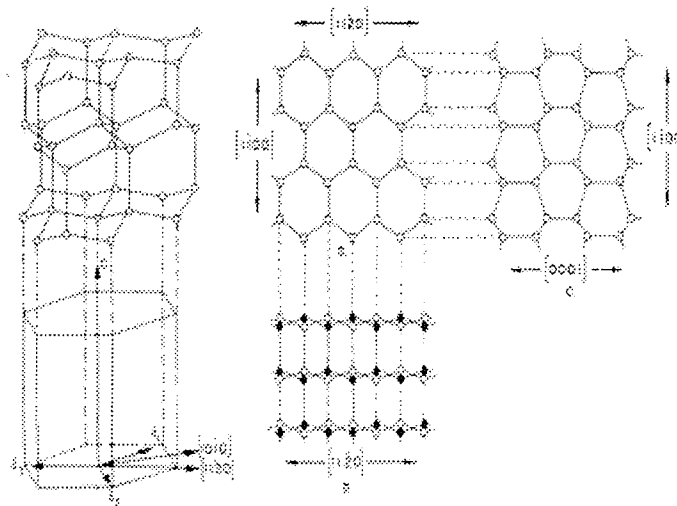
In freshwater, the temperature of maximum density is 4°C, below which water becomes less dense and remains at the surface, forming ice crystals at 0°C. With the addition of salt, the temperature of maximum density is depressed until salinity reaches 24.695psu (marking the transition from estuarine to the oceanic environment) where it coincides with the freezing point. In seawater (>24.694psu), vertical convection resulting from the densification of cooling water at the surface and further mixed by wind and waves occurs until the freezing point (-1.86°C for 34psu) is reached within the ocean surface layer defined at some depth by the pycnocline.

Ice Crystal Structure

Sea ice floats on the ocean surface because solid H₂O is less dense than liquid H₂O, a geophysical idiosyncrasy owed to the open structure of ice made possible by hydrogen bonding. A hydrogen bond is formed in H₂O when a hydrogen (H) atom, bonded covalently to a highly negative oxygen (O) atom is also attracted to a highly negative oxygen atom of a nearby molecule. The O atom covalently bonded to one H atom pulls an electron pair away from the H nucleus leaving the proton nucleus unshielded, giving it the ability to be attracted to a lone pair of electrons on a nearby O atom in another H₂O molecule forming intermolecular bonds. At 0°C water molecules are packed more tightly together in liquid form than in solid form, making

the solid form less dense. It is this property of H₂O that enables seas to freeze from the surface downward in part providing conditions for the sustainability of Arctic marine ecosystems.

Figure 2.1. The crystal structure of ice Ih, indicating the basal (0001) plane, the c-axis and prism face (1100). From Weeks and Ackley (1986)



More than nine different crystal forms of ice (polymorphs) exist at various densities (depending on their atomic arrangement at lower temperatures and higher pressures) than exist on the earth's surface; however under normal conditions the only structure encountered is ice Ih, where 'I' refers to the specific polymorph and 'h' refers to its hexagonal symmetry (Hobbs, 1974). In the crystal structure of ice Ih, each oxygen atom is at the center of a tetrahedron consisting of an oxygen atom bonded at each of the apices. At 0°C, the distance between oxygen atoms is 0.276nm (Weeks and Ackley, 1986) creating a low density, open arrangement. Within the structure of ice Ih (Figure 2.1.), the basal (0001) plane refers to a series of parallel planes of oxygen atoms in close proximity,

perpendicular to which occur the prism face (1100) plane and principle crystallographic (c-) axis, resulting in anisotropy with respect to the physical and mechanical properties of ice (*Weeks, 1998*). Each crystal unit cell of ice Ih contains four oxygen atoms resulting in preferential cleavage of the crystal structure along the basal (a-axes) plane, requiring only two bonds to be ruptured. Cleavage along any other plane requires that at least four bonds are broken. The basal plane is usually the plane of fastest ice growth, resulting in new ice crystals with thickness-to-width ratios ranging from 1:10 to 1:100 (*Hobbs, 1974*) because less energy is required to add atoms to the existing basal plane than to begin forming a new plane. These a-axis directions are equivalent in length, and correspond to (i) the arms of dendritic sea ice crystals growing on the freezing ocean surface, (ii) the preferred direction for downward growth of sea ice crystals in a sheet, (iii) the internal melt features which form inside the ice crystal structure, and (iv) the arms of snowflakes growing from vapour (*Weeks, 1998*).

Sea ice growth, structure and properties

Frazil ice

In quiescent conditions, a skim of crystals forms as 2-3mm diameter discs floating on the surface forms and grows outward in the a- and b-axis directions with its c-axis oriented vertically (*Weeks, 1998*). These individual crystals grow outward until the original disc shape is no longer stable, resulting in a hexagonal shape with fragile, dendritic arms extending across the surface. Frazil crystals grow into water which has been super-cooled by 0.01 to 0.1°C, beginning by natural seeding and

proceeding quickly by collision breeding (*Weeks, 1998*). Even slight motion causes conditions where the long crystal arms break up, eventually creating a slushy suspension of arms and disc shapes in water which become new nuclei nearest the surface called frazil, where discs and dendritic crystals can be up to 10mm thick with randomly oriented c-axes (*Weeks, 1998*). With time frazil coagulates into a layer on the surface termed grease ice due to its slick appearance (*WMO, 1970*). Further coagulation into an ice sheet occurs next forming a thin, elastic ice mat of ice termed first termed dark nilas when less than 5cm thick and then light nilas when less than 10cm thick (*WMO, 1970*), getting whiter as it thickens.

Frazil-Pancake cycle

In rough conditions such as those that occur at ice edges, not all frazil transitions smoothly from its liquid, slushy form to the more solid and elastic nilas. Vertical turbulence, waves and associated wind energy may keep substantial amounts of frazil ice in dense suspension near the ocean surface all the while undergoing cyclic compression as a result of a wave field (*Weeks and Ackley, 1986*). When frazil crystals are compressed, they form small pans of increasingly solid slush which grow larger by continual accretion of suspended crystals. Collisions between these pans while they grow larger result in raised rims of frazil occurring around them that drain, turning whiter in the process and giving ice an appearance similar to that of a pancake. Frazil ice continues to grow within the ocean surface layer, made possible by open water between pancakes able to dispose of latent heat to the atmosphere directly. Given wave field attenuation with distance from the ice edge,

pancakes coalesce into floes made up of several pancakes and eventually into an ice sheet where heat conduction upward through the ice layer becomes the primary mode of ice growth. During the consolidation process, individual pancakes and floes of several pancakes may be rafted, affecting their thickness, surface roughness and bottom roughness.

Congelation ice

Simply, congelation ice is that which has grown thermodynamically by accretion at the existing ice bottom, occurring first in the transition zone below the frazil layer, and then in the columnar zone.

Once direct heat transfer to the atmosphere has been cut off from the ocean below by a continuous sheet of sea ice in a region, the mechanism of further sea ice growth is restricted to the conduction of latent heat upward through the volume from the sea ice-seawater interface to the atmosphere, resulting in ice crystal formation at the bottom of the ice sheet. At this point the growth rate at the bottom of the ice sheet is determined by the temperature gradient and its effective conductivity (*Weeks and Ackley, 1986*) forming a transition zone within the crystal fabric of the sea ice sheet. As a contiguous layer of sea ice is formed, crystals lose some freedom with respect to their growth direction; unless the crystal c-axis is perpendicular to the sea ice-seawater interface, each crystal's growth interferes with the growth of other crystals (*Weeks and Ackley, 1986*). In this zone, ice crystals oriented with their c-axis perpendicular to the direction of heat conduction are geometrically selected, growing slightly faster than those not in the preferred c-axis

orientation (*Weeks, 1998*). Geometric selection is further rationalized by *Weeks and Ackley (1986)* using crystal growth theory which predicts that growth normal to the basal plane in ice would require the formation of a new plane of atoms, a process which takes more energy than adding atoms to an existing plane. Secondly, sea ice is a layered composite of ice and brine which is more thermally conductive perpendicular to the c-axis than parallel to it (*Weeks, 1998*). This transition region is typically 10-20cm thick in the Arctic (*Weeks and Ackley, 1986*) and eventually ends with all the basal planes parallel to the temperature gradient allowing latent heat to flow from the bottom of the sea ice to the atmosphere above in a thermodynamically efficient way.

Weeks and Ackley (1986) borrow from the characteristics of crystals in metal ingots in defining the columnar zone in sea ice as an area of pronounced crystal orientation with strong crystal elongation parallel to the direction of heat flow and increased crystal size with distance from the heat source. While it would be reasonable to assume that the c-axis alignment in this zone would be random, *Wadhams (2000)* notes that Russian literature contains observations of highly oriented c-axes in large areas within the Kara Sea (e.g. *Cherapanov, 1971*). It is now understood that c-axis alignment typically occurs when sea ice growth is influenced by a preferred shear current direction; ice crystals in this case orient themselves perpendicular to the current direction which may occur when the current is parallel to the shore in fast ice areas (*Weeks and Gow, 1978; Weeks and Gow, 1980*). As ice crystals grow downward along their a- and b-axes at the sea ice-seawater interface, currents parallel to the c-axes cause turbulent mixing of a solute-limited boundary

layer nearest the ice of slightly elevated salinity due to brine rejection that would otherwise slightly retard sea ice growth (*Weeks and Gow, 1978*).

Constitutional super-cooling in the skeletal layer

The physical characteristic of sea ice which allows for the formation of a non-planar, dendritic sea ice-seawater interface (the skeletal layer) is constitutional super-cooling (*Weeks and Ackley, 1986*) where water is cooled below its freezing temperature without changing phase. A gradient in salt concentration occurs as a result of brine rejection at the sea ice-seawater interface that gives rise to salt diffusion away from the interface and the diffusion of heat toward the interface (*Eicken, 2003*). The transfer of heat from the ocean to the sea ice interface (a transfer of momentum) is about ten times faster than the diffusion of salt away from the interface (a transfer of ions) (*Eicken, 2003*). A thin layer below the interface is formed which has been cooled but not yet salinated, cooling the seawater below its theoretical freezing point. In this layer, growing dendrites have the thermodynamic advantage of growing into water from which 'extra' heat can be extracted in comparison to the part of the dendrite above the constitutionally super-cooled layer. The salt rejected by the dendrite in the constitutionally super-cooled layer depresses the freezing point of brine between the dendrites above the constitutionally super-cooled layer. The constitutionally super-cooled layer determines most of the bulk salinity and microstructure of the growing sea ice sheet (*Eicken, 2003*).

Multi-year sea ice

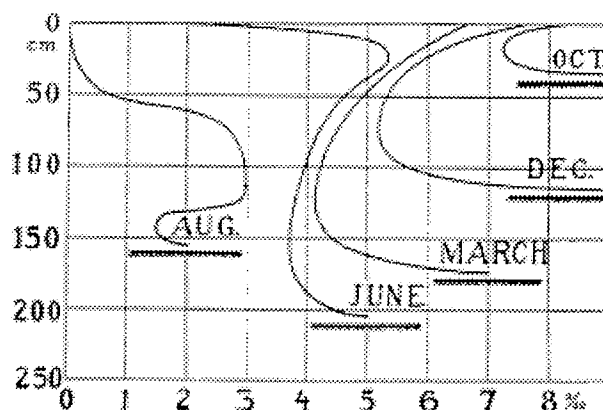
Arctic sea ice that has survived a summer melt season is termed second year sea ice, and then multi-year sea ice (MYI) once it has survived at least two summer melt cycles. Both these are subsets of old ice (WMO, 1970). Multi-year sea ice is typically characterized physically by (i) a hummocky surface which results from differential melt at areas which become ponded during summer and higher, drained areas, (ii) salinity that increases from near-zero above water to about 3psu at depth in the ice and (iii) in some cases thicknesses in excess of 2.5m, although evidence suggests that there is a trend toward thinning MYI in the Arctic (*McPhee et al.*, 1998; *Rothrock et al.*, 1999). Multiyear sea ice is also structurally different from first-year sea ice, as annual melt cycles not only alter the surface features of the sea ice, but also reduce its thickness from both the top and bottom. Over a summers' melt the surface frazil layer is eroded away, replaced above sea level with low density, drained hummocks in between melt ponds created as snow and ice melt drains to low lying areas. The sea ice bottom is also eroded in a similar fashion due to local differences in the optical and thermal properties of the snow-covered sea ice slab that will be discussed later. Congelation growth may occur at the ice bottom each winter.

Sea ice salinity and temperature

The strong polarity of H₂O molecules allows for sea salt ions to be surrounded with hydrate shells in seawater, but in sea ice the crystal structure severely restricts the size and number of sea salt ions that can be incorporated. The crystal structure

of ice Ih limits the size and charge of ions and/or molecules and the type of bond they may form to the point where only fluorine and ammonium ions and some gases are not rejected into the seawater below as the sea ice-seawater interface grows downward (*Weeks, 1998*). However, none of these compounds (e.g. F^- , HF, NH_4^+) are present in seawater to any great degree (*Weeks, 1998*). Ocean salts and ice Ih therefore do not form a solid solution, but rather the salinity of sea ice is the result of liquid inclusions of concentrated brine called brine cells/channels, due to the entrapment of seawater as ice grows.

Figure 2.2. The evolution of sea ice salinity with depth over time as determined by Malmgren (1927).



The fact that salt is included in sea ice differentiates it from all other floating ice, determining to the mechanical, thermal, and electromagnetic properties of the ice sheet (*Eicken, 2003*). In practice, c-shaped salinity profiles are characteristic of thin first-year sea ice, where the highest salinity values are found near the top and bottom of the profile with lower values occurring in the middle of the sea ice sheet

(Figure 2.2). As the ice grows thicker, the vertical extent of the lower salinity zone increases and the average salinity of the thickness decreases, but the c-shaped nature of the profile remains until late summer (Figure 2.2.). *Cox and Weeks* (1974) showed that there is a clear relationship between sea ice bulk salinity and sea ice thickness, consisting two separate linear trends, steeply sloped between 0 and 0.30m thickness and more shallowly sloped thereafter.

Brine cell formation and dynamics

As dendritic crystals advance downward the ice rejects brine solution into a thin layer immediately below the sea ice-seawater interface and it accumulates between the crystals. Ice bridges form between advancing dendrites as they grow, trapping brine solution in the interstices. The initial size of each brine cell is reduced further by freezing at its walls until the salinity of the remaining liquid brine is high enough to stop further decreases in size (~0.5mm diameter) (*Wadhams*, 2000). Brine cell formation occurs in a coordinated way, where sheet-like layers of cells form one below the next between growing dendrites. As a result of several studies (e.g. *Nakawo and Sinha*, 1984; *Cole and Shapiro*, 1988) *Weeks and Ackley* (1986) conclude that there occurs a positive correlation between the growth rate of a sea ice sheet and salinity. Further, the distance between adjacent layers of brine pockets (a_0) measured parallel to the crystal c-axis orientation is inversely proportional to the growth rate and smallest when the c-axis is perpendicular to the preferred growth direction (*Weeks and Ackley*, 1986). The salinity profile of a sea ice sheet is initiated by entrapment of salt, the amount of which depends on the

salinity of the seawater from which it forms (*Nakawo and Sinha, 1981*). Several physical processes occur throughout the growth of a sea ice sheet that reduces its salinity with time.

As soon as a brine cell is formed it is subject to the vertical temperature gradient responsible for the downward growth of the sea ice sheet. This gradient can easily reach $30^{\circ}\text{C}/\text{m}$, which equates to a temperature difference of 0.015°C from the bottom to the top of a 0.5mm diameter brine cell (*Wadhams, 2000*). Brine cells exist in thermal equilibrium with the solid ice surrounding them at very cold temperatures because their salinity prevents them from freezing solid, but a small vertical temperature gradient exists across the cell as long as the ocean is warmer than the atmosphere above it, allowing freezing to occur at the top of the cell. This freezing increases the salinity of the brine contained in the cell, which reduces the freezing point of the solid ice at the bottom of the cell causing melt, allowing movement of the cell downward in the sea ice sheet (*Wadhams, 2000*). As the brine cell moves in this fashion, it moves down the temperature gradient, becoming larger and eventually draining from the bottom of the sea ice sheet (*Wadhams, 2000*). The speed at which brine cells migrate downward may increase due to imperfections in the sea ice crystal fabric the cell may encounter (*Wadhams, 2000*).

Brine expulsion occurs when the sea ice surrounding a brine cell cools as the sheet thickens causing thermal contraction in the ice greater than in the brine cell. This may rupture the cell perpendicular to the c-axis due to increased internal pressure, forcing the brine upward or downward (*Weeks, 1998*).

Gravity drainage is an important desalination mechanism of a sea ice sheet over time. For this mechanism to occur, the brine cells must be connected by a system of very fine pores which could allow hydrostatic pressure (pressure exerted by a liquid at rest) created in the portion of the sea ice sheet which is above sea level to be transmitted between them (*Weeks and Ackley, 1986*). A density gradient within the interconnected brine network helps drive brine downwards whenever a positive downward temperature gradient exists; this causes brine densities to be higher in the cold upper section of the ice sheet and lower closer to the warm ocean (*Cox and Weeks, 1975*).

Brine drainage channels are the principle mechanism of winter brine movement within sea ice. Their geometry is similar to a vertically oriented river attended to radially by smaller streams (*Weeks and Ackley, 1986*). These channels are enlarged through time as colder brine from the top portion of the ice sheet moves downward and is warmed above its equilibrium temperature by horizontal heat flow through the ice which melts the channel wall, cools the ice, and dilutes the brine and re-establishing thermal equilibrium (*Weeks and Ackley, 1986*).

The last significant method of sea ice desalination is flushing, which is simply gravity drainage that begins with the sea ice melt season. Flushing begins with snowmelt on top of the sea ice providing a hydrostatic head and requires that the sea ice is permeable. It is thought to proceed using brine drainage channels formed throughout the winter where heat from melt water above the freezing point melts sea ice, enlarging brine channels as it moves downward (*Wadhams, 2000*).

Solid salts in sea ice

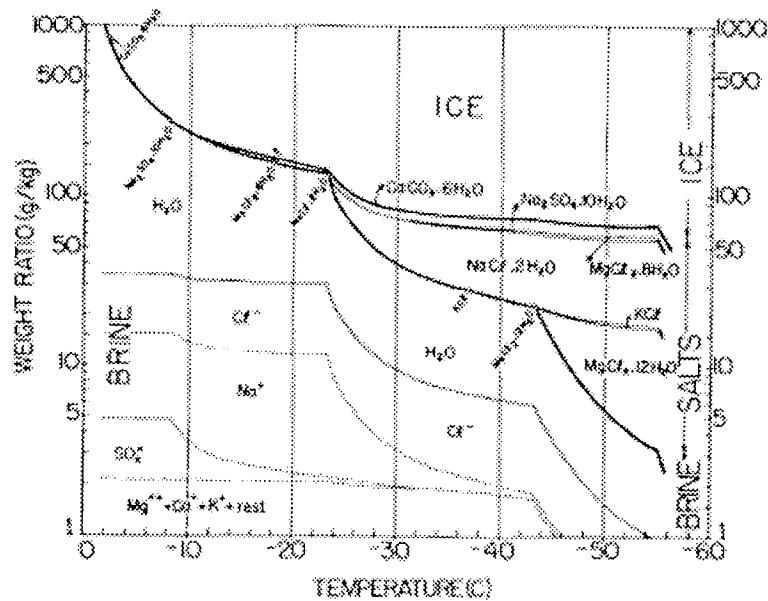
Sea ice also contains solid salts in the form of hydrates: $\text{NaCl}\cdot 2\text{H}_2\text{O}$, $\text{Na}_2\text{SO}_4\cdot 10\text{H}_2\text{O}$, $\text{CaCO}_3\cdot 6\text{H}_2\text{O}$, which precipitate out of solution at specific temperatures of -22.9°C , -8.2°C and -2.2°C respectively (*Weeks and Ackley, 1986*). Other salts including KCl, $\text{MgCl}_2\cdot 12\text{H}_2\text{O}$ and $\text{CaCl}_2\cdot 6\text{H}_2\text{O}$ are not usually found in sea ice samples because they do not precipitate until temperatures reach -36.8°C , a temperature at which sea ice is rarely seen (*Weeks and Ackley, 1986*). Larger brine inclusions collapse into smaller, near-spherical brine pockets with decreasing sea ice temperature (*Grenfell, 1983*). *Light et al.* (2003) documented the thermal evolution of the microstructure of first-year sea ice in a temperature controlled environment, showing that the shape, size and number density of brine inclusions vary with sea ice temperature. Brine inclusions are larger and have a lower number density with increased temperature and the cross-sectional area of inclusions increases dramatically below -23°C and above -5°C (*Light et al., 2003*).

Sea ice phase relationships

The relationship between phase composition, amount and temperature in sea ice, is best understood by appreciating the phase diagram created by *Assur* (1958) (Figure 2.3.), which was created using an idealized standard seawater solution with salinity of 34.325 and a freezing temperature of -1.86°C . As the temperature is depressed below freezing, (assuming that each phase is in thermodynamic equilibrium) the mass fraction of ice increases steadily. Because salts dissolved in the seawater cannot be incorporated into the crystal structure of

ice Ih, the concentration of salt in the entrapped liquid brine increases, which decreases the freezing point of the brine. As the temperature is depressed below -8.2°C , the brine solution present as inclusions within the ice crystal structure becomes supersaturated with sodium sulfate (Na_2SO_4), which precipitates as a hydrate ($\text{Na}_2\text{SO}_4 \cdot 10\text{H}_2\text{O}$) called mirabilite. Salt hydrates continue to be precipitated with decreased sea ice temperature (Figure 2.3).

Figure 2.3. Sea ice phase diagram indicating the (top) mass fraction of ice (middle) solid salts and (bottom) liquid brine with respect to temperature in a closed volume of standard seawater. From Assur (1958).



In order to determine the total porosity of sea ice, an important physical characteristic both thermally and mechanically, the gas and brine volumes of a sea ice sampled must be determined. Using equations derived by *Cox and Weeks* (1983)

which account for solid salt (after *Frankenstein and Garner* (1967) who did not account for solid salt) relative brine volume, solid salt, and gas volumes may be calculated given density, temperature and salinity between -2°C and -30°C. The brine volume fraction (v_b) in sea ice may be determined because of the requirement that brine and sea ice be in thermal equilibrium (*Cox and Weeks*, 1983):

$$v_b = \frac{\rho_{si} S_{si}}{F_1} \quad [2.1]$$

where ρ_{si} is the sea ice density ($\text{g}\cdot\text{cm}^{-3}$) and S_{si} is the sea ice salinity (ppt). Sea ice air volume fraction (v_a) may also be calculated:

$$v_a = \frac{1 - \rho_{si}}{\rho_{pi} + v_b F_2} \quad [2.2]$$

using ρ_{pi} (the density of pure ice) = $0.917 - 1.403 \times 10^{-4} T_{si}$, where T_{si} is the sea ice temperature in °C. In these equations, F_1 and F_2 represent constants dependent on temperature found in *Cox and Weeks* (1983) and *Leppäranta and Manninen* (1988).

Snow cover on sea ice - Formation, physical and thermal properties and distribution

Snow cover is critically important to the thermodynamic nature of Arctic sea ice. Snow begins in the atmosphere as gaseous H_2O and is made precipitable by condensation when the temperature is sufficiently reduced (*Granberg*, 1998). This allows the vapour pressure to become saturated, provided small particles exist in the clouds which act as nuclei (*Granberg*, 1998). Ice crystals may be formed by homogeneous nucleation, formed from super-cooled water droplets at -40°C, or by one of three types of heterogeneous nucleation: (i) ice nuclei may come in contact/collide with super-cooled water droplets, (ii) immersion-freezing may

occur when an ice nucleus is embedded in a super-cooled water droplet with a radius greater than 100\AA , or (iii) deposition of water vapour may occur on ice nuclei with a radius greater than 1000\AA (*Granberg, 1998*).

Once formed, snow crystals may grow from the vapour phase caused by increased super-saturation due to decreased temperature over the ice crystal compared to a water droplet, through aggregation in which ice crystals collide and to form larger ones, or by riming in which super-cooled water adheres to the ice crystal. These particles become snowflakes, whose shape depends on the amount of super-saturation, the temperature and the type of nuclei from which they formed and may change shape as they fall through the atmosphere due to changing temperature and vapour pressure (*Granberg, 1998*).

Snow consists of ice, air, and depending on temperature, water vapour, brine, and/or solid salts. Snow on sea ice may range in density between about $100\text{kg}\cdot\text{m}^{-3}$ and $450\text{kg}\cdot\text{m}^{-3}$ (*Mellor, 1977; Barber et al., 1995; Warren et al., 1999; Sturm et al., 2002; Langlois et al., 2007*). Destructive metamorphism begins as soon as the snow reaches the surface and becomes part of the snow pack (*Granberg, 1998*). On sea ice, snow crystals are no longer in equilibrium with air strongly super-saturated with water vapour, so in order to maintain equilibrium with the snow, the specific surface area of the crystal must decrease dramatically (*Granberg, 1998*). Vapour pressure gradients heat concave parts of the ice crystal using latent heat released in condensation, and cool convex parts of the crystal by evaporation creating similarly uniform ice temperature conditions under which vapour transfer occurs due to conduction between areas with small temperature differences (*Granberg, 1998*).

The physical nature of snow crystals in the snow pack evolves from deposition to melt, but initially snow on sea ice is typically first characterized as either dry or wet.

Dry snow may be further subdivided into equilibrium growth grains or kinetic growth grains (e.g. *Colbeck, 1982*). In the absence of a large temperature gradient, equilibrium growth crystals are formed at comparatively higher temperatures and slower growth rates and limited by vapour diffusion; conditions which allow growth on each crystal face to be nearly equivalent resulting in well rounded grains (*Colbeck, 1982*). In the presence of a large temperature gradient, the vapour pressure gradient increases across the snow crystal and growth occurs rapidly resulting in snow grains which are faceted and occur at the expense of rounded, equilibrium forms (*Colbeck, 1982*), a process further enabled by convection (*Sturm, 1991*). *Armstrong (1980)* theorized that the critical vapour pressure gradient enabling kinetic growth to occur is $0.05\text{mbar}\cdot\text{cm}^{-1}$, which would be formed by a temperature gradient of $10^{\circ}\text{C}\cdot\text{m}^{-1}$, although heat transfer depends to a certain extent on snow temperature and density.

Colbeck (1982) subdivides wet snow into the pendular (unsaturated snow where air occupies the pore spaces) and funicular (saturated snow where water occupies the pore spaces) regimes at less than and greater than 7% liquid water-by-volume respectively. The pendular regime is characterized by of hundreds of grains adhered to one another three or four at a time creating large single clusters with densities of $0.5\text{-}0.6\text{kg}\cdot\text{m}^{-3}$ which occur in snow packs of relatively low density due to the amount of air present between them (*Colbeck, 1982*). The funicular regime creates well-rounded crystals because the thermal conductivity of water is much

greater than that of air, allowing quicker heat transfer along small temperature gradients (Granberg, 1998). Barber *et al.* (1995) showed that the size and shape of snow grains occurs as a function of depth, with the largest grains occurring in the most saline layer closest to the sea ice surface.

Snow on sea ice in the Arctic accumulates rapidly in September and October before slowing in November to almost nil in December and January and then accumulating more rapidly again from February to May (Warren *et al.*, 1999). Accumulation rates are geographically variable, but by February snow depth across the Arctic was found to be uniform around 30cm over multi-year sea ice and thinner over seasonal sea ice (~23cm in April and May) (Warren *et al.*, 1999). Snow is affected throughout its annual cycle by precipitation and wind-driven redistribution events as well as the surface characteristics of the sea ice.

Thermal properties and the surface energy balance of snow-covered sea ice

The thermal properties of sea ice are important because they determine growth and melt rates and in particular phase transitions, which occur during these processes. Of particular importance are thermal conductivity, specific heat, latent heat of fusion and the coefficient of extinction for radiation (Wadhams, 2000). Without knowledge of these parameters the temperature, variation in thickness or heat exchange of a snow-covered sea ice slab cannot be determined.

Sea ice and snow alter the surface energy exchange between the atmosphere and ocean, changing the balance of the exchange of radiation, convection of sensible and latent heat, conduction and ocean heat flux (Maykut, 1986). A surface is defined

as a zero-mass plane where energy input must equal energy output (*Oke, 1987*) under the convention that positive terms represent energy added to the system and negative terms represent energy lost by the system, but the Arctic reality is that shortwave radiation penetrates the surface affecting the internal energy of the snow and sea ice volume through changes of phase and temperature.

Several studies have dealt with Arctic surface energy fluxes (*Persson et al., 2002*; see table 6) but typically contain some parameterization of fluxes with inherent inaccuracies. Using observed values, *Persson et al. (2002)* describe the annual evolution of the surface energy balance and the near-surface environment at one location in the Beaufort Sea pack between 1997 and 1998. On a day-to-day basis, all of the surface energy budget terms vary considerably due to substantial variability in both shortwave and longwave fluxes, and turbulent fluxes resulting in constant variation in the total energy flux at the snow or sea ice surface (F_{tot}) (*Persson et al., 2002*). In winter, F_{tot} ranges from $-25\text{W}\cdot\text{m}^{-2}$ to $12\text{W}\cdot\text{m}^{-2}$ when it is cloudy and the net longwave flux is near zero (*Persson et al., 2002*). In July it ranges from $37\text{W}\cdot\text{m}^{-2}$ to $129\text{W}\cdot\text{m}^{-2}$ (*Persson et al., 2002*).

Between December and February, air temperatures range between -40°C and -19°C , often undergoing transitions related to the occurrence of low clouds (*Persson et al., 2002*). During periods of extreme cold, the surface temperature has been up to 5°C lower than the 10m-air temperature (*Persson et al., 2002*). The Arctic spring transition occurs in March and April, and the summer melt season begins at the end of May when near-surface temperatures hover around 0°C , until the middle of August (*Persson et al., 2002*). Winds tend to be easterly in the spring and fall,

northerly in the winter and southerly in the summer with the strongest winds in the winter and weakest winds in the summer (*Persson et al., 2002*).

Radiative fluxes

The Stefan-Boltzmann law dictates that the total energy radiated from a body (j^* , $\text{W}\cdot\text{m}^{-2}$) per unit area is proportional to its absolute temperature taken to the fourth power:

$$j^* = \varepsilon\sigma T^4 \quad [2.3]$$

where σ is the Stefan-Boltzmann constant ($5.67 \times 10^{-8} \text{W}\cdot\text{m}^{-2}\text{K}^{-4}$), and T is the absolute temperature of the material (in $^{\circ}\text{K}$) and ε is the emissivity of the material. Emissivity is the fraction of energy radiated from a material ($\varepsilon < 1$) compared to energy radiated from a perfect emitter ($\varepsilon = 1$) at the same temperature. Radiative energy which reaches the earth is divided up into shortwave (F_r) and longwave (F_L) spectra, whose intensity maxima occur at wavelengths (λ) of $0.5\mu\text{m}$ ($\lambda = 0.3\text{-}3\mu\text{m}$) and $12\mu\text{m}$ ($\lambda > 3\mu\text{m}$) respectively. Almost no overlap occurs in their distributions (*Maykut, 1986*) which are further divided into their up-welling (\uparrow) and down-welling (\downarrow) components.

Incoming shortwave radiation (F_r) is seasonally variable in the Arctic and asymmetrically large before and during the summer solstice, where it reaches about $300 \text{W}\cdot\text{m}^{-2}$, when it then monotonically decreases to almost zero in December and January (*Maykut, 1982; Maykut, 1986; Ebert and Curry, 1993; Lindsay, 1998; Persson et al., 2002*: see figure 22b) varying based on changes in cloud cover and albedo.

The net shortwave maximum typically occurs near the summer solstice in combination with rapidly decreasing surface albedos (*Persson et al.*, 2002).

The optical properties of a material are a very important component of the Arctic sea ice heat balance because they determine its interaction with shortwave radiation, which drives the annual summer melt of Arctic sea ice (e.g. *Maykut and Untersteiner*, 1971; *Ebert and Curry*, 1993). Albedo (α) is the fraction of incident solar radiation which is reflected from a surface. *Perovich et al.* (2002) indicates that the albedo at a particular wavelength is:

$$\alpha(\lambda) = \frac{F_r^\uparrow(\lambda)}{F_r^\downarrow(\lambda)} \quad [2.4]$$

and the total (wavelength-integrated) albedo is the ratio of the reflected irradiance to the incident irradiance is:

$$\alpha_t = \frac{\int_{300}^{3000} \alpha(\lambda) F_r^\uparrow(\lambda) d\lambda}{\int_{300}^{3000} F_r^\downarrow(\lambda) d\lambda} \quad [2.5]$$

Albedos vary little between 400-700nm through most of the visible spectrum and decrease in the red wavelengths beyond 700nm due to the absorption of these wavelengths by liquid water (*Maykut*, 1986). At the red end of the visible spectrum, light penetration is small, making α_λ dependent on the properties of the surface while in the short, blue wavelengths α_λ is determined by backscatter from the medium beneath the surface layer (*Maykut*, 1986).

Perovich et al. (2002) determined that for more than nine months over an entire annual cycle, the albedo of a multiyear ice cover is spatially uniform and high

(0.8-0.9). In summer, however, albedo decreases and becomes more spatially variable, going from 0.1 over leads to 0.2 for dark melt ponds to 0.4 for light melt ponds to 0.6-0.7 for melting multi-year sea ice (*Perovich et al., 2002*). The albedo of different surface types varies differently with time; bare multiyear sea ice changes little during melt due to continual renewal of the highly scattering surface layer, while melt pond albedos changed constantly with the area, depth and thickness of ice underneath them (*Perovich et al., 2002*). There occur five distinct phases of seasonal evolution over multiyear sea ice, which include dry snow ($\alpha = 0.8-0.9$), melting snow ($\alpha = 0.8-0.7$), pond formation ($\alpha = 0.7-0.5$), pond evolution ($\alpha = 0.5-0.4$) and fall freeze-up ($\alpha = 0.4-0.8$) (*Perovich et al., 2002*). Multiyear sea ice albedos are typically larger under the same conditions as first year sea ice as melting and drainage create a surface scattering layer atop the multiyear type.

In the case of seasonal sea ice, albedos are sensitive to thickness changes during the initial growth stages at all wavelengths; as sea ice thickens albedo increases rapidly due to increases in scattering opportunities created by air bubbles and entrapped brine (*Perovich, 1996*). This occurs until the ice is sufficiently thick that only a negligible amount of light penetrates to the ice bottom where it is backscattered without being absorbed (*Perovich, 1996*). At this point the sea ice is considered optically thick.

Absorption of incoming solar radiation is determined by properties of the material and the incidence angle of the incoming solar radiation. Extinction of solar radiation in a medium is governed by Beer's Law which states that extinction is

exponential with depth and represented by the spectral extinction coefficient ($\kappa(z,\lambda)$) such that:

$$I(z,\lambda) = I_o(\lambda)\exp\left(-\int_0^z \kappa dz\right) \quad [2.6]$$

where $I(z,\lambda)$ is the intensity of radiation at penetration depth (z), and $I_o(\lambda)$ is the net radiation which penetrated the surface:

$$I_o = \int_0^\infty (1 - \alpha)F_o(0,\lambda)d\lambda \quad [2.7]$$

and F_o is the net total shortwave radiation remaining at the surface (*Wadhams, 2000*). When applied to thermodynamic modeling, it may be sufficient to use a bulk extinction coefficient (k_z) calculated by weighing $\kappa(z,\lambda)$ by the shortwave energy distribution at depth (z) over the range of the shortwave spectrum (*Wadhams, 2000*).

The sea ice albedo feedback is a positive feedback mechanism which operates in the Arctic whenever shortwave occurs at the surface. This feedback occurs as increasing shortwave radiation at the snow/sea ice surface reduces the albedo of that surface. Any reduction of albedo allows more incoming shortwave to penetrate the surface, causing further melting, which in turn lowers the albedo. This feedback is particularly pronounced over snow covered sea ice because during spring melting, the amount of incoming shortwave radiation increases daily until the summer solstice and changes in albedo can be both drastic and extremely fast, potentially beginning with snow (0.9) and changing to a melt pond or even open ocean (0.1) a matter of days to weeks (e.g. *Curry et al., 1995*). Although the sea ice-albedo feedback mechanism is most often discussed with respect to the annual

evolution of a sea ice cover, evidence of large scale and inter-annual operation of this feedback has also been brought to light (e.g. *Perovich et al.*, 2008).

Surface temperature (T_{sfc}) is an important parameter in the surface energy balance, but difficult to measure directly (e.g. *Persson et al.*, 2002). It may be calculated from broadband longwave radiation flux measurements using equation 2.8:

$$T_{sfc} = \left\{ \frac{[F_L^\uparrow - (1 - \epsilon_s)F_L^\downarrow]}{[\epsilon_s \sigma]} \right\}^{0.25} \quad [2.8]$$

which is limited by the uncertainty in ϵ_s (surface emissivity) and errors in the radiative fluxes (*Persson et al.*, 2002). During their measurements, *Persson et al.* (2002) set $\epsilon_s = 0.99$ regardless of whether the surface was snow or sea ice based on a study done by *Grenfell et al.* (1998) where $\epsilon_s = 0.98-0.995$, suggesting that errors in the radiative fluxes would have a greater effect than small changes in ϵ_s .

Longwave radiation (F_L) dominates Arctic heat exchange during much of the year, having the net effect of removing heat from sea ice because the radiative temperature of sea ice is almost always higher than that of the atmosphere (*Maykut*, 1986). Longwave emissivities of sea ice, leads and melt ponds are near 0.97 while snow cover increases ϵ_L to 0.99 (*Maykut*, 1986). Incoming longwave over an annual cycle is lowest in December–February ($\sim 150 \text{ W}\cdot\text{m}^{-2}$) before increasing to a maximum of $\sim 300 \text{ W}\cdot\text{m}^{-2}$ in June, July and August (*Maykut*, 1982; *Maykut*, 1986; *Ebert and Curry*, 1993; *Lindsay*, 1998; *Persson et al.*, 2002: see figure 22c). Annually, the net longwave flux prescribes to one of two general modes, ranging between -50

and $-30\text{W}\cdot\text{m}^{-2}$ or near-zero, with its minimum occurring in early summer when clear skies prevail and the surface temperature is high (*Persson et al.*, 2002).

Influence of clouds

The influence of clouds on radiative fluxes is dependent on the cloud properties, namely cloud fraction, height, depth, amount of condensed water (*Curry and Ebert*, 1992). Extensive low clouds and substantial atmospheric water vapour present near the surface in summer and early autumn minimize net longwave losses by allowing near-surface atmospheric temperatures to nearly equal surface temperatures (*Maykut*, 1986). Fewer, higher clouds in the winter decrease atmospheric water vapour, increasing net longwave loss from the relatively warmer surface (*Maykut*, 1986).

Clouds also affect incoming shortwave radiation by diffusing it for much of the summer months, causing the aforementioned skewness in the distribution of F_r around the summer solstice by increasing the optical thickness of the atmosphere over time (*Maykut*, 1986). Clouds may reduce F_r by 50%, increasing the proportion of diffuse radiation reaching the surface which increases the albedos of snow and seawater by 8-12% versus clear sky due to their dependence on solar angle (*Grenfell and Perovich*, 1984; *Curry et al.*, 1996). Arctic clouds transmit energy between $0.7\mu\text{m}$ and $1.4\mu\text{m}$; absorbing almost all energy above $1.4\mu\text{m}$ (*Grenfell and Perovich*, 1984: see table 3; *Curry et al.*, 1996) leading to a larger relative contribution of reflective shorter wavelengths in cloudy conditions (*Maykut*, 1986). The total transmission of energy through clouds depends on the atmospheric water content

(Maykut, 1986: see figures 3 and 4). Curry and Ebert (1992) note that the phase and size of the cloud particles and is dominated by shortwave flux to the top of the atmosphere, and the average effect of polar clouds when compared to clear-sky conditions is to warm the surface in all months except July (Curry and Ebert, 1992). They attributed this net warming to the absence of incoming shortwave radiation during fall, winter and spring in combination high surface albedos. Clouds were found to cool the surface for about two weeks in summer by reflecting a larger portion of incoming shortwave radiation than the surface would if the sky was clear (Curry and Ebert, 1992). Similar results to those of Curry and Ebert (1992) were found by Zhang *et al.* (1996).

More recently, Intrieri *et al.* (2002) used an annual cycle of surface energy balance and cloud observations to examine the impact of clouds on both radiative and turbulent fluxes in comparison to fluxes in clear-sky conditions. Their results showed that over an annual cycle the net effect of Arctic clouds is to warm the surface save for a small time frame midsummer when the surface is cooled by the presence of clouds compared to what would occur in clear-sky conditions (Intrieri *et al.*, 2002: see figures 10 and 11). Intrieri *et al.* (2002) also note the importance of using appropriate albedo values, which may change the net surface cloud forcing by up to $40\text{W}\cdot\text{m}^{-2}$ and even change the sign of the forcing.

Turbulent fluxes

In addition to emitted longwave radiation, turbulent fluxes of sensible and latent heat are the only way for energy to flow from the surface to the atmosphere.

Although turbulent fluxes may be an order of magnitude or two smaller than radiative fluxes, their contribution to the energy balance is still significant when compared to net radiation (*Maykut, 1986*). The rate at which heat is transferred by the turbulent fluxes is dependent on surface roughness, wind speed, stability of the boundary layer and the size of the temperature and water vapour gradients (*Maykut, 1986*). Turbulent fluxes may be calculated using eddy correlation methods (e.g. *Ruffieux et al., 1995*) or the bulk aerodynamically formulae (e.g. *Lindsay, 1998*), the latter of which will be discussed next.

Sensible heat (F_s) refers to the addition or loss of energy from a body, sensed as an increase or decrease in its physical temperature. It may be calculated using a bulk aerodynamic formula:

$$F_s = \rho c_p C_s u (T_a - T_o) \quad [2.9]$$

where ρ is the surface air density (in $\text{kg}\cdot\text{m}^{-3}$), c_p is the specific heat of air (in $\text{J}\cdot\text{kg}^{-1}\text{K}^{-1}$), C_s is the bulk transfer coefficient for sensible heat (e.g. $C_s = 0.0023$ (*Lindsay, 1998*)), u is wind speed at the reference height, T_a is the air temperature at a reference height and T_o is the surface temperature.

The latent heat flux (F_E) derived from phase change may also be calculated using a bulk aerodynamic formula:

$$F_E = \rho L C_L U (q_{air} - q_o) \quad [2.10]$$

where L is the latent heat of evaporation (in $\text{J}\cdot\text{kg}^{-1}$, including the latent heat of melting if the surface is below freezing (*Lindsay, 1998*)) and C_L is the exchange coefficient for latent heat. The specific humidity at the reference height (q_{air}) and

the surface (q_o) are calculated using measured relative humidity (RH) and temperature according to:

$$q = RH \frac{0.622 e_{sat}}{p} \quad [2.11]$$

where p is the atmospheric pressure and the saturated partial pressure of water vapour (e_{sat}) is approximated by:

$$e_{sat} = \exp(-6763.6/T - 4.9283 \log T + 54.219) \quad [2.12]$$

Potential shortcomings of the bulk aerodynamic method include that the constants C_s and C_L are not necessarily constant, depending in reality on surface roughness and atmospheric stability (*Lindsay, 1998*). Further, they are derived using data at a reference height which assumes that wind, temperature and humidity profiles between the reference height and the surface are monotonic (*Lindsay, 1998*).

Sensible and latent heat fluxes vary considerably more than radiative fluxes over daily-weekly time scales, and increase in magnitude substantially during high wind speed synoptic events (*Ruffieux et al., 1995; Persson et al., 2002*). There seems to be some debate however, over the direction of these fluxes in part due to sea ice type/age over which they were measured as well as inter-annual variability and latitude. *Steffen and DeMaria (1996)* propose that the sensible heat flux over seasonal sea ice in winter (November, January and February) in Barrow Strait is largely positive, especially in November during the early stage of sea ice formation. Measurements of latent heat flux during the same period yielded small positive values in November and near-zero values in January and February (*Steffen and DeMaria, 1996*). *Ruffieux et al. (1995)* found that multiyear sea ice with adjacent

leads north of Prudhoe Bay, AK had a small, positive sensible heat flux for much of April before it became largely negative due to wind speeds in excess of $10\text{m}\cdot\text{s}^{-1}$ over about 5 days. Using forcing parameters from former Soviet Union Arctic drifting station (NP-30) for 1990, *Lindsay* (1998) found that the winter sensible heat flux was positive ($7\text{-}10\text{W}\cdot\text{m}^{-2}$) and negative only in May, when increasing F_r creates conditions where the surface is warmer than the air temperature. *Lindsay* (1998) found that latent heat flux was near-zero in the winter, while averaging about $-10\text{W}\cdot\text{m}^{-2}$ in June. Fluxes calculated by *Lindsay* (1998) agree well with fluxes from *Maykut* (1982) except for sensible heat flux in summer, which was similar in magnitude but opposite in sign. Recently, *Persson et al.* (2002) measured F_s and F_E during the SHEBA project (1997-1998) finding that F_s was small and negative for much of November through March before oscillating between small positive and negative values for the remainder of the time series ending in September. *Persson et al.* (2002) found that F_E was near-zero for much of the year, becoming positive in May and June ($\sim 12\text{W}\cdot\text{m}^{-2}$), then decreasing back to zero by July. The observed SHEBA annual cycle of turbulent fluxes is similar to previous studies (*Maykut*, 1982; *Maykut*, 1986; *Ebert and Curry*, 1993; *Lindsay*, 1998; *Persson et al.*, 2002) albeit composed of smaller F_s and F_E magnitudes.

Conductive flux

Sea ice grows downward due to the conduction of heat (F_c) from a warm ocean to a cold atmosphere during much of the year. Heat conduction in sea ice is a function of air volume in the ice, solid salt content and most importantly liquid

brine. Saline liquid at the freezing point in phase equilibrium with the surrounding ice absorbs latent heat when the ice warms, releasing it when the ice cools allowing brine cells to act as a thermal reservoirs which impede changes in temperature within the ice (*Wadhams, 2000*). The amount of heat conducted is controlled by the temperature gradient at the surface and the thermal conductivity of the ice (k_{si}):

$$F_c = k_{si} \left(\frac{\partial T}{\partial z} \right)_o \quad [2.13]$$

Thermal conductivity (k) is a measure of a material's ability to conduct heat (measured in $\text{W}\cdot\text{m}^{-1}\text{K}^{-1}$), or, the flux of heat through an area in time divided by a temperature difference over the distance traveled. *Untersteiner (1961)* approximated the thermal conductivity of sea ice as:

$$k_{si} = k_o + \frac{\beta S_i}{T_i} \quad [2.14]$$

where k_o is the thermal conductivity of pure ice at T_i ($k_o = 9.828^{(-0.0057T)}$, where T is the ice temperature ($^{\circ}\text{K}$) (*Yen, 1981*)), T_i the ice temperature ($^{\circ}\text{C}$), β is $0.13 \text{ W}\cdot\text{m}^{-1}$ and S_i is ice salinity. The approximation above neglected air bubble content, which is important because the thermal conductivities of brine and air are about 25% and 1% that of pure ice, respectively (*Wadhams, 2000*). Conduction by air bubbles in both brine and the ice was treated by *Ono (1968)* who showed that young ice which is warm and saline has a thermal conductivity 2-3 times less than colder, lower salinity ice. Sea ice thermal conductivity values vary slightly around $2.10 \text{ W}\cdot\text{m}^{-1}\text{K}^{-1}$ (*Makhtas, 1998; Pringle et al., 2006*) but k_{si} calculations do not take into account convection in brine or air, which would increase the thermal conductivity of warm saline ice (*Wadhams, 2000*).

The specific heat of a material is the quantity of heat required to change the temperature of one gram of the material by one degree (measured in $\text{J}\cdot\text{g}^{-1}\text{C}^{-1}$). *Ono* (1967) proposed an empirical relationship for the specific heat of sea ice (c_i),

$$c_i = c_o + aT_i + b \frac{S_i}{T_i} \quad [2.15]$$

where c_o is the specific heat of pure ice, ($2113\text{J}\cdot\text{kg}^{-1}\text{C}^{-1}$), T_i is in Celsius, S_i is ice salinity (psu) and 'a' and 'b' are constants of $7.53\text{J}\cdot\text{kg}^{-1}\text{C}^{-2}$ and $0.018\text{MJ}\cdot\text{C kg}^{-1}$ respectively. *Anderson* (1976) calculated the specific heat of snow (c_s , $\text{J}\cdot\text{kg}^{-1}\text{K}$) as a linear function of temperature:

$$c_s = 92.88 + 7.364T_s \quad [2.16]$$

where T_s is in Kelvin degrees.

The co-existence of solid and liquid phases in sea ice at temperature makes understanding latent heat of fusion less than straight-forward because theoretically it is the energy associated with a materials phase change from solid to liquid. As a result, calculation of latent heat of fusion (q) for sea ice is typically limited to temperatures above -8.2°C , below which precipitation of sodium sulfate surrounded by a hydrate shell complicates the situation, but is accounted for by *Ono* (1968) and summarized by *Yen et al.* (1991) in equation 2.17:

$$q_i = 4.187(79.68 - 0.505T_i - 0.0273S_i + 4.3114 \frac{S_i}{T_i} + 0.0008S_iT_i - 0.009T_i^2) \quad [2.17]$$

While the snow cover in the Arctic is generally much thinner than the sea ice below it, the thermal conductivity of snow (k_s) remains significant because it is 6-8 times smaller than that of sea ice (*Makshtas*, 1998). k_s is described empirically by

Ebert and Curry (1993) accounting for direct thermal conductivity and water vapour diffusion using snow density (ρ_s , $\text{kg}\cdot\text{m}^{-3}$) and temperature (T_s , $^{\circ}\text{K}$) in the equation below:

$$k_s = 2.845 \times 10^{-6} \rho_s^2 + 2.7 \times 10^{-4} \left(2^{(T_s - 233)/5} \right) \quad [2.18]$$

The thermal conductivity of snow on sea ice falls in the range of 0.03 to 0.5 $\text{W}\cdot\text{m}^{-1}\text{K}^{-1}$ (*Sturm et al.*, 2002).

The annual evolution of conductive heat flux is critically dependent on the value of thermal conductivity (k) used in its calculation and whether it has been calculated in snow and/or sea ice (*Maykut*, 1982; *Persson et al.*, 2002). Generally, results from these studies indicate that F_c is small and positive (ranging between 3 and $15\text{W}\cdot\text{m}^{-2}$) indicating that the volume is gaining energy in the winter between September and May, before becoming small and negative through the summer, reaching its minimum in July and August ($\sim -2\text{W}\cdot\text{m}^{-2}$) (*Persson et al.*, 2002: see figure 22f). Modeling work done by *Lindsay* (1998), contradicts these results in September and October, indicating that inter-annual, geographical and other variations play an important role in these measurements.

Influence of snow cover on thermodynamic processes in sea ice

Snow on Arctic sea ice affects the annual evolution of a sea ice sheet thermodynamically. The high albedo (0.6-0.9) of snow (*Grenfell and Maykut*, 1977; *Flanner and Zender*, 2006) tends to dominate the shortwave energy balance of northern regions as it is much larger than the albedo of bare sea ice (0.5-0.7) (*Laine*, 2004) or open ocean (~ 0.1) (*Grenfell and Maykut*, 1977). The thermal conductivity

of snow (0.1 to $0.4 \text{W}\cdot\text{m}^{-1}\cdot\text{K}^{-1}$) is an order of magnitude lower than that of sea ice due to the large fractional volume of air whose thermal conductivity is only $0.025 \text{W}\cdot\text{m}^{-1}\cdot\text{K}^{-1}$, making snow an excellent insulator (*Prinsenberg, 1992; Sturm et al., 1997, 2002; McKay, 2000; Pollard and Kasting, 2005*) in spite of its comparatively low volume. Snow also has a lower specific heat and heat of fusion than ice, causing changes in temperature and phase to occur more rapidly in it than in ice (*Ledley, 1991*). Using a coupled, energy balance climate-thermodynamic model, *Ledley (1991)* determined that of these competing effects, reduction of absorbed shortwave energy caused by increased albedo dominates, producing a reduction in air temperatures meaning that added snow has a net cooling effect on climate (*Ledley, 1991*).

Ocean heat flux

The concept of an 'ocean heat flux' (F_w), a product of heat and turbulence) as it pertains to sea ice thermodynamics began with *Maykut and Untersteiner (1971)* demonstrating that changes in sea ice thickness are in part enabled by a flux of sensible heat from the ocean below to the sea ice bottom. *Maykut (1982)* used a model to suggest sea ice required a flux of $2 \text{W}\cdot\text{m}^{-2}$ to maintain an equilibrium ice thickness of 3m, but observational data varies considerably, as does methodology. Early on it was assumed that this energy resulted from diffusion of heat from depth upwards (*Coachman and Barnes, 1962*) but heat lost upward by the Atlantic layer gets trapped below the surface mixed layer (*Rudels et al., 1996*). So, other processes that could cause F_w were explored. *Maykut (1982)* postulated that F_w

originates with shortwave radiation absorbed in the upper ocean and distributed evenly in the horizontal immediately below sea ice, though shortwave absorbed in the ocean was about 1.5 times as large as needed to maintain 3m thick sea ice. This extra energy is thought to be used to erode ridge keels and/or may be lost through leads (*Maykut, 1982*). Work conducted during the Coordinated Eastern Arctic Experiment (CEAREX) showed that oceanic heat flux may vary substantially under a single mobile sea ice floe, ranging from near-zero to almost $70\text{W}\cdot\text{m}^{-2}$ at a sub-kilometer scale in a fifty-day period (*Wettlaufer, 1991*: see figure 8). *Wettlaufer (1991)* attributed F_w maxima to (i) a storm during which wind speeds reached $35\text{m}\cdot\text{s}^{-1}$ and ocean currents in the surface layer reached $30\text{cm}\cdot\text{s}^{-1}$ corresponding to an intrusion of Atlantic water to the mixed layer; (ii) bathymetric features which may have forced warmer water from depth toward the surface.

F_w may be parameterized based on direct measurements of the vertical eddy flux of sensible heat to the underside of an ice sheet; however this entails a making a myriad of difficult time series measurements including profiles of ocean salinity, temperature and currents, and requires that the sea ice bottom roughness be estimated (*McPhee, 1992; Maykut and MCPhee, 1995*). Instead, *Perovich and Elder (2002)* used what *Wettlaufer (1991)* referred to as a modified Stefan equation, taking into account that mass balance at the ice ocean interface results from the combined effects of turbulent heat flux from the ocean to the sea ice and the speed at which the sea ice conducts the heat upward. Ocean heat flux is treated as the residual of the conductive (F_c), specific (F_s) and latent (F_E) heats of the sea ice:

$$F_w = \left(\frac{1}{\Delta t} \right) (F_C + F_S + F_E) \quad [2.19]$$

They accomplished this using ice temperature profiles at 10cm thickness intervals and measurements of changes in sea ice thickness over long time periods. A limit of this method is the accuracy with which the ablation/accretion occurs at the sea ice bottom, for example $\pm 0.5\text{cm}$ thickness represents $1.5\text{MJ}\cdot\text{m}^{-2}$ making this method work best when averaging over long time steps (*Perovich and Elder, 2002*).

Over the course of an annual cycle in multiyear sea ice in the Beaufort Sea, monthly averages of ocean heat flux were low in the winter ($< 5\text{W}\cdot\text{m}^{-2}$) between October and February, increasing sharply to $16\text{W}\cdot\text{m}^{-2}$ in March before decreasing again to $\sim 2\text{W}\cdot\text{m}^{-2}$ in April (*Perovich and Elder, 2002*) again illustrating the seasonal dependence of F_w first described by *Maykut and McPhee (1995)*. High ocean heat flux values in March 1998 were attributed to the entrainment of warmer, deeper water as the floe drifted over the shallow Chukchi Cap during a storm in concert with rapid ice motion ($25\text{km}\cdot\text{day}^{-1}$) which resulted in bottom ablation despite air temperatures lower than -30°C (*Perovich and Elder, 2002*). From April to July F_w increased steadily to a maximum of $16.8\text{W}\cdot\text{m}^{-2}$ before decreasing slightly in August and September (*Perovich and Elder, 2002*: see figure 1). Ocean heat flux is also dependent on ice type and the level of deformation it has experienced, as melt-ponded areas experience very high monthly averaged ocean heat flux which may be due to the enhanced transmission of solar radiation through ponds and relatively thin bare ice (*Perovich and Elder, 2002*). *Krishfield and Perovich (2005)* found that annual-averaged ocean heat flux over the Arctic Ocean pack ice was between 3 and

$4 \text{ W}\cdot\text{m}^{-2}$, with the greatest inter-annual variability of ocean heat flux occurring in the Beaufort Gyre.

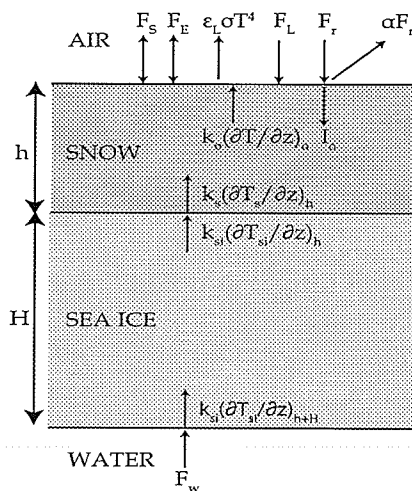
Thermodynamic growth and decay of sea ice

The thermodynamic growth and decay of a uniform snow-covered sea ice sheet was first modeled by *Maykut and Untersteiner* (1971) and then modified based on more recent data by *Maykut* (1986). The model includes a seasonally specified snowfall and a given ocean heat flux and considers a seasonal cycle of shortwave and longwave radiation fluxes on a sea ice sheet of variable thickness. Several assumptions are made, including: (i) the sea ice sheet is an infinite horizontally homogenous slab, precluding any thickness variation due to deformation processes; (ii) the ocean below is at rest, meaning heat transfer due to friction between it and the sea ice slab cannot occur; (iii) heat is transferred between the ocean and atmosphere by conduction affected by brine cells in the ice and shortwave radiation that penetrates the surface of the ice; (iv) the annual snow cover influences the radiative and conductive transfer and is therefore considered as a second and separate layer in the model (*Maykut and Untersteiner*, 1971). It is also assumed that changes in mass and the absorption of energy can only occur at the top and bottom of the snow and the sea ice layers despite the reality that energy absorption occurs in a layer of finite thickness. At the top of the snow or bare sea ice layer melt may occur but mass can only be added through snowfall and at the bottom of the sea ice accretion or ablation may occur (*Maykut and Untersteiner*, 1971) which precludes super-imposed sea ice formation in spring. Figure 2.4. is a graphical representation

of the *Maykut and Untersteiner* (1971) thermodynamic sea ice model discussed below.

At the top of the snow layer, there occurs a balance of radiation and turbulent fluxes. Incoming (downwelling) radiation includes incoming shortwave (F_r) from the sun which reaches the surface after penetrating the atmosphere and incoming longwave (F_L) from the atmosphere (including clouds) emitted as a function of absolute temperature. Upwelling radiation includes the fraction of F_r reflected at the surface termed αF_r , and outgoing longwave from the surface represented by $\epsilon_L \sigma T_s^4$ (Stefan-Boltzmann's Law). Absorption of incoming solar radiation is determined by the properties of the material and incidence angle and extinction of the penetrating shortwave is governed by Beer's Law and summarized by a bulk extinction coefficient. The turbulent sensible and latent heat fluxes (F_s and F_E) can direct energy in the form of heat either away from or toward the snow surface.

*Figure 2.4. Fluxes in a uniform snow-covered ice sheet
Redrawn after Maykut and Untersteiner, (1971).*



Within the snow layer, a flux of shortwave radiation that penetrates into the snow volume (I_o) occurs if the albedo is less than unity, and the conductive heat flux (F_c) is directionally dependent on the temperature gradient. All the above noted fluxes balance, determining the surface temperature when it is below 273.16°K (T_f) but above T_f the snow surface will melt causing an imbalance in energy flux reducing snow thickness (h) (*Maykut and Untersteiner, 1971*). The energy balance equations are therefore:

$$(1 - \alpha)F_r - I_o + F_L - \varepsilon_L \sigma T_o^4 + F_s + F_e + k_s \left(\frac{\partial T}{\partial z} \right)_o = 0 \text{ if } T_o < 273.16^\circ\text{K} \quad [2.20]$$

$$(1 - \alpha)F_r - I_o + F_L - \varepsilon_L \sigma T_o^4 + F_s + F_e + k_s \left(\frac{\partial T}{\partial z} \right)_o = - \left[qd \frac{(h + H)}{dt} \right]_o \text{ if } T_o = 273.16^\circ\text{K} \quad [2.21]$$

where subscript 'o' refers to the upper surface and q is the latent heat of fusion of the surface material (*Maykut and Untersteiner, 1971*). While heat is conducted along a temperature gradient within the snow, absorption of penetrating solar radiation also occurs, depending on the snow physical structure, wavelength and incidence angle. Absorption at depth is treated for simplicity's sake in terms of the bulk extinction coefficient (κ_s) and the thermal conductivity of the snow (k_s) is held constant (*Maykut and Untersteiner, 1971*).

$$\rho_s c_s \frac{\partial T_s}{\partial z} = \frac{\partial}{\partial z} k_s \left(\frac{\partial T_s}{\partial z} \right) + I_o \kappa_s e^{-\kappa_s z} \quad [2.22]$$

Conduction is assumed to be continuous through the snow-sea ice interface such that:

$$k_s \left(\frac{\partial T_s}{\partial z} \right)_h = k_{si} \left(\frac{\partial T_{si}}{\partial z} \right)_h \quad [2.23]$$

where the temperature gradients are immediately above and below the interface (*Maykut and Untersteiner, 1971*). Snow is relatively insulative compared to sea ice, changing the slope of the temperature profile between the snow top and sea ice bottom in winter at the snow-sea ice interface. Heat conduction and radiative absorption occur in sea ice in the same way as in snow, so the same heat conduction equation may be used as [equation 2.22] save for the fact that the specific heat and thermal conductivity of sea ice vary with salinity and temperature and should be substituted into the heat conduction equation.

At the sea ice-seawater interface, the ocean heat flux (F_w) (which gives rise to melting at the sea ice bottom) and the conductive heat flux in the sea ice (which gives rise to ice growth) near the interface are the only two fluxes considered, with one dominating dependent on season (*Maykut and Untersteiner, 1971*). The equilibrium thickness of a sea ice sheet is physically justified then, as the ice may grow thick enough for the magnitude of F_w to exceed that of F_c at the sea ice bottom, even mid-winter (*Wadhams, 2000*). *Maykut and Untersteiner (1971)* therefore express the heat balance at the sea ice bottom as:

$$F_c - F_w = \left[qd \frac{(h+H)}{dt} \right]_{h+H} \quad [2.24]$$

Although it is generally accepted as a very sophisticated treatment of snow and sea ice thermodynamics through the annual cycle, *Ebert and Curry (1993)* noted that *Maykut and Untersteiner's (1971)* model noted some deficiencies, namely, (i) the summertime melting ice albedo of 0.64 is too high, directly resulting in comparatively small annual surface ablation amounts. *Shine and Henderson-Sellers*

(1985) showed the performance of thermodynamic models is quite sensitive to albedo parameterization by using different albedos for different surface types and accounting for clouds; (ii) *Maykut and Untersteiner* (1971) assumed that 17% of incoming shortwave penetrated into the interior of the sea ice, but that amount depends on the ratio of diffuse to direct radiation (*Ebert and Curry, 1993*) and (iii) ocean heat flux was set at $2\text{W}\cdot\text{m}^{-2}$, which is an oversimplification of a poorly understood variable. *Ebert and Curry* (1993) focused on sea ice-atmosphere interactions including albedo and leads, introducing an albedo parameterization sensitive to surface state including melt ponds of variable depth, a lead parameterization accounting for lateral accretion/ablation in response to lead fraction, a prescribed divergence rate allowing for the absorption of solar radiation by the ocean and a time-varying heat flux to the sea ice base.

Low winter air temperatures above a snow-covered sea ice slab create a situation in which net energy into the slab does not result in immediate decreases in slab thickness; a positive energy flux to the sea ice sheet results first in warming of the sea ice at the microscopic scale, coincident with reduced surface salinity. When the sea ice has temperature reaches the melting point, additional energy input reduces the thickness of the slab through ablation at the surface, generating melt water which remains at the surface in ponds, flushes down through the sea ice slab reducing the salinity, or drains off the surface into the upper ocean (*Eicken, 2003*). Although surface ablation of Arctic sea ice is substantial, *McPhee et al.* (1998) found that up to 0.5m may be ablated from the bottom of multi-year sea ice in the Beaufort Sea in a single year. This amount of bottom melt could not be explained solely by a

flux of heat from the ocean below the surface mixed layer, leading to the postulation that shortwave energy that penetrates the surface mixed layer may be in part responsible for the additional heat flux required to account for greater than expected bottom ablation (*McPhee et al.*, 1998). Studies of radiative transfer in sea ice have made it clear that shortwave penetration of the ocean surface mixed layer is enabled greatly by the presence of very thin sea ice and/or open water. This leads us to a discussion of dynamic processes which enable these conditions.

2. Sea ice dynamics

Although the thermodynamics of sea ice are well defined in the previous section, for simplicity it is assumed that the sea ice is not moving, and (sometimes) it is even assumed that the ocean beneath is also at rest. In reality, almost all sea ice in the northern hemisphere is in motion, save for a small fringe of landfast sea ice fixed to coastlines. Sea ice is in a state of constant motion and deformation, resulting in a myriad of different physical characteristics on several scales. Motion is governed by Newton's Laws governing inertia, momentum, and action and reaction. In this section I will deal with the physical explanation of sea ice motion, which in combination of our understanding of sea ice thermodynamics will yield some insight to the complexities of ocean-sea ice-atmosphere interaction.

For the sake of organization sea ice dynamics is divided here into three aspects of ocean-sea ice-atmosphere interaction: (i) the momentum balance, which accounts for motion and subsequent deformation due to atmospheric and oceanic forces on an ice cover, (ii) sea ice strength, which describes the type and magnitude

of stress necessary to fracture a sea ice cover making it discontinuous, and (iii) sea ice rheology, which describes the way in which sea ice as a material reacts under various stresses.

Momentum Balance

The momentum balance of an area of sea ice cover corresponds to the balance of five forces, namely air stress, water stress, the Coriolis force, internal ice stress, and the stress attributed to the tilt of the ocean surface (*Hibler, 1979*). Air stress, water stress and Coriolis force typically dominate with internal sea ice stress becoming important when sea ice is closely packed and/or in an enclosed area like the Canadian Arctic Archipelago (*Wadhams, 2000*).

Air (wind) stress is an important transfer mechanism of momentum from the atmosphere to sea ice, affecting the physical characteristics of an ice pack, ocean currents and turbulence, and even sea surface tilt (*Guest et al., 1995*). The air stress (τ_a) on an area of sea ice is represented by the air-ice drag coefficient (C_a), a constant of proportionality linking wind speed to the stress it exerts on the sea ice surface, which is a function of sea ice surface roughness:

$$\tau_a = \rho_a C_a |U_a - U_i| (U_a - U_i) \quad [2.25]$$

where ρ_a is the air density, C_a is the air-ice drag coefficient, U_a is the wind velocity at a reference height and U_i is the ice velocity. This allows for the ice velocity to be much smaller than the wind speed, and uses the relative velocity of the wind and ice to determine the stress (*Reynolds et al., 1985*). C_a ranges between 0.0014 and 0.0021 for sea ice but varies substantially based on ice type and location (*Wadhams,*

2000: see table 4.1), so the roughness of the top and underside of the ice cover must be known and categorized based on scale. Large-scale features range in size and length on the order of meters to kilometers respectively compose form drag due to changes in the large-scale flow of wind. Small-scale features on the order of millimeters to meters in size and length respectively compose skin friction drag over relatively un-deformed sea ice. Generally, as the surface roughness increases, so to does C_a as form drag around large-scale roughness elements increases, draining the momentum of the wind (*Andreas et al.*, 1993). Air stress has been measured over sea ice from aircraft (*Overland*, 1985; *Fairall and Markson*, 1987) from ships (*Andreas et al.*, 1993) and even buoys (*Reynolds et al.*, 1985) and not surprisingly, the method has some effect on the final product, as horizontal variability caused by substantial variations in the surface and boundary layer conditions occurs (*Guest et al.*, 1995).

Water stress (τ_w) is the force on the ice bottom relative to the motion of the ocean beneath it, calculated in the same way as air stress. The difference being that the water velocity is measured under sea ice at a depth of 1-2m (e.g. *McPhee*, 1979; *Reynolds et al.*, 1985). *McPhee* (1979) and *Reynolds et al.* (1985) calculated C_w values around 0.0054; *Hibler* (1979) used 0.0055 in his model. C_w is also a function of the ice bottom roughness and varies considerably, and the difference between smooth and rough sea ice is much greater for water stress than air stress. The ocean mixed layer depth dealt with here may only be 30m compared to the atmospheric boundary layer that may be 1000m thick; a ridge with a 1m sail and a 5m keel is protruding to a proportionally much greater depth in the ocean than in the

atmosphere, so form drag becomes a much greater component of C_w than C_a (Wadhams, 2000). McPhee (1986) notes that C_w should ideally be measured in neutrally stable density conditions (in the absence of melting/freezing) because the addition of freshwater to the near-surface ocean layer increases the strength of density stratification, reducing vertical momentum transfer and decreasing drag.

The fact that any body on the earth's surface is being accelerated as a result of the earth's rotation is accounted for by the Coriolis force. The magnitude of which is given by:

$$F_C = 2m\omega U_i \sin \phi \quad [2.26]$$

where m is the product of the ice density and thickness for a unit area, $\omega = 7.272 \times 10^{-5} \text{ rad}\cdot\text{s}^{-1}$ (angular velocity of Earth), U_i is ice velocity and ϕ is the latitude at which the measurement is made. The Coriolis force decreases with latitude moving away from the poles and is proportional to mass; so thicker ice is more substantially affected than thinner ice per unit area.

Sea surface height is defined with respect to a surface of constant gravitational potential called the geoid. Stress due to sea surface tilt occurs because the sea surface does not always correspond to the geoid. The distribution of ocean and continental crust and mid-ocean ridges may cause the sea surface to be uneven, as does uneven heating, evaporation and precipitation. More water with respect to the geoid in some areas creates a horizontal pressure gradient which attempts to move the 'extra' water to areas with less (depressions). The geostrophic current occurs where the sea surface tilt gradient force is balanced by the Coriolis force.

Internal ice stress (τ_i) accounts for the force acting on an area of ice within an ice sheet due to stress transmitted through the ice from the surrounding sea ice. τ_i is constantly changing, dependent on ice rheology, strength and the areal mass balance, valid only if the spatial scale at which it is approximated is much bigger than the floes from which the pack is composed (Hibler, 1986). Early approximations of sea ice dynamics ignored the problem of internal ice stress, instead focusing on free drift solutions for the momentum balance, assuming that the sea ice cover moves as a single floe without interacting with other floes.

Sea ice motion in free drift

In the presence of air stress only, ice moves in the direction of the air stress diverted to the right of the wind in the northern hemisphere due to the Coriolis force. Increased velocity causes increases in the turning effect of the Coriolis force until the floe's velocity includes a component working against the air stress. This causes the floe to slow down as it reaches a point directly to the right of its initial position perpendicular to the wind direction, creating a trajectory called an inertial loop. When the water stress is added to the scenario, partial inertial loops occur because water stress slows the floe more quickly than in the previous example. This allows the floe to end up downwind and to the right ($\sim 45^\circ$) of its initial position. The stronger the Coriolis force and the thicker the sea ice, the greater the turning angle, but the angle decreases with increased air and water stress.

While the wind and water stresses are acting on a sea ice floe, the drag of the sea ice in the ocean boundary layer causes motion in the ocean surface layer at a

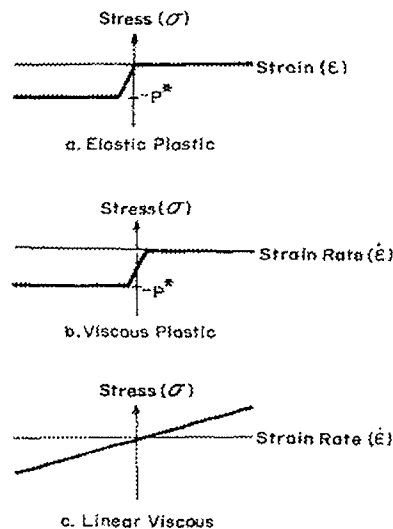
direction increasing in angle to the right of the ice motion direction with increasing depth. This current structure is called an Ekman spiral and is caused by the Coriolis force. Two layers are normally delineated, the first is the surface layer, where shear occurs and water velocity is in the same direction as the sea ice. The second is called the Ekman layer, which begins a few meters below the surface dominated by the Coriolis force which creates a clockwise spiral of mean current velocity relative to the direction of ice motion with increasing depth. The same process occurs in the atmosphere, where at ten meters height the wind is smaller in magnitude and turned to the left by about 25° (in the northern hemisphere) in comparison to the geostrophic wind at the top of the atmospheric boundary layer. Therefore without a geostrophic current, ice drifts in the direction of the geostrophic wind, parallel to the isobars (Zubov's Law).

While the above suffices as a general explanation of sea ice motion occurring in free drift, the Arctic reality is (again) severely complicated in comparison. For much of the annual cycle in the entire Arctic sea ice does not move as one floe, creating strain unrelated to ice velocity. Rather, it moves discontinuously and non-linearly in time and space, in part due to variable internal ice stress and further complicated by coastal boundaries. This brings us to a discussion of the behavior of a sea ice area under normal conditions.

Sea ice Strength and Rheology

The strength of a sea ice cover may be thought of in terms of stress (σ , force per unit area) and strain (ϵ , displacement per unit length usually expressed as a percent) which can be partitioned into normal ($//$) or shear (\perp) strain based on the direction of the displacement (*Mellor, 1986*). Sea ice compressive strength is described by the maximum stress developed at a specific strain rate before failure occurs and is largely controlled by the sea ice temperature and type (*Mellor, 1986; Timco and Johnston, 2002; Johnston et al., 2003*). Sea ice compressive strength and temperature have been shown to be linearly related between -18°C and 2°C , but in sea ice warmer than about -4°C the relationship becomes weaker (*Johnston et al., 2003*). This is particularly interesting in the context of work by *Golden (2003)* who while studying the fluid permeability of sea ice noted a critical threshold temperature of -5°C at which a transition between low and high permeability regimes occurs. The presence of brine and air in sea ice and their relative amounts actually control the compressive strength of sea ice because they do not contribute to its mechanical strength (*Mellor, 1986*) and of course are in part controlled by temperature but also by factors discussed previously including growth rate, age and growth conditions such as the salinity of the seawater from which it grew.

Figure 2.5. A one-dimensional comparison of sea ice rheologies. The viscous-plastic rheology is considered a nonlinear viscous fluid with the inclusion of a minimum pressure term (P^*). From Hibler (1979).



In order to account for the complexity of sea ice motion not in free drift, *Hibler* (1979) suggested that ice interaction be treated using a constitutive law to relate forces within the sea ice cover to strain and/or deformation. In order to accomplish this, *Hibler* (1979) followed by *Zhang and Hibler* (1997) used a viscous-plastic approach (Figure 2.5.), considering sea ice a non-linear viscous compressible fluid. Sea ice is treated like a plastic under flow; the nonlinear viscosities are adjusted so sea ice acts as a rigid plastic at normal deformation rates and as a linear viscous fluid under very small deformation rates (*Hibler*, 1979). For the sake of comparison, an elastic-plastic material resists compression with a fixed stress once a certain converging deformation occurs and bears no resistance to diverging strains, while in the viscous-elastic case the stress rate is determined by the

magnitude of the strain rate ($\dot{\epsilon}$) rather than the strain (Figure 2.5.) (Hibler, 1979). A major difference between these two laws is the way they treat motionless situations; The elastic-plastic law may maintain a high stress situation without any motion, while the viscous-plastic law approximates high stress situations using a very slow flow (creep) (Hibler, 1979). Finally, the linear viscous approach is different from both elastic-plastic and viscous-plastic because the stresses are large even for small strain rates and almost independent of the rate of deformation (Figure 2.5.) (Hibler, 1979). Viscous-plastic sea ice rheology fits the actual behavior of Arctic pack ice, but the model only used two categories of sea ice thickness to relate ice strength (Hibler, 1979).

3. Sea ice morphology and thickness distribution: thermodynamics and dynamics

In the previous two sections the physical nature of thermodynamic evolution and sea ice motion has been described. The sea ice thickness distribution represents the degree to which the large-scale physical properties of a sea ice cover depend on thermodynamic and dynamic forcing (which may be oceanic and/or atmospheric), the combination of which yields variable sea ice morphology throughout an annual cycle. In turn, a combination of dynamic and thermodynamic sea ice morphological features in a region variably affects thermodynamic and dynamic forcing. Over an annual cycle, thermodynamic processes attempt to create a single equilibrium thickness by thinning thick ice and thickening thin sea ice, all the while dynamic processes attempt to create very thin and very thick sea ice.

In a changing climate, the ability to determine changes in the Arctic sea ice cover is very important and areal cover may be assessed on a near-daily basis using space-borne remote sensing instruments like AMSR-e. However, determining changes in sea ice volume is vitally important in determining ocean-atmosphere heat and momentum exchange, regional mass and associated salt and freshwater fluxes, as well as the strength and mechanical properties of an ice cover which all play important roles in our climate system. From the perspective of climate variability and change, it is vital that both thermodynamic and dynamic processes be accounted for. Decreases in sea ice volume may not occur despite reduction of thickness in some areas, as thinner areas are more easily ridged. *Haas (2003)* goes so far as to suggest that even ice edge retreat may not necessarily be linked to decreases in sea ice volume. It could also be that extent and thickness are decreasing. The morphology and resultant thickness distribution in the Arctic is much different from that of the Antarctic as are thermodynamic and dynamic forcing which create it, so again I restrict my discussion to the northern hemisphere only.

The probability distribution function of sea ice thickness

In a given area, the characteristics of a sea ice cover may include leads, ridges, rafted sea ice, any variation in thermodynamically grown sea ice thickness, and even open water. *Thorndike et al. (1975)* defined the sea ice thickness distribution ($g(h)$, m^{-1}) in a finite area (R) as:

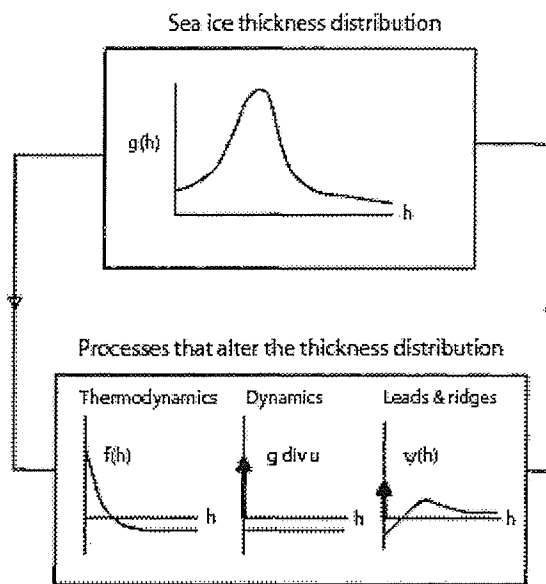
$$g(h)dh = \frac{dA(h, h + dh)}{R} \quad [2.27]$$

where $dA(h, h+dh)$ represents the area within region (R) covered by sea ice with thickness between h and $h+dh$. Sea ice distributions are most often dominated by a mode representing level sea ice thickness, and a right-skewed tail representing many classes of dynamically thickened sea ice. The area under the curve to the left of the mode encompasses thinner sea ice which may exist in leads, and even open water at $h = 0$. The sea ice thickness distribution of a region is also always changing with time, expressed mathematically by:

$$\partial g / \partial t = \text{div}(vg) - \partial(fg) / \partial h + \psi(h) \quad [2.28]$$

where $f(h)$ at a time and point equals $\partial h / \partial t$, the thermodynamic growth rate, v is the horizontal velocity vector, and ψ is a function that redistributes sea ice from one thickness class to another (Wadhams, 1998). The effects of these processes on the sea ice thickness distribution of a region are diagrammatically represented in Figure 2.6. The first term on the right-hand side [equation 2.28] accounts for divergence (and therefore advection), reducing the ice-covered area. Divergence generates open water areas, such as leads and polynyas where sea ice may re-form thermodynamically. The second term accounts for thermodynamic processes and the redistribution function (ψ) accounts for lead and ridge formation by convergence. The redistribution function is the least well understood of the three terms, depending on the mechanical characteristics of the sea ice cover, and making rheology an important consideration regionally (Hibler, 1979; Wadhams, 1998).

Figure 2.6. A probability distribution function of sea ice thickness (top) shown with the processes which may alter it over the course of an annual cycle (bottom). Modified from Thorndike et al. (1992).



Sea ice thickness seems like an easy measurement to make, but in practice meaningful studies of sea ice thickness are difficult; the snow may be measured and scraped away from the sea ice surface and a hole drilled in sea ice, but due to the spatial variability of snow thickness and sea ice thickness, that measurement must be repeated thousands if not hundreds of thousands of times on the kilometer scale in order to meaningfully represent the sea ice volume in an area. Different methodologies have been employed to make snow-plus-sea ice 'slab' thickness measurements, both from above the sea ice using electromagnetic induction systems (e.g. Haas et al., 1997) and from below using submarine-borne sonar equipment (e.g. Wadhams, 1992) but these methods are far from perfect. Technology is continually advancing but snow thickness is not differentiated from

sea ice thickness, a simplification which is less than ideal with respect to areal energy budgets due to the differences in snow and sea ice thermal properties.

In the Arctic, the sea ice thickness distribution contains a set of distinct features; open water and leads containing thin sea ice are contained in classes between 0 and 1m thickness. A second small peak typically occurs near the 2m thickness corresponding to un-deformed first-year sea ice. Multi-year sea ice has been represented by a large peak between 3 and 5m thickness, but there is evidence showing that this peak may be shifting toward thinner classes (*Rothrock et al., 1999*). Thickness classes greater than 4-5m represent significantly deformed sea ice that may be first-year or multi-year.

Ridges are formed when a sea ice sheet is stressed in excess of its failure threshold by convergence. These failures are typically linear or some variation and much thicker than the surrounding un-deformed sea ice. Between 30 and 80% of the sea ice volume in a given area may be contained in pressure ridges, so the amount and thickness of sea ice ridging dominates sea ice mass balance in the Arctic, making dynamic processes more important than thermodynamics (*Haas, 2003*).

Leads are also typically linear features of an ice cover which occur as a result of divergent sea ice motion. Leads open perpendicular to the direction of the tensile stress that caused the sea ice cover to fail (*Mellor, 1986*).

Polynyas are areas of open water in time and space where one would expect to find sea ice. These areas typically surrounded by sea ice cover and/or coastline are maintained by one or a combination of the two following processes: sensible

heat polynyas are kept open by upwelling of warm water from depth, vertical diffusion of heat or convection which provides enough ocean heat flux to reduce the thickness of or eliminate the sea ice cover altogether (*Smith et al., 1990*). Latent heat polynyas are kept open by advection of the sea ice from the area, where the heat required to balance heat loss to the atmosphere is provided by the latent heat of continually forming sea ice (*Smith et al., 1990*). Heat exchange at the open water surface of a lead or polynya is 100 times greater than through the surrounding snow covered sea ice, so even though polynyas and leads represent a small fraction of the Arctic surface area, they may dominate the energy balance regionally (*Maykut, 1978*).

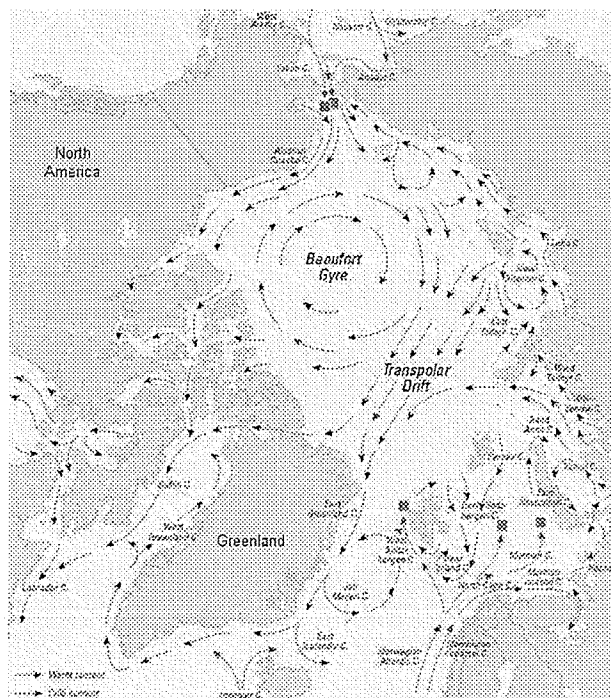
4. Large-scale processes and changing climate

Circulation

Atmospheric circulation on Earth is driven by differential heat input at its surface. A great deal more of the sun's energy reaches the surface at the equator than at the poles due to the relative thin-ness of the earth's atmosphere at the equator, and due to the relatively oblique angle at which the sun's energy reaches the poles. Air at the equator is warmed, becoming less dense, and lifts, creating low pressure at the surface. Air cools as it rises, eventually regaining the density required to descend back to the surface at subtropical latitudes, setting up what is known as the Hadley Cell between 0° and 30°. This same process sets up the Ferrel cell between 30° and 60° and the Polar cell above 60°, enabled by the earth's rotation and the resultant Coriolis force. At ~60°N, air is moved aloft by

convergence creating the Polar Vortex (cyclonic low) at the top of the troposphere due to the Coriolis force. The warm air cools as it converges on the pole, becoming denser and eventually descending to the surface through the troposphere forcing divergence to occur at the surface. Due to the Coriolis force, the outward motion of the air at the surface is pushed to the right in the northern hemisphere causing an anticyclone (high, clockwise) called the Beaufort High which is typically strongest in winter. In addition to the Beaufort High, several other semi-permanent pressure centers occur at Arctic latitudes, including the Icelandic Low, which is typically situated west of Iceland, the Aleutian Low near the Aleutian Islands (most intense in winter), and a strong high centered over Greenland.

Figure 2.7. Arctic Ocean circulation showing the average position of the Beaufort Gyre and the Transpolar Drift stream. From AMAP (1998: figure 3.29).



Discussion of circulation in the Arctic atmosphere as it pertains to sea ice motion is often centered on the North Atlantic Oscillation (NAO) (*Hurrell, 1995*) and the Arctic Oscillation (AO) (*Thompson and Wallace, 1998*). The NAO is associated with changes in the difference in normalized sea level pressure in winter (division of the seasonal pressure by the long-term mean from 1894-1994) between Lisbon, Portugal and Stykkisholmur, Iceland and is represented by the NAO index between ± 1 (*Hurrell, 1995*). The positive phase of the NAO occurs when the gradient between a high pressure center over Portugal and an area of low pressure over Iceland increases. The AO was first defined as the leading empirical orthogonal function of monthly sea level pressure anomalies in the winter, north of 20°N (*Thompson and Wallace, 1998*). They further proposed that the NAO was encompassed by their new index, a claim later seconded by *Kwok and Rothrock (1999)*. The argument is that the NAO is a regional pattern in the Atlantic sector of the AO, and that the AO is a more important and fundamental structure due to its resemblance to the dominant mode of circulation variation in the lower stratosphere, its similarity to the spatial pattern of circulation in the southern Hemisphere (i.e. it has an Antarctic analog) and its positive trend in the past several decades, representing a strengthening of the polar vortex from sea level to the stratosphere in winter (*Deser, 2000*). However, the fact remains that the AO and NAO indices are statistical representations of pressure differences between locations.

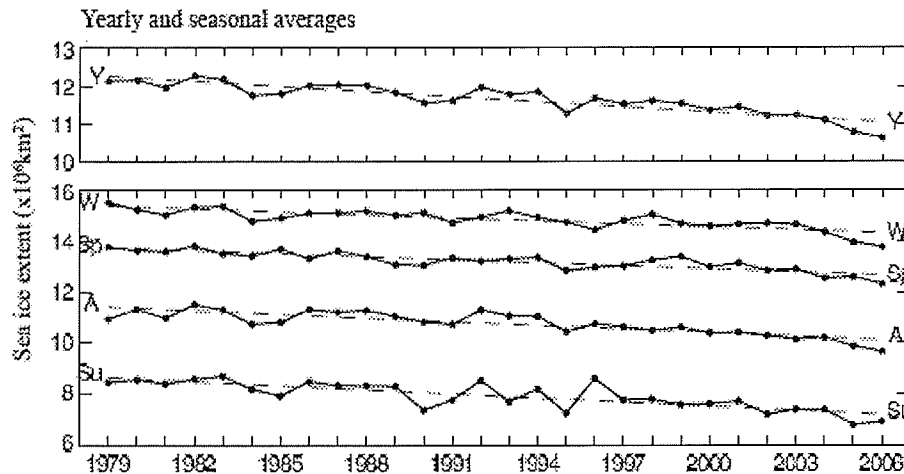
The long-term average positions of the above-mentioned Arctic pressure centers and the geometry of the Arctic basin give rise to the dominant ocean and sea

ice circulation patterns in the Arctic, namely the Beaufort Gyre and the Transpolar Drift (Figure 2.7.) (*Vowinckel and Orvig, 1970; Colony and Thorndike, 1984*). The Beaufort Gyre is a large anticyclone that occupies much of the western section of the Arctic basin, the Canada Basin. The Transpolar Drift stream in the Eurasian Basin moves sea ice from the Russian coastal seas over the pole and out of the Arctic through Fram Strait between Svalbard and Greenland, in part due to the presence of the strong high over Greenland which is responsible for winds that drag water and sea ice down the east coast of Greenland. The residence time of a perennial sea ice floe in the Arctic Basin was estimated by *Colony and Thorndike (1985)* to be about 5-7 years, but the nature of averaging ice motion over long time scales may overshadow the nature of large variability on shorter (yearly) time scales. Although average sea ice velocities are $\sim 2\text{cm}\cdot\text{s}^{-1}$, the daily standard deviation can be up to $7\text{cm}\cdot\text{s}^{-1}$ (*Colony and Thorndike, 1984*). The oldest, thickest sea ice in the Arctic is created by this circulation system, which pushes sea ice up against the coasts of northern Greenland and the western side of the Canadian Arctic Archipelago, dynamically thickening it. The youngest, thinnest sea ice in the Arctic is found along the Russian shelves, from where it is continually exported over the pole by the Transpolar Drift stream (*Haas, 2003*). The Beaufort Gyre has been shown to undertake reversals on occasion, from anticyclonic to cyclonic in response to cyclonic atmospheric activity in the spring, summer and fall (*Serreze et al., 1989; Lukovich and Barber, 2006*).

Sea ice extent and thickness

Historical studies of sea ice concentration, extent and area are numerous, and vary in their spatial and temporal focus (*Parkinson et al.*, 1999; *Lynch et al.*, 2001; *Rothrock and Zhang*, 2005; *Ngheim et al.*, 2006; *Parkinson and Cavalieri*, 2008). Most recently *Parkinson and Cavalieri* (2008) analyzed Arctic sea ice extent between 1979 and 2006 (28.2 years) using passive microwave sea ice concentration data to determine sea ice extent (pixels containing concentrations greater than 15%), updating previous studies by the author and others. They report a negative trend in northern hemisphere sea ice extent of $-45100 \pm 2000 \text{ km}^2 \cdot \text{year}^{-1}$, with the highest magnitude slope ($-53400 \pm 7900 \text{ km}^2 \cdot \text{year}^{-1}$) occurring in the summer months and the weakest trend ($-39500 \pm 5600 \text{ km}^2 \cdot \text{year}^{-1}$) occurring in the winter, with all trends statistically significant above 95% confidence (Figure 2.8.). In comparison to the same study done for 1978-1996 (*Parkinson et al.*, 1999) the spring trend is less negative with the additional 10 years of data, while the summer, fall and winter trends are much more negative (*Parkinson and Cavalieri*, 2008). On a monthly basis, September contained the largest negative sea ice extent trend ($56800 \pm 9700 \text{ km}^2 \cdot \text{year}^{-1}$, equivalent to $-7.6\% \pm 1.3\% \cdot \text{decade}^{-1}$) noting that this trend is particularly influenced by the extreme loss of sea ice extent in September 2005.

Figure 2.8. Yearly and seasonal sea ice extents from 1979-2006. The winter (W), spring (Sp), summer (Su) and autumn (A) values cover JFM, AMJ, JAS, and OND respectively. Modified from Parkinson and Cavalieri (2008).

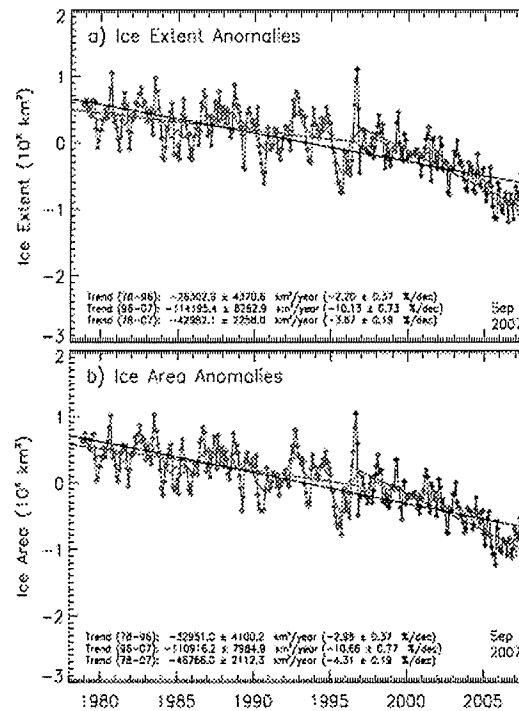


Regionally, the areas contributing to most to the yearly average decline are the Kara and Barents Seas and the Arctic Ocean, although the largest decline by percent occurred in the Greenland Sea and Baffin Bay/Labrador Sea (Parkinson and Cavalieri, 2008: see figure 1b). Seasonally, the most substantial contributions to ice decrease in the northern hemisphere occur in Baffin Bay/Labrador Sea, the Greenland Sea and Kara and Barents Seas in winter, the Kara and Barents Seas in spring, the Arctic Ocean in summer, and the Arctic Ocean in fall (Parkinson and Cavalieri, 2008).

Recently, much attention has been paid not only to the results of multi-decadal trend analysis, but also to recent massive reductions in northern hemisphere sea ice extent. Although sea ice cover in the north hemisphere has been declining on average since 1979, since 2002 the multi-year sea ice extent and area have been low in comparison to the previous 22 years of measurements

available in the process establishing several new record minimums (Figure 2.9.) (Comiso et al., 2008).

Figure 2.9. Monthly ice extent (a) and ice area (b) anomalies from November 1978 to September 2007 (green and blue) with 12-month running average (red) and linear trend lines for three periods (full record: black; 1978-1996: green; 1996-2007: blue). From Comiso et al. (2008).



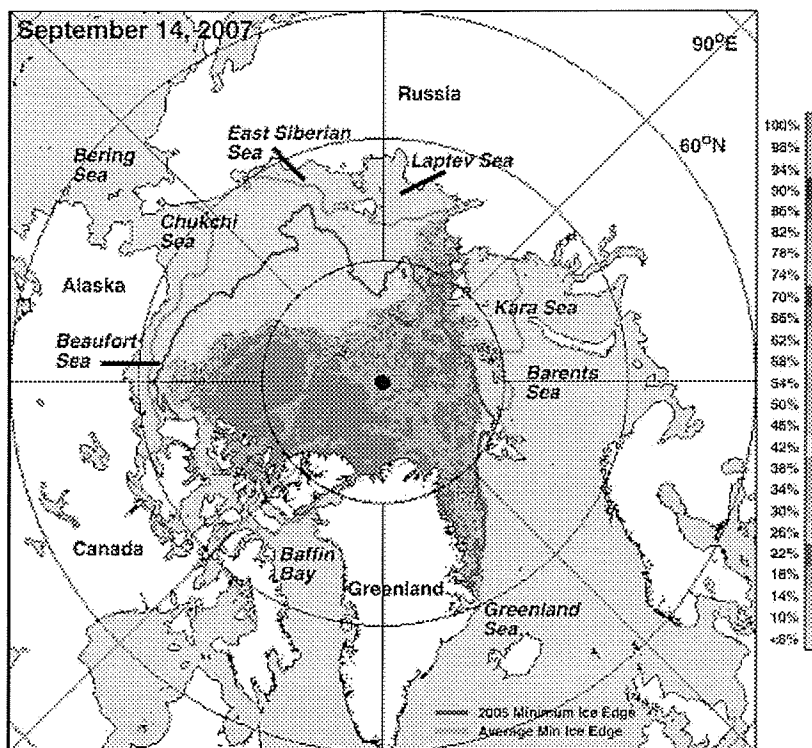
Most recently, passive microwave data revealed that in the summer of 2007, Arctic sea ice extent reached a record minimum of $4.1 \times 10^6 \text{ km}^2$, 24% lower than the previous record low from 2005 (Comiso et al., 2008). The consensus in the arctic science community has been for some time that perennial arctic sea ice cover will disappear in summer, and studies are numerous in efforts to determine the

mechanism(s) underlying these continual annual sea ice extent reductions. I will begin with the most recent Arctic sea ice minimum recorded in September 2007.

Until mid-June 2007, northern hemisphere sea ice cover was similar to ice cover experienced in 2005 and 2006, after which it declined quickly to its lowest measured value ever in September (Figure 2.10.) (*Comiso et al., 2008*). Much of the 'new' sea ice cover loss occurred in the East Siberian, Chukchi and Beaufort Seas and was attributed to anomalously warm air temperatures between February and July of 2007 with respect to the 1982-2007 monthly temperature averages (*Comiso et al., 2008*). The authors go on to note that their findings correspond well with the findings of *Parkinson and Cavalieri (2008)*.

It is obvious that Arctic sea ice extent is decreasing at about $10\% \cdot \text{decade}^{-1}$, (*Stroeve et al., 2005; Parkinson and Cavalieri, 2008*), but the slope of the decreasing trend has changed in the nearly three-decade-long time series of passive microwave data (Figure 2.9.) (*Comiso et al., 2008*). Less obvious are the underlying mechanisms, to what degree they contribute to the trend of net sea ice loss, and how they are related. The Arctic sea ice cover is influenced by a myriad of physical factors, thermodynamic and dynamic. Temperature, radiative and turbulent fluxes, ocean heat storage, winds, associated large scale atmospheric circulation and ocean currents all contribute to the extent of Arctic sea ice.

Figure 2.10. Arctic sea ice concentration and extent on 14 September 2007. The gold contour represents the average sea ice cover edge from 1979-2006 and the red contour represents the previous record minimum sea ice cover in 2005. From Comiso et al. (2008).



Arctic air temperatures have been shown to be on the rise by *Rigor et al.* (2000), whose trend analysis indicated that warming dominates during winter (DJF) and spring (MAM), and that warming over northern Eurasia extends out over the eastern Arctic Ocean. Over the eastern Arctic Ocean, the annual trends indicate that warming north of the Laptev and East Siberian Seas is occurring at the rate of $\sim 1^{\circ}\text{C}\cdot\text{decade}^{-1}$, resulting in a shortening of the sea ice season in the eastern Arctic and a lengthening in the western Arctic between 1979-1997 (*Rigor et al.*, 2000). *Ogi and Wallace* (2007) further noted that summer circulation anomalies and their

associated surface air temperature anomalies are largest over marginal seas, coinciding with large reductions in summer sea ice especially on the Russian side of the Arctic.

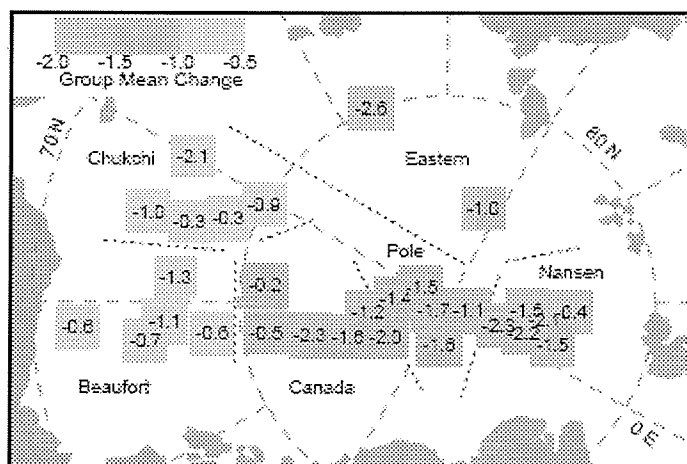
Many studies have also examined the role of atmospheric circulation on the evolution of Arctic sea ice cover. Studies concur that decreases in Arctic sea ice cover between the 1960s to the early 1990s were partially driven by trends in wintertime atmospheric circulation patterns, (e.g. the AO and NAO) more often now referred to as the Northern annular mode (e.g. *Proshutinsky and Johnson, 1997; Deser, 2000; Zhang et al., 2000; Rigor et al., 2002; Stroeve et al., 2005; Lukovich and Barber, 2006*) whereby anomalous low sea level pressure over the Canada Basin of the Arctic Ocean between the 1960s and 1990s in the winter flushed old, thick multi-year sea ice through Fram Strait and out of the Arctic, leaving younger thinner pack ice which would melt more easily in summer.

Since the early 1990s however, the AO has regained its former positive index value as the Beaufort Sea High regained its former strength (*Deser and Tang, 2008*). Therefore, declines in sea ice cover after about 1993 are inconsistent with the notion that they are caused by atmospheric forcing (*Deser and Tang, 2008*). Other studies have brought light to bear on reasons for this disconnect. *Lindsay and Zhang (2005)* postulate that thermodynamic changes related to the positive sea ice-albedo feedback have dominated changes in Arctic sea ice cover since the late 1980s. *Francis et al. (2005)* found that about 40% of the variability of sea ice edge position was driven by variations in the downwelling longwave radiative flux in the six marginal seas between 1979-2004, noting that the proposed relationship is two-

way (positive feedback); open water emits more longwave than the sea ice it has replaced, which is absorbed by clouds and re-emitted toward the surface. But, results from 1979-2004 (*Francis et al.*, 2005) were contradicted by *Kay et al.* (2008) who suggest that in a warmer Arctic with thinner sea ice, cloud and shortwave radiation anomalies will become increasingly important in modulating summer sea ice extent. *Kay et al.* (2008) were expanding on the ideas of *Ogi and Wallace* (2007) who argued that southerly winds enhance the northward transport of heat, and reduced cloud caused by a strong Beaufort High allows for increased downwelling shortwave to reach the surface. *Kay et al.* (2008) further note that the sea ice extent minima of 2005 and 2007 occurred associated with anti-cyclonic surface pressure and reduced cloudiness.

Although studies of sea ice cover are plentiful, true measurements of a sea ice mass balance are based on volume and require knowledge of sea ice thickness. A study conducted by *Rothrock et al.* (1999) compared sea ice draft data from submarine transects of the Arctic Ocean during 1958 to 1976 with transects in the same regions between 1993 and 1997 yielding average decreases throughout the study area (Figure 2.11.). Mean draft had decreased in all regions studied by an average of 1.3m, from 3.1m to 1.8m between the two periods (*Rothrock et al.*, 1999) amounting to a 42% reduction in sea ice thickness. The eastern Arctic and Nansen Basin thinned the most between the two periods, by 1.8m and 1.7m respectively (Figure 2.11.) (*Rothrock et al.*, 1999).

Figure 2.11. Mean draft changes between 1958-1976 and 1993-1997 at regions in the Arctic Ocean derived from submarine surveys. From Rothrock et al. (1999).



Using a coupled thermodynamic-dynamic model, *Hilmer and Lemke (2000)* simulated sea ice thickness over the Arctic Ocean from 1958-1998 generating results which generally agreed with the measurements of *Rothrock et al. (1999)*, revealing a net reduction in sea ice volume of $-4\% \cdot \text{decade}^{-1}$. When they divided the modeled ice volume time series into three 12-year periods (1964-1975, 1976-1986, 1987-1998) the decrease within the last period was 3-6 times larger than in the previous two periods (*Hilmer and Lemke, 2000*). It should be noted that these decreases were only forced by changes in surface air temperatures and wind (*Hilmer and Lemke, 2000*) so the effects of oceanic forcing or radiative forcing and cloudiness were not accounted for. Sea ice draft data from the periods 1985-1988 and 1992-1994 from Alaska to the North Pole were similar to those of *Hilmer and Lemke (2000)* showing mean sea ice draft decreased by 1.5m between the two

periods (*Tucker et al., 2001*). *Tucker et al. (2001)* attributed their reported rapid sea ice thinning to changes in the atmospheric circulation which reduced the strength of the Beaufort Gyre in the 1980s and early 1990s. As the Beaufort High at the surface became weaker, the clockwise circulation in the sea ice and ocean surface developed as a result also became weaker, leading to divergence and the creation of more thin sea ice in open water areas like leads and polynyas and less convergent deformation which typically creates thick sea ice (*Tucker et al., 2001*). The same central question arises pertaining to sea ice thickness; why has sea ice in the Arctic continued to thin since the early 1990s if the Beaufort High has regained its strength? *Rothrock and Zhang (2005)* explained that Arctic sea ice was extraordinarily thin in the 1990s, caused by strengthened cyclonic circulation in the atmosphere and sea ice combined with anomalously warm springtime air temperatures, but their study only simulated the years 1948-1999, leaving the most prominent decade of sea ice decreases out of the analysis. Sea ice loss of late in terms of extent and volume was dealt with by *Maslanik et al. (2007)* who argued that following massive reductions in sea ice volume that occurred in the late 1980s and early 1990s, changes in sea ice thickness are in part due to changes in the age structure of the Arctic sea ice. This is postulated to be due to a ramping up of sea ice transport from the Bering Strait side of the Arctic to the Fram Strait side, resulting in net loss from the Chukchi and Beaufort Seas, combined with losses from the East Siberian Sea (*Maslanik et al., 2007*). *Maslanik et al. (2007)* also argue that since the late 1990s, sea ice that used to circulate for several years in the Beaufort Gyre all-the-while thickening no longer survives the southern portion of its

clockwise journey around the surface of the Canada Basin. This sea ice loss in the southern Beaufort Sea contributes to a younger, thinner perennial sea ice cover. Sea ice loss to melt in the Beaufort Sea was further explored by *Perovich et al.* (2008) using autonomous ice mass balance buoys drifting with the ice pack from 1994 to 2007. They found that bottom melt of sea ice at a buoy in the Beaufort Sea in 2007 was 2.10m, more than six times the annual average in the 1990s (0.34m) and two and half times the bottom melt that occurred in 2006 (*Perovich et al.*, 2008). This incredible amount of sea ice volume reduction from the ice bottom required the presence of a substantial amount of heat in the upper ocean, which *Perovich et al.* (2008) attribute to solar radiation absorbed in open water areas due to its low albedo. When the amount of shortwave radiation input to the upper ocean was calculated between January and September 2007, it was 400-500% higher than the 1979-2005 average even when energy absorbed through sea ice is neglected, due to a much larger than average open water fraction in 2007 (*Perovich et al.*, 2008). This is representative of the classic sea ice-albedo feedback mechanism.

5. Conclusions

A great deal is known about sea ice thermodynamics and dynamics and their interaction with each other, the ocean, and the atmosphere from the extremely small scale to the hemispheric scale. However, very few measurements of the physical characteristics of the ocean, atmosphere and snow-covered sea ice have been made in the last hundred years due to the difficulty that is entailed in making them. Satellite remote sensing continues to advance as a tool for measuring sea ice

extent and even some surface physical properties, but a dearth of atmospheric, oceanic and sea ice volume measurements in the central Arctic Ocean still exists, reducing the scientific community's ability to accurately parameterize ocean-sea ice-atmosphere processes through the annual cycle, especially when feedback mechanisms like those caused by clouds and the sea ice cover itself are constantly evolving the Arctic climate system. We are put at a further disadvantage by the fact that climate change, anthropogenic or otherwise, is changing the Arctic ocean-sea ice-atmosphere system continually, leaving the scientific community to try and play catch-up on two fronts. Ultimately, it falls on those who choose to study Arctic system science to gain as much data and turn it into information as fast as possible, for then the far-reaching effects of a significantly reduced Arctic sea ice cover or even an ice-free Arctic in summer can hopefully be not only understood but mitigated.

Literature Cited

- Aagaard, K., L.K. Coachman and E. Carmack, 1981. On the halocline of the Arctic Ocean. *Deep Sea Res., A*, 28(6):529-545.
- AMAP, 1998. AMAP Assessment Report: Arctic Pollution Issues. Arctic Monitoring and Assessment Programme (AMAP), Oslo, Norway. Xii+859pp.
- Andreas, E.L., M.A. Lange, S.F. Ackley and P. Wadhams, 1993. Roughness of Weddell sea ice and estimates of the air-ice drag coefficient, *J. Geophys. Res.*, 98(C7):12439-12452.
- Armstrong, R.L., 1980. An analysis of compressive strain in adjacent temperature-gradient and equi-temperature layers in a natural snow cover, *J. Glaciol.*, 26(94):283-289.
- Assur, A., 1958. Composition of sea ice and its tensile strength, *Arctic Sea Ice*. U.S. National Academy of Sciences-National Research Council, Pub. 598, 106-138.
- Barber, D.G., S.P. Reddan and E.F. LeDrew, 1995. Statistical characterization of the geophysical and electric properties of snow on land-fast first-year sea ice, *J. Geophys. Res.*, 100(C2):2673-2686.
- Cherepanov, G.P., 1971. Spatial arrangement of sea ice crystal structure, *Probl. Arkt. Antarkt.*, 38:176-181, (English translation by Amerind Publ. Co., New Delhi, 1973).
- Coachman, L.K. and C.A. Barnes, 1962. The contribution of Bering Sea water to the Arctic Ocean. *Arctic*, 14:147-161.
- Colbeck, S.C., 1982. An overview of seasonal snow metamorphism, *Rev. Geophys. Space phys.*, 20(1):45-61.
- Cole, D.M. and L.H. Shapiro, 1998. Observations of brine drainage networks and microstructure of first-year sea ice, *J. Geophys. Res.*, 103(C10): 21739-21750.
- Colony, R. and A.S. Thorndike, 1984. An estimate of the mean field of Arctic sea ice motion. *J. Geophys. Res.*, 89(C6):10623-10629.
- Colony, R. and A.S. Thorndike, 1985. Sea ice motion as a drunkard's walk. *J. Geophys. Res.*, 90(C1):965-974.
- Comiso, J. C., C.L. Parkinson, R. Gersten and L. Stock, 2008. Accelerated decline in the Arctic sea ice cover. *Geophys. Res. Lett.*, 35, doi:10.1029/2007GL031972.
- Cox, G.F.N. and W.F. Weeks, 1974. Salinity variations in sea ice. *J. Glaciol.*, 13(67):109-120.

- Cox, G.F.N. and W.F. Weeks, 1975. Brine drainage and initial salt entrapment in sodium chloride ice. *CRREL research reports*, #345, Hanover, New Hampshire.
- Cox, G.F.N. and W.F. Weeks, 1983. Equations for determining the gas and brine volumes in sea ice samples. *J. Glaciol.*, 29(102):306-316.
- Curry, J.A. and E.E. Ebert, 1992. Annual cycle of radiation fluxes over the Arctic Ocean: Sensitivity to cloud optical properties. *J. Clim.*, 5:1267-1280.
- Curry, J.A., J.L. Schramm and E.E. Ebert, 1995. Sea ice-albedo feedback mechanism. *J. Clim.*, 8:240-247.
- Curry, J.A., W.B. Rossow, D. Randall and J.L. Schramm, 1996. Overview of arctic cloud and radiation characteristics. *J. Clim.*, 9:1731-1764.
- Deser, C., 2000. On the teleconnectivity of the "Arctic Oscillation". *Geophys. Res. Lett.*, 27(6):779-782.
- Deser, C. and H. Teng, 2008. Evolution of Arctic sea ice concentration trends and the role of atmospheric circulation forcing, 1979-2007. *Geophys. Res. Lett.*, 35, doi:10.1029/2007GL032023.
- Ebert, E.E. and J.A. Curry, 1993. An intermediate one-dimensional thermodynamic sea ice model for investigating ice-atmosphere interactions. *J. Geophys. Res.*, 98(C6):10085-10109.
- Eicken, H., 2003. From the microscopic scale to the macroscopic to the regional scale: Growth, microstructure and properties of sea ice, in Thomas, D.N. and G.S. Dieckmann (eds.), *Sea ice: An introduction to its physics, chemistry, biology and geology*, 22-81, Blackwell Science, Oxford.
- Fairall, C.W. and R. Markson, 1987. Mesoscale variations in surface stress, heat fluxes, and drag coefficient in the marginal ice zone during the 1983 Marginal Ice Zone Project. *J. Geophys. Res.*, 92(C7):6921-6932.
- Flanner, M. G., and C.S. Zender, 2006. Linking snowpack microphysics and albedo evolution. *J. Geophys. Res.*, 111, doi:10.1029/2005JD006834.
- Francis, J.A., E. Hunter, J.R. Key and X. Wang, 2005. Clues to variability in Arctic minimum sea ice extent. *Geophys. Res. Lett.*, 32, doi:10.1029/2005GL024376.
- Frankenstein, G. and R. Garner, 1967. Equations for determining the brine volume of sea ice from -0.5°C to -22.9°C. *J. Glaciol.*, 6(48):943-944.
- Golden, K.M., 2003. Critical behavior of transport in sea ice. *Physica B*, 338:274-283.

- Gow, A.J. and W.B. Tucker III, 1991. Physical and dynamic properties of sea ice in the polar oceans. *CRREL monograph 91-1*, Office of Naval Research, Hanover, New Hampshire.
- Granberg, H. B., 1998. Snow cover on sea ice, in M. Leppäranta (ed.), *Physics of Ice-Covered Seas*, II, 605-649, Helsinki Univ. Press, Helsinki.
- Grenfell, T. C. and G.A. Maykut, 1977. The optical properties of ice and snow in the Arctic basin, *J. Glaciol.*, 18:445-463.
- Grenfell, T.C. and D.C. Perovich, 1984. Spectral albedos of sea ice and incident solar irradiance in the southern Beaufort Sea. *J. Geophys. Res.*, 89(C3):3573-3580.
- Grenfell, T.C., D.G. Barber, A.K. Fung, A.J. Gow, K.C. Jezek, E.J. Knapp, S.V. Nghiem, R.G. Onstott, D.K. Perovich, C.S. Roesler, C.T. Swift, and F. Tanis, 1998. Evolution of electromagnetic signatures of sea ice from initial formation to the establishment of thick first-year ice. *IEEE Trans. Geosci. Rem. Sens.*, 36(5):1642-1654.
- Guest, P.S., J.W. Glendening and K.L. Davidson, 1995. An observation and numerical study of wind stress variations within marginal ice zones. *J. Geophys. Res.*, 100(C6):10887-10904.
- Haas, C., S. Gerland, H. Eicken and H. Miller, 1997. Comparison of sea ice thickness measurements under summer and winter condition in the Arctic using a small electromagnetic induction device. *Geophys.*, 62(3):749-757.
- Haas, C., 2003. Dynamics vs. thermodynamics: the sea ice thickness distribution, in Thomas, D.N. and G.S. Dieckmann (eds.), *Sea ice: An introduction to its physics, chemistry, biology and geology*, 82-111, Blackwell Science, Oxford.
- Hibler III, W.D., 1979. A dynamic thermodynamic sea ice model. *J. Phys. Ocean.*, 9:815-846.
- Hibler, III, W.D., 1986. Ice dynamics, in N. Untersteiner, (ed.), *The Geophysics of Sea Ice*, Plenum, New York, 577-640.
- Hilmer, M. and P. Lemke, 2000. On the decrease of Arctic sea ice volume. *Geophys. Res. Lett.*, 27(2):3751-3754.
- Hobbs, P.V., 1974. *Ice Physics*. Oxford University Press, Oxford.
- Hurrell, J.W., 1995. Decadal trends in the North Atlantic Oscillation: Regional temperatures and precipitation. *Science*, 269(5224):676-679.

Intrieri, J.M., C.W. Fairall, M.D. Shupe, P.O.G. Persson, E.L. Andreas, P.S. Guest and R.E. Moritz, 2002. An annual cycle of Arctic surface cloud forcing at SHEBA. *J. Geophys. Res.*, 107(C10), doi:10.1029/2000JC000439.

Johnston, M., G. Timco and R. Frederking, 2003. Developing an ice strength algorithm for level, landfast first-year sea ice in the high Arctic. *Canadian hydraulics center technical report for the Canadian ice service*.

Jordan, R.E., E.L. Andreas and A.P. Makshtas, 1999. Heat budget of snow-covered sea ice at North Pole 4. *J. Geophys. Res.*, 104(C4):7785-7806.

Kay, J.E., T. L'Ecuyer, A. Gettelman, G. Stephens and C. O'Dell, 2008. The contribution of cloud and radiation anomalies to the 2007 Arctic sea ice extent minimum. *Geophys. Res. Lett.*, 35, doi:10.1029/2008GL033451.

Krishfield, R.A. and D.K. Perovich, 2005. Spatial and temporal variability of oceanic heat flux to the Arctic ice pack. *J. Geophys. Res.*, 110, doi:10.1029/2004JC002293.

Kwok, R. and D.A. Rothrock, 1999. Variability of Fram Strait ice flux and North Atlantic Oscillation. *J. Geophys. Res.*, 104(C3):5177-5189.

Laine, V., 2004. Arctic sea ice regional albedo variability and trends, 1982-1998, *J. Geophys. Res.*, doi: 10.1029/2003JC001818.

Langlois, A., C.J. Mundy and D.G. Barber, 2007. On the evolution of snow thermophysical properties over land-fast first-year sea ice, *Hydrol. Process.*, 21:705-716.

Ledley, T.S., 1991. Snow on sea ice: competing effects in shaping climate. *J. Geophys. Res.*, 96(D9): 17195-17208.

Leppäranta, M. and T. Manninen, 1988. The brine and gas content of sea ice with attention to low salinitiea and high temperatures. *Finnish Institute Marine Research Internal Report*, 88-2, Helsinki.

Leppäranta, M., 1998. The dynamics of sea ice, in M. Leppäranta (ed.), *Physics of Ice-Covered Seas*, I, 305-342, Helsinki Univ. Press, Helsinki.

Light, B., G.A. Maykut, and T.C. Grenfell, 2003. Effects of temperature on the microstructure of first-year Arctic sea ice, *J. Geophys. Res.*, doi:10.1029/2001JC000887.

Lindsay, R.W., 1998. Temporal variability of the energy balance of thick Arctic pack ice. *J. Clim.*, 11:313-333.

- Lindsay, R.W. and J. Zhang, 2005. The thinning of Arctic sea ice, 1988-2003: Have we passed the tipping point? *J. Clim.*, 18:4879-4895.
- Lukovich, J.V. and D.G. Barber, 2006. Atmospheric controls on sea ice motion in the southern Beaufort Sea. *J. Geophys. Res.*, 11, doi:10.1029/2005JC006408.
- Lynch, A.H., J.A. Maslanik, and W. Wu, 2001. Mechanisms in the development of anomalous sea ice extent in the western Arctic: A case study. *J. Geophys. Res.*, 106(D22):28097-28105.
- Malmgren, F., 1927. On the properties of sea ice. *Norweg. North Pole Exped. "Maud" 1918-1925.*, 1(5):1-67.
- Makshtas, A.P., 1998. Thermodynamics of sea ice, in M. Leppäranta (ed.), *Physics of Ice-Covered Seas*, I, 289-304, Helsinki Univ. Press, Helsinki.
- Maslanik, J.A., C. Fowler, J. Stroeve, S. Drobot, J. Zwally, D. Yi and W. Emery, 2007. A younger, thinner Arctic sea ice cover: Increased potential for rapid, extensive sea-ice loss. *Geophys. Res. Lett.*, 34, doi:10.1029/2007GL032043.
- Maykut, G.A. and N. Untersteiner, 1971. Some results from a time-dependent thermodynamic model of sea ice. *J. Geophys. Res.*, 76(6):1550-1575.
- Maykut, G.A., 1978. Energy exchange over young sea ice in the central Arctic. *J. Geophys. Res.*, 83:3646-3658.
- Maykut, G.A., 1982. Large-scale heat exchange and ice production in the central Arctic. *J. Geophys. Res.*, 87:7971-7984.
- Maykut, G.A., 1986. The surface heat and mass balance, in N. Untersteiner (ed.), *The Geophysics of Sea Ice*, Plenum, New York, 395-464.
- Maykut, G.A. and M.G. McPhee, 1995. Solar heating of the Arctic mixed layer. *J. Geophys. Res.*, 100(C12):24691-24703.
- Mellor, M., 1977. Engineering properties of snow, *J. Glaciol.*, 19:15-66.
- Mellor, M., 1986. Mechanical behavior of sea ice, in N. Untersteiner, (ed.), *The Geophysics of Sea Ice*, Plenum, New York, 165-281.
- McKay, C. P., 2000. Thickness of tropical ice and photosynthesis on a snowball Earth, *Geophys. Res. Lett.*, 27(14): 2153-2156.
- McPhee, M.G., 1979. The effect of the oceanic boundary layer on the mean drift of pack ice: application of a simple model, *J. Phys. Ocean.*, 9:388-400.

McPhee, M.G., 1986. The upper ocean, in N. Untersteiner, (ed.), *The Geophysics of Sea Ice*, Plenum, New York, 339-394.

McPhee, M.G., 1992. Turbulent heat flux in the upper ocean under sea ice. *J. Geophys. Res.*, 97(C4):5365-5379.

McPhee, M.G., T.P. Stanton, J.H. Morison and D. G. Martinson, 1998. Freshening of the upper ocean in the Arctic: Is perennial sea ice disappearing? *Geophys. Res. Lett.*, 25(10):1729-1732.

Nakawo, M. and N.K. Sinha, 1981. Growth rate and salinity profile of first-year sea ice in the high Arctic. *J. Glaciol.*, 27(96):315-330.

Nakawo, M. and N.K. Sinha, 1984. A note on brine layer spacing of first-year sea ice, *Atmos. Ocean*, 22: 193-206.

Ngheim, S.V., Y. Chao, G. Neumann, P.Li, D.K. Perovich, T. Street and P. Clemente-Colon, 2006. Depletion of perennial sea ice in the east Arctic Ocean. *Geophys. Res. Lett.*, 3, doi:10.1029/2006GL027198.

Ogi, M. and J.M. Wallace, 2007. Summer minimum Arctic sea ice extent and the associated summer atmospheric circulation. *Geophys. Res. Lett.*, 34, doi:10.1029/2007GL29897.

Oke, T.R., 1987. *Boundary layer climates*. Routledge, London.

Ono, N., 1967. Specific heat and heat of fusion of sea ice, in H. Oura (ed.), *Physics of snow and ice*, 1, 599-610, Inst. Low Temp. Sci., Hokkaido, Japan.

Ono, N., 1968. Thermal properties of sea ice. IV. Thermal constants of sea ice. *Low Temp. Sci.*, A26:329-349.

Overland, J.E., 1985. Atmospheric boundary layer structure and drag coefficients over sea ice, *J. Geophys. Res.*, 90(C5):9029-9049.

Parkinson, C.L., D.J. Cavalieri, P. Gloersen, H.J. Zwally and J.C. Comiso, 1999. Arctic sea ice extents, areas, and trends, 1978-1996. *J. Geophys. Res.*, 104(C9):20837-20856.

Parkinson, C.L. and D. J. Cavalieri, 2008. Arctic sea ice variability and trends, 1979-2006. *J. Geophys. Res.*, 113, doi:10.1029/2007JC004558.

Perovich, D.K., 1998. The optical properties of sea ice. *CRREL monograph 96-01*, Office of Naval Research, Hanover, New Hampshire.

- Perovich, D.K., 1998. The optical properties of sea ice, in M. Leppäranta (ed.), *Physics of Ice-Covered Seas*, I, 195-230, Helsinki Univ. Press, Helsinki.
- Perovich, D.K and B. Elder, 2002. Estimates of ocean heat flux at SHEBA. *Geophys. Res. Lett.*, 29(9), doi:10.1029/2001GL014171.
- Perovich, D.K., T.C. Grenfell, B. Light and P.V. Hobbs, 2002. Seasonal evolution of the albedo of multiyear Arctic sea ice. *J. Geophys. Res.*, 107(C10), doi:10.1029/2000JC000438.
- Perovich, D.K., J.A. Richter-Menge, K.F. Jones and B. Light, 2008. Sunlight, water and ice: Extreme Arctic sea ice melt during the summer of 2007. *Geophys. Res. Lett.*, 35, doi:10.1029/2008GL034007.
- Persson, P.O.G., C.W. Fairall, E.L. Andreas, P.S. Guest and D.K. Perovich, 2002. Measurements near the atmospheric surface flux group tower at SHEBA: Near-surface conditions and surface energy budget. *J. Geophys. Res.*, 107(C10), doi:10.1029/2000JC000705.
- Pollard, D., and J.F. Kasting, 2005. Snowball Earth: A thin-ice solution with flowing sea glaciers, *J. Geophys. Res.*, 110, doi: 10.1029/2004JC002525.
- Polyakov, I.V., R.V. Bekryaev, G.V. Alekseev, U.S. Bhatt, R.L. Colony, M.A. Johnson, A.P. Makshtas and D. Walsh, 2003. Variability and trends of air temperature and pressure in the maritime Arctic, 1875-2000. *J. Clim.*, 16:2067-2077.
- Pringle, D.J., H.J. Trodahl and T.G. Haskell, 2006. Direct measurement of sea ice thermal conductivity: no surface reduction. *J. Geophys. Res.*, 111, doi:10.1029/2005JC002990.
- Prinsenberg, S.P., 1992. Effect of snow cover on ice growth rates at land-fast ice stations in the Canadian Arctic. *Proceedings of the 11th international symposium on ice*, 2:633-644. 15-19 June, Banff, Alberta, Canada.
- Proshutinsky, A.Y. and M.A. Johnson, 1997. Two circulation regimes of the wind-driven Arctic Ocean. *J. Geophys. Res.*, 102(C6):12493-12514.
- Reynolds, M., C.H. Pease and J.E. Overland, 1985. Ice drift and regional meteorology in the southern Bering Sea: results from MIZEX West. *J. Geophys. Res.*, 90(C6):11967-11981.
- Rigor, I.G., R.L. Colony and S. Martin, 2000. Variations in surface air temperature in the Arctic, 1979-1997. *J. Clim.*, 13:896-914.
- Rothrock, D.A., Y. Yu and G.A. Maykut, 1999. Thinning of the Arctic sea-ice cover. *Geophys. Res. Lett.*, 26(23):3469-3472.

Rothrock, D.A. and J. Zhang, 2005. Arctic Ocean sea ice volume: What explains its recent depletion? *J. Geophys. Res.*, 10, doi:10.1029/2004JC002282.

Rudels, B., L.G. Anderson and E.P. Jones, 1996. Formation and evolution of the surface mixed layer and halocline of the Arctic Ocean. *J. Geophys. Res.*, 101(C4):8807-8821.

Ruffieux, D., P.O.G. Persson, C.W. Fairall and D.E. Wolfe, 1995. Ice pack and lead surface energy budgets during LEADDEX 1992. *J. Geophys. Res.*, 100(C3):4593-4612.

Serreze, M.C., R.G. Barry and A.S. McLaren, 1989. Seasonal variations in sea ice motion and effects on sea ice concentration in the Canada Basin. *J. Geophys. Res.*, 94(C8):10955-10970.

Shine, K.P. and A. Henderson-Sellers, 1985. The sensitivity of a thermodynamic sea ice model to changes in surface albedo parameterization. *J. Geophys. Res.*, 90(D1):2243-2250.

Smith, S.T., R.B. Muench and C.H. Pease, 1990. Polynyas and leads: an overview of the physical processes and environment. *J. Geophys. Res.*, 95(C6): 9461-9479.

Steffen, K. and T. DeMaria, 1996. Surface energy fluxes of Arctic winter sea ice in Barrow Strait. *J. Appl. Met.*, 35:2067-2079.

Stroeve, J.C., M. C. Serreze, F. Fetterer, T. Arbetter, W. Meier, J. Maslanik and K. Knowles, 2005. Tracking the Arctic's shrinking ice cover: ANother extreme September minimum in 2004. *Geophys. Res. Lett.*, 32, doi:10.1029/2004GL021810.

Sturm, M., 1991. The role of thermal convection in heat and mass transport in the subarctic snow cover. *CRREL monograph 91-19*, Office of Naval Research, Hanover, New Hampshire.

Sturm, M., J. Holmgren, M. Konig, and K. Morris, 1997. The thermal conductivity of seasonal snow. *J. Glaciol.*, 43: 26-51.

Sturm M, J. Holmgren and D.K. Perovich, 2002. Winter snow cover on the sea ice of the Arctic Ocean at the Surface Heat Budget of the Arctic Ocean (SHEBA): Temporal evolution and spatial variability. *J. Geophys. Res.*, 107(C10), doi: 10.1029/2000JC000400.

Thompson, D.W.J. and J.M. Wallace, 1998. The Arctic Oscillation signature in the wintertime geopotential height and temperature fields. *Geophys. Res. Lett.*, 25(9):1297-1300.

- Thorndike, A.S., D.A. Rothrock, G.A. Maykut and R. Colony, 1975. The thickness distribution of sea ice. *J. Geophys. Res.*, 80(33):4501-4513.
- Thorndike, A.S., C. Parkinson and D.A. Rothrock (Eds.), 1992. Report of the sea ice thickness workshop, 19-21 November, New Carrollton, Maryland. Polar Science Center, Applied Physics Laboratory, Univ. of Washington, Seattle.
- Timco, G.W. and M.E. Johnston, 2002. Sea ice strength during the melt season, in *Ice in the environment: proceedings of the 16th IAHR international symposium on sea ice*, Dunedin, New Zealand, 2-6 December.
- Tucker III, W.B., J.W. Weatherly, D.T. Eppler, L.D. Farmer, and D.L. Bentley, 2001. Evidence for rapid thinning of sea ice in the western Arctic Ocean at the end of the 1980s. *Geophys. Res. Lett.*, 28:2851-2854.
- Untersteiner, N., 1961. On the mass and heat budget of Arctic sea ice. *Met. Atmos. Phys.*, 12(2):151-182.
- Vowinckel, E. and S. Orvig, 1970. The climate of the North Polar Basin, in S. Orvig (ed.), *Climates of the Polar Regions, World Survey of Climatology*, 14:283-299, Elsevier Publ. Co., Amsterdam, Netherlands.
- Wadhams, P., 1992. Sea ice thickness distribution in the Greenland Sea and Eurasian Basin, May 1987. *J. Geophys. Res.*, 97(C4):5331-5348.
- Wadhams, P., 1998. Sea ice morphology, in M. Leppäranta (ed.), *Physics of Ice-Covered Seas*, I, 231-287, Helsinki Univ. Press, Helsinki.
- Wadhams, P., 2000. *Ice in the ocean*. Gordon and Breach Science Publishers, London.
- Warren, S.G., I.G. Rigor, N. Untersteiner, V.F. Radionov, N.N. Bryazgin, Y.I. Aleksandrov and R. Colony, 1999. Snow depth on Arctic sea ice. *J. Clim.*, 12:1814-1829.
- Weeks, W.F., 1998. Growth conditions and the structure and properties of sea ice, in M. Leppäranta (ed.), *Physics of Ice-Covered Seas*, I, 25-104, Helsinki Univ. Press, Helsinki.
- Weeks, W.F. and S.F. Ackley, 1986. The growth, structure, and properties of sea ice, in N. Untersteiner, (ed.), *The Geophysics of Sea Ice*, Plenum, New York, 9-64.
- Weeks W.F. and A.J. Gow, 1978. Preferred crystal orientation in the fast ice along the margins of the Arctic Ocean. *J. Geophys. Res.*, 83(C10):5105-5121.

Weeks W.F. and A.J. Gow, 1980. Crystal alignments in the fast ice of Arctic Alaska. *J. Geophys. Res.*, 85(C2):1137-1146.

Wettlaufer, J.S., 1991. Heat flux at the ice-ocean interface. *J. Geophys. Res.*, 96(C4):7215-7236.

World Meteorological Organization(WMO), 1970. Part 1 Ice terms arranged by subject. In *WMO Sea ice nomenclature*, WMO rep.#259, T.P.145, 6pp, Geneva.

Yen, Y.C., 1981. Review of thermal properties of snow, ice and sea ice. *CRREL monograph* 81-10, Office of Naval Research, Hanover, New Hampshire.

Yen, Y.C., K.C. Cheng, and S. Fukosako, 1991. Review of intrinsic thermophysical properties of snow, ice, sea ice, and frost, in Zarling, J.P. and S.L. Faussett (eds.) *Proceedings 3rd international symposium on cold regions heat transfer, Fairbanks, AK, June 11-14, 1991*, University of Alaska, Fairbanks, Alaska.

Zhang, T., K. Stamnes, and S.A. Bowling, 1996. Impact of clouds on surface radiation fluxes and snowmelt in the Arctic and sub-Arctic. *J. Clim.*, 9: 2110-2123.

Zhang, J. and W.B. Hibler III, 1997. On an efficient numerical method for modeling sea ice dynamics. *J. Geophys. Res.*, 102(C4): 8691-8702.

Zhang, J., D. Rothrock and M. Steele, 2000. Recent changes in Arctic sea ice: the interplay between ice dynamics and thermodynamics. *J. Clim.*, 13: 3099-3114.

CHAPTER THREE: OBSERVATIONS OF GEOPHYSICAL AND DIELECTRIC PROPERTIES AND GROUND PENETRATING RADAR SIGNATURES FOR DISCRIMINATION OF SNOW, SEA ICE AND FRESHWATER ICE THICKNESS

Galley, R.J., M. Tractenberg, A. Langlois, D.G. Barber, 2009. Observations of geophysical and dielectric properties and ground penetrating radar signatures for discrimination of snow, sea ice, and freshwater ice thickness. *Cold Regions Science and Technology*, 57: 29-38.

Introduction

Co-located snow and sea ice thickness measurements are vital to our understanding of thermodynamic and dynamic processes across the Arctic ocean-sea ice-atmosphere interface. Snow-covered sea ice variably modifies ocean-atmosphere coupling by affecting the transfer of energy, mass and momentum between them. Specifically, the thermal conductivity of snow is an order of magnitude lower than that of sea ice due to the large fractional volume of air, making it an excellent insulator. Snow on sea ice smoothes the sea ice surface, decreasing the ice-air drag coefficient and the bulk transfer coefficients for sensible and latent heat. Melting snow and sea ice also seasonally changes the freshwater and salt content of the upper ocean. Sea ice thickness in part determines sea ice strength, extent and duration, especially in seasonal ice zones. Snow and sea ice thickness also plays a substantial role in the amount of light reaching the ice bottom, controlling photosynthetic activity with ubiquitous ecological implications. Accurate snow and ice thickness data are also important to northern residents, government and corporations, who depend upon ice for the construction of ice roads, ice airfields, offshore development, and ship and port logistics.

In the past, spatial snow and ice thickness measurements have been very difficult to collect due to the time and amount of physical work required to make them. Studies of sea ice thickness have been undertaken using drill-hole measurements (e.g. *Lange and Eicken, 1991*), electrical ice thickness gauges (e.g. *Perovich et al., 2003*), ship-based camera systems (e.g. *Dumas et al., 2007*), inferred from draft with upward-looking-sonar from moorings (e.g. *Melling et al., 2005*) and submarines (e.g. *Wadhams, 1987*), and from above using surface-based (e.g. *Haas et al., 1997; Haas, 2004*) and helicopter-mounted electromagnetic (EM) induction equipment (e.g. *Kovacs and Holladay, 1990; Prinsenbergh and Holladay, 1993*). While methodologies are numerous, only drill-hole measurements yield separate snow and sea ice thickness data at a single location. Drill-hole and electrical thickness gauge measurements are relatively simple and accurate, but spatial information is difficult to collect. Sonar ice draft data approximate sea ice thickness, however the overlying snow thickness that dominates the transfer of heat and light between ocean and atmosphere cannot be determined. Submarine-based sonar data are prohibitively expensive to collect and mooring-based sonar instruments do not yield spatial data and are sometimes lost. EM induction is effective in measuring snow-plus-sea ice-thickness (referred to herein as 'slab thickness') in areas where ice occurs atop seawater, but requires a laser altimeter to measure the distance between the instrument and the top of the snow-plus-sea ice slab. Snow thickness cannot be determined, and EM systems fail to resolve the ice-water interface when ice resides above freshwater.

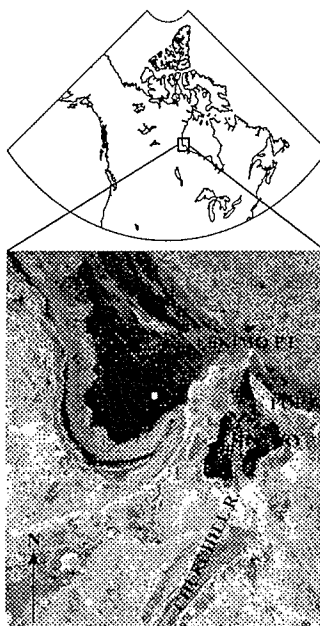
Ground penetrating radar (GPR) has been used in previous studies in cold environments to investigate the properties of permafrost (*Pilon et al., 1992*) and glaciers, specifically to measure changes in glacial mass balance both spatially and temporally (*Kohler et al., 1997; Winther et al., 1998; Palli et al., 2002; Harper and Bradford, 2003; Sinisalo et al., 2003*) and to detect internal structure (*Deng and Sun, 2004; Travassos and Simoes, 2004*). Thickness profiles of river ice have been made using helicopter-borne ground penetrating radar over both dry (*Arcone and Delaney, 1987; Arcone, 1991*) and wet river ice sheets (*Arcone, 1991*) where in both cases the dielectric constant of river ice was assumed to be 3.2. Over sea ice, *Kovacs and Morey (1992)* measured snow-plus-sea ice thickness and sea ice thickness using GPR and drill-hole measurements on two floes of second year sea ice. However, they did not make separate snow and sea ice thickness measurements at each location, nor did they calculate the dielectric constant of the snow or sea ice using ice core data (*Kovacs and Morey, 1992*). Their two-way travel time results were compared to drill-hole thickness measurements and found to be highly correlated, a relationship from which they derived an apparent dielectric constant for frequencies of 80 and 120MHz (*Kovacs and Morey, 1992*). The literature contains no coincident physical, dielectric and GPR return studies in spite of the fact that using GPR to make thickness measurements depends on the radar velocity in the medium, which depends principally on the medium's dielectric constant at frequency used. In this work, the physical and dielectric properties of snow, river ice and sea ice in the Churchill River estuary (a freshwater site) and Button Bay (a marine site) are presented and compared to coincident GPR return data at 250MHz and 1GHz to

determine the physical factors contributing to radar velocity, return signal timing and amplitude. Using these data, we were able to make separate snow and ice thickness measurements at the same location.

Methods

Data were collected over snow-covered ice in Button Bay and near the mouth of the Churchill River estuary, southwestern Hudson Bay in March 2006 (Figure 3.1). The physical properties of the snow and sea ice in Button Bay are quite different from the Churchill River estuary. Button Bay is saline (31.5psu) (Kuzyk *et al.*, 2007), growing sea ice in winter and resulting in salinity within the snow lying atop it (Barber *et al.*, 1995).

Figure 3.1. (Top) Map of Canada showing the Churchill River estuary and Button Bay (black box) and (bottom) Radarsat-1 scanSAR image of Button Bay and the Churchill River estuary in southwestern Hudson Bay, Canada.



Snow and ice physical properties

Shaded snow pits were excavated over the Churchill River estuary and Button Bay. Beginning at the air-snow interface, snow samples were extracted using a 66.8cm³ snow density cutter at 2cm intervals, bagged and weighed to calculate snow density. Snow samples were melted at room temperature and the conductivity of the melt water was measured using a conductivity meter (Hoskin Scientific Cond 330i) and converted to practical salinity units (psu) (*Fofonoff and Millard, 1983*). Snow wetness was calculated from capacitance plate measurements at the middle of the 2cm depth intervals (after *Denoth, 1989*). Snow thickness is conventionally positive upward from the snow-ice interface ($z_s = 0\text{m}$).

Two ice cores (9cm diameter) were extracted at each location. One was used to measure ice temperatures starting 5cm from the surface and proceeding at 10cm intervals to the ice bottom by drilling a small hole to the middle of the core and inserting a digital thermometer (Traceable – model 4000). Ice salinity was determined by cutting the second core into 10cm sections and melting the pieces at room temperature in sealed plastic containers, then measuring the conductivity of the melt water using a conductivity meter. Conductivity was converted to psu, and brine volume was calculated for each snow and ice sample using the equations of *Cox and Weeks (1983)* after *Frankenstein and Garner (1967)*. Sea ice thickness at the coring location was measured with an ice thickness gauge. Ice thickness is conventionally measured from the snow-ice interface ($z_i = 0$) downward to the ice-water interface.

Snow and ice dielectric properties

Snow and ice physical data were used to compute the real (permittivity, ϵ') and imaginary (loss, ϵ'') components of the complex dielectric constant (ϵ) of snow and sea ice at two frequencies:

$$\epsilon = \epsilon' - j\epsilon'' \quad [3.1]$$

which obey the Debye equations and depends upon frequency and temperature. Permittivity represents the ability of a medium to transmit incident energy and loss refers to the extinction of the incident energy within the medium.

Dry snow (<1% water by volume) may contain brine which is treated as the inclusion dielectric within a dry snow host dielectric (*Langlois and Barber, 2007, after Mätzler, 1987 and Drinkwater and Crocker, 1988*). The permittivity and loss in dry snow samples were calculated using a dielectric mixture model of the form proposed by Polder-Van Santen and later modified by De Loor (*Ulaby et al., 1990*) assuming that spherical brine inclusions were the only scatterers within a uniform ice background medium. The dielectric constant of a dry saline snow mixture over first-year sea ice is expressed as:

$$\Delta\epsilon^*_{mix} = \chi \cdot V_b \cdot \left\{ \frac{\epsilon^*_{b} - \epsilon^*_{ds}}{1 + \left[\frac{\epsilon^*_{b} - 1}{\epsilon^*_{ds}} \right] \cdot A_0} \right\}, \quad [3.2]$$

where ϵ^*_{ds} and ϵ^*_{b} are complex terms representing the dielectric constant of dry snow and brine, χ is the fraction of brine accounted for, A_0 is a depolarization factor and V_b is the brine volume within the snow layer.

In wet snow (>1% water-by-volume), the permittivity (ϵ'_{wet}) and loss (ϵ''_{wet}) are independent of snow temperature and salinity. The dielectric constant of wet snow (ϵ^*_{wet}) was calculated using the permittivity and loss of both dry snow and pure water (Tiuri et al., 1984). The Polder-Van Santen approach was used to treat the dry snow as the 'host dielectric' and the pure water as the 'inclusion dielectric' such that:

$$\epsilon'_{ws} = \epsilon'_{ds} + \epsilon'_w \cdot (0.1 \cdot W_v + 0.8 \cdot W_v^2) \quad [3.3]$$

$$\epsilon''_{ws} = \epsilon''_w \cdot (0.1 \cdot W_v + 0.8 \cdot W_v^2), \quad [3.4]$$

where W_v is the snow wetness (%), and ϵ'_{ds} is the permittivity of dry snow as needed in $\Delta\epsilon^*_{mix}$ and given by:

$$\epsilon'_{ds} = (1 + 0.51 \cdot \rho_s)^3, \quad [3.5]$$

$$\epsilon''_{ds} = \frac{0.34 \cdot \frac{\rho_s}{0.916} \cdot 0.001}{\left(1 - \left(0.417 \cdot \frac{\rho_s}{0.916}\right)\right)^2}, \quad [3.6]$$

Both wet and dry snow dielectric constant calculations are dependent upon snow density and the frequency used.

The dielectric properties of brine in sea ice were calculated from salinity:

$$\epsilon'_b = \epsilon_{w\infty} + \frac{\epsilon_{b0} - \epsilon_{w\infty}}{1 + (2\pi f \tau_b)^2}, \quad [3.7]$$

$$\epsilon''_b = (2\pi f \tau_b) \cdot \left\{ \frac{\epsilon_{b0} - \epsilon_{w\infty}}{1 + (2\pi f \tau_b)^2} \right\} + \frac{\sigma_b}{2\pi f \epsilon_0}, \quad [3.8]$$

where $\epsilon_{w\infty}$, ϵ_{b0} , f , τ_b , σ_b and ϵ_0 are the high frequency limit of the dielectric constant of brine, the static dielectric of brine, the frequency, the relaxation time of brine, the

ionic conductivity of the brine solution and the permittivity of free space respectively (Stogryn, 1971; Stogryn and Desargeant, 1985). Further details are available in Barber *et al.* (1998).

Ground penetrating radar

The velocity of radio wave propagation and attenuation within a medium is mostly a function of the composition of the medium and water content. It is dependent upon the speed of light in free space ($c = 0.3\text{m/ns}$), the relative dielectric constant (ϵ_r) of the medium and the relative magnetic permeability (μ_r , unity for non-magnetic materials). GPR measurements depend on the media's ability to transmit radio waves and the contrast in relative dielectric constant between adjacent layers which reflect a fraction of the incident energy. By measuring the time it takes for these reflections to return to a receiving antenna, we can estimate the depth of the dielectric interface which caused them as long as we know the velocity, which is dependent on the medium's physical and dielectric properties.

We employed bi-static GPR systems operating at centre frequencies of 250MHz and 1GHz manufactured by Sensors and Software Ltd. Typically the actual free-space center frequencies decrease as a result of antenna loading associated with coupling the antennas to the surface and variation in snow and ice properties creates variation in the center frequency of the wavelet spectra, but the amount of variation was not determined here. We therefore used the manufacturers designated antenna frequency in our work (after Kovacs and Morey, 1992). The system consisted of a digital data-logger connected to a transmitting antenna and a

receiving antenna for each center frequency by serial cables and was easily operated despite the relatively cold temperatures encountered. The transmitter and receiver for each frequency were shielded and mounted in skid plates at fixed separation distances (0.15m for 1GHz and 0.38m for 250MHz). A perpendicular broad-side arrangement was chosen for the antennas at each frequency as it has a broader footprint and tends to give a radar section that is more representative of a two-dimensional slice through the subsurface compared to an end-fire arrangement (Annan and Cosway, 1992). Temporal sampling intervals of 0.1 ns were used at both frequencies over a time window of 25ns enabling simultaneous data collection. At 1GHz (250MHz) a 25ns time window corresponds to 3.75m (3.75m) in free space, and 2.16m (2.15m) in a medium of $\epsilon' = 3$ with antenna separation of 0.15m (0.38m). Four traces were stacked at each location with the average of those traces recorded. GPR return data were collected at points without moving the antenna array and/or in profile mode as the antennas were dragged along the surface.

The velocity of radio waves in a material (V_m) is calculated by:

$$V_m = \frac{c}{\left\{ \left(\frac{\epsilon_r \mu_r}{2} \right) [(1 + P^2) + 1] \right\}^{1/2}} \quad [3.9]$$

Where c , ϵ_r , and μ_r are the speed of light in free space (0.3m/ns), the real permittivity of the medium, and the relative magnetic permeability of the medium (=1). The loss factor (P) in equation 3.9 is calculated by:

$$P = \frac{\sigma}{2\pi\alpha f \epsilon} \quad [3.10]$$

where σ is the conductivity of the medium, f is the frequency and ϵ is ϵ_r multiplied by the permittivity of free space (8.8854×10^{-12} F/m). Assuming snow and sea ice are low-loss materials ($P \ll 1$), the velocity of a radar wave in a medium (V_m) is:

$$V_m = c/\sqrt{\epsilon_r} \quad [3.11]$$

Practically, accurate two-way travel times (t) derived from GPR return data require that the antenna separation distance be accounted for:

$$V_m t = (x^2 + 4z^2)^{0.5} \quad [3.12]$$

where x is the antenna separation, and z is snow or ice thickness. In each case, two-way travel time (t) was determined using the first positive amplitude point in time within the return signal (marked on the trace plots with a horizontal dashed line).

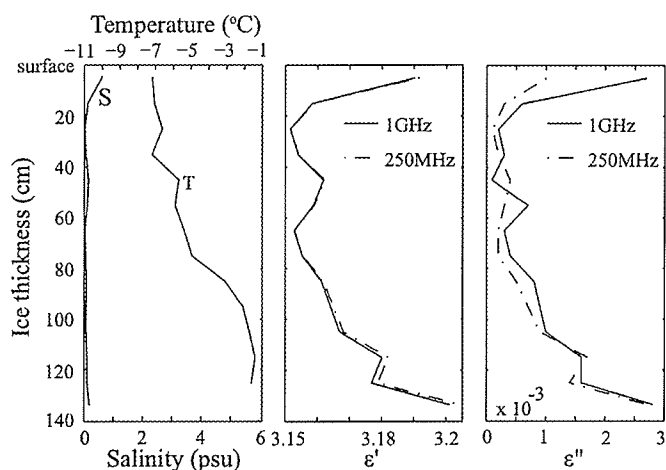
For each GPR measurement discussed below, the mean ϵ' calculated from the physical samples of snow and/or ice ($\epsilon'_{\text{dielectric}}$) was used to calculate the dielectric radar velocity ($V_{m_{\text{dielectric}}}$) in the medium. Using the GPR two-way travel time (t , in ns) and $V_{m_{\text{dielectric}}}$ the medium's dielectrically-derived thickness was calculated ($z_{i_{\text{dielectric}}}$) and compared to the observed thickness. Using the measured or ice thickness ($z_{i_{\text{obs}}}$) and the two-way travel time, the GPR derived radar velocity in the medium was calculated ($V_{m_{\text{GPR}}}$) from which the apparent permittivity (ϵ'_{GPR}) was calculated.

Results and Discussion

Churchill River estuary ice and snow - physical and dielectric properties

Cores from the Churchill River estuary on 6 March 2006 were used to determine the ice temperature and salinity (Figure 3.2). The two ice cores were 1.37m and 1.32m thick at nominally the same location.

Figure 3.2. Salinity and temperature profiles of river ice in the Churchill River estuary (left), permittivity (ϵ') profiles of river ice (middle) and dielectric loss (ϵ'') profiles of river ice (right) on 6 march 2006 ($z_i = 135\text{cm}$).

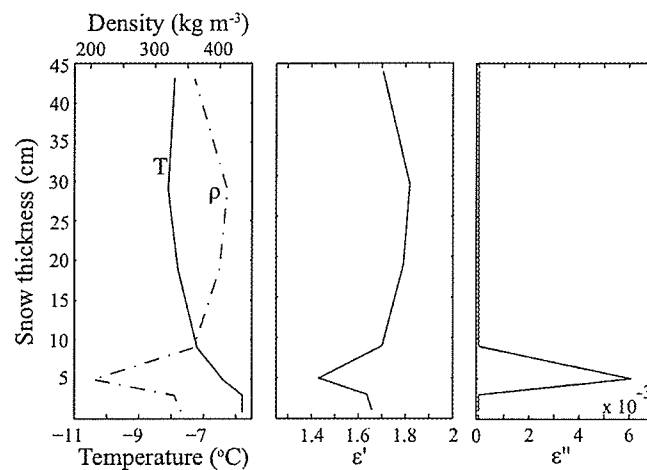


The salinity profile indicates ice in the Churchill River estuary was formed from freshwater (Figure 3.2). Ice temperatures increased slowly from about -7°C near the ice surface to about -5°C at 0.75m, then more rapidly to less than -2°C near the ice bottom (Figure 3.2: left). Permittivity profiles at 1GHz and 250MHz were nearly identical, varying little around a mean of 3.17 (Figure 3.2: middle), yielding a calculated dielectric radar velocity of 0.169m/ns. Permittivity was relatively greater in the top of the ice core due to small amounts of salinity. Increased

temperature at between 40 and 50cm coincided with an increase in permittivity, as did temperature increases in the bottom 50cm of the core. Loss at both frequencies was extremely small (Figure 3.2: right) due to negligible salinity within the ice.

On 6 March 2006, a snow pit ($z_s = 0.44\text{m}$) was excavated near the middle of the Churchill River estuary. The two-meter air temperature was -8.9°C , and the snow surface temperature was -8.4°C . The snow temperature profile ranged from -7.9°C near the air-snow interface to -5.8°C near the snow-ice interface with a minimum temperature of -8.1°C at $z_s = 29\text{cm}$ (Figure 3.3: left). The temperature gradient was inversely related to density through much of the snow pack due to the increasing fractional volume of air, decreasing heat transfer (e.g. *Sturm et al.*, 2002) (Figure 3.3: left).

Figure 3.3. Snow temperature and density (left), permittivity (ϵ') at 1GHz (middle) and dielectric loss (ϵ'') at 1GHz (right) profiles on the Churchill River estuary ($z_s = 44\text{cm}$).



Snow density decreased substantially around $z_s = 5\text{cm}$ which signified the presence of depth hoar near the base of the snow pack, but increased in the bottom most two centimeters of the snow pack (Figure 3.3: left). The density profile here was within the typical range, which can vary for dry snow from $100\text{kg}\cdot\text{m}^{-3}$ (newly fallen snow) to $500\text{kg}\cdot\text{m}^{-3}$ (refrozen snow) (e.g. *Hallikainen and Winebrenner, 1992, Langlois et al., 2007*). Snow over ice in the Churchill River estuary was not detectably saline at any depth.

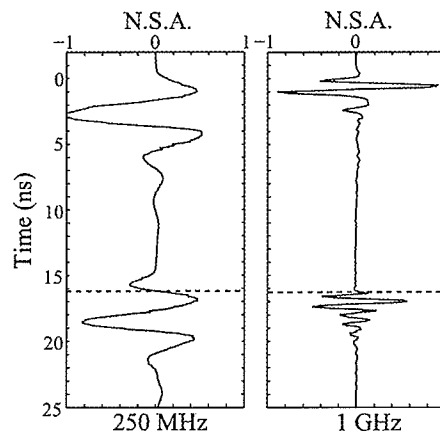
The 1GHz snow permittivity (ϵ') profile followed the snow density profile as expected (Figure 3: middle) in the absence of salinity and varied between 1.43 in the low density snow layer around $z_s = 5\text{cm}$ to 1.81 where the snow was most dense. Nearest the snow-ice interface the real permittivity was 1.66. The mean permittivity in this profile was 1.68, yielding a theoretical 1GHz radar velocity of 0.231m/ns . The snow volume had extremely small dielectric loss (ϵ'') at all depths (Figure 3.3: right) due to lack of brine (mean loss was 0.0009). Loss was 0.0061 at 0.05m where the only detectable wetness in the snow pack (0.006%) occurred.

Churchill River estuary GPR returns

Two events are clear in the trace plots at both frequencies in reflection data over bare ice (no snow) in the Churchill River estuary; the top event at each frequency is the direct wavelet and a reflection occurred due to the dielectric interface between the river ice ($\epsilon'_{\text{avg}} = 3.17$) and the water below ($\epsilon' \approx 80$) at a two-way travel time of 16.3ns at 250MHz and 1GHz (Figure 3.4) ($z_i = 1.38\text{m}$). This two-way travel time yielded an observed radar velocity of 0.171m/ns at 250MHz and

0.170m/ns at 1GHz, slightly faster than the permittivity-derived velocity of 0.169m/ns (Table 3.1). Over bare ice at both frequencies, the ice-water interface reflection event is opposite in polarity from the direct wavelet (Figure 3.4). These reflection data also indicate the basic shape of the direct wavelet which becomes important when distinguishing it from reflections caused a potential snow-ice dielectric interface.

Figure 3.4. Trace plot returns over bare ice at 250MHz and 1GHz on 6 March 2006 in the Churchill River estuary ($z_i = 1.38m$).



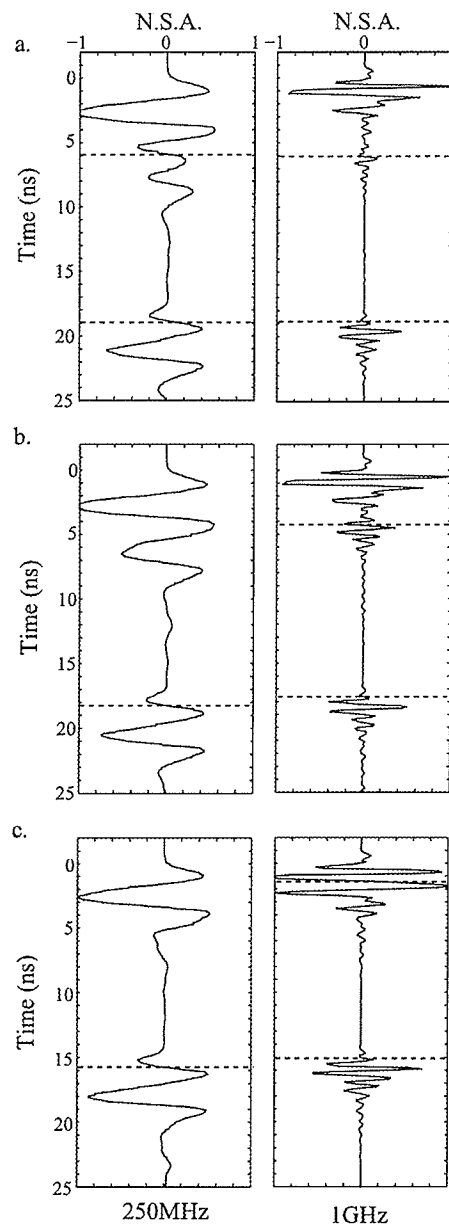
Accurate resolution of snow thickness requires that the direct wavelet be separable in time from the reflection caused by the snow-ice interface ($\epsilon'_{avg} = 1.68$ for snow and 3.17 for ice), but due to the relative snow thin-ness and frequency-dependent range resolution this is not always possible. Snow thicknesses of 0.65m, 0.44m and 0.15m were investigated using 250MHz and 1GHz GPR systems. Over 0.65m snow on 1.12m ice, a reflection event is clear at 250MHz at 6.0ns due to the snow-ice dielectric interface (Figure 3.5a: left) corresponding to a 250MHz radar

velocity of 0.23m/ns in snow, almost equal the 0.231m/ns predicted by dielectric information which in combination with a 6.0ns two-way travel time would have yielded 0.69m snow (a 0.04m or 6.1% difference). A clear reflection at 250MHz also occurred at 19.0ns due to the ice-water interface (Figure 3.5a: left). A two-way travel time of 13ns and an ice thickness of 1.12m equal an observed 250MHz radar velocity of 0.175m/ns. Using the 250MHz radar velocity determined in the previous section over bare ice (0.171m/ns) and a 13ns two-way travel time, the predicted ice thickness was 1.11m, 0.01m (0.9%) less than the physically measured ice thickness. However, the 250MHz system is of limited utility over typical snow depths on ice due to their relative thinness. At 1GHz the snow-ice reflection occurred at 6.1ns (Figure 3.5a: right) yielding an observed 1GHz radar velocity of 0.22m/ns in snow, compared to 0.231m/ns from permittivity, which overestimated the snow thickness by 0.05m (7.7%) (Table 3.1). A two-way travel time of 12.8ns and an ice thickness of 1.12m give an observed 1GHz radar velocity of 0.175m/ns and a GPR-derived apparent permittivity of 2.94 (Table 3.1). Using the permittivity-derived 1GHz radar velocity (0.169m/ns) and a 12.8ns two-way travel time, the ice thickness derived from dielectric radar velocity was 1.08m, 0.04m (3.6%) less than the measured ice thickness (Table 3.1). This underestimation of ice thickness may be attributed to a substantial decrease in ice density due to the skeletal structure that may occur in the bottom five-to-ten centimeters of ice (e.g. *Ehn et al., 2008*). It may also be reasonable to assume that the ice measured by the GPR system was not exactly the same thickness as the point where ice thickness was physically

measured as we have showed two cores may be up to 6cm different at nominally the same location.

Reflection measurements over 0.44m snow atop 1.17m ice in the Churchill River estuary indicate that the direct wavelet and snow-ice interface reflection event cannot be separately resolved at 250MHz, as only one of the two peaks of the snow-ice reflection event are present below the direct wavelet (Figure 3.5b: left). The direct wavelet and snow-ice reflection event overlap creating three positive amplitude nodes at the top of the trace plot, where the second hump of the direct wavelet is enlarged in time due to the superimposition of the first positive node of the reflection event (Figure 3.5b: top) enabling the inference that there is snow between the antennas and the top of the ice. Following the direct wavelet and superimposed snow-ice interface reflection between 0 and 9ns at 250MHz (Figure 3.5b: left), a distinct reflection event at 18.3ns at the ice-water dielectric interface occurred (Figure 3.5b: left), but the ice thickness cannot be determined because accurate snow thickness cannot be resolved at 250MHz.

Figure 3.5. Trace plot returns on 6 March 2006 over snow-covered river ice in the Churchill river estuary at 250 MHz (left column) and 1GHz (right column) where (a) $z_s = 0.65\text{m}$ and $z_i = 1.12\text{m}$, (b) $z_s = 0.44\text{m}$ and $z_i = 1.12\text{m}$ and (c) $z_s = 0.15\text{m}$ and $z_i = 1.20\text{m}$.



At 1GHz both snow and ice thicknesses were determined at this location (Figure 3.5b: right). Within the 1GHz trace plot two distinct reflection events are visible

below the direct wavelet (Figure 3.5b: right). At 4.3ns the snow-ice interface resulted in an observed 1GHz radar velocity of 0.21m/ns in snow, slower than the dielectric radar velocity in snow at 1GHz (0.231m/ns) (Table 3.1). The second (ice-water) reflection at 17.7ns yielded a 13.4ns two-way travel time between the snow-ice and ice-water interface and an observed radar velocity in ice of 0.175m/ns (Table 3.1). Using the previously calculated 1GHz radar velocity in ice (0.170m/ns) and the time difference between the two reflection events (13.4ns) the predicted ice thickness at this location was 1.14m, 0.03m (2.6%) less than measured physically (Table 3.1).

Two different frequencies are used to solve the problem of increasing penetration depth versus decreasing range resolution that may inhibit studies employing a single frequency. As snow thickness decreases, range resolution at each frequency becomes more important, as does the shape of the direct wavelet. Over 0.15m snow atop 1.20m ice, it is obvious both from theoretical calculations of range resolution and from the trace plot (Figure 3.5c: left) that the 250MHz system cannot separate the snow-ice interface return from the direct wavelet, but readily detects the ice-water dielectric interface at 15.8ns (Figure 3.5c: left and Table 3.1). Using $V_i = 0.171\text{m/ns}$ (from the bare ice case) the 250MHz system predicted a slab thickness of 1.35m, exactly the snow-plus-ice thickness measure, but it is important thermodynamically to accurately separate snow thickness from ice thickness. The 1GHz trace plot shows a large positive amplitude peak at 1.4ns after the direct wavelet (Figure 3.5c: right) at the snow-ice interface resulting in a radar velocity in snow of 0.24m/ns and an apparent snow permittivity of 1.6 (Table 3.1). The snow-

ice reflection is realized almost immediately after the direct wavelet meaning 1.4ns is nearing the minimum two-way travel time distinguishable from the direct wavelet. The 1GHz return also elucidates the ice-water interface at 15.2ns (Figure 3.5c: right) resulting in a two-way travel time of 13.8ns through 1.20m ice, corresponding to an observed 1GHz radar velocity in ice of 0.174m/ns and an apparent ice permittivity of 2.97 (Table 3.1). At 1GHz the radar velocity in ice derived from dielectric data (0.169m/ns) over a two-way travel time of 13.8ns would have yielded 1.16m ice, 0.04m (3.3%) less than measured physically (Table 3.1).

Table 3.1. Summary snow and ice thickness and observed radar velocities calculated from GPR returns compared against those calculated using dielectric information for the Churchill River estuary (fresh ice).

6 March - River Ice

f (MHz)	Z_i obs (m)	twf (ns)	V_i GPR (m/ns)	ϵ' GPR	ϵ' dielectric	V_i dielectric (m/ns)	Z_i dielectric (m)	$(Z_i \text{ obs}) - (Z_i \text{ dielectric})$ (%)
1000	1.38	16.3	0.170	3.11			1.38	0
1000	1.12	12.8	0.175	2.94			1.08	3.6
1000	1.17	13.4	0.175	2.94	3.17	0.169	1.13	3.4
1000	1.20	13.8	0.174	2.97			1.16	3.3
250	1.38	16.3	0.171	3.08	3.17	0.169	1.36	1.4

6 March - River Snow

f (MHz)	Z_s obs (m)	twf (ns)	V_s GPR (m/ns)	ϵ' GPR	ϵ' dielectric	V_s dielectric (m/ns)	Z_s dielectric (m)	$(Z_s \text{ obs}) - (Z_s \text{ dielectric})$ (%)
1000	0.65	6.1	0.22	2.0			0.70	7.7
1000	0.44	4.3	0.21	2.1	1.68	0.231	0.49	11
1000	0.15	1.4	0.24	1.6			0.14	6.7

Results from snow depths in the estuary ranging from 0.15m to 0.65m indicate that the average observed 1GHz radar velocity in snow was 0.22m/ns, 4.3% slower than 0.231m/ns predicted using dielectric information. Both 250MHz and

1GHz radar returns clearly determine the two-way travel time to the sea ice-seawater interface, and when combined with 1GHz returns from the snow-ice interface determine separate snow and ice thickness values at the same location on snow-covered river ice.

GPR return data at ice core locations in the Churchill River estuary revealed that ϵ' derived from two-way travel time and actual ice thickness measurements were slightly lower than the average ϵ' derived from ice core samples. This leads to slightly faster GPR derived radar velocities in fresh ice than radar velocities calculated from dielectric information, which tended to slightly under-estimate the ice thickness (Table 3.1). On the contrary, dielectrically-derived radar velocity in snow was slightly faster than those calculated from two-way travel time and actual snow thickness. In snow, ϵ' and radar velocity derived from dielectrics over-estimate snow thickness (Table 3.1). Although there occurred a low-density layer of snow near the snow-ice interface, it appears that this layer does not lower the real permittivity of the snow enough to produce a GPR reflection so close to the snow-ice dielectric interface, which produces large amplitude reflections in the GPR data.

Button Bay ice and snow - physical and dielectric properties on 4 March 2006

Snow physical properties were sampled over sea ice in Button Bay on 4 March near the location marked (white square) on Figure 3.1. The 2m air temperature was -12.5°C and the snow surface temperature was -12.2°C over 0.12m snow. The snow temperature profile decreased near-linearly from -10.8°C near the snow surface to -9.4°C at the snow-ice interface (Figure 3.6a). The snow salinity

was mostly near zero, but increased to 12.9 psu nearest the snow-sea ice interface (Figure 3.6a). The snow density was greatest at the snow surface but decreased by almost half around $z_s = 3\text{cm}$, before increasing again nearest the snow-ice interface (Figure 3.6a) indicating the presence of a hoar layer near the snow-sea ice interface.

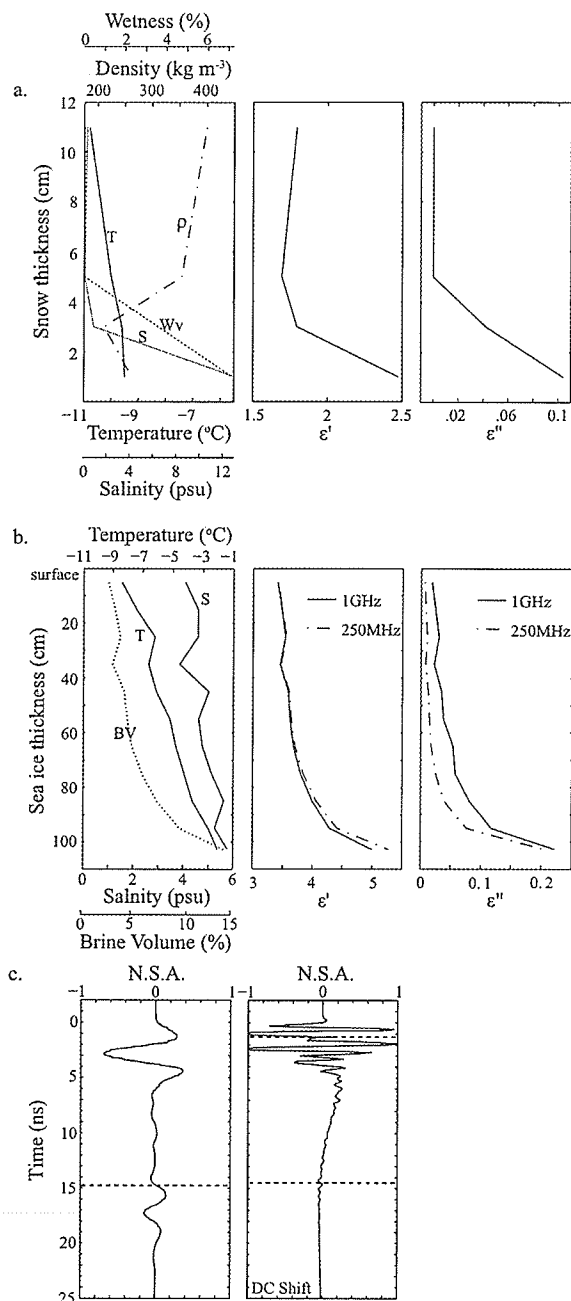
The snow permittivity at 1GHz was density-driven in the top half of the snow pack and driven by salinity and wetness in the bottom half (Figure 3.6a). The permittivity was 1.79 near the snow surface, and decreased to 1.69 due to decreased density in a lower density layer around $z_s = 5\text{cm}$ where no salinity or wetness occurred, before increasing sharply to 2.47 around $z_s = 1\text{cm}$ due to increased salinity and wetness in the snow and in spite of decreased density (Figure 3.6a). The mean snow permittivity was 1.94, which corresponded to a 1GHz dielectric radar velocity of 0.217m/ns (Table 3.2). The loss at 1GHz increased nearest the bottom half of the snow due to the presence of salinity and wetness (Figure 3.6a); the mean loss at 1GHz was 0.037.

The sea ice salinity ($z_i = 1.055\text{m}$) profile in Button Bay increased slightly with depth, while the location of the salinity minimum (3.85psu) indicated that this sea ice may have formed initially by rafting of thin floes (Figure 3.6b). Temperature in the sea ice ($z_i = 1.05\text{m}$) increased with depth from -8.39°C near the snow-sea ice interface to -2°C near the sea ice bottom (Figure 3.6b). The sea ice brine volume profile generally followed the salinity profile, ranging from about 2% near the top of the sea ice to almost 15% at the sea ice-seawater interface (Figure 3.6b: left).

Sea ice permittivity profiles at 250MHz and 1GHz were similar, varying between 3.41 and 5.28 (Figure 3.6b). The permittivity at both frequencies varied

around 3.5-4 through much of the volume with small fluctuations in brine volume, but increased substantially in bottom fifteen centimeters coincident with a similar increase in brine volume (Figure 3.6b). The mean permittivity was 3.8 (1GHz) and 3.86 (250MHz) corresponding to dielectric radar velocities of 0.155m/ns (1GHz) and 0.154m/ns (250MHz) (Table 3.2). The loss was slightly lower at 250MHz than at 1GHz (Figure 3.6b), and was especially high in the bottom fifteen centimeters of the sea ice due to increased temperature and salinity (Figure 3.6b). The mean dielectric loss was 0.063 at 1GHz and 0.038 at 250MHz.

Figure 3.6. (a) Snow temperature, salinity, density, and water-by-volume (Wv) (left), permittivity (ϵ') at 1GHz (middle) and dielectric loss (ϵ'') at 1GHz (right) profiles on 4 March 2006 in Button Bay ($z_s = 0.12m$), (b) Salinity, temperature and brine volume profiles of sea ice (left) and calculated permittivity (ϵ') profiles (middle) and dielectric loss (ϵ'') profiles (right) within Button Bay 4 March 2006 ($z_i = 1.05m$), (c) Trace plots over snow-covered ice at 250 MHz (left) and 1 GHz (right) on 04 March 2006 in Button Bay, $z_s = 0.12m$ and $z_i = 1.05m$.



Button Bay GPR returns - 4 March 2006

GPR reflection returns were recorded over snow-covered sea ice in Button Bay near the physical sampling site over 0.12m snow and 1.07m sea ice, where salinity and/or wetness in the sea ice and snow in Button Bay (Figure 3.6a, b) in comparison to the estuary was readily apparent (Figure 3.6). The average loss in sea ice was larger than in river ice, so the snow and sea ice in Button Bay attenuated frequencies much more than snow and ice on the Churchill River. 250MHz reflection results clearly show the sea ice-seawater interface at 14.8ns, but attenuation of the wavelet within sea ice is demonstrated by the relatively low amplitude of that reflection event (Figure 3.6c: left). Using the dielectrically-derived radar velocity in sea ice and a two-way travel time of 14.8ns at 250MHz, the slab thickness predicted was 1.12m, 0.07m (5.9%) less than the observed snow-plus-sea ice thickness (1.19m) (Table 3.2).

After applying a DC shift to the 1GHz return, the direct wavelet and a reflection event at the snow-sea ice interface ($z_s = 0.12\text{m}$) was returned at 1.3ns (Figure 3.6c: right), yielding an operational radar velocity in snow of 0.22m/ns at 1GHz, slightly faster than predicted by the permittivity (Table 3.2). Separation between the direct wavelet and snow-sea ice reflection was near the operational limit for minimum snow thickness in this case. A second reflection event at the sea ice-seawater interface occurred at 14.4ns (Figure 3.6c: right) giving a two-way travel time in the sea ice of 13.1ns and yielding an operational radar velocity in sea ice of 0.164m/ns and an apparent permittivity of 3.35 (Table 3.2). If the dielectric radar velocity at 1GHz is used to calculate an apparent sea ice thickness ($z_{i_dielectric}$)

for a two-way travel time of 13.1ns, $z_{i_dielectric} = 1.01\text{m}$ (Table 3.2). The sea ice thickness difference between the observed thickness (1.07m) and the apparent thickness (1.01m) is 5.6%, likely due to the reflection event occurring slightly above the physical bottom of the ice as a result of incorporated brine and seawater which may have penetrated the skeletal layer at the sea ice bottom elevating the permittivity above the sea ice-seawater interface.

Table 3.2. Summary snow and ice thickness and observed radar velocities calculated from GPR returns compared against those calculated using dielectric information over snow-covered sea ice in Button Bay on 4 March 2006.

4 March - Sea Ice

f (MHz)	$Z_{i\ obs}$ (m)	twf (ns)	$V_{si\ GPR}$ (m/ns)	$\epsilon'_{\ GPR}$	$\epsilon'_{\ dielectric}$	$V_{i\ dielectric}$ (m/ns)	$Z_{i\ dielectric}$ (m)	$(Z_{i\ obs}) - (Z_{i\ dielectric})$ (%)
1000	1.07	13.1	0.164	3.35	3.8	0.155	1.01	5.6

4 March - Snow

f (MHz)	$Z_{s\ obs}$ (m)	twf (ns)	$V_{s\ GPR}$ (m/ns)	$\epsilon'_{\ GPR}$	$\epsilon'_{\ dielectric}$	$V_{s\ dielectric}$ (m/ns)	$Z_{s\ dielectric}$ (m)	$(Z_{s\ obs}) - (Z_{s\ dielectric})$ (%)
1000	0.12	1.3	0.22	1.9	1.94	0.217	0.12	0

4 March - Snow-plus-sea ice

f (MHz)	$Z_{s\ obs}$ (m)	twf (ns)	$V_{slab\ GPR}$ (m/ns)	$\epsilon'_{\ GPR}$	$\epsilon'_{\ dielectric}$	$V_{i\ dielectric}$ (m/ns)	$Z_{i\ dielectric}$ (m)	$(Z_{slab\ obs}) - (Z_{slab\ dielectric})$ (%)
250	1.19	14.8	0.163	3.39	3.86	0.154	1.12	5.9

In the past, GPR reflection surveys of snow and ice have typically been conducted using a single frequency and without *in situ* physical sampling (i.e. *Arcone and Delaney, 1987; Arcone, 1991; Kovacs and Morey, 1992*), so post-processing the data to elucidate weak reflection events while quantifiably determining their origin could not always be reproduced methodologically over snow and ice surfaces with different physical and dielectric properties. In this case, multiple frequency GPR

returns and *in situ* physical sampling eliminate subjective methodology and return separate snow and ice thickness measurements at the same time and place.

Button Bay ice and snow - physical and dielectric properties on 7 March 2006

Physical samples were taken on 7 March in 0.12m snow in Button Bay. The 2m air temperature was -5.9°C and the snow surface temperature was -5.7°C . Compared to 4 March, the snow temperature decreased slightly throughout the volume (Figure 3.7a: left). The salinity and wetness of the snow were near-zero through much of the volume, but increased around $z_s = 1\text{cm}$ (Figure 3.7a: left). The snow was most dense near the surface and decreased with depth to minimum density near the snow-sea ice interface (Figure 3.7a: left).

The snow real permittivity on 7 March at 1GHz was driven by density in much of the profile due to low salinity and low wetness, while a density-driven decrease in permittivity was inhibited in the bottom two centimeters of snow by increases in salinity and wetness despite decreased density (Figure 3.7a: left, middle). The permittivity was highest near the snow surface owing to high density and decreased slightly toward the snow-sea ice interface despite snow wetness of 1.09% and 2.8psu salinity (Figure 3.7a: left). The average permittivity of snow at 1GHz was 1.67 corresponding to a radar velocity of 0.233m/ns and an apparent permittivity of 1.89 (Table 3.3). The dielectric loss at 1GHz was very low throughout the snow and averaged 0.003 (Figure 3.7a: right). The snow contained much less salinity and water-by-volume than on 4 March which resulted in lower dielectric loss on 7 March, despite a warmer, near-isothermal temperature profile.

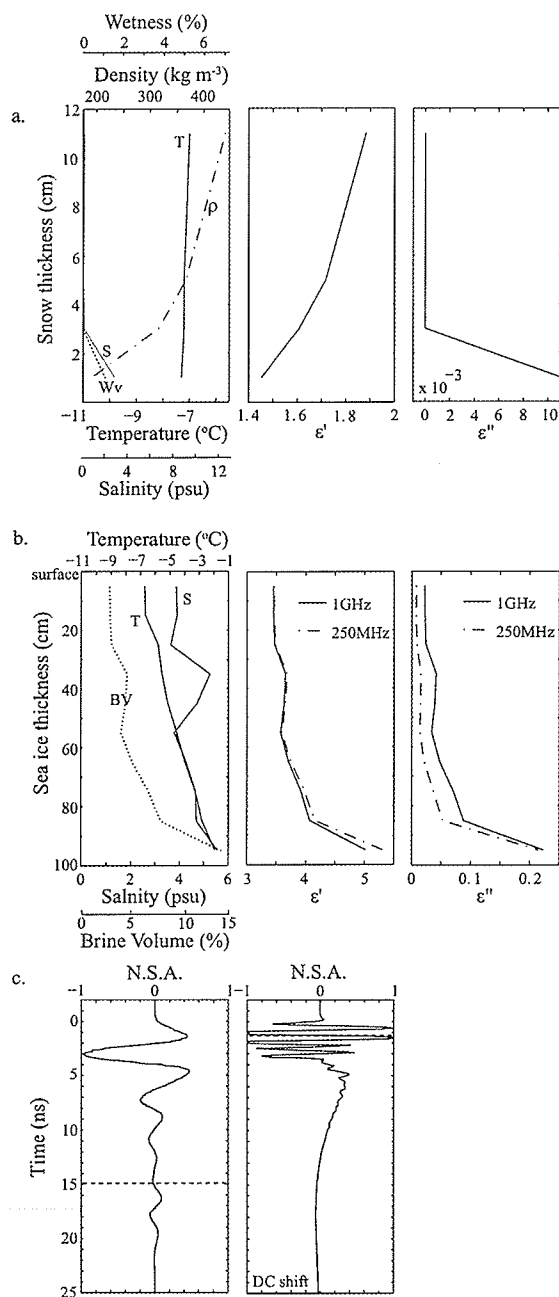
On fresh ice in the Churchill River estuary (Figure 3.3: left) and on sea ice in Button Bay on both March 4th (figure 3.6a: left) and 7th (Figure 3.7a: left), there occurred a low-density layer of snow near the snow-ice interface, which was most likely depth hoar. In each case this low-density layer coincided with changes in the ϵ' profile (Figures 3.3: middle, 3.6a: middle and 3.7a: middle) but the magnitude and sign of the change in the ϵ' profile differs in each case. In the Churchill River estuary on March 6th, a pronounced decrease in density lead to an intimately related decrease in ϵ' from slightly above 1.7 to about 1.4, however the magnitude of this change is much less than the change in ϵ' from the snow pack average of 1.68 (1GHz) to the ice below where $\epsilon' = 3.17$ at 1GHz (Table 3.1). The magnitude of the interfacial dielectric difference determines the amplitude of the reflection; therefore the snow-ice dielectric interface should dominate the return. In the two snow cases over sea ice on March 4th and 7th, the snow density decreased in a layer near the snow-sea ice interface, but contrary to the river (fresh) ice case, ϵ' in these two locations increased substantially in the bottom 4cm of the snow pack due to the influence of increased salinity and wetness (Figures 3.6a: left and 3.7a: left). So, despite the fact that a lower density depth hoar layer occurred over sea ice in the snow sampled, it was not the predominant driver changing ϵ' in those lower layers. This highlights again the need for physical snow and ice samples when GPR is used to measure snow and (sea) ice thickness due to the number of variables which may differentially dominate ϵ' .

Sea ice sampled on 7 March in Button Bay was 1.01m thick. Sea ice salinity was 3.87psu nearest the snow-sea ice interface, but in contrast to measurements

made on 4 March in the same area, a layer of increased salinity around 0.35m (Figure 3.7b: left) which again probably resulted from rafting of thin floes during early stages of ice formation. The sea ice temperature on 7 March increased with thickness (Figure 3.7b: left) and the shape of the temperature profile on 7 March was similar to 4 March, but the sea ice had warmed by about 2°C throughout much of the thickness in response to increased air temperatures. The sea ice brine volume profile (Figure 3.7b: left) roughly followed the shape of the salinity profile and ranged between about 2.5% in the top of the profile to near 14% near the sea ice-seawater interface.

The sea ice permittivity at 1GHz and 250MHz were similar, ranging between 3.45 and 4.05 for much of the sea ice thickness, then increasing sharply in the bottom ten centimeters to 5.02 (1GHz) and 5.31 (250MHz) due to increased salinity and temperature (Figure 3.7b: middle) in a shape similar to that of 4 March. Mean permittivity was 3.8 at 1GHz and 3.85 at 250MHz, yielding radar velocities of 0.155m/ns and 0.154m/ns respectively. It appears that the shape of the permittivity (Figure 3.7b: middle) and loss (Figure 3.7b: right) profiles closely follow the shape of the brine volume profile (Figure 3.7b: left) as they did on 4 March. The loss at both frequencies was similar, but greater at 1GHz through the volume (Figure 3.7b: right). Mean dielectric loss was 0.061 at 1GHz and 0.039 at 250MHz. Mean permittivity and loss in the sea ice on 7 March remained almost the same as on 4 March at both frequencies.

Figure 3.7. (a) Snow temperature, salinity and density (left), permittivity (ϵ') at 1GHz (middle) and dielectric loss (ϵ'') at 1GHz (right) profiles on 7 March 2006 in Button Bay ($z_s = 0.12\text{m}$), (b) Salinity, temperature and brine volume profiles of sea ice (left) and calculated permittivity (ϵ') profiles (middle) and dielectric loss (ϵ'') profiles (right) within Button Bay 7 March 2006, $z_i = 1.01\text{m}$, (c) Trace plots over snow-covered ice at 250MHz (left) and 1GHz (right) on 7 March 2006 in Button Bay $z_s = 0.12\text{m}$ and $z_i = 1.01\text{m}$.



Button Bay GPR returns - 7 March 2006

Sea ice reflection surveys were conducted in Button Bay on 7 March coincident to ice coring. The 250MHz GPR yielded a reflection at the sea ice-seawater interface at 14.9ns (Figure 3.7c: left) yielding an observed radar velocity of 0.154m/ns through a 1.13m slab of snow (0.12m) and sea ice (1.01m), the same as using a radar velocity of 0.154m/ns in sea ice calculated from permittivity (Table 3.3).

After applying a DC shift to the 1GHz radar return data over the snow and sea ice, a reflection event at the snow-sea ice interface occurred at 1.3ns (Figure 3.7c: right) corresponding to a 1GHz radar velocity in snow of 0.22m/ns through 0.12m snow. In this instance however, the sea-ice seawater interface could not be discerned using the 1GHz return data. The 250MHz radar velocity derived from permittivity yielded a snow-plus-sea ice slab thickness of 1.13m, and the 1GHz radar velocity calculated using dielectric information yielded a snow thickness of 0.13m and therefore the sea ice thickness calculated using dielectric radar velocities on 7 March was 1.00m, 0.01m or 0.9% less than physically measured (Table 3.3).

Table 3.3. Summary snow and ice thickness and observed radar velocities calculated from GPR returns compared against those calculated using dielectric information over snow-covered sea ice in Button Bay on 7 March 2006.

7 March - Snow

f (MHz)	Z_s obs (m)	twt (ns)	V_s GPR (m/ns)	ϵ' GPR	ϵ' dielectric	V_i dielectric (m/ns)	Z_i dielectric (m)	$(Z_s \text{ obs}) - (Z_s \text{ dielectric})$ (%)
1000	0.12	1.3	0.22	1.9	1.67	0.233	0.13	8.3

7 March - Snow-plus-sea ice

f (MHz)	$Z_{\text{slab obs}}$ (m)	twt (ns)	$V_{\text{slab GPR}}$ (m/ns)	ϵ' GPR	ϵ' dielectric	V_i dielectric (m/ns)	Z_i dielectric (m)	$(Z_{\text{slab obs}}) - (Z_{\text{slab dielectric}})$ (%)
250	1.13	14.9	0.154	3.79	3.85	0.154	1.13	0

Conclusion

The dielectric permittivity of river ice was driven by the ice temperature and salinity profiles and was similar at 250MHz and 1GHz and dielectric loss was very low in river ice at both frequencies. Both the 250MHz and 1GHz GPR systems easily resolved the ice-water interface under freshwater ice in the Churchill River estuary within 3.6% of the measured ice thickness, with the 1GHz system being the more accurate center frequency (Table 3.1). In snow over fresh ice, the 1GHz system resolved snow thicknesses of 15cm, 44cm and 65cm (Table 3.1).

Over snow-covered sea ice, separate snow and sea ice thickness measurements were made using the combination of 250MHz and 1GHz GPR systems yielding snow thickness results less than 8.3% different than those observed and sea ice thickness that were very nearly identical to those physically measured (Tables 3.2, 3.3). The minimum snow thickness detected at 1GHz was 12cm which is very near the operational minimum thickness at that frequency (~8cm). In some sea ice locations the 1GHz system can detect both the snow-sea ice interface and the sea ice-seawater interface, however using the 1GHz system to elucidate snow thickness while using a 250MHz GPR system to resolve snow-plus-sea ice thickness reliably yielded separate snow and ice thicknesses at the same location.

The GPR system employed here proved operationally robust for snow, river ice and first year sea ice thickness measurements at a time of the year where thicknesses are typically at or near maximum and prior to the spring melt season. One must only make 'calibration' return measurements over known snow and/or ice thicknesses to determine the velocity of the incident wavelet at each frequency

before proceeding with profiling. A variety of snow thicknesses were measured using a bi-static GPR operating at 1GHz, although snow thicknesses less than 12cm may not be resolved due to range resolution at that frequency. Profiles of snow thickness over ice that has not been dynamically roughened produced an abundance of spatial snow thickness measurements especially when the antennas are pulled beside a snow-machine.

River ice thickness greater than 1m can be easily measured even below very thick snow using a GPR system operating at 1GHz due to the very low attenuation of the incident signal within the media and did not require the use of a second, lower frequency system. Snow and river ice thicknesses were made using unprocessed return data from both the 1GHz and 250MHz GPR systems.

Snow thickness on sea ice was measurable at 1GHz, although range resolution at that frequency limited operationally snow thickness measurements to greater than about 12cm. Due to the range resolution of the 250MHz system, it cannot accurately resolve typical (10-30cm) snow thickness on sea ice, but regardless of snow thickness the 250MHz system easily resolves the snow-plus-sea ice thickness. When the snow thickness measurement made using the 1GHz system are subtracted from the slab thickness measured using the 250MHz at the same location to yield sea ice thickness, the results match physical measurements quite well.

Literature Cited

- Annan, A.P. and S.W. Cosway, 1992. Ground penetrating radar survey design, in *Proceedings of the symposium on the application of geophysics to engineering and environmental problems*, 2: 329–351.
- Arcone, S.A. and A.J. Delaney, 1987. Airborne river-ice thickness profiling with helicopter-borne UHF short-pulse radar. *J. Glaciol.*, 33(115): 1-11.
- Arcone, S.A., 1991. Dielectric constant and layer-thickness interpretation of helicopter-borne short-pulse radar waveforms reflected from wet and dry river-ice sheets. *IEEE Trans. Geosci. Rem. Sens.*, 29(5): 768-777.
- Barber, D.G, S.P. Reddan, and E.F. LeDrew, 1995. Statistical Characterization of the Geophysical and Electrical Properties of Snow on Landfast First-Year Sea Ice. *J. Geophys. Res.*, 100(C2): 2673-2686.
- Barber, D.G., A.K. Fung, T.C. Grenfell, S.V. Nghiem, R.G. Onstott, V. Lytle, D.K. Perovich, and A.J. Gow, 1998. The Role of Snow on Microwave Emission and Scattering over First-Year Sea Ice. *IEEE Trans. Geosci. Rem. Sens.*, 36(5): 1750-1763.
- Cox, G.F.N. and W.F. Weeks, 1983. Equations for determining the gas and brine volumes in sea-ice samples. *J. Glaciol.* 29(102): 306-316.
- Deng, S. and B. Sun, 2004. Ice-surface based radar detection revealed the basic internal structure characteristics of Amery Ice Shelf, East Antarctica. *Tenth international conference on Ground Penetrating Radar*, 21-24 June, Delft, Netherlands.
- Denoth, A., 1989. Snow dielectric measurements. *Advances in Space Research*, 9, 233-243.
- Drinkwater, M. R., and G.B. Crocker, 1988. Modeling changes in the dielectric and scattering properties of young snow-covered sea ice at GHz frequencies. *J. Glaciol.*, 34, 274–282.
- Dumas, J.A., H. Melling, G.M. Flato, 2007. Late-summer pack ice in the Canadian archipelago: Thickness observations from a ship in transit. *Atmos-Ocean*, 45(1):57-70.
- Ehn, J., C.J. Mundy, and D.G. Barber, 2008. Bio-optical and structural properties inferred from irradiance measurements within the bottommost layers in an Arctic landfast sea ice cover. *Journal of Geophysical Research*, 113, C03S03, doi:10.1029/2007JC004194.
- Frankenstein, G. and R. Garner, 1967. Equations for determining the brine volume of sea ice from -0.5°C to -22.9°C. *J. Glaciol.*, 6: 943-944.

Fofonoff, P., and R.C. Millard Jr., 1983. Algorithms for computation of fundamental properties of seawater. *UNESCO Tech. Pap. Mar. Sci.*, 44: 53pp.

Haas, C., S. Gerland, H. Eicken, and H. Miller, 1997. Comparison of sea-ice thickness measurements under summer and winter conditions in the Arctic using a small electromagnetic induction device. *Geophys.*, 62(3): 749-757.

Haas, C., 2004. Late-summer sea ice thickness variability in the Arctic Transpolar Drift 1991-2001 derived from ground-based electromagnetic sounding. *Geophys. Res. Lett.*, doi:10.1029/2003GL019394.

Hallikainen, M. and D.P. Winebrenner, 1992. Chapter 3: The Physical Basis for Sea Ice Remote Sensing. In: F. D. Carsey, (Editor), *Microwave Remote Sensing of Sea Ice*, Vol. 68. American Geophysical Union. p. 30.

Harper, J.T. and J.H. Bradford, 2003. Snow stratigraphy over a uniform depositional surface: spatial variability and measurement tools. *Cold Reg. Sci. Tech.*, 37: 289-298.

Kohler, J., J. Moore, M. Kennett, R. Engeset, and H. Elvehoy, 1997. Using ground-penetrating radar to image previous years' summer surfaces for mass-balance measurements. *Ann. Glaciol.*, 24: 355-360.

Kovacs, A. and J.S. Holladay, 1990. Sea-ice thickness measurements using a small airborne electromagnetic sounding system. *Geophys.*, 55: 1327-1337.

Kovacs, A. and R.M. Morey, 1992. Estimating sea ice thickness from impulse radar sounding time of flight data. Geological Survey of Canada Paper 90-4: 117-124.

Kuzyk, Z.A., R.W. MacDonald, M.A. Granskog, R.K. Scharien, R.J. Galley, C. Michel, D. Barber and G. Stern, 2007. Sea ice, hydrological and biological processes in the Churchill River estuary region, Hudson Bay. *Estuar. Coast. Shelf Sci.*, doi: 10.1016/j.ecss.2007.09.030.

Lange, M. A., and H. Eicken, 1991. The sea ice thickness distribution in the northwestern Weddell Sea. *J. Geophys. Res.*, 96(C3): 4821-4837.

Langlois, A., C.J. Mundy, and D.G. Barber, 2007. On the winter evolution of snow thermophysical properties over landfast first year sea ice. *Hydrol. Process.*, 21: 705-716.

Langlois, A. and D.G. Barber, 2007. Passive Microwave Remote Sensing of Seasonal Snow Covered Sea Ice. *Prog. Phys. Geog.*, 31(6), 539-573, doi: 10.1177/0309133307087082.

Mätzler, C. 1987. Applications of the interaction of microwaves with natural snow cover. *Remote Sensing Reviews*, 2, 259-387.

Melling, H., D.A. Riedel, and Z. Gedalof, 2005. Trends in draft and extent of seasonal pack ice, Canadian Beaufort Sea. *Geophys. Res. Lett.*, doi:10.1029/2005GL024483.

Palli, A., J.C. Kohler, E. Isaksson, J.C. Moore, J.F. Pinglot, V.A. Pohjola and H. Samuelsson, 2002. Spatial and temporal variability of snow accumulation using ground-penetrating radar and ice cores on a Svalbard glacier. *J. Glaciol.*, 48(162): 417-424.

Perovich, D.K., T.C. Grenfell, J.A. Richter-Menge, B. Light, W.B. Tucker III, and H. Eicken, 2003. Thin and thinner: Sea ice mass balance measurements during SHEBA. *J. Geophys. Res.*, doi:10.1029/2001JC001079.

Pilon, J.A., M. Allard, M.K. Seguin, 1992. Ground probing radar in the investigation of permafrost and subsurface characteristics of surficial deposits in Kangiqsualujjuaq, northern Quebec. Geological Survey of Canada Paper 90-4: 165-175.

Prinsenbergh, S.J. and J.S. Holladay, 1993. Using air-borne electromagnetic ice thickness sensor to validate remotely sensed marginal ice zone properties. In: HSVA(Editor), Port and ocean engineering under arctic conditions (POAC 93), 2: 936-948.

Sinisalo, A., A. Grinsted, J.C. Moore, E. Karkas and R. Pettersson, 2003. Snow-accumulation studies in Antarctic with ground-penetrating radar using 50, 100, 800 MHz antenna frequencies. *Ann. Glaciol.* 37: 194-198.

Stogryn, A. 1971. Equations for calculating the dielectric constant of saline water. *IEEE Transactions on Microwave Theory and Technology*, MTT-19, 733-736.

Stogryn, A. and G.J. Desargant, 1985. The dielectric properties of brine in sea ice at microwave frequencies, *IEEE Transactions on Antennas and Propagation*, AP-33: 523-532.

Sturm, M. and J. Holmgren, 2002. Winter snow cover on the sea ice of the Arctic Ocean at the Surface Heat Budget of the Arctic Ocean (SHEBA): Temporal evolution and spatial variability, *J. Geophys. Res.*, 107(C10), doi:10.1029/2000JC000400.

Tiuri, M., A. Sihvola, E. Nyfors, M.T. Hallikainen, 1984. The complex dielectric constant of snow at microwave frequencies. *IEEE J. Oceanic Engineering*, OE-9, 277-382.

Travassos, J.M. and J.C. Simoes, 2004. High-resolution radar mapping of internal layers of a subpolar ice cap, King George Island, Antarctica. *Pesquisa Antractica Brasileira*, 4: 57-65.

Ulaby, F.T., R.K. Moore, and A.K. Fung, 1990. Microwave Remote Sensing Active and Passive: From Theory to Applications. Vol. 3, Norwood: Artech House.

Wadhams, P. 1987. Sea ice thickness distribution in the Greenland Sea and Eurasian Basin, May 1987. *J. Geophys. Res.* 97(C4):5331-5348.

Winther, J.-G., O. Bruland, K. Sand, A. Killintveit, and D. Marechal, 1998. Snow accumulation distribution in Spitsbergen, Svalbard, in 1997. *Polar Research*, 17(2): 155-164.

CHAPTER FOUR: ON THE LINK BETWEEN SAR-DERIVED SEA ICE MELT AND DEVELOPMENT OF THE SUMMER UPPER OCEAN MIXED LAYER IN THE NORTH OPEN WATER POLYNYA

Galley, R.J., D.G. Barber and J.J. Yackel, 2007. On the link between SAR-derived sea ice melt and the development of the summer ocean mixed layer in the North Open Water Polynya. *International Journal of Remote Sensing*, 28(18): 3979-3994.

1. Introduction and Background

Ocean-sea-ice-atmosphere interaction processes play a vital role in the assessment of climate variability and change on local to global scales. In particular, temporal and spatial variation in sea ice physical properties modulate energy exchange between the ocean and atmosphere, affecting the physical (*Perovich and Elder, 2002*) and biological nature of the Arctic marine ecosystem (*Smith et al., 1990*). Polynyas are defined (*World Meteorological Organization, 1970*) as areas of open water or partially ice covered ocean in polar regions where under the region's climatic conditions a complete ice cover is expected (*Smith et al., 1990*). Polynyas are of particular importance because they occur at latitudes postulated to be the earliest and most affected by climate variability and change, responding quickly to changes in atmospheric and oceanic forcing (*Barber et al., 2001; ACIA, 2004*). In turn, polynyas are physically important to polar ecosystems and affect a wide range of physical oceanographic properties due to their mechanisms of formation, persistence and dissolution. These areas of open water or significantly reduced ice concentration permit ocean-to-atmosphere energy exchange which can be orders of magnitude larger than over surrounding sea ice. Polynyas are almost completely

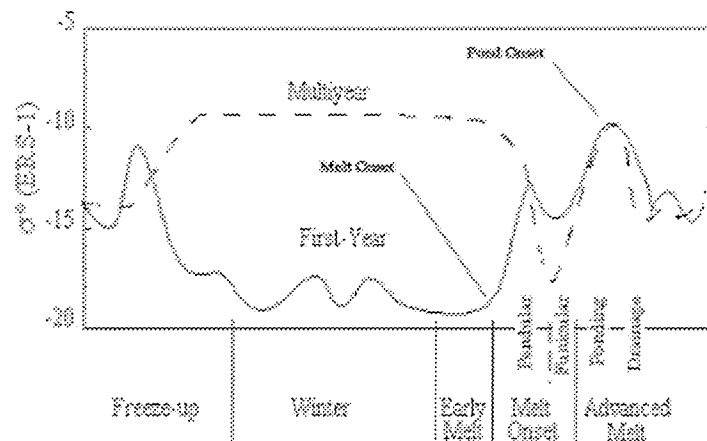
responsible for the regional heat budget, exerting influence on the ocean below and the atmosphere above (*Wadhams, 2000*).

The North Water Polynya occurs annually, spanning north Baffin Bay and south Smith Sound between Ellesmere Island and Greenland, from approximately 76°N to 80°N, where an ice bridge spanning Nares Strait forms in winter preventing sea ice in the Lincoln Sea and Kane Basin from being advected south into northern Baffin Bay (*Steffen, 1985; Barber et al., 2001*). Once the ice bridge forms, sea ice within the polynya is blown southward opening the polynya. While removal of sea ice by drift within the region dominates the formation of the polynya, thermodynamic processes between the atmosphere and ocean dominate the landfast first-year sea ice (FYI) properties surrounding the polynya. The polynya remains small throughout winter until April, producing sea ice that is exported from the polynya southwards (*Wilson et al., 2001*). In spring the polynya enlarges rapidly due to atmospheric forcing as warm air is advected northwards along its eastern edge creates a southeast to northwest gradient in melt onset and pond onset (*Barber et al., 2001; Ingram et al., 2002*). Recently, *Marsden et al. (2004)* argued that the polynya may also be 'self sustaining' after its initial formation reaches some threshold size. They propose that buoyancy forcing supplied by the polynya to the atmosphere may induce a low pressure cell over the polynya whose rotation maintains the polynya by disallowing cold ambient air of terrestrial origin from entering and refreezing the surface of the ocean.

The onset of melt and surface ponding in landfast FYI surrounding the North Water Polynya is atmospherically forced and variable in space and time, and can be

remotely estimated using a time series of microwave scattering (Yackel *et al.*, 2001). We use this technique to link melt water flux from the sea ice to the re-establishment of the shallow, summer upper ocean mixed layer that was deepened in winter by buoyancy mixing due to salt rejection from growing landfast ice and mobile pack ice within the polynya.

Figure 4.1. The seasonal evolution of σ° from the ERS-1 SAR for thick first-year and multi-year sea ice over the annual sea ice cycle (after Barber *et al.*, 1998).



A time series of microwave backscatter coefficient (σ°) derived from synthetic aperture radar (SAR) is related to the temporal evolution of thermodynamic properties within a sea ice volume (Barber *et al.*, 1995). A seasonal temperature increase at the snow/ice interface causes a proportional brine volume increase within the sea ice, increasing its complex dielectric constant (ϵ^*) which is detected as an increase in σ° from the stable winter period by SAR (Figure 4.1) (Barber *et al.*, 1995). Thick first year ice in winter primarily has a smooth, specular reflecting surface, causing σ° to remain low and stable (Figure 4.1) with small

atmospherically induced changes in surface dielectric properties (*Barber and Thomas, 1998*). SAR-derived melt onset over landfast thick FYI is determined by an increase in depth hoar grain size, increased brine volume and water in liquid phase occurring through the diurnal cycle (*Barber and Yackel, 1999*). The funicular regime (*Colbeck, 1982*) is important as it occurs very briefly before liquid water begins to drain out of the snow pack (*Barber and Yackel, 1999*). Drainage allows progression to an advanced melt state on the sea ice surface when the snow becomes saturated and slush forms at the snow-ice interface rapidly decreasing surface albedo, accelerating absorption of incident solar radiation and related snow melt, drainage and pond formation. A second, larger peak in the temporal evolution of σ° (Figure 4.1) following the initial melt onset increase indicates pond onset over smooth, thick first-year sea ice (*Yackel et al., 2001*).

Beneath the sea ice, physical oceanographic processes along with ice cover buoyancy fluxes contribute to the structure of the water column within the North Water Polynya. Northern Assembly water flows south through Smith and Jones Sounds from the Arctic Ocean, with a 70-100m mixed layer and salinity greater than 33.6 psu which overlies warm halocline of Arctic origin typically colder than 0°C (*Bacle et al., 2002*). This surface mixed layer is generated by buoyancy mixing due to salt rejection by growing pack ice and by turbulent current mixing in the narrow strait of the Archipelago. Southern Assembly water is conveyed north by the West Greenland Current from the North Atlantic (Labrador Sea and Baffin Bay) with a mixed layer depth of ~100m (*Bacle et al., 2002*). The depth of the upper ocean mixed layer determines the ocean's ability to transfer heat, mass and momentum

from the atmosphere and ice cover to depth and the strength of the stratification determines the influence the mixed layer has on fluxes at its base (*Schneider and Muller, 1990*). The upper ocean mixed layer has been widely studied in mid-latitude oceans due to its importance in air-sea interaction processes (*Ikeda, 1986; Schneider and Muller, 1990; Alexander et al., 2000; Kara et al., 2000; Kara et al., 2003*) and is ultimately important in the Arctic where the flux of energy, mass and momentum between the ocean and atmosphere is constrained by sea ice, in both time and space.

2. Objective

The objective of this paper is to determine the ability of SAR-derived melt onset and pond onset over landfast FYI to predict the timing of the thinning and stable stratification of the summer ocean mixed layer in the North Water Polynya. We first examine the 'local scale' where in situ data allows examination of the connection between melting sea ice and mixed layer evolution in the northwestern section of the polynya. The local scale analysis is then applied to the entire polynya, illustrating how the regional scale summer ocean mixed layer stratification responds to the timing of landfast sea ice melt within the entire North Water Polynya.

3. Methods

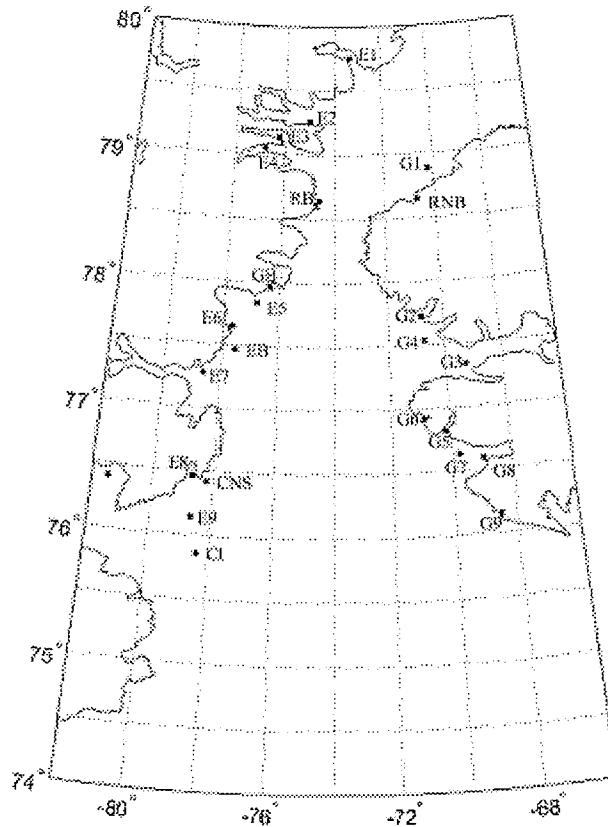
67 Radarsat-1 ScanSAR images in time series from year-day (YD) 21 to YD 183 in 1998 were used to derive melt onset and pond onset dates for sample locations (Table 4.1) on landfast FYI surrounding the North Water following *Yackel*

et al. (2001). ScanSAR combines Radarsat-1 SAR Wide A and B beams, transmitting and receiving horizontally polarized (HH) electromagnetic radiation at 5.3 GHz over a 460 km wide swath with a near incidence angle of 20° and a far incidence angle of 49.4°. The theory for using the time series SAR data to derive melt and pond onset dates is well developed in the literature (*Barber and Yackel, 1999, Yackel et al. 2001*). A series of sites (Figure 4.2) were selected over landfast FYI in the North Water Polynya region and σ° was sampled throughout the time series.

Table 4.1. Melt onset and pond onset dates for each scanSAR sample location (after Yackel et al., 2001).

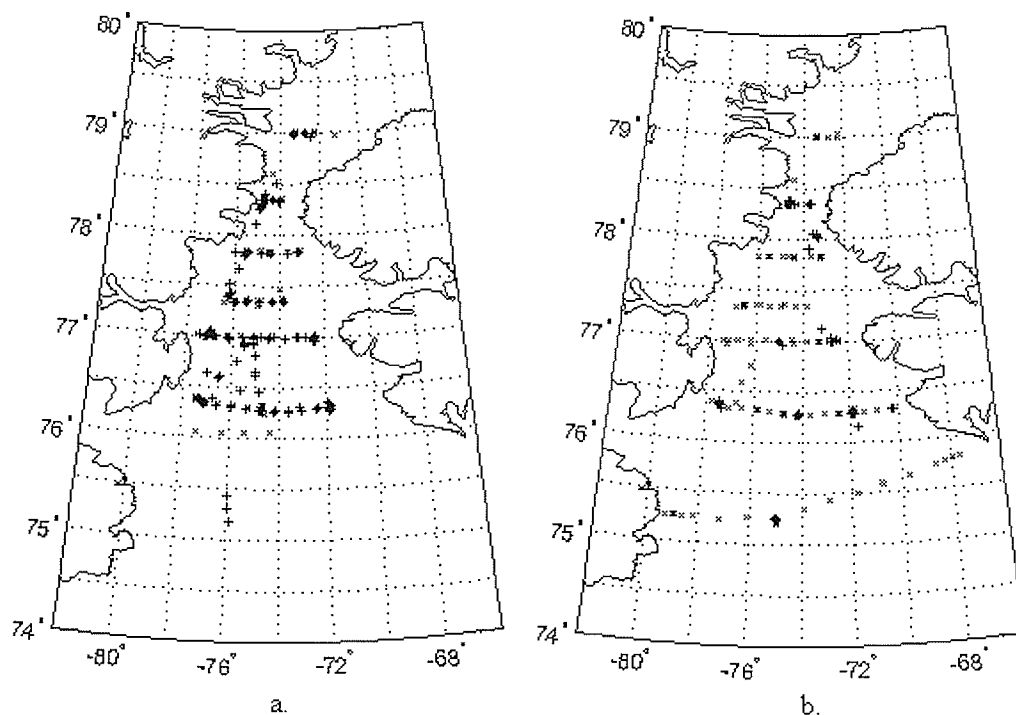
Site Name	Latitude	Longitude	Melt Onset (YD)	Pond Onset (YD)
Rosse Bay (RB)	78.645917 N	-74.578528	151	161
Rensselaer Bay (RNB)	78.652667 N	-70.720528	148	155
Goding Bay (GB)	77.965028 N	-76.324472	141	164
Eskimo Bluff (EB)	77.468500 N	-77.528222	143	172
Cape Norton Shaw (CNS)	76.420861 N	-78.189778	142	154
Coburg Island (CI)	75.858389 N	-78.403139	147	163
E1	79.752083 N	-73.312667	153	162
E2	79.258306 N	-74.983472	152	161
E3	79.140833 N	-76.243722	153	158
E4	79.053389 N	-76.782972	151	158
E5	77.841444 N	-76.843944	143	154
E6	77.650528 N	-77.667167	141	153
E7	77.277722 N	-78.582667	149	154
E8	76.465528 N	-78.674444	147	155
E9	76.144083 N	-78.654333	149	153
E10	76.405139 N	-81.461194	147	157
G1	78.882667 N	-70.178667	148	160
G2	77.724806 N	-70.772528	132	146
G3	77.338111 N	-69.303111	137	147
G4	77.541806 N	-70.731778	128	147
G5	76.815528 N	-70.153944	102	114
G6	76.920417 N	-70.857222	101	115
G7	76.631194 N	-69.713583	101	116
G8	76.594556 N	-68.916583	101	106
G9	76.146444 N	-68.540472	101	104

Figure 4.2. Radarsat-1 scanSAR sample site locations over landfast first-year sea ice surrounding the North Water Polynya (after Yackel et al., 2001).



Over the course of the International North Water Program in 1998, 441 CTD profiles were collected (Figure 4.3) over a 104-day cruise of the C.C.G.S Pierre Radisson between YD 98 (08 April) and YD 202 (21 July). Salinity was calculated and output automatically with temperature by the instruments and potential density (σ_θ) was calculated using the UNESCO (1983) algorithm. Mixed layer depth was calculated following the approach of Schneider and Muller (1990), who proposed that MLD be calculated based on potential density (σ_θ) difference from the surface.

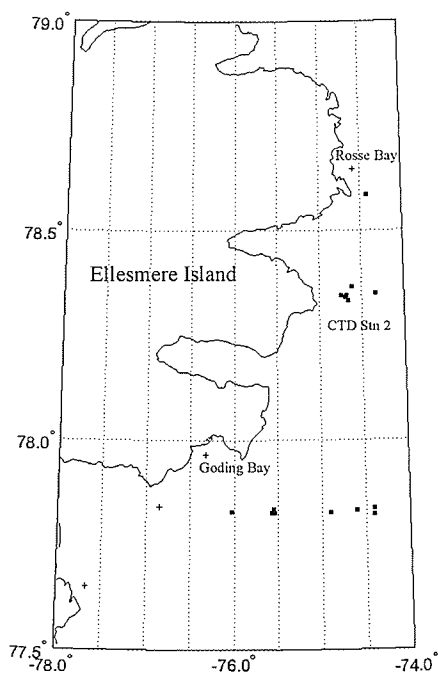
Figure 4.3. Location of CTD profiles in: (a) April (x) and May (+) and (b) in June (x) and July (+).



4. Results and Discussion – Local Scale

CTD profiles collected at station 2 (78.36160°N , $-74.71095^{\circ}\text{E}$) which lies between ScanSAR sample sites Rosse Bay and Goding Bay (Figure 4.4). CTD station 2 was chosen as the site for our local scale analysis because it was sampled most often (6 times) and at least once each month. These data illustrate that low salinity melt water resulting from the melt of landfast sea ice is connected to the formation of the shallow summer ocean mixed layer in the North Water polynya.

Figure 4.4. Local scale study area on the west side of Smith Sound, including CTD station 2, Rosse Bay and Goding Bay Radarsat-1 scanSAR sites.



Melt onset occurred at the Rosse Bay (RB) ScanSAR sample site on YD 151 and pond onset occurred 10 days later on YD 161 (Table 4.1). At the Goding Bay (GB) ScanSAR test site, Melt onset occurred on YD 141 and 13 days later pond onset occurred on YD 164 (see table 4.1).

Figure 4.5 depicts the temporal evolution of temperature, salinity, potential density and associated mixed layer depths using six profiles in time from YD 98 to YD 199. Near-surface temperatures warm with each successive profile in time. Surface salinity decreases substantially through time, with a small inversion occurring between YD 129 and YD 158. Potential density derived from salinity and temperature profiles behaved in a near-identical way to salinity near CTD station 2,

signifying that density stratification of the water column is driven almost solely by surface salinity reduction. The first CTD profile collected in the North Water Polynya at station 2 occurred on YD 98 (April 08). The water column was isothermal and isohaline to a depth of 114 dbars where a very steep thermocline and halocline occurred (see figures 4.5a and 4.5b). At this time the potential density profile of the water column (see figure 4.5c) and associated deep winter mixed layer (see figure 4.5d) is a result of buoyancy mixing due to salt rejection from the growing landfast and mobile ice cover and turbulent mixing.

When CTD station 2 was revisited on YD 129 (May 09), a warming shift in the temperature profile (see figure 4.5a) had occurred. The surface layer of the ocean was isothermal around -1.70°C except for a near surface increase. A smaller thermocline developed beginning at 84 dbars, below which the water column gradually warmed to a depth of 200 dbars. On YD 129, the sea surface salinity (see figure 4.5b) was isohaline about 32.5 psu to 27 dbars, decreasing from the previous profile in time.

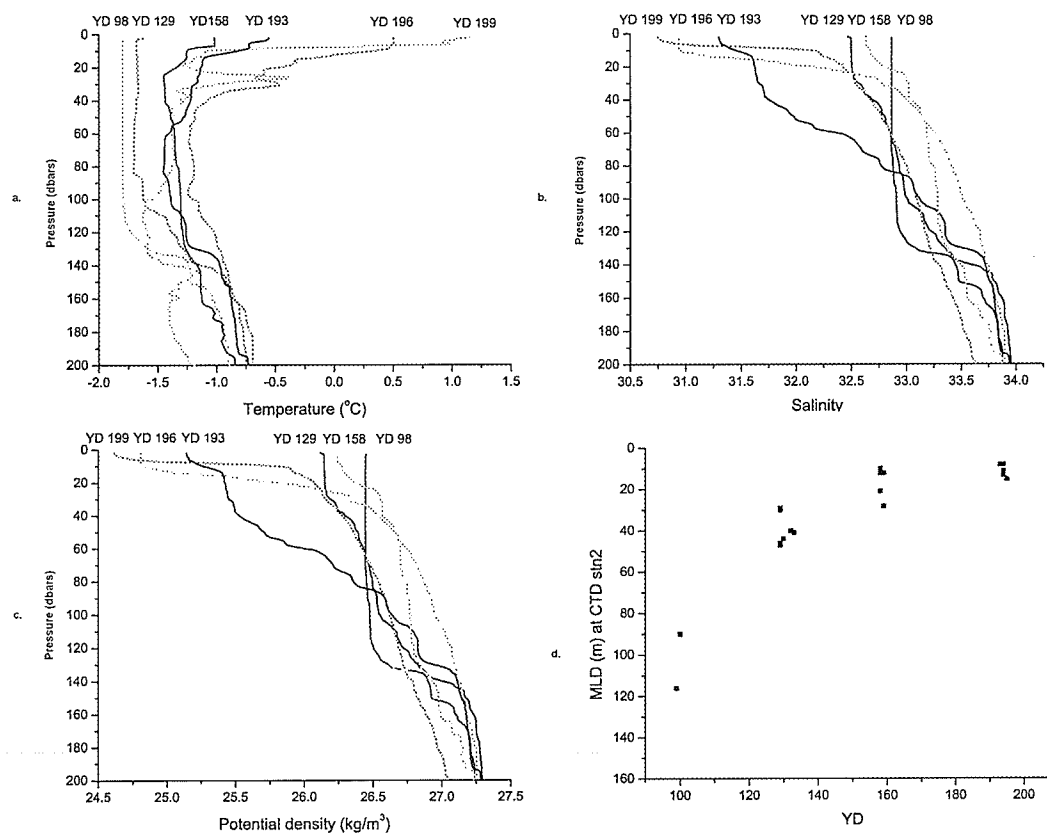
On YD 158 (June 07), the warm surface layer created by increased absorption of solar energy was more pronounced to 8 dbars where a more marked thermocline occurred. The surface salinity had increased with respect to the previous profile in time, but was still less than the winter surface salinity as seen in the first profile on YD 98.

On YD 193 (July 12) sea surface temperature (see figure 4.5) had risen to -0.558°C and surface salinity at CTD station 2 had decreased to 31.3 psu.

On YD 196 (July 15) station 2 was sampled for the fifth time (see figure 4.5). In three days the sea surface temperature (at 2 dbars) had risen to 0.502°C. The sea surface salinity was 30.941 psu, isohaline to 10 dbars where a near surface halocline occurred, increasing the salinity of the water column to 32.998 psu at 40 dbars.

On YD 199 (July 18) the sea surface temperature had increased to 1.147°C. The sea surface salinity reached a sampled minimum of 30.743 psu, the start of a surface halocline that reached 32.219 psu at 12 dbars. Below 12 dbars, water column salinity decreased with depth gradually to 33.627 psu at 200 dbars.

Figure 4.5. (a) Temperature (b) salinity, and (c) potential density profiles at CTD station 2, (d) mixed layer depth at CTD station 2.



Potential density profiles calculated from the above T and S profiles (see figure 4.5c) follow their corresponding salinity profiles (see figure 4.5b) showing that decreases in salinity driven down through the water column from the surface completely dominate potential density stratification in the North Water Polynya. We therefore focus our discussion around several interesting features of the temperature and salinity profiles. At the time of the first profile, the surface layer of the water column was isohaline and relatively saline. The second salinity profile shows a surface reduction in salinity between YD 98 and YD 129 which is almost certainly due to mobile sea ice within the polynya proper, melting laterally and from the bottom as it is driven southward by the wind. The salinity profile of YD 158 (see figure 4.5c) is the most significant from our perspective for two reasons; it occurs temporally between SAR-derived melt and pond onset dates for Goding Bay and Rosse Bay ScanSAR sample sites (Table 4.1), and salinity and potential density in the ocean surface layer increase relative to the east of YD 129, but are still less than the winter base-line indicated by the profile of YD 98 (see figure 4.5b). This profile captures the increase in surface salinity as the melting landfast ice surrounding the polynya reaches the point in its thermodynamic evolution where the ice is sufficiently warm to allow for brine channel drainage. The profiles of YD 193, 196 and 199 at CTD station 2 (see figure 4.5b) follow the thermodynamic evolution and freshwater fluxes from the landfast ice surrounding the polynya, clearly depicting a substantial reduction of salinity as the landfast ice melts contributing low-salinity (~3psu) melt water to the upper ocean mixed layer.

Algorithms designed to detect the depth of the ocean mixed layer from CTD profiles are typically created using data from mid-latitude studies (*Schneider and Muller, 1990; Kara et al., 2003*). The *Schneider and Muller (1990)* algorithm is no exception, designed to discern the difference between the pycnocline and the thermocline because mid-latitude mixed layer depths are typically much shallower than the top of the thermocline. The *Schneider and Muller (1990)* MLD algorithm successfully delineates the seasonal structure of the upper ocean mixed layer in the North Water Polynya, where changes in potential density are driven by changes in salinity rather than changes in temperature.

The MLD at CTD station 2 (see figure 4.5d) in the North Water Polynya is relatively deep in winter, derived from the deep isothermal and isohaline surface layer of YD 98 (figures 4.5a and 4.5b). As previously stated, the mixed layer at the end of winter is a result of buoyancy-driven mixing due to salt rejection from the growing pack ice and strong current mixing in the narrow straits of the Arctic Archipelago. Due to freshwater flux from sea ice resulting in decreased surface salinity on YD 129, the MLD at station 2 was much shallower. Coincident in time, ScanSAR data captured melt onset and pond onset in the landfast sea ice at the Rosse Bay and Goding Bay sample sites (Table 4.1), the MLD at station 2 became very shallow and remained stable for the duration of the sampling period.

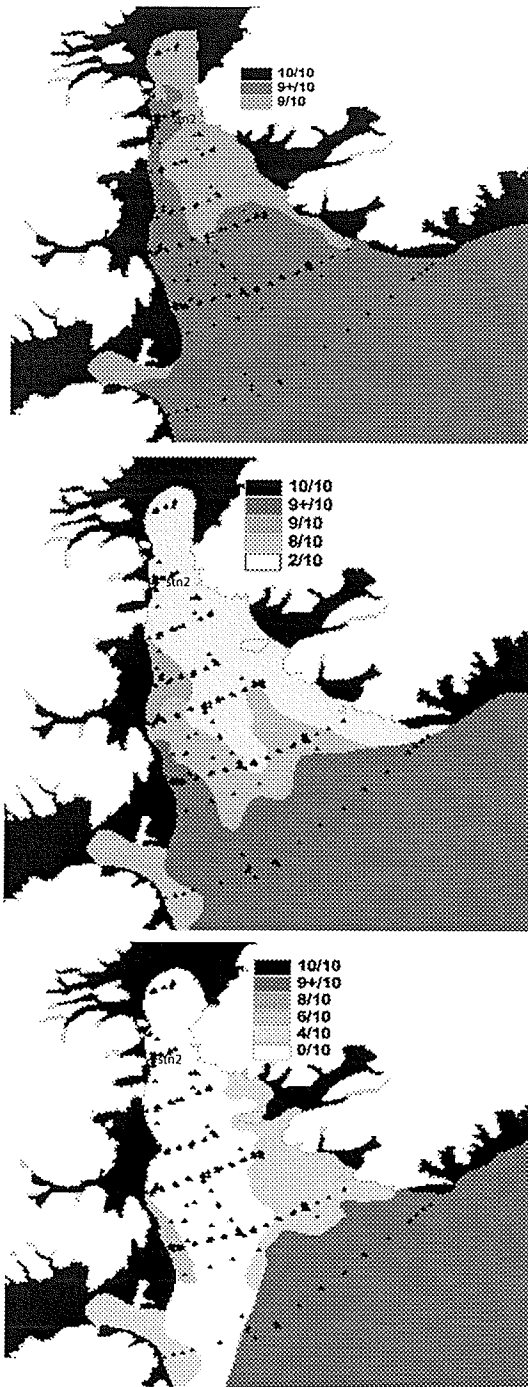
Melt onset and pond onset dates are derived from microwave backscatter in the microwave region, but of ultimate importance is how properties of a sea ice surface lend valuable insight into the volume is affected by environmental forcing. Seasonal progression from polar winter dictates a gradual increase in solar angle

combined with gradual increases in total daily incoming shortwave radiation. Snow covered sea ice begins to melt when the atmospheric boundary layer, having absorbed sufficient incoming shortwave radiation to experience an increase in temperature, increases the temperature of the snow and sea ice volume (*Yackel et al., 2001*). The temperature in both the snow and sea ice volumes increase as a function of the thermal diffusivity of the material. The snow cover gains heat energy from the air and warms first, followed by the sea ice below as heat is conducted downward by the resulting temperature gradient between the cold ice and warmer air above. As the snow-covered sea ice surface enters the pendular and then funicular regime, the temperature of the sea ice volume increases in a linearly with depth, and due to the lower thermal diffusivity of sea ice this occurs more gradually than in the snow cover. Increased temperature within the sea ice volume causes changes in the size, shape and connectedness of the brine inclusions within the sea ice (*Eicken, 2003*). As the ice volume warms, the brine channels within it gradually become connected, eventually allowing gravity to drive melt water from above the ice through the brine channels, flushing highly saline liquid brine content (*Eicken, 2003*). Once the brine is flushed from the sea ice, low salinity surface melt water is free to percolate through the ice volume (*Eicken, 2003*). Concurrent to changes in the brine inclusions within the sea ice, the sea ice thickness is reduced by a positive feedback mechanism caused by decreased surface albedo on top of the ice, with thermal and mechanical erosion from beneath playing a small part. Sea ice thickness reduction creates a large freshwater flux to the ocean surface.

5. Results and Discussion – Regional Scale

Sea ice within the North Water Polynya follows a reasonably well known pattern, displayed by Canadian Ice Service (C.I.S.) ice charts (Figure 4.6) (*Barber et al., 2001; Wilson et al., 2001*). The C.I.S. digital ice charts provide a useful summary of the evolution of the North Water Polynya during the 1998 study period. The dynamic nature of mobile ice within the North Water region is different than the thermodynamically-driven evolution of the landfast ice which bounds it on the west and east sides. We recall that *Yackel et al. (2001)* showed thermodynamic processes dominate the seasonal evolution of the landfast sea ice surrounding the North Water Polynya while *Wilson et al., (2001)* showed that dynamic processes dominate the mobile ice zone of the North Water.

Figure 4.6. Canadian Ice Service digital charts showing ice concentration and relative extent. Top: YD 121(1 May), middle: YD 135 (15 May) and bottom: YD 152 (1 June).



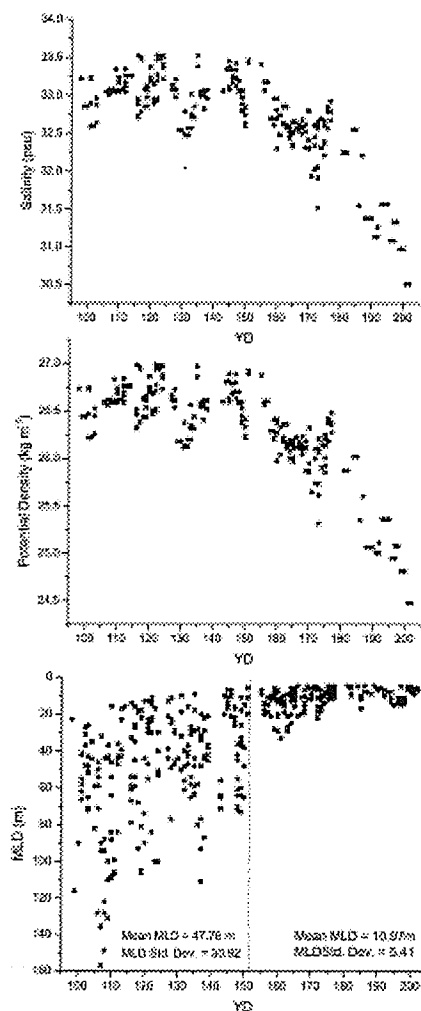
On YD 121, the polynya is almost completely covered in sea ice (see figure 4.6a) with CTD station 2 under 9+/10 sea ice concentration (SIC). The rest of the North Water is covered by landfast sea ice surrounding the polynya proper, or by 9/10 sea ice concentration within the polynya. The next digital ice chart (see figure 4.6b) in the time series occurred for YD 135 (May 15), by which time the sea ice within the polynya proper had almost been completely removed by wind, resulting in 2/10 SIC to dominate the polynya, bounded by landfast sea ice. On YD 135 CTD station 2 was very near the landfast ice edge in 2/10 SIC. By YD 152 (June 01), the polynya including CTD station 2, was ice-free bounded by landfast sea ice (see figure 4.6c). Regardless of the dynamic evolution of the sea ice within the polynya, the general extent of the landfast sea ice bounding the polynya on the Ellesmere and Greenland sides did not change.

Mixed layer depths were calculated for each of the 441 CTD profiles made during the program. CTD profiles from station 2 provide an example of how reduced salinity decreases potential density in spring, thinning and more stably stratifying the surface mixed layer. Here, we illustrate variability in the regional (polynya-wide) seasonal evolution of salinity (see figure 4.7a) duplicated by potential density (see figure 4.7b) at 5 dbars. The 5-dbar depth was employed because it was the closest meaningful value to the ocean surface contained in each profile.

On YD 151, (see figure 4.7a) freshwater input from snow and sea ice melt begins to decrease surface salinity values over the time series. This figure relates the overall seasonal decrease in salinity at the surface, which drives the potential

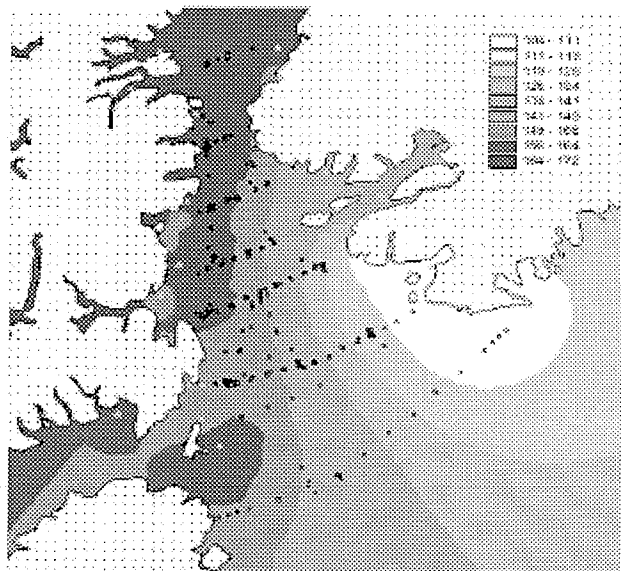
density values at depth (see figure 4.7b) and results in the thinning and more stable stratification of the summer ocean mixed layer (see figure 4.7c). Figures 4.7a and 4.7b also shows variation in surface salinity and potential density at 14-day intervals coinciding with the period the tidal current takes to reach its maximum. Upon closer inspection of the predicted tidal current for this region a strong relationship between observed MLD maxima and tidal current maxima occurs.

Figure 4.7. Time series evolution of: near surface salinity (top), near surface potential density (middle), and mixed layer depth (bottom in the North Water Polynya.



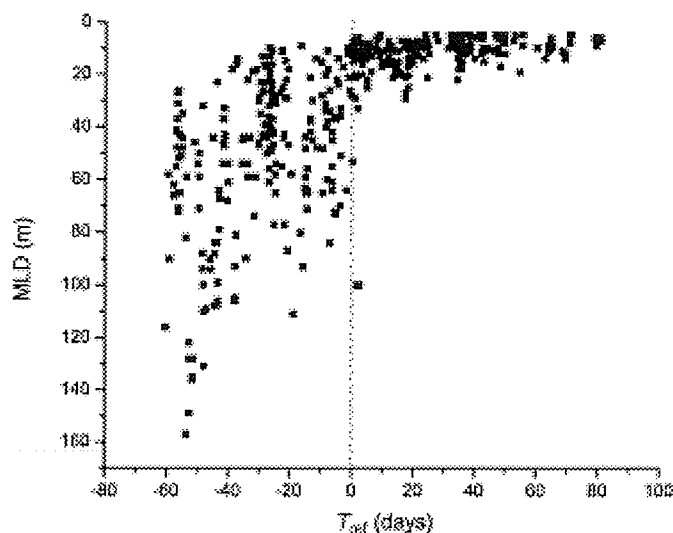
The MLD within the North Water Polynya undergoes a very similar evolution with time as near surface salinity. Prior to YD 151, the summer ocean mixed layer in the North Water Polynya was in most cases undefined before YD 151 (see figure 4.7c) as the MLD algorithm is actually calculating the depth of the deep, permanent halocline discussed by *Bacle et al.* (2002). This deep winter mixed layer is more dependent upon the bathymetric depth of each station sampled than on changes in the properties at the surface of the water column (*Bacle et al.*, 2002). The average MLD (n = 259) prior to YD 151 was 47.02 m, with a standard deviation of 30.52. However, after YD 151 (no profiles were collected between YD 151 and 155) the MLDs were shallow, and the values, despite location (Figure 4.3b) and therefore bathymetry were stable. The average MLD (n = 182) conducted after YD 151 was 10.95 m, with a standard deviation of 5.43.

Figure 4.8. Sar-derived pond onset date interpolated over the polynya, overlaid by all CTD profiles conducted in 1998. ScanSAR sample sites are denoted by grey triangles.



In order to further illustrate the coincident nature of thermodynamically-driven evolution of landfast sea ice surrounding the polynya and the freshening of the surface mixed layer, pond onset date for the whole polynya was interpolated (see figure 4.8) over a 2km² cell grid, capturing the SE to NW progression of sea ice thermodynamic evolution. The pond onset date of each grid cell where a MLD value also occurred was referenced against the date of the CTD profile used to derive it. For example, if a MLD was calculated using a profile on YD 140 and the pond onset value at that point in the grid was YD 150, then that MLD would have a time reference in days (T_{ref}) of -10, as it occurred 10 days prior to the interpolated pond onset at that point. When T_{ref} is calculated for each of the MLDs, (see figure 4.9) it becomes shallow and stable coincident with the interpolated pond onset date for each location. We have therefore shown the ability to determine the timing of a shallow spring MLD in the North Water from SAR remote sensing.

Figure 4.9. Mixed layer depth time-referenced against pond onset date at the same location within the North Water Polynya.



The underlying theme to three different processes, (1) the dynamic sea ice retreat that occurs within the polynya proper, (2) the thermodynamically-driven evolution of landfast ice properties surrounding the polynya described by melt and pond onset dates calculated from time series ScanSAR images, and (3) the seasonal evolution of salinity and resulting surface mixed layer of the North Water Polynya that drive summer MLD stabilization, is that they are temporally concurrent. The digital ice charts show that between YD 135 and YD 152 the sea ice within the polynya is completely removed during which time the landfast ice surrounding the polynya undergoes melt onset and pond onset, signifying thermodynamic changes within the sea ice volume. The case study discussed above showed that the CTD profile data in the North Water Polynya capture changes in the physical properties of the water column caused by the thermodynamically-driven evolution of the adjacent landfast sea ice volume, which occur at the same time.

6. Conclusions

We conclude that the spring melt occurring within the landfast sea ice nearest CTD station 2 is coincident to the evolution of surface salinity and resultant mixed layer depth at that location within the North Water Polynya. SAR-derived sea ice melt onset and pond onset can be used to determine the timing of this ice-ocean connected process at the local scale as melt within the sea ice volume occurs and is reflected by changes captured at the surface by RADARSAT-1 ScanSAR imagery, while CTD profiles at station 2 capture the evolution of the upper ocean. At the regional scale, we conclude that polynya-wide decreases in surface salinity and

associated thinning and more stable stratification of the upper ocean caused by the introduction of low salinity sea ice melt water can be predicted using SAR-derived pond onset date. The timing of pond onset in landfast sea ice coincides in time with a shallow, stably stratified summer mixed layer within the polynya, illustrating the utility of SAR data for monitoring the spatial and temporal variability in MLD using time series σ° .

This work is an important first step in revealing how the physical oceanographic system of a polynya responds to thermodynamically-driven evolution of surrounding landfast sea ice. It is hypothesized that the stratification of the upper ocean mixed layer in the North Water Polynya controls in part primary production within the polynya in summer (*Odate et al., 2002*), forming the basis of a highly productive arctic food web. Changing sea ice concentration and extent within the Arctic could alter the seasonal physical oceanographic evolution of the ocean column entering the North Water Polynya in the future. The ice bridge in Nares Strait may become less stable thereby allowing more sea ice into the NOW polynya region, altering the existing temporal and spatial patterns of sea ice in the region and thereby affecting the relationship between sea ice melt and stabilization of the upper ocean mixed layer and related ecosystem productivity.

Literature Cited

- ACIA, 2004. Impacts of a warming climate – Arctic climate impact assessment, 144 pp. Cambridge University Press, Cambridge, England.
- Alexander, M.A., J.D. Scott and C. Deser, 2000. Processes that Influence Sea Surface Temperature and Ocean Mixed Layer Depth Variability in a Coupled Model. *J. Geophys. Res.*, 105(C7): 16823-16842.
- Bacle, J., E.C. Carmack and R.G. Ingram, 2002. Water Column Structure and Circulation under the North Water during Spring Transition: April-July 1998. *Deep Sea Research II*, 49: 4907-4925.
- Barber, D.G., R. Marsden, P. Minnett, G. Ingram and L. Fortier, 2001. Physical Processes within the North Water (NOW) Polynya. *Atmosphere-Ocean*, 39(3): 163-166.
- Barber, D.G., T.N. Papakyriakou, E.F. LeDrew and M.E. Shokr, 1995. An examination of the relation between the spring period evolution of the scattering coefficient and radiative fluxes over landfast sea ice. *Int. J. Rem. Sens.*, 16: 3343-3363.
- Barber, D.G. and A. Thomas, 1998. The influence of cloud cover on the radiation budget, physical properties and microwave scattering coefficient of first-year and multi-year sea ice. *IEEE Trans. Geosci. R. Sens.*, 36(1): 38-50.
- Barber, D.G. and J.J. Yackel, 1999. The physical, radiative and microwave scattering characteristics of melt ponds on Arctic landfast sea ice. *Int. J. Rem. Sens.*, 20: 2069-2090.
- Colbeck, S.C., 1982. An overview of seasonal snow metamorphism. *Rev. Geophys. Space Phys.*, 20: 45-61.
- Eicken, H., 2003. Chapter 2: From the microscopic, to the macroscopic, to the regional scale: growth, microstructure and properties of sea ice. In *Sea Ice: An Introduction to its Physics, Chemistry, Biology and Geology*. Thomas, D. and Dieckmann, G.S. pp. 22-81, Blackwell Publishing.
- Ikeda, M., 1986. A mixed layer beneath melting sea ice in the marginal ice zone using a one-dimensional turbulent closure model, *J. Geophys. Res.*, 91(C4): 5054-5060.
- Ingram, R.G., J. Bacle, D.G. Barber, Y. Gratton and H. Melling, 2002. An overview of physical processes in the North Water. *Deep Sea Research. II*, 49: 4893-4906.
- Kara, A.B., P.A. Rochford and H.E. Hurlburt, 2003. Mixed layer variability of the global ocean. *J. Geophys. Res.*, 108(C3), 3079, doi: 10.1029/2000JC000736.

- Kara, A.B., P.A. Rochford and H.E. Hurlburt, 2000. An optimal definition for ocean mixed layer depth. *J. Geophys. Res.*, 105(C7): 16803-16821.
- Marsden, R., J. Serdula, E. Key and P.J. Minnett, 2004. Are polynyas self-sustaining? *Atmosphere-Ocean*, 42(4): 251-265.
- Melling, H., Y. Gratton, and G. Ingram, 2001. Ocean circulation within the North Water Polynya of Baffin Bay. *Atmosphere-Ocean*, 39(3): 301-325.
- Odate, T., T. Hirawake, S. Kudoh, B. Klein, B. LeBlanc and M. Fukuchi, 2002. Temporal and spatial patterns in the surface-water biomass of phytoplankton in the North Water. *Deep Sea Research II*, 49: 4947-4958.
- Perovich, D.K. and B. Elder, 2002. Estimates of ocean heat flux at SHEBA. *Geophys. Res. Lett.*, 29(9), 1344, doi:10.1029/2001GL014171.
- Schneider, N. and P. Muller, 1990. The meridional and seasonal structures of the mixed-layer depth and its diurnal amplitude observed during the Hawaii-to-Tahiti Shuttle experiment, *J. Phys. Oceanogr.*, 20: 1395-1404.
- Smith, S.D., R.D. Muench and C.H. Pease, 1990. Polynyas and Leads: An overview of physical processes and environment. *J. Geophys. Res.*, 95(C6): 9461-9479.
- Steffen, K., 1985. Warm water cells in the North Water, northern Baffin Bay during winter. *J. Geophys. Res.*, 90: 9129- 9136
- UNESCO, (1983). Algorithms for computation of fundamental properties of seawater. *UNESCO Tech. Pap. Marine Science*, 44, p.53.
- Wadhams, P., 2000. *Ice in the Ocean*, 351 pp. Gordon and Breach Science Publishers, London.
- World Meteorological Organization, 1970. WMO sea ice nomenclature. *WMO Rep.* 259, T.P. 145, 147 pp.+ 8 suppl., Geneva.
- Wilson, K.J, D.G. Barber and D.J. King, 2001. Validation of production of RADARSAT-1 derived ice motion maps in the North Water (NOW) Polynya, January – December 1998. *Atmosphere-Ocean*, 39(3): 257-278.
- Yackel, J.J., D.G. Barber and T.N. Papakyriakou, 2001. On the estimation of spring melt in the North Water Polynya using RADARSAT-1. *Atmosphere-Ocean*, 39(3): 195-208.

CHAPTER FIVE: SPATIAL AND TEMPORAL VARIABILITY OF SEA ICE IN THE SOUTHERN BEAUFORT SEA AND AMUNDSEN GULF: 1980 – 2004

Galley, R.J. E. Key, D.G. Barber, B.J. Hwang, and J. Ehn, 2008. Spatial and temporal variability of sea ice in the southern Beaufort Sea and Amundsen Gulf: 1980-2004. *Journal of Geophysical Research*, 113, C05S95, doi: 10.1029/2007JC004553.

1. Introduction

Recent variability in Arctic sea ice thickness and extent has been attributed to seasonal changes in dynamic and thermodynamic forcing (*Zhang et al.*, 2000). A shift in the sea level pressure pattern over the central Arctic Ocean during the 1990's led to a weakening of the Beaufort Gyre (*Lukovich and Barber*, 2006) and increased observations of southerly and easterly winds in the western Arctic (*Rothrock et al.*, 1999) that advect ice north and west away from the continental coast. *Rothrock et al.* (1999) also note that southerly winds were accompanied by positive anomalies in surface air temperatures which increased melt, leading to thinner perennial ice and more open water. Increased open water and thinner perennial sea ice contributes to increases in heat content in the upper water column further reducing ice thickness and extent (*Rigor and Wallace*, 2004). *Polyakov and Johnson* (2000) also note that a 60 to 80 year pressure oscillation came in phase with the decadal decrease in sea level pressure during the 1990's, accounting for the persistence and amplitude of the negative pressure anomaly, and enhanced warm air advection. These factors contributed to sea ice extent reduction in the 1990's, and the record negative sea ice extent anomalies in the Beaufort Sea during 2002 (*Serreze et al.*, 2003), 2003, and 2004 (*Stroeve et al.*, 2005).

Regional and inter-annual sea ice motion, such as the circulation of ice in the Beaufort Gyre and convergence and divergence of sea ice along the Beaufort Sea coast have occurred since the beginning of the satellite record (*Thorndike, 1986; Serreze et al., 1989*). Sub-decadal cycles in sea ice thickness have also been observed (*Mysak and Manak, 1989*). Thinning of perennial sea ice in the Arctic has been related to transpolar sea ice drift exporting sea ice out of the Arctic through Fram Strait at approximately seven year intervals (*Mysak and Manak, 1989*).

The longer-term in situ record suggests a continuing trend towards polar-amplified warming of surface air temperatures (*Polyakov et al., 2002*), increased cyclone activity (*Zhang et al., 2004*), and earlier melt onset and later re-freeze (*Belchansky et al., 2004*). Models however, vary widely in their predictions of Arctic sea ice extent and stage of development. Forecasting scenarios range from a stabilization of current conditions to the possibility of a seasonally ice-free Arctic (*Meehl et al., 2007*). Results from the Community Climate System Model also show wide variation of predicted future decreases in perennial sea ice volume (*Holland et al., 2006*), which has been shown by *Rothrock et al. (1999)* to have been in significant decline since the 1960's. Despite broad disagreement on the rate and extent of the sea ice decay, the spatial pattern of summer melt favors retreat towards the west coast of the Canadian Arctic Archipelago, exposing a larger seasonally ice-free area (*Flato et al., 2000*).

Sea ice thickness and extent determines the exchange of heat between the ocean and atmosphere (*Maykut, 1982*), is an important variable in determining the strength of sea ice in a region (*Andreas et al., 1993*), and has an obvious influence on

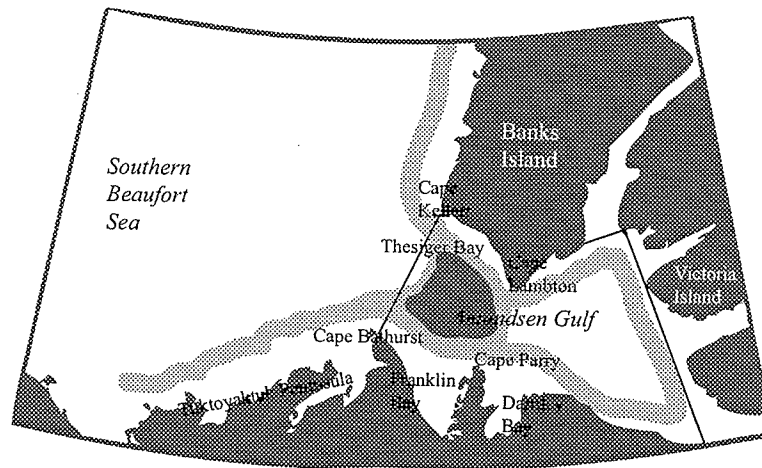
the ice mass flux (*Aagard and Carmack, 1989*) and therefore the freshwater storage in a region (*Wadhams, 2000*). Polynyas and flaw leads may be open months before the annual melt begins, allowing for enhanced ocean-atmosphere heat exchange year-round and albedo feedbacks which contribute to the instability or mobility of the surrounding ice pack. These areas of reduced sea ice concentration and/or thickness are important to biological and physical oceanography. Sea ice provides a substrate for significant primary production within and below the ice, as well as affording mammals an opportunity to forage and rear young (*Dunbar, 1981*). Consequently, Inuit people have hunted in and around these areas for at least the past three thousand years (*Smith et al., 1990*)

Monitoring long-term variation of sea ice extent is very important in both the estimation of current climate trends and the prediction of future change. Satellite-borne passive microwave (PMW) sensors are typically relied upon to monitor sea ice temporal and spatial variation of sea ice at the hemispheric scale. PMW sea ice extent data have shown significant decreases in northern hemisphere, the amount of which is dependent upon the time period and area(s) studied (i.e. (*Stroeve et al., 2005; Serreze et al., 2003, Zhang et al., 2000, Gloersen et al., 1999, Parkinson et al., 1999*)).

At the regional scale, *Drobot and Maslanik (2003)* explored the inter-annual variability of Beaufort Sea ice conditions, noting that summer ice conditions north of Alaska were related to dynamic mechanisms in the preceding winter and thermodynamic processes during summer. Sea ice retreat and formation play an integral role in creating a physically favorable environment for biological

production in western Amundsen Gulf (*Arrigo and Van Dijken, 2004*). *Barber and Hanesiak (2004)* note the scale-dependence of sea ice anomalies in the southern Beaufort Sea and Amundsen Gulf, associating local sea ice anomalies with local-scale advection and regional-scale sea level pressure and surface temperatures. Timing of sea ice formation and breakup in Amundsen Gulf for the years 1964-1974 were examined by *Hammill (1987)*, using ice summaries and analysis reports for the Canadian Arctic prepared by the Canadian Department of Transport (1964-1972) and The Sea Ice Atlas of Arctic Canada (1973, 1974). For the purpose of classifying ice retreat and formation into early, medium and late years, Amundsen Gulf was considered ice free when 80% of the gulf was open, and freeze up was considered complete when 80% of the gulf was covered in sea ice (*Hammill, 1987*). The eleven years studied by *Hammill (1987)* were almost evenly distributed into early break-up (1968, 1970, 1971, 1973), medium break-up (1965, 1969, 1972) and late break-up (1964, 1966, 1967, 1974). Early ice formation occurred in 1964, 1967, and 1974 while medium ice formation years were 1965, 1966, 1970, and 1972 while ice formation occurred late in 1968, 1969, 1971 and 1973 (*Hammill, 1987*). *Hammill (1987)* also describes the location of a polynya in Amundsen Gulf, although in 1964, 1968, and 1973 it did not form at all, and for only two of the other 9 years did it form in the same position.

Figure 5.1. The southern Beaufort Sea and Amundsen Gulf, western Canadian Arctic. Black lines delineate the study area used in Section 5. The area normally occupied by the flaw lead system is shown in grey.



In this study, 25 years (1980-2004) of Canadian Ice Service (CIS) digital ice chart data over Amundsen Gulf and the southeastern Beaufort Sea are used to determine the extent and change of interactions between a seasonal sea ice zone and the perennial Arctic pack. This dataset is unique in that it contains sea ice stage of development information, including classifications of total, old (a superset of second-year and multi-year sea ice), first-year (a superset of thin, medium and thick first year), young and new sea ice. The CIS dataset delineates stages of development by thickness, including new ice ($h_i < 10\text{cm}$), young ice ($h_i = 10\text{-}30\text{cm}$) and first-year ice ($h_i > 30\text{cm}$). Subsets of first year ice include thick first year ($h_i > 120\text{cm}$), medium first year ($70\text{cm} < h_i < 120\text{cm}$) and thin first year ($30\text{cm} < h_i < 70\text{cm}$) sea ice (Fequet, 2002). Old sea ice is defined as sea ice which has survived a summer's melt, including second-year and multi-year sea ice and is not defined by thickness. Total

sea ice concentration is the sum of old, first year, young and new sea ice concentrations (expressed in tenths). A focus is placed on the conditions of sea ice development in Amundsen Gulf and southeastern Beaufort Sea where the seasonal sea ice zone and perennial Arctic pack interact. This thermodynamically and dynamically active area has been the focus of recent attention, including the Canadian Arctic Shelf Exchange Study (CASES), ArcticNet, and the International Polar Year (IPY) Circumpolar Flaw Lead (CFL) Study. This area of the continental shelf is the only North American analog to the vast Russian continental shelves. The interaction of annual and old sea ice in these regions gives rise to flaw lead formation, which has implications on ecology, shipping, and oil exploration.

Amount, position, and seasonal to inter-annual cycles of these ice types allow for: [1] characterization of mean winter and mean summer sea ice concentration as a function of sea ice type in the region; [2] calculating the trend in concentration of each sea ice type during winter and summer over the time series, [3] quantifying patterns in the timing and duration of break-up and freeze-up in the region and [4] discussion of the variability of break-up and freeze-up in Amundsen Gulf in terms of regional dynamics and the evolving seasonal ice cover in this area. We consider this regional sea ice climatology an important component of the ocean-sea ice-atmosphere system in the southern Beaufort Sea and in particular a key element in how changes in sea ice conditions may affect physical-biological coupling in the region.

2. Study Area, Data and Methods

2.1. Amundsen Gulf and the southern Beaufort Sea

Amundsen Gulf is connected to the Beaufort Sea through an outlet bounded to the north by Banks Island and to the south by Cape Bathurst (Figure 5.1). Landfast ice along the perimeter of the basin extends generally to the continental shelf break, where the water depth is 50 to 100m. West of Banks Island lies the perennial Beaufort Sea ice pack. Its position is correlated with large-scale pressure patterns, and motion within the pack is largely determined by the local geostrophic wind (*Thorndike and Colony, 1982*). Annually recurrent leads make up the extensive flaw lead system in the southeastern Beaufort Sea which persists from the completion of freeze up to break up in spring (*Carmack and MacDonald, 2001; Barber and Hanesiak, 2004*). The regional flaw lead system forms in three main areas: (1) parallel to the continental coastline and north of the landfast ice edge along the coast of the Tuktoyaktuk Peninsula, Cape Bathurst, Franklin Bay and Cape Parry, (2) west of the landfast ice edge along the west and southwest coast of Banks Island and, (3) along the west coast of Victoria Island in eastern Amundsen Gulf (Figure 5.1).

In some years between late April and mid-May, a lead also forms at the interface between the mobile ice pack and high concentration sea ice in eastern Amundsen Gulf, running north-south between the south tip of Banks Island and Cape Bathurst. This dynamic area is further characterized by a constricted airflow that lends to accelerations of air velocities downwind (*Torneby, 2006*), relatively strong tidal mixing (*Kleim and Greenberg, 2003*), and upwelling along shallow

shelves (*Carmack and Macdonald, 2002*). Using this area of open water, ice sometimes enters Amundsen Gulf blocking ice advection out of the gulf and stalling the open water season.

2.2. Sea ice concentration data

CIS digital ice charts are available from an on-line archive at <http://ice.ec.gc.ca>. This sea ice dataset integrates a number of data sources including aerial and marine surveys, satellite remote sensing data including Radarsat-1, NOAA AVHRR and Envisat ASAR as well as *in situ* observations. CIS digital ice charts are created manually by expert ice analysts at the CIS who derive total and partial concentrations for each sea ice stage of development. *Agnew and Howell (2003)* used CIS ice chart data as a baseline to evaluate PMW ice concentration data. Their results showed a considerable discrepancy between CIS and PMW data; tie points used in calibrating the NASA Team sea ice extent algorithm perform better at the hemispheric scale rather than for specific areas, performing poorly in seasonal ice zone areas throughout the annual cycle, and during melt and freeze-up conditions, where they consistently underestimate total sea ice extent. They also showed the usefulness of the CIS dataset in long-term regional monitoring of sea ice, particularly because the CIS data has comparatively high spatial resolution and are composed using multiple datasets to categorize sea ice cover. Conversely, ice concentration and extent data produced using PMW data contain only total ice concentration and no thickness information. The stability of the CIS digital dataset through time may be affected by advances in remote sensing

platforms and changing shipping routes which subject the dataset to shifts in bias and variance, but the *Canadian Ice Service Archive Documentation Series* quality index indicates statistical analysis is appropriate in the region (*Canadian Ice Service Archive Documentation Series*, 2006). We used 802 sea ice charts available for the western Arctic between January 1, 1980 and December 31, 2004. Prior to 1980, CIS data were only available for year weeks 24-48, which coincided with the majority of ice retreat and advance in the Beaufort Sea region but did not contain any winter sea ice data. Starting in 1980, winter chart data were produced monthly, while between year-weeks 23 (~ 10 June) and year-week 48 (~ 01 December), weekly charts of total and partial concentrations of sea ice and type are available.

Each CIS data file was converted from its native .e00 GIS format to a grid in a Lambert conformal conic projection where each grid cell was four km² (n = 99977 grid cells). Four square kilometers was chosen because it is small enough to adequately capture coastlines and polygon edges without losing valid near-shore ice data but still allowed for manageable data volumes. Sea ice concentration (in tenths) for each stage of development was extracted.

Mean summer sea ice concentration for each grid cell was calculated by averaging all digital ice chart data for July, August and September (JAS) in each year. Mean winter sea ice concentration for each grid cell was calculated by averaging all CIS chart data for each grid cell in January, February and March (JFM) in each year. It is possible for the monthly winter CIS dataset to have misrepresented the presence of dynamic features within the study area such as leads. However, independent analysis using daily PMW data indicates that lead areas in the region

are persistent both within the winter season and inter-annually (*Barber and Hanesiak, 2004*), making us confident that the monthly charts represent average winter conditions in the region. The mean statistic was used because the CIS dataset contains sea ice concentration in decimal-tenths (i.e. 0.3 tenths, 0.6 tenths, which convey trace concentrations and 9.7 tenths, which describes very high concentration sea ice which is typically not landfast).

To determine the trend in sea ice concentration for each ice type in summer and winter, a least squares linear regression was calculated for the concentration at each grid cell over the 25-year period (*Parkinson et al., 1999*), where the slope of the regression indicates the trend (%/year) for each ice type. Although we explored various non-linear models in the regression analysis, an examination of the residual plots from the linear model appeared to be uniformly distributed through the range of the models. Therefore the linear model was judged most statistically appropriate for the trend analysis performed. For each trend at each grid cell, an F-test ($df = 23$) was used to test the null hypothesis of slope = 0. We rejected the null hypothesis for all those grid cells containing trends with statistical significance greater than 90%, mapping only those trends which are significant at the 90, 95 and 99% level.

Temporal variability in the onset of break-up and freeze-up was examined by identifying the year-week (YW) for each grid cell when total ice concentration reached thresholds used by *Hammill (1987)*. The start of break-up was defined as the YW when sea ice concentration decreased to $\leq 80\%$ and continued until the cell contained $\leq 20\%$ sea ice. Freeze-up began when the grid cell contained $\geq 20\%$ sea ice and was completed when the cell contained $\geq 80\%$ sea ice. Advection of large

floes from the Beaufort Sea into the Amundsen Gulf during summer can introduce short-term increases in total ice concentration above 20% during summer, so freeze-up onset was further constrained temporally, occurring no earlier than YW 33 (third week in August).

Finally, Amundsen Gulf was defined by a north-south line between Cape Bathurst and Cape Kellett (*after Kwok, 2006*) and all grid cells were averaged to produce one value of sea ice concentration for the gulf (Figure 5.1). This was done so direct comparisons of inter-annual variability and trends in the timing and duration of break-up and freeze-up could be made with data from *Hammill (1987)*.

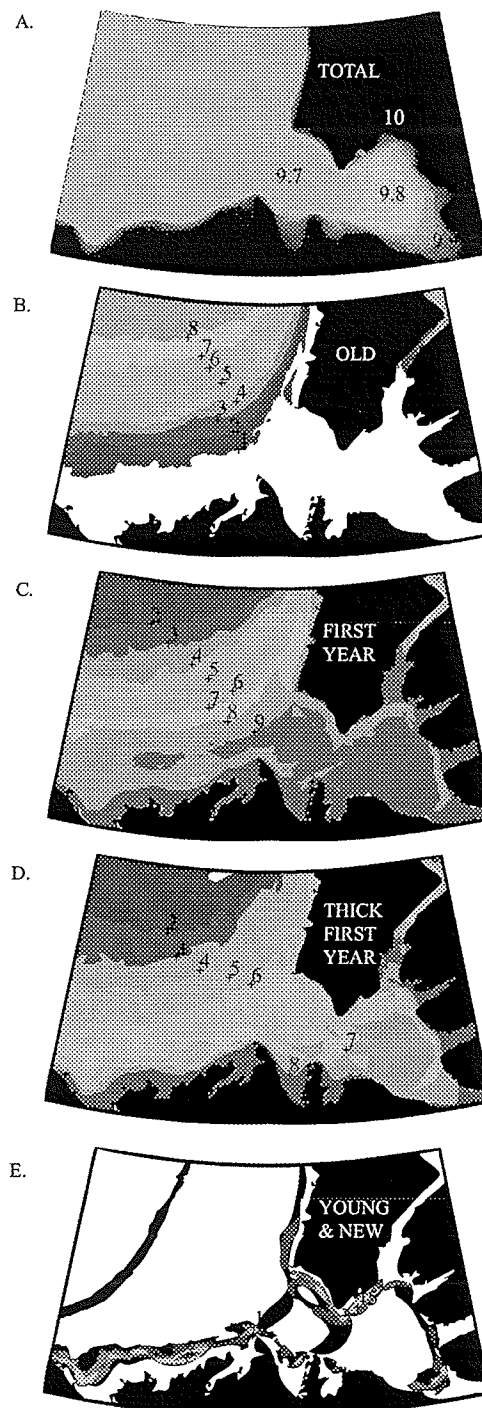
3. Sea ice climatology and trends

3.1. Sea ice in the southern Beaufort Sea and Amundsen Gulf

3.1.1. Winter sea ice climatology: 1980-2004

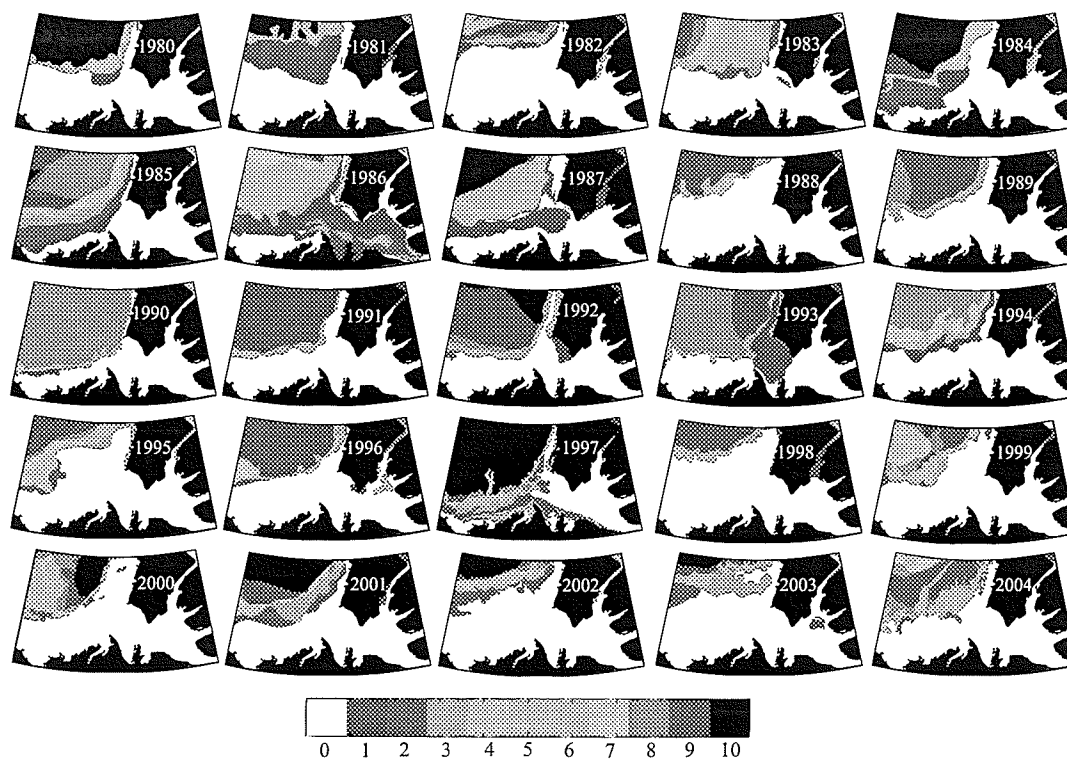
During the winter months (JFM), the mean total sea ice coverage over the study region is $3.9 \times 10^5 \text{ km}^2$ (~98%). The average winter area not covered by sea ice is 8900 km^2 (~2%). The region contains near-complete winter sea ice cover in each of the 25 years studied here. On average, three sea ice regimes are observed (Figure 5.2a); (1) A landfast (10/10ths) sea ice fringe in dark red, (2) a high concentration mobile ice area in eastern Amundsen Gulf shown in yellow, and (3) a lower concentration mobile sea ice zone in the southern Beaufort Sea and western Amundsen Gulf shown in light blue.

Figure 5.2. Average winter sea ice concentration by type between 1980 and 2004 (a) total sea ice, (b) old sea ice, (c) first year, (d) thick first year, (e) young and new sea ice.



The average winter old ice coverage in the study region is $1.4 \times 10^5 \text{ km}^2$ (~36%) within its average winter position (Figure 5.2b). Old sea ice is located offshore west of Banks Island and north of Cape Kellett. Old sea ice concentration increases from 2/10ths moving northwest as the central Arctic perennial pack is approached and the old ice concentration becomes 8-9/10ths (Figure 5.2b). Inter-annually, old ice concentration in the region is variable. The presence of old ice in Amundsen Gulf during winter has occurred 5 times (1986, 1987, 1992, 1993, 1997) (Figure 5.3).

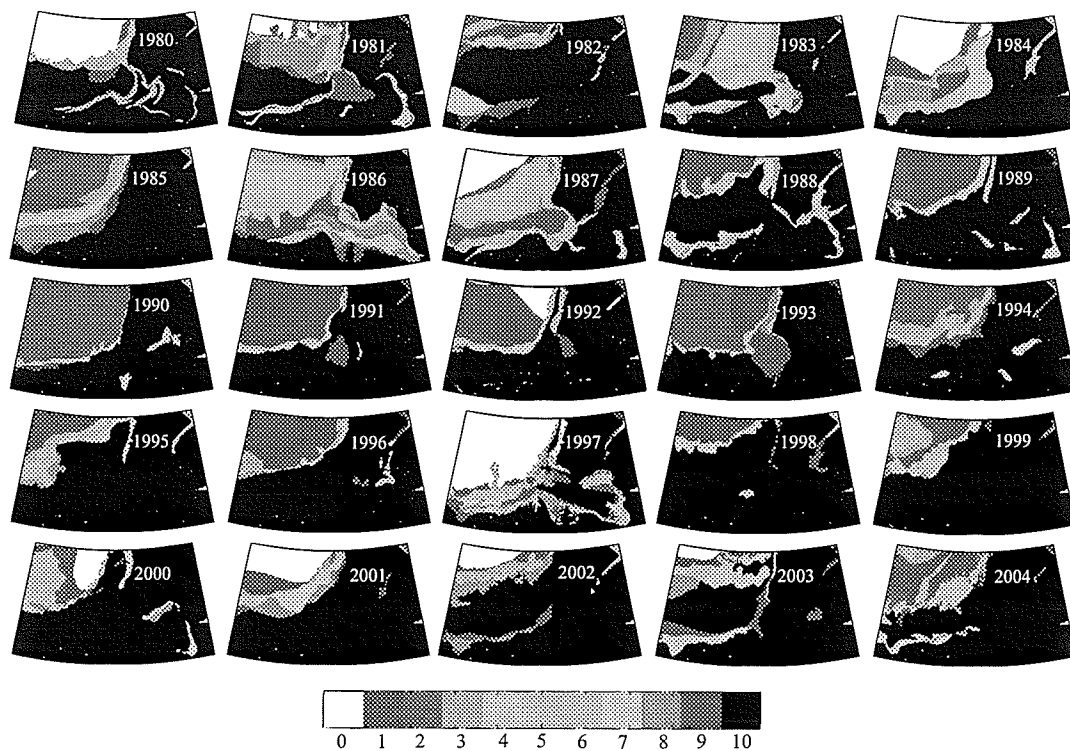
Figure 5.3. Average winter old sea ice concentration by year from 1980 to 2004



Four of these occurrences (1986, 1987, 1993, 1997) are associated with a reduction of winter old ice concentration within the Arctic pack, while in 1992 an area of 1/10 old ice occurred in Thesiger Bay while the old ice concentration in the Beaufort Sea remained high (9/10ths).

The study area is $\sim 62\%$ ($2.5 \times 10^5 \text{ km}^2$) covered by seasonal sea ice (first year, young and new ice) in winter on average (Figures 5.2c, d, e). First year sea ice occurs within the near shore regions of the southern Beaufort Sea, and within Amundsen Gulf (Figure 5.2c, 5.4) where old ice concentrations are very low.

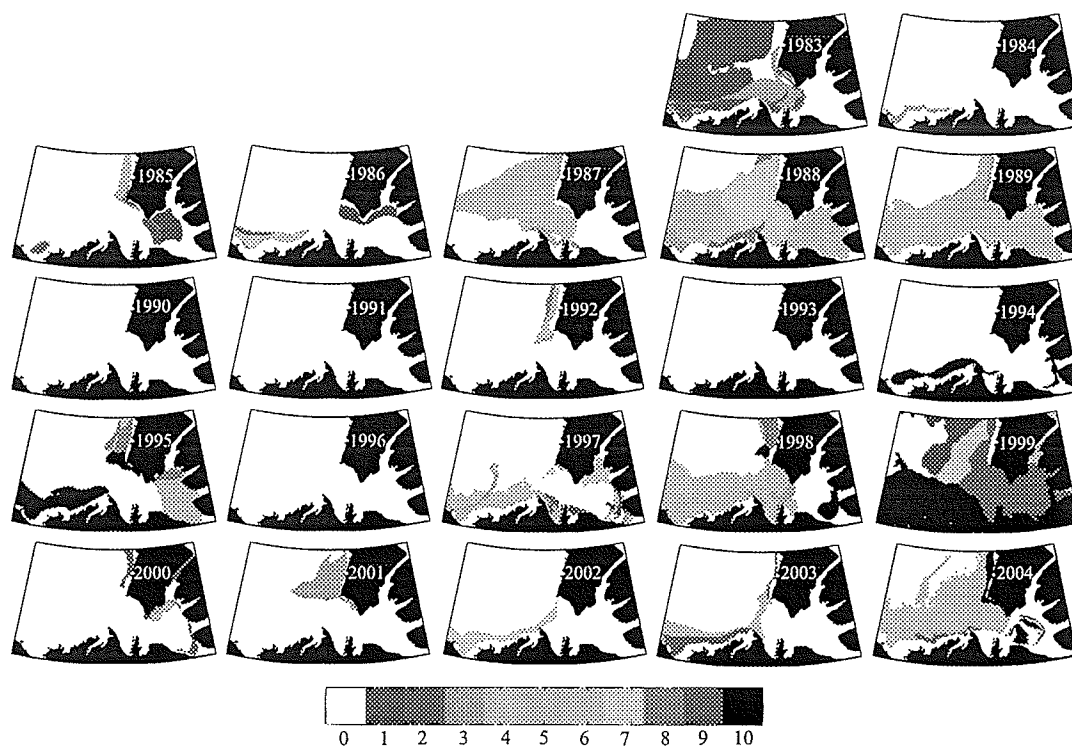
Figure 5.4. Average winter first year sea ice concentration by year from 1980 to 2004



The average annual sea ice exchange between Amundsen Gulf and the Beaufort Sea was 85000 km² to the Beaufort Sea, predominantly in fall and winter (*Kwok, 2006*). The sea ice motion responsible for this export in fall and winter creates variability in sea ice stage of development within the seasonal sea ice zone as leads continually open and re-freeze. In winter, substantial amounts of thin first year, young and new sea ice are present on average during winter (Figures 5.2e, 5.5, 5.6), between the landfast ice edge and areas of thick first year ice within Amundsen Gulf (Figures 5.2d).

First year sea ice concentration and extent is inter-annually variable along the west coast of Banks Island and in Amundsen Gulf (Figure 5.4). The position of the flaw lead system is denoted by new and young ice (Figure 5.2e, 5.6). The relative degree to which the flaw lead forms changes inter-annually, along with the relative concentrations of thin first year, young and new sea ice that reside within it.

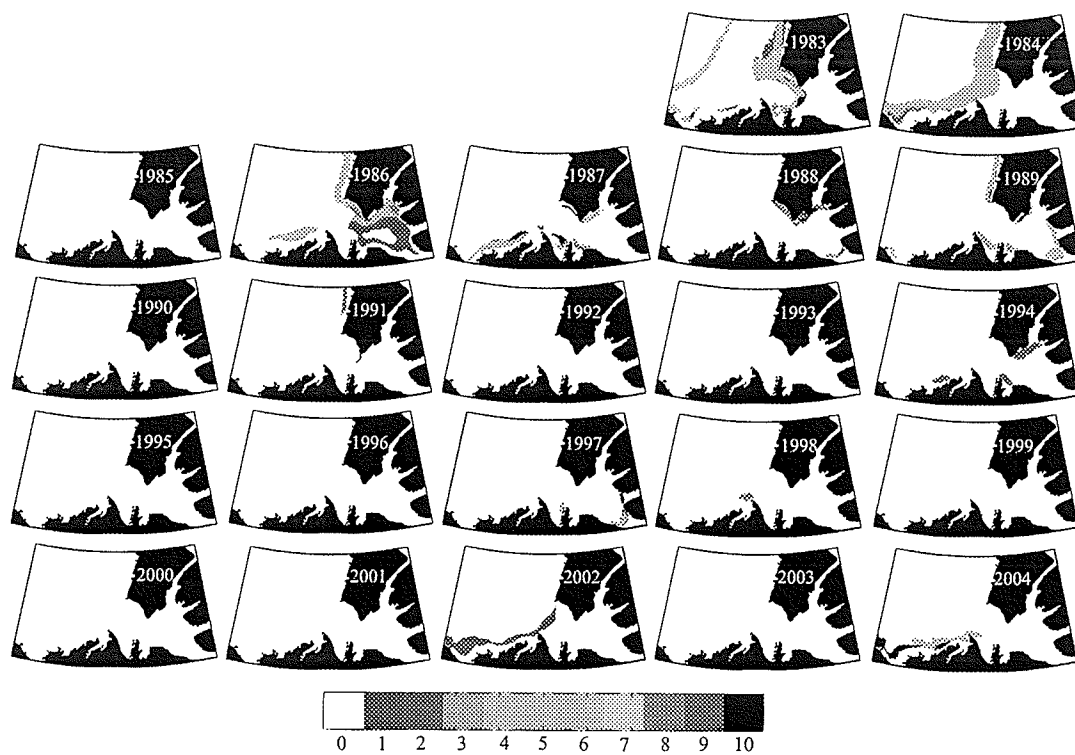
Figure 5.5. Average winter thin first year sea ice concentration by year from 1980 to 2004



Inter-annual variation of thin first year (Figure 5.5) and young and new sea ice (Figure 5.6) show the extent to which the flaw lead system forms inter-annually. The flaw lead may form off the west coast of Banks Island and the north coast of the Tuktoyaktuk Peninsula to Cape Bathurst. This occurred in 1982, 1983, 1984, 1987, 1991, 1992, 2002, and 2003. The flaw lead system occurred within Amundsen Gulf along the southeast coast of Banks Island, the west coast of Victoria Island and/or across the mouths of Franklin and Darnley Bays. This occurred in 1980, 1981, 1986, 1988, 1989, 1994, 1995, 1997, 1998, 1999 and 2000 and 2004. The study region did not contain any thin first year, young or new sea ice in 1993 or 1996 in winter

(Figures 5.5, 5.6). Ten of the twenty-five years contain evidence of reduced ice thickness or concentration between Cape Lambton and Cape Parry. Seven of those ten years occurred in the 1980's (1980, 1981, 1983, 1985, 1986, 1987, 1988) while only 1995, 1998 and 2004 contain this feature since 1988. This suggests that the nature of the flaw lead system in the region may have changed since the late 80's.

Figure 5.6. Average winter young and new sea ice concentration by year from 1980 to 2004



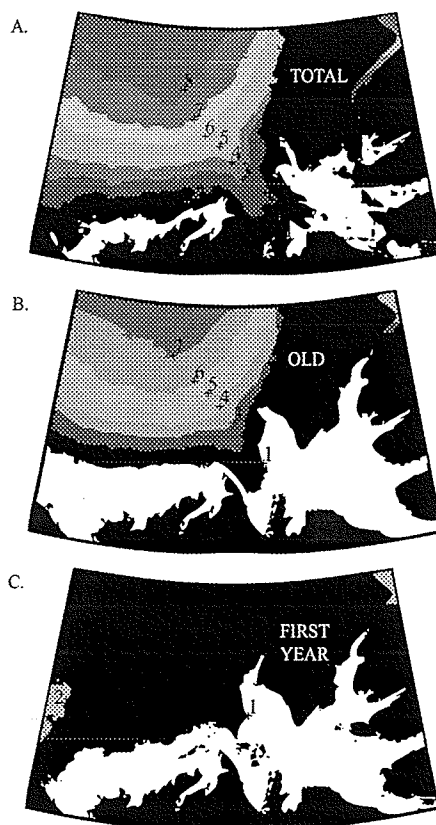
In winter, new, young and thin first year sea ice types account for 2-9/10ths of the total sea ice concentration in the near-shore regions of Amundsen Gulf, along the west coast of Banks Island and the Tuktoyaktuk Peninsula. Western Amundsen Gulf

between Thesiger Bay and Franklin Bay also contains substantial new and young sea ice on average (Figure 5.2e). The flaw lead areas may not necessarily be an area of reduced ice concentration (Figure 5.2a) but may be an area of reduced ice thickness, containing a substantial amount of thin first year and young sea ice (Figure 5.6).

3.1.2. Summer sea ice climatology: 1980-2004

The mean summer sea ice area in the study region is $1.8 \times 10^5 \text{ km}^2$ (~46%); the average summer open water area is $2.2 \times 10^5 \text{ km}^2$ (~54%).

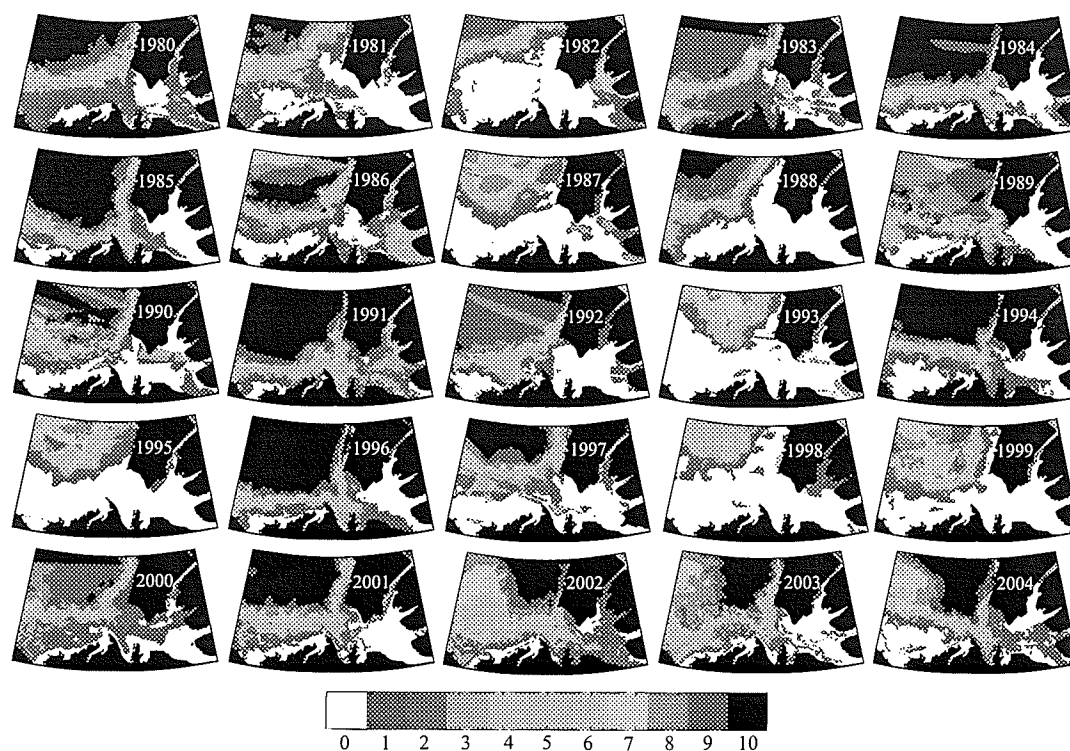
Figure 5.7. Average summer sea ice concentration by type between 1980 and 2004 (a) total sea ice, (b) old sea ice, and (c) first-year sea ice



In summer, total sea ice concentration increases from 1 to 2/10ths at the mouth of Amundsen Gulf moving northwest toward the perennial Arctic pack. Much of eastern Amundsen Gulf is ice-free (Figures 5.7a, 5.8), but a tongue of 1 to 2/10ths sea ice reaches from the diffuse edge of the summer pack into Amundsen Gulf and south into Franklin Bay on average (Figure 5.7a). The continental shelf north of the Tuktoyaktuk Peninsula and across the mouth of Liverpool Bay are also ice-free on average (Figure 5.7a).

Almost all of the summer sea ice in the region is composed of old (78%) and thick first year (20%) sea ice on average (Figures 5.7b, 5.7c). Where the total sea ice concentration is $\leq 2/10$ ths (Figure 5.7a), about half is old ice (Figure 5.7b) and half is thick first year (Figure 5.7c). Northwest of the 2/10ths total sea ice concentration contour (Figure 5.7a) the total concentration becomes heavily dependent upon old ice (Figure 5.7b). Medium first year, thin first year, young and new ice are present only in negligible amounts ($<1/10$ th) spatially coincident with 8/10ths total sea ice. This may occur because the Arctic pack contains some open water areas allowing space for new ice production, while the ocean below is kept near freezing by the relatively high sea ice concentration and therefore high albedo. Any energy absorbed by the surface would first be used for bottom and lateral ablation of the sea ice present (Wadhams, 2000).

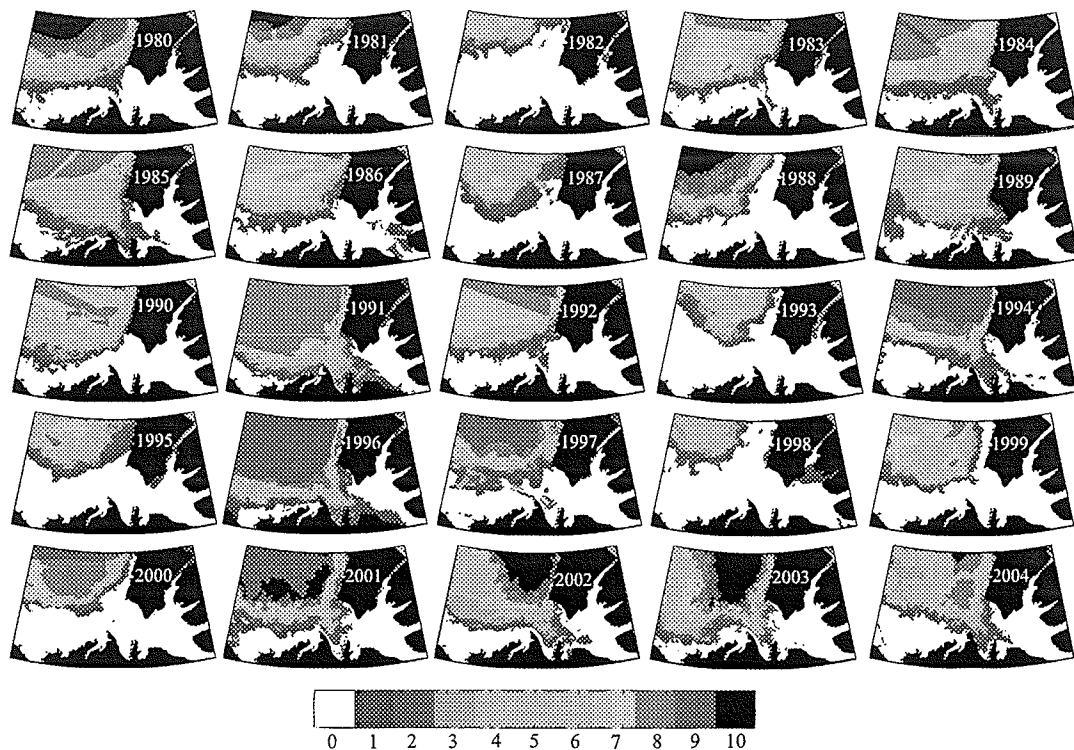
Figure 5.8. Average summer total sea ice concentration by year from 1980 to 2004



Summer sea ice concentration in the region is variable between years. In 1991, the entire area remained almost completely ice covered in summer, save for a small ice-free area along the south coast of Banks Island and north of the Tuktoyaktuk Peninsula (Figure 5.8: 1991). Other heavy sea ice years include 1986, 1989, 1994, 1996, 2000, 2001, 2002, 2003, and 2004 (Figure 5.8). The last four heavy summer ice years (2001-2004), coincide with record hemispheric scale reductions in the area occupied by the perennial Arctic pack (Serreze *et al.*, 2003; Stroeve *et al.*, 2005). The northwest quadrant of the study area is normally occupied

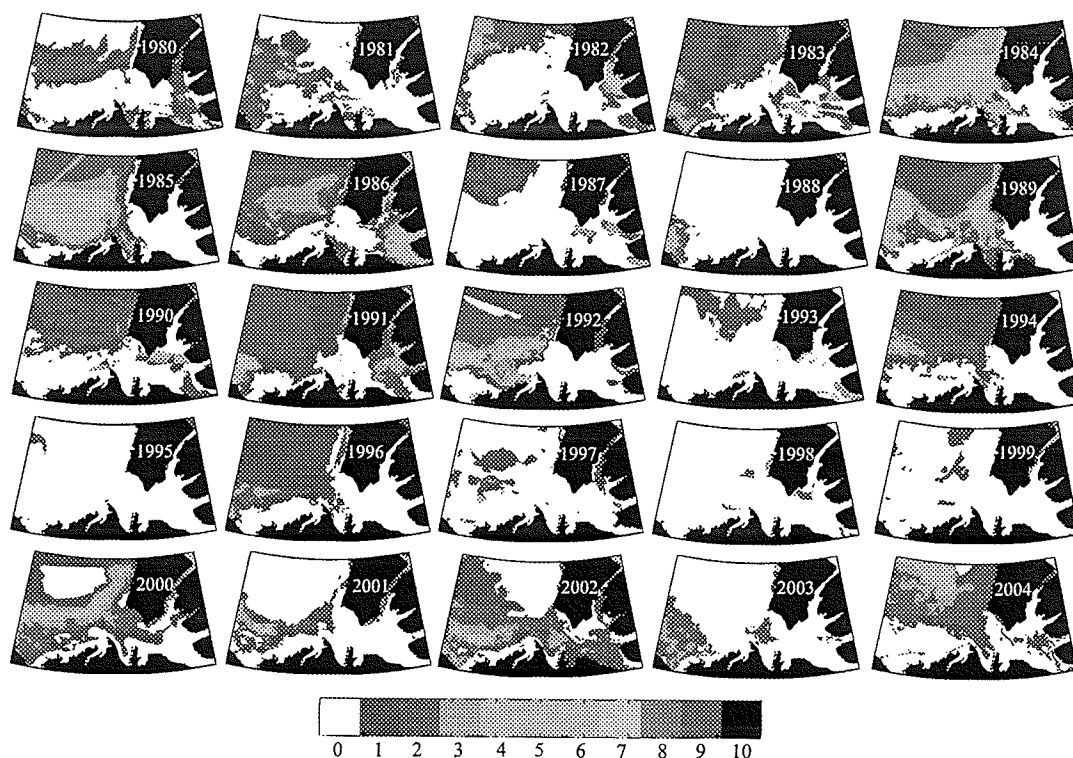
by a large area of 8-9/10ths sea ice. In 1998, the portion of the study area covered was very small and contained only $\leq 7/10$ ths sea ice concentration. Other years in which the regional ice concentration was comparatively light also occur, including 1982, 1988, 1993, 1995, 1998 and 1999 (Figure 5.8). These years are characterized by a retreat of the old ice pack to the north and northwest, leaving western Amundsen Gulf ice-free and even creating large ice-free areas along the west coast of Banks Island. Since 1998, summer sea ice in the southern Beaufort Sea and Amundsen Gulf has recovered to a degree (Figure 5.8); by 2000 the summer sea ice concentration and extent was similar to pre-1998 conditions. However, 2002, 2003 and 2004 suggest that the extent of high concentration perennial sea ice in the southern Beaufort Sea has been reduced and has shifted east toward Banks Island, leaving decreased old sea ice concentration farther west (Figures 5.8, 5.9). The total sea ice concentration in the area depends almost completely on old sea ice in each year (Figures 5.8, 5.9).

Figure 5.9. Average summer old sea ice concentration by year from 1980 to 2004



Summer first year sea ice concentration is low, and its extent is inter-annually variable (Figure 5.10). Prior to 1997 (except 1988 and 1995), first year sea ice was generally included in the old ice pack (Figures 5.9 and 5.10). However, in 1997 almost no summer first year sea ice occurred, and similar conditions prevailed during the summers of 1998 and 1999 (Figure 5.10).

Figure 5.10. Average summer first year sea ice concentration by year from 1980 to 2004



In 2000, summer first year sea ice recovered somewhat but was not spatially coincident with the old ice pack; rather it occurred to the east and south of the old ice (Figure 5.9, 5.10). The same conditions prevailed in 2001, 2002, 2003, before the summer first year sea ice was again collocated with the old ice pack in 2004. It appears that low summer sea ice concentration and extent in 1997, 1998 and 1999 created a situation where the old ice and first year sea ice became spatially disconnected for several years. Reductions in the summer old sea ice extent (Figure 5.9: 1998, 1999, 2000) forced increased first year sea ice extent in winter (Figure 5.4: 1998, 1999, 2000, 2002, 2003) in order to completely cover the region in ice.

The remnants of high winter first year ice concentrations can be seen in the summer data (Figure 5.10: 2000, 2001, 2002 2003). By 2004, summer old and first year sea ice had become spatially coincident similar to pre-1997 conditions but first year sea ice replaced old ice in the west (Figures 5.9, 5.10) while lower concentrations of first year sea ice were present in the edge of the perennial pack (Figure 5.10).

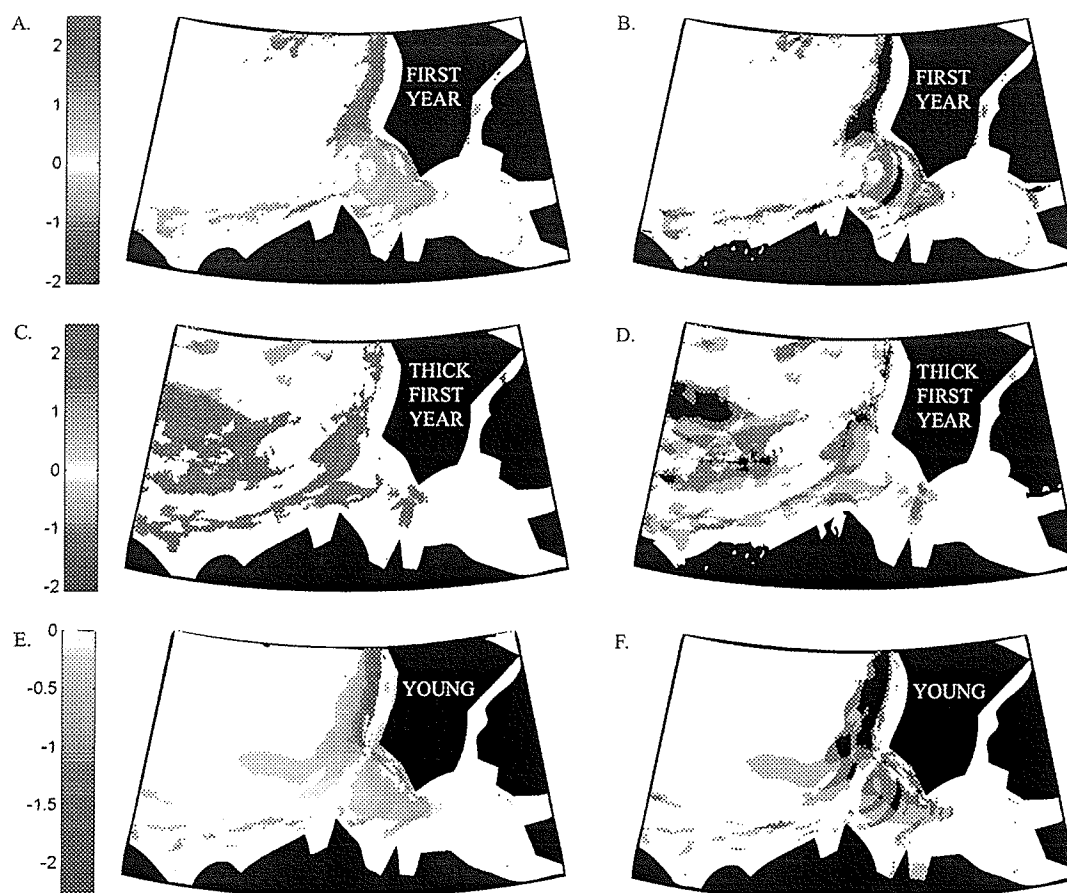
This shift in the location of seasonal and perennial sea ice gives us insight into how the ice regime will potentially operate in times of reduced or eliminated summer old ice (i.e. Holland et al., 2006). It appears that under current climatic conditions, seasonal sea ice extent and concentration will increase to make up for the perennial ice loss. This has already been shown to impact the formation of the annually recurrent flaw lead system. In years when the perennial ice pack retreats to the northwest, seasonal sea ice is allowed to grow thicker in a greater portion of the region. This is due to reduction in dynamic processes within the ice field, normally caused by the Arctic pack moving against the landfast ice fringe. The seasonal sea ice is larger, thicker and less affect by any connection to the Arctic ice pack, devolving the flaw lead system.

3.2. Sea ice concentration trends

3.2.1. Winter trends in sea ice concentration: 1980-2004

Winter total sea ice concentration shows no trend because the region is near-completely ice covered each year. Statistically significant trends in winter first year, thick first year and young ice have occurred (Figure 5.11).

Figure 5.11. Winter sea ice concentration trend (%/year) in the left column and statistical significance in the right column for (a, b) old sea ice, (c, d) first year, (e, f) thick first year, (g, h) young sea ice. Black areas in the right column indicate statistical significance at the 99% level, dark grey areas indicate statistical significance at the 95% level and light grey areas indicate statistical significance at the 90% level



Winter first year sea ice showed an increasing trend of 1 to 2.5%/year west of Banks Island, within western Amundsen Gulf, across the Tuktoyaktuk Peninsula and along the west coast of Victoria Island (Figure 5.11a). The statistical significance of these trends is shown at three levels (90%, 95%, and 99%) in Figure 5.11b. The most dramatic increasing trend (>2%/year) in first year ice occurred immediately

west of Banks Island is statistically significant at the 99% level (Figure 5.11b). This area is part of the flaw lead system on average, containing 5 to 6/10ths new and young sea ice in winter (Figure 5.2e). A similar positive trend also occurred north of the Tuktoyaktuk Peninsula that contains 4-5/10ths new and young sea ice on average (Figure 5.2e) significant at the 95% level (Figure 5.11b). In much of western Amundsen Gulf, increasing trends in winter first year sea ice occur (Figure 5.11a) where on average 1 to 3/10ths new and young sea ice occur in winter (Figure 5.2e). Positive trends in first year sea ice concentration in western Amundsen Gulf are statistically significant at the 95% level (Figure 5.11b). The west coast of Victoria Island also contains a positive trend in first year sea ice concentration (Figure 5.11a) significant at the 95% level (Figure 5.11b). First year sea ice concentration has been increasing in the flaw lead system between 1980 and 2004.

It follows that trends in thick first year sea ice concentration have also occurred (Figure 5.11c). The largest changes (2.5%/year) occurred in the flaw lead area west of Banks Island, north of the Tuktoyaktuk Peninsula and within the southern Beaufort Sea across the mouth of Amundsen Gulf (Figure 5.11c). There is a trend toward more first year ice in the flaw lead system, with much of it growing quite thick over the winter. There is also a trend toward more thick first year sea ice in the western part of the study area, making up for losses in perennial sea ice in the same area.

In the flaw lead system, thicker sea ice showed increasing trends and young sea ice concentrations have decreased. The area immediately west of Banks Island which on average contains 5-6/10ths new and young sea ice (Figure 5.2e)

experienced young ice loss at the rate of $>1.5\%/year$ (Figure 5.11e) which is significant at the 99% level (Figure 5.11f). Smaller negative trends in young sea ice ($0.5-1.5\%/year$) occurred parallel to the Tuktoyaktuk Peninsula, within western Amundsen Gulf, and extending west from the mouth of Amundsen Gulf (Figure 5.11e). The trends in most of these areas are significant at the 95% level (Figure 5.11f).

3.2.2. Summer trend in sea ice concentrations: 1980-2004

A positive trend in summer old sea ice concentration (1 to $2\%/year$) is observed west of Banks Island reaching into the mouth of Amundsen Gulf (Figure 5.12a). This area is composed of 2 to 5/10ths total summer sea ice on average, where the total summer sea ice is comprised of equal parts old ice and thick first year sea ice (Figure 5.7a-c). The trends are significant at the 95% level (Figure 5.12b). A statistically significant (95%) positive old ice trend in the flaw lead area west of Banks Island also occurred.

Figure 5.12. Summer sea ice concentration trend (%/year) in the left column and statistical significance in the right column for (a, b) old sea ice and (c, d) first year sea ice. Black areas in the right column indicate statistical significance at the 99% level, dark grey areas indicate statistical significance at the 95% level and light grey areas indicate statistical significance at the 90% level.



Significant trends in first year summer sea ice were exclusively negative (Figure 5.12c), occurring within an area occupied by 6 to 8/10ths total summer ice concentration (Figure 5.7). Small areas of significant first year sea ice reduction also occurred in eastern Amundsen Gulf.

3.3. Discussion – Sea ice concentration trends

3.3.1. Winter trends in sea ice concentration: 1980-2004

Recently, the Beaufort Sea perennial pack has undergone a change in the types of ice which make it up; perennial ice has replaced by seasonal ice in winter (Figure 5.4: 2002, 2003, 2004). The extent of perennial sea ice cover in the Arctic

has been decreasing annually while the sea ice that remains is getting younger and thinner (*Maslanik et al.* 2007). This transition from thick old sea ice to thinner old ice or seasonal ice has been attributed to (1) atmospheric-forced sea ice divergence and/or (2) thermodynamic loss.

Atmospheric-forced divergence reduces sea ice concentration in the periphery of the old ice pack enhancing melt through the ice-albedo feedback mechanism. *Yu et al.* (2004) showed increased fractional open-water and first-year ice areas in the central Arctic Basin between the 1960's and the middle 1990's, balanced by an 11% reduction in level-multiyear and ridged ice thicker than 2.0m. They attributed these changes in ice mass balance to increased export through Fram Strait in the late 1980's and early 1990's driven by variability in the North Atlantic Oscillation (NAO) and Arctic Oscillation (AO), and to changes in thermal forcing (*Yu et al.*, 2004). As the AO index becomes increasingly positive the resulting surface level pressure pattern leads to divergent ice motion within the southern Beaufort Sea as well as positive surface air temperature anomalies, resulting in thinner than normal spring sea ice conditions (*Rigor et al.*, 2002). *Rothrock et al.*, (1999) note that the mean draft of perennial sea ice in the Arctic Ocean decreased by 1.3m (~40%) between the 1990s and data acquired between 1958 and 1976, with mean draft decreases of about 1m in the Beaufort Sea. This resulted from thinning of perennial sea ice in the Arctic Ocean as a whole and not advection of thinner stages of development from one region to another (*Rothrock et al.*, 1999).

The transition from thinner (new, young and thin first year) to thicker first year ice was observed within the seasonal ice zone, especially in the flaw lead

system. In the absence of a decreasing trend in winter air temperatures (*Howell et al., 2007*) the increasing trend of thick first year ice west of Banks Island may be attributed to the reduction in old ice concentration allowing seasonal sea ice in these areas to grow thicker. First sea ice has been replacing young ice in winter in the flaw lead system (Figure 5.11a, c, e).

3.3.2. Summer trends in sea ice concentrations: 1980-2004

The increasing trend in old sea ice (~ 1 to $2.5\%/year$) west of Banks Island (Figure 5.12a) is likely due to increased cyclonic motion and therefore divergence. Very high old ice concentration ($>9/10$ ths) areas in the northwest may be losing ice to the 7 and $8/10$ ths old ice areas, increasing their concentration. These trends in summer old ice concentration can be attributed to differential reduction in perennial sea ice between the eastern to western Arctic (divided by 0° and 180° longitude) (*Nghiem et al., 2006*). Nghiem et al. (2006) showed the east Arctic Ocean lost 48% of its perennial sea ice between consecutive Decembers (2004 and 2005), while the west Arctic Ocean gained 0.95×10^6 km² perennial sea ice over the same period, replacing seasonal ice. Further, recent research has shown that summer cyclonic motion in the pack creating divergence is occurring with greater frequency (*Lukovich and Barber, 2006*), resulting in more old ice being dynamically driven toward Amundsen Gulf in the summer, causing an increase in the old ice concentration near the mouth of Amundsen Gulf. Decreasing summer first year ice trends in the region (Figure 5.12c) maybe attributed to enhanced melt in summer due to divergence in the pack allowing the ice-albedo feedback to take affect.

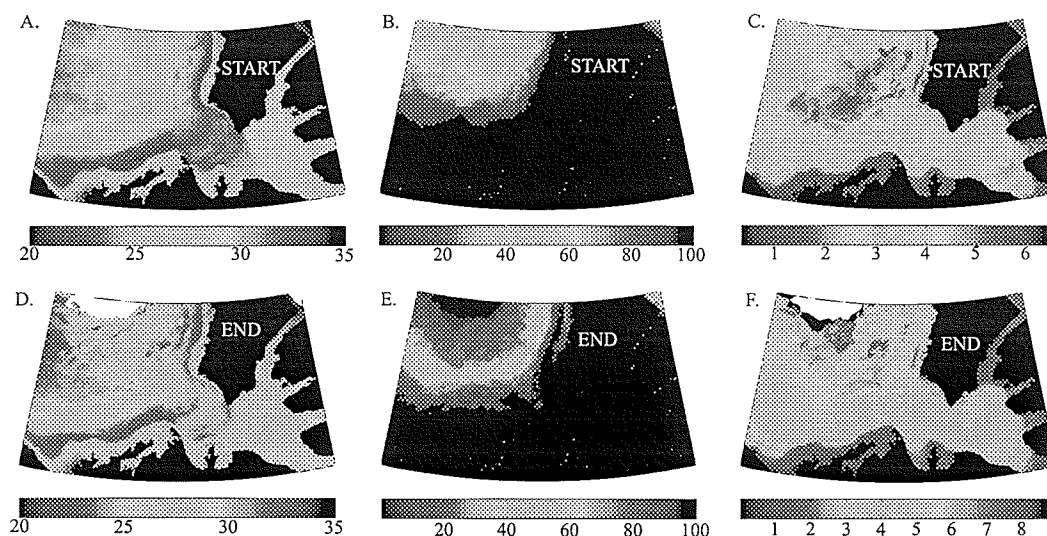
The yearly minimum extent of perennial sea ice in the Arctic has been declining since the start of the passive microwave record at a rate of between 3 and 7% per decade, depending on the years studied (*Parkinson et al.* 1999, *Comiso*, 2002, *Serreze et al.*, 2003, *Stroeve et al.*, 2005). Our work demonstrates that statistically significant (>95%) trends in summer old ice in the southern Beaufort Sea have increased despite hemispheric losses. first year sea ice occurred between 1980 and 2004, and further that summer losses of first year ice have also occurred.

4. Break-up and freeze-up within the southern Beaufort Sea and Amundsen Gulf

4.1. Average break up

As a result of the high old ice concentration in some areas, break up does not always occur in all grid cells (Figure 5.13b,d). In this discussion, we consider only those grid cells which break up each year (100% occurrence) (Figure 5.13b, d). On average, the flaw lead area north of the Tuktoyaktuk Peninsula and west of Banks Island, joined across the mouth of Amundsen Gulf begin to break up first around YW 21 (Figure 5.13a: *shown in dark blue*). Western Amundsen Gulf begins to break up between YW 22 and YW 24 (Figure 5.13a). Eastern Amundsen Gulf begins breaking up after YW 25 (Figure 5.13a: *shown in light blue*). Finally, the landfast sea ice in the region begins to break up around YW 30.

Figure 5.13. Mean break-up (a) start year-week (b) start occurrence (%), (c) start mean standard deviation (weeks), (d) end year-week (e) end occurrence (%) and (f) end mean standard deviation (weeks) for each grid cell between 1980 and 2004. Occurrence is defined as the amount of times each grid cell began to break up or finished breaking up in 25 years, expressed as a percent.



Break-up within the flaw lead system and across the mouth of Amundsen Gulf takes 1-2 weeks (Figure 5.13a, d). Eastern Amundsen Gulf finishes breaking up around YW 28 on average and finally the landfast ice in the region finishes breaking up after YW 30. This substantial reduction in concentration in the region over 1-2 weeks is due to the relative thinness of sea ice in the flaw lead area in winter allowing thermodynamic weakening to occur more easily than in the surrounding thick sea ice. This thin, weak sea ice is then advected away from the area in as little as a few days. Our results are similar to those of *Hammill (1987)*, who concluded that the ice retreat pattern in the region was related to the locations of atmospheric pressure patterns in the area.

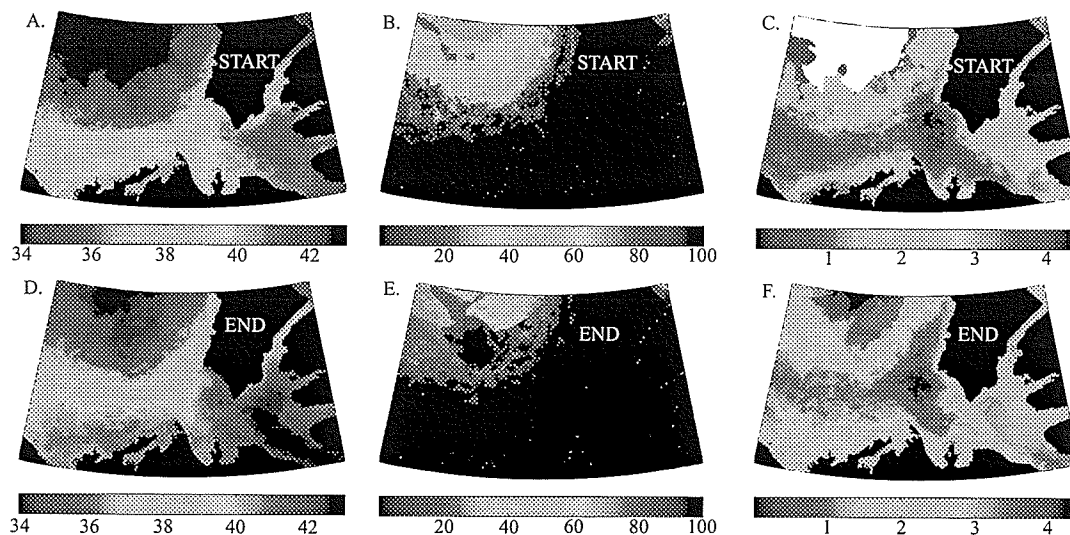
While a broad expanse of open water (the "Cape Bathurst Polynya") occurred between Thesiger Bay and Franklin Bay occurred in 15 of 25 years, several occurrences of what *Hammill* (1987) termed an "eastern polynya" were found in our time series. Like the formation of the Cape Bathurst Polynya, the location of the eastern polynya was always determined by where the mobile pack edge met landfast ice. In 1981, 1994, 1996, and 1999, the mobile pack edge reached deep into the gulf, so that a large open water area formed near Victoria Island. In other years, the primary open water area was a shore lead extending eastward from Cape Parry. These instances were noted in 1988, 1989, 1993, and 1998. With the exception of 1998, when above-average surface air temperatures melted a thin ice cover, all other occurrences of a southern flaw lead in the gulf tended to be later in the season, forming in late May (YW20) and early-to-mid June (YW's 22-24). The remaining two years in which the first open water area did not occur in Amundsen Gulf were 1992 and 2000, when the Mackenzie River shelf was the primary source of break-up and open water. In both cases, these were late melt-onset years, occurring in mid-June (YW 25).

4.2. Average freeze up

In the seasonal ice zone, the mean freeze up start year-week varies from YW 37 off-shore of the Tuktoyaktuk Peninsula and in Franklin Bay to YW 41 nearby Victoria Island (Figure 5.14a). Our analysis shows that the first areas to freeze are those with some sea ice (about half old ice and half thick first year) in summer (Figure 5.7). Areas covered by less sea ice in summer develop an ice cover later. Eastern Amundsen Gulf

contains only trace concentrations of sea ice in summer, and are the last to begin to freeze up. Sea ice present at the end of summer can cause the ocean below to be cooler because it increases the albedo of the surface, decreasing the amount of energy the ocean can absorb. If sea ice is already present even in very low concentrations, it acts as a congelation agent for sea ice growth. Both factors lessen the oceanic heat available to reduce sea ice growth, causing the near-surface ocean column to approach its freezing point more quickly than if sea ice was not present (Wadhams, 2000).

Figure 5.14. Mean freeze-up (a) start year-week (b) start occurrence (%), (c) start mean standard deviation (weeks), (d) end year-week (e) end occurrence (%) and (f) end mean standard deviation (weeks) for each grid cell between 1980 and 2004. Occurrence is defined as the amount of times each grid cell began to freeze up or finished freezing up in 25 years, expressed as a percent.

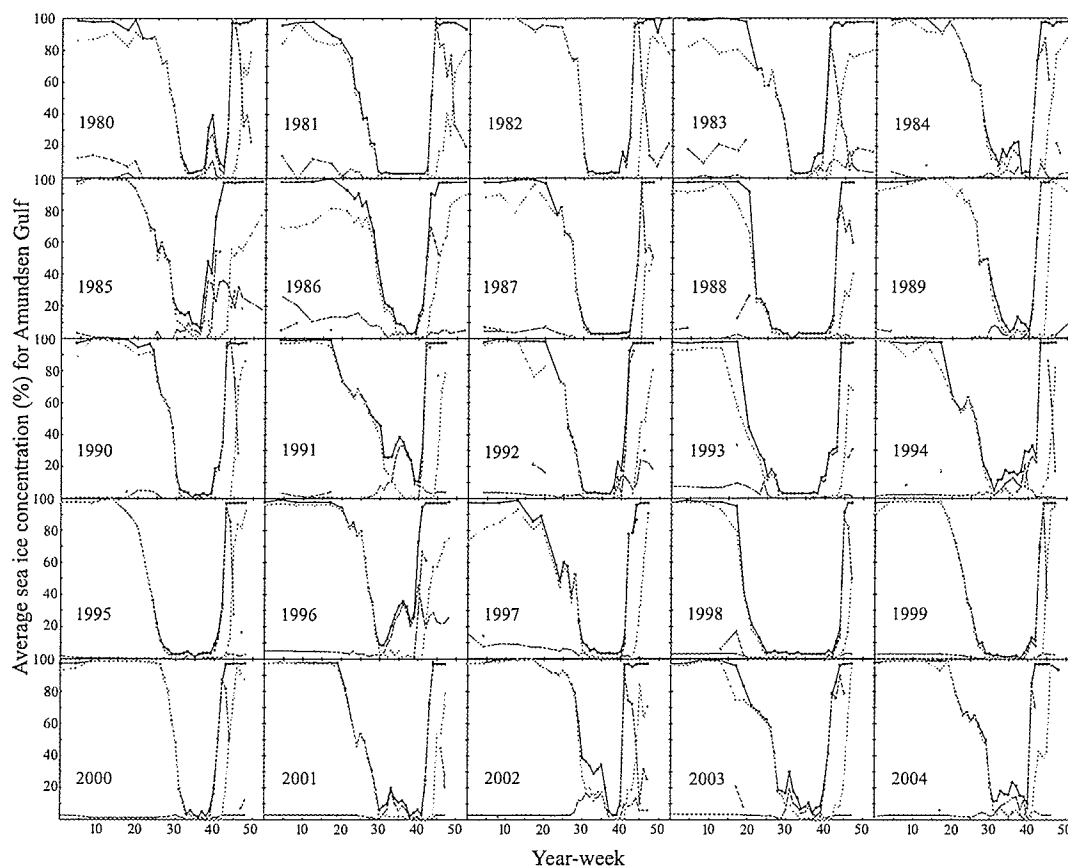


The region freezes up very quickly (Figure 5.14a,d). The average duration of freeze-up within the seasonal ice zone is 1-2 weeks. The atmosphere, ocean and sea ice

regime seem to meet a threshold time in the year, between YW 38 and 41 (~23 Sep to ~14 Oct), where the atmospheric temperature is sufficiently low, the near-surface ocean column reaches its freezing point and there is some small concentration of sea ice in the region to kick-start ice growth.

5. Break-up and freeze-up timing and duration in Amundsen Gulf

Figure 5.15. Sea ice concentration in Amundsen Gulf averaged over all grid cells for each year studied by year-week. Total (black), old (blue), first year (green), new & young (red).



5.1. Break-up variability

Duration of break-up in the seasonal ice zone showed a much greater variability than that of freeze-up (Figure 5.15). *Hammill* (1987) indicates that between 1964-1974, sea ice break-up was almost evenly divided between early, medium, and late years; if open water occurred in July, it was an early break up year; if in August, a medium, and in September, a late break up year. The sea ice concentration curves for 1980-2004 (Figure 5.15) show that there has been a substantial shift towards earlier break-up since 1964-1974. The average break-up start week between 1980 and 2004 was YW22, seven weeks earlier than the earliest break-up start found by *Hammill* (1987). The range of break up start between 1980 and 2004 was broad, with the earliest occurring at week 18 in 1991, 1993, 1994, and 1998. The latest break up start was recorded in 2000, at week 29, which corresponds to the week of early break up for 1964-1974 (*Hammill*, 1987).

Each break-up over the 25-year time series is summarized in Table 1. When the whole of Amundsen Gulf is examined, the average break-up lasted more than 8 weeks, which is almost 2 weeks longer than between 1964-1974 (*Hammill*, 1987). The longest break-up duration (22 weeks) occurred in 1991. 1991 was particularly anomalous as the open water duration was only one week as a result of old ice influx into Amundsen Gulf in summer. The year in which break-up occurred most rapidly was 2000, taking only 3 weeks. However, this was also the latest year for break-up start, allowing thermodynamic melt to thin and weaken the sea ice in Amundsen Gulf. It was also a low sea ice extent in the Beaufort Gyre (*Serreze et al.*, 2003), which created a larger than average seasonal ice zone (Figure 5.9).

The slope of the total sea ice concentration curve through time in spring is indicative of break-up processes (Table 5.1). Smaller negative slopes indicate gradual, melt and/or restriction of clearing the Amundsen Gulf due to exchanges of old ice with the Beaufort Gyre. Floes from the gyre may enter the gulf, effectively blocking the exit of sea ice through the mouth of Amundsen Gulf. Larger negative slopes characterize years where ice is advected out of Amundsen Gulf quickly. The year with the largest negative slope was 2000, when ice was removed from the gulf within 3 weeks. Other years with large negative slopes include the El Nino years 1982, 1987-1988, 1993, and 1996, as well as 1998, when anomalous warming characterized the entire Canadian Archipelago. The smallest negative slope was in 1991, when open water duration was brief, and in 1985 and 1994 (Table 5.1).

Table 5.1. Year week in each year where the average total sea ice concentration in Amundsen Gulf reaches spring break-up, the open water (OW) season and fall freeze-up. The slopes of the total concentration curves (Figure 15) are shown for break-up and freeze-up.

Year	<80%	start OW	length OW	end OW	>80%	Break-up Slope	Freeze-up Slope
1980	26	31	6	37	44	-11.23	44.8
1981	22	29	13	42	44	-8.24	45.89
1982	26	30	11	41	43	-14.53	42.15
1983	22	31	8	39	41	-7.78	39.22
1984	23	30	10	40	43	-7.99	31.2
1985	22	30	6	36	41	-6.85	15.93
1986	27	32	9	41	43	-10.83	34.9
1987	23	29	13	42	45	-12.48	30.98
1988	22	25	17	42	44	-15.14	41.53
1989	25	32	8	40	43	-8.17	30.9
1990	25	30	11	41	43	-13.08	25.53
1991	20	39	1	40	42	-3.99	43.35
1992	24	29	11	40	42	-9.11	21.37
1993	20	25	15	40	44	-10.51	20.76
1994	20	29	9	38	43	-6.69	16.03
1995	23	26	15	41	43	-11.71	40.45
1996	24	29	4	33	41	-11.49	9.08
1997	23	30	11	41	44	-7.17	27.5
1998	19	23	21	44	45	-13.67	72.28
1999	21	26	16	42	44	-9.78	42.55
2000	29	31	9	40	42	-20.3	32.67
2001	24	29	12	41	44	-7.82	31.22
2002	28	36	4	40	41	-7.2	84.83
2003	21	28	11	39	43	-7.17	19.29
2004	21	31	9	40	41	-7.29	74.67
AVG	23	30	10	40	43	-10	36

Break up timing is highly variable between years, controlled in part by the position of the Beaufort Sea ice pack in winter and spring. In order for break up to occur in Amundsen Gulf, the sea ice has to be thermodynamically weak enough to be moved, and it must have an area to move to. Break up is sometimes retarded by increased concentrations of old ice and/or first year sea ice occurring at year-weeks within the break up period (Figure 5.15).

5.2. Open water

Open water was defined as the amount of time where the sea ice concentration fell below 20%. The average week in which open water occurred in Amundsen Gulf was around YW 29.6 ± 3.3 weeks between 1980 and 2004. This is 2 to 5 weeks earlier than medium ice retreat in *Hammill* (1987). The earliest occurrences of open water occurred in 1988 (YW25), 1993 (YW25), and 1998 (YW23) (mid-June). In two of the three cases (1988, 1998), the preceding re-freeze occurred relatively late (YW45), and warming associated with El Nino (in 1988) or a hemispheric anomaly (in 1998) may have contributed to the rapid ice retreat. The latest appearances of open water were observed in 1991 and 2002, at week 39 (~01 Oct) and 36 (~09 Sep), respectively (Figure 5.15). The delay in open water formation during both 1991 and 2002 was due to anomalously large influxes of old ice to Amundsen Gulf beginning on around YW28 and ending around YW38 delaying the open water season.

The duration of open water averaged 10.4 ± 4.4 weeks during 1980-2004. Using the *Hammill* (1987) medium ice breakup and medium freeze up dates as indicators of the open water duration during 1964-1974, the average length of open water for the *Hammill* (1987) dataset was about 8 weeks. Those years with the earliest break-up and latest freeze-up, corresponding to the longest open water seasons, were 1988 (16 weeks), 1998 (20 weeks), and 1999 (15 weeks). Those with the shortest ice-free duration were 1991 (1 week), 1996 (3 weeks), and 2002 (3 weeks) when old ice influx to Amundsen Gulf occurred (Figure 5.15).

5.3. Freeze-up Variability

Freeze-up in Amundsen Gulf between 1980 and 2004 was fairly consistent with the results of *Hammill* (1987), occurring over a period of about 3 weeks (Table 5.1) while medium ice advance took 2 weeks to complete between 1964 – 1974 (*Hammill*, 1987). This rapid freeze-up started on average, around YW40 and was completed by YW43 for the years 1980 – 2004. This agrees with the timing of medium ice growth conditions in *Hammill* (1987) (~YW 40 to 42). Compared to break-up there was little variability in the start of freeze-up in either the 1964-1974 (*Hammill*, 1987) or our 25-year dataset. The earliest instance of freeze-up onset occurred in 1996 on week 33, which also recorded the longest freeze-up duration (8 weeks). In all 25 years, freeze-up was complete between weeks 41-45. During 1998, 2002, and 2004, complete freeze up occurred within 1 week. These were anomalous years in terms of ice conditions in the archipelago (in 1998 due to anomalously warm surface air temperatures) or the southern Beaufort Sea (in 2002, 2004 (*Stroeve et al.*, 2005)).

Focusing on the average conditions, in which freeze-up occurred at YW 40 and was completed by YW 43, a survey of the available radiation was made. Using a mid-point within the Amundsen Gulf [70°N, 118°W] as a geographical reference, the geometry and envelope of daily radiation incident at the top of the atmosphere was calculated. During YW 38, the maximum amount of shortwave radiation at the top of the atmosphere decreases to half its summertime maximum, from 910 W/m² to 455 W/m². It is also at this time that the number of daylight hours where the sun is above the horizon, corresponding to a solar zenith angle > 90°, decreases below 12

hours. While further radiative transfer modeling is necessary to determine the actual amount of radiation reaching the surface and its role in ice re-freeze onset, these basic characteristics suggest that a radiative threshold is reached by YW 39 at this latitude and longitude.

6. Conclusions

In this study, we examined the spatial and temporal variability of various sea ice types in the Southern Beaufort Sea and Amundsen Gulf region over 1980-2004, using CIS digital ice chart data. In winter, high concentrations of mobile sea ice dominated the southern Beaufort Sea and Amundsen Gulf on average. Winter sea ice in Amundsen Gulf is almost entirely composed of seasonal ice types, which interact with the perennial sea ice in the southern Beaufort Sea to create and maintain a flaw lead system, composed of predominantly new, young, and thin first year sea ice, surrounded by mostly thick first year sea ice. The results showed significant shifts in sea ice type and therefore mass balance within the flaw lead system between perennial and annual sea ice in winter over the 25-year time series. Linear regression analysis indicated an increasing trend in thick first year sea ice in the flaw lead system. In the flaw lead system in winter, thick first year sea ice also showed a significant increasing trend, balanced by decreasing young sea ice concentrations. These shifts in sea ice type have serious implications for the presence of the flaw lead network in the region. Reduction in the persistence or extent of the flaw lead system could lead to substantial changes in the way

Amundsen Gulf breaks up in spring, reducing the biological productivity of the region and affecting the lives of the area's inhabitants.

In summer the sea ice present in the region was mainly old ice, with some thick first year sea ice; much of the southern Beaufort Sea was ice covered each year. Heavy sea ice years occurred in the 1990's and 2000's when summer sea ice extended from the southern Beaufort Sea perennial pack into Amundsen Gulf. Sea ice was present in eastern Amundsen Gulf in summer through the 1980's, and then again in 2002 and 2004. Following a massive reduction in summer sea ice extent in 1998, the region rebounded, regaining much of the summer sea ice extent which occurred prior to 1998. We found a eastward shift in the high concentration perennial pack ice within the southern Beaufort Sea toward the west coast of Banks Island. We found a trend toward increasing old ice concentration west of Banks Island, and a trend toward decreasing first year ice concentrations in the 5-8/10ths total sea ice contours. Old sea ice has reduced the amount of open water in the southern Beaufort Sea and Amundsen Gulf in summer over the 25 years studied, and the summer transition zone between open water and high concentration sea ice in the southern Beaufort Sea gained first year sea ice. This has important implications particularly for navigation of the Northwest Passage, as old sea ice may continue to block the western waterway to ship navigation.

Rapid sea ice break-up in the study area occurs dynamically; presumably after the sea ice reaches a thermodynamic threshold which weakens the ice, making it susceptible to motion. Break up begins within near shore areas of reduced ice thickness along the coast of the Tuktoyaktuk Peninsula and the west coast of Banks

Island respectively, followed by sections of Amundsen Gulf from west to east. The area covered by thin first year, young and new ice is in decline, which may reduce the ability of sea ice in the region to break up normally. Thicker sea ice is more difficult to remove dynamically and thermodynamically. Freeze-up in the seasonal ice zone is complete within 1 to 2 weeks occurring first within the seasonal to perennial ice transition zone off-shore, then in western and finally in eastern Amundsen Gulf. Additional sea ice in the region in summer may enable freeze up to happen sooner each year by keeping the ocean cooler and seeding new ice growth with ice already in the region.

The timing and duration of break-up within Amundsen Gulf is widely variable in comparison with freeze-up. The duration of break-up, open water and freeze-up depend to some degree on the presence of old sea ice within the region. Old ice influx can delay the end of break-up (and therefore the beginning of the open water season), and can also influence the timing of freeze-up in Amundsen Gulf. Break-up occurred much earlier on average during 1980-2004 than during 1964-1974.

Generally, melt began earlier, leading to a slightly longer open water season after which a rapid re-freeze covered the basin at or about the same time as in the *Hammill* (1987) dataset. Re-freeze was generally consistent between the two datasets, occurring the week following a 50% reduction in available shortwave energy at the top of the atmosphere and a reduction in daylight hours to 12 or less.

Literature Cited

- Aagard, K.L. and E.C. Carmack, 1989. The role of sea ice and other fresh water in the Arctic circulation, *J. Geophys. Res.*, 94(C10):14485-14498.
- ACIA, 2005. Future Climate Change: Modeling and Scenarios for the Arctic, Chapter 4 in *Arctic Climate Impact Assessment*, URL: www.acia.uaf.edu.
- Andreas, E.L., M.A. Lange, S.F. Ackley, and P. Wadhams, 1993. Roughness of Weddell Sea ice and estimates of the air-ice drag coefficient, *J. Geophys. Res.*, 98(C7):12439-12452.
- Agnew, T.A. and S. Howell, 2003. The use of operational ice charts for evaluating passive microwave ice concentration data, *Atmosphere-Ocean*, 41(4), 317-331.
- Arrigo, K.R. and G.L. van Dijken, 2004. Annual cycles of sea ice and phytoplankton in Cape Bathurst polynya, southeastern Beaufort Sea, Canadian Arctic. *Geophys. Res. Lett.*, 31, L08304, doi:10.1029/2003GL018978.
- Barber, D.G. and J.M. Hanesiak, 2004. Meteorological forcing of sea ice concentration in the southern Beaufort Sea over the period 1979 to 2000, *J. Geophys. Res.*, 109, C06014, doi:10.1029/2003JC002027.
- Barber, D.G. and R.A. Massom, 2006. The role of sea ice in Arctic and Antarctic Polynyas, *Polynyas: Windows to the world*, Smith Jr., W.O. and D.G. Barber, eds., 1-40, Elsevier Publishers, Holland.
- Belchansky, G.I., D.C. Douglas, and N.G. Platonov, 2004. Duration of the Arctic sea ice melt season: Regional and interannual variability, 1979-2001, *J. CLim.*, 17 p. 67-80.
- Canadian Ice Service Archive Documentation Series, 2006. Regional Charts: History, Accuracy, and Caveats (http://ice.ec.gc.ca/IA_DOC/cisads_no_001_e.pdf) September 2006.
- Carmack, E.C., and R.W. MacDonald, 2002. Oceanography of the Canadian Shelf of the Beaufort Sea: A Setting for Marine Life, *Arctic*, 55, Supp. 1, p. 29-45
- Carmack, E. and D.C. Chapman 2003. Wind-driven shelf/basin exchange on an Arctic shelf: The joint roles of ice cover extent and shelf-break bathymetry, *Geophys. Res. Lett.*, 30, 1778, doi:101029/2003GL017526.
- Cattle, H. and J. Crossley, 1995. Modeling Arctic climate change, *Phil. Trans. R. Soc. Lond. A*. 352, 201 - 213.
- Comiso, J.C., D. Cavalieri, C. Parkinson and P. Gloerson, 1997. Passive microwave algorithms for sea ice concentrations, *Rem.Sens.Env.* 60, pp. 357-384.

- Comiso, J., 2002. A rapidly declining perennial sea ice cover in the Arctic, *Geophys. Res. Lett.* 29, 1956, doi:10.1029/2002GL015650.
- Dunbar, M.J., 1981. Physical Causes and Biological Significance of Polynyas and other Open Water in Sea Ice. *In: Polynyas in the Canadian Arctic*, I. Stirling and H. Cleator, (Eds). Can. Wildlife Service, Occasional Paper 45, pp. 29-43.
- Flato, G.M., G.J. Boer, W.G. Lee, N.A. McFarlane, D. Ramsden, M.C. Reader, A.J. Weaver, 2000. The Canadian Climate Centre for Climate Modeling and Analysis global coupled model and its climate, *Climate Dynamics*, 16, 451 - 467.
- Fequet, D. (ed.), 2002. MANICE: Manual of standard procedures for observing and reporting ice conditions 9th edition, Canadian Ice Service - Environment Canada, Ottawa, ON.
- Gloersen, P., C.L. Parkinson, D.J. Cavalieri, J.C. Comiso and H.J. Zwally, 1999. Spatial distribution of trends and seasonality in the hemispheric sea ice covers: 1978 - 1996, *J. Geophys. Res.*, 104(C9), 20827 - 20835.
- Hammill, M.O., 1987. The effects of weather on ice conditions in the Amundsen Gulf, N.W.T., Canadian manuscript report of the Fisheries and Aquatic Sciences no. 1900.
- Holland, M.M., C.M. Bitz, and B. Tremblay, 2006. Future abrupt reductions in the summer Arctic sea ice, *Geophys. Res. Lett.*, 33, L23503, doi:10.1029/2006GL028024.
- Howell, S..E.L., A. Tivy, J.J. Yackel and S. McCourt, 2007. Multi-year sea ice conditions in the Northwest Passage: 1968 - 2006, *Atmosphere-Ocean* (accepted).
- IPCC, 2007. Climate Change 2007: The physical science basis, summary for policymakers, Contribution of working group I to the fourth assessment report of the intergovernmental panel on climate change, Paris, February 2007.
- Kleim, N. and D.A. Greenberg, 2003. Diagnostic simulations of the summer circulation in the Canadian Arctic Archipelago, *Atmos-Ocean*, 41(4), pp. 273-289.
- Kwok, R., 2006. Exchange of sea ice between the Arctic Ocean and the Canadian Arctic Archipelago, *Geophys. Res. Lett.*, 33, L16501, doi:10.1029/2006GL027094.
- Lukovich, J.V. and D.G. Barber, 2006. Atmospheric controls on sea ice motion in the southern Beaufort Sea, *Journal of Geophysical Research*, v111, D18103, doi:10.1029/2005JD006408.
- Maslanik, J.A., C. Fowler, J. Stroeve, S. Drobot, J. Zwally, D. Yi and W. Emery, 2007. A younger, thinner Arctic ice cover: Increased potential for rapid, extensive sea-ice loss, *Geophys. Res. Lett.*, 34, L24501, doi:10.1029/2007GL032043.

- Maykut, G.A., 1982. Large-scale heat exchange and ice production in the Central Arctic, *J. Geophys. Res.*, 87(C10):7971-7984.
- McFarlane, N.A., G.J. Boer, J.-P. Blanchet, and M. Lazare, 1992. The Canadian Climate Centre second-generation general circulation model and its equilibrium climate, *J. Clim.*, 5(10), 1013 - 1044
- Meehl, G. A., T. F. Stocker, W. D. Collins, P. Friedlingstein, A. T. Gaye, J. M. Gregory, A. Kitoh, R. Knutti, J. M. Murphy, A. Noda, S. C. B. Raper, I. G. Watterson, A. J. Weaver, Z.-C. Zhao, "Global Climate Projections", in *Climate Change 2007: The Physical Science Basis. Contribution of Working Group I to the Fourth Assessment Report of the Intergovernmental Panel on Climate Change*, edited by S. Solomon and D. Qin and M. Manning and Z. Chen and M. Marquis and K. B. Avery and M. Tignor and H. L. Miller, 747-845, 2007
- Melling, H., D.A. Riedel and Z. Gedalof, 2005. Trends in the draft and extent of seasonal pack ice, Canadian Beaufort Sea, *Geophys. Res. Lett.*, 32, L24501, doi:10.1029/2005GL024483.
- Mysak, L.A. and D.K. Manak, 1989. Arctic sea ice extent and anomalies 1953-84, *Atmos.-Ocean*, 27(2), 346-505.
- Ngheim, S.V., Y. Chao, G. Neumann, P. Li, D.K. Perovich, T. Street and P. Clemente-Colón, 2006. Depletion of perennial sea ice in the East Arctic Ocean, *Geophys. Res. Lett.*, 33,L17501, doi:10.1029/2006GL027198.
- Parkinson, C., D.J. Cavalieri, P. Gloerson, H.J. Zwally, and J.C. Comiso, 1999. Arctic sea ice extents, areas and trends, 1978-1996, *J. Geophys. Res.*, 104(C9), 20837-20856.
- Parkinson, C., D. Rind, R.J. Healy and D.G. Martinson, 2001. The impact of sea ice concentration accuracies on climate model simulations with the GISS GCM, *J. Clim.*, 14, 2060-2623.
- Polyakov, I.V. and M.A. Johnson, 2000. Arctic decadal and interdecadal variability, *Geophys. Res. Lett.*, 27(24), 4097-4100.
- Rigor, I.G., J.M. Wallace, and R.L. Colony, 2002. Response of sea ice to the Arctic Oscillation, *J. Clim.*, 15, 2648-2663.
- Rigor, I.G., and J.M. Wallace, 2004. Variations in the age of Arctic sea ice and summer sea ice extent, *Geophys. Res. Lett.*, 31, L09401, doi:10.1029/2004G101949.
- Rothrock, D.A., Y. Yu and G.A. Maykut, 1999. Thinning of the Arctic sea-ice cover, *Geophys. Res. Lett.*, 26(23), 3469-3472.

- Serreze, M.C., R.G. Barry and A.S. McLaren 1989. Seasonal variations in sea ice motion and effects on sea ice concentration in the Canada Basin, *J. Geophys. Res.*, *94(C8)*, 10955-10970.
- Serreze, M. C., J.A. Maslanik, T.A. Scambos, F. Fetterer, J. Stroeve, K. Knowles, C. Fowler, S. Drobot, R.G. Barry, and T.M. Haran 2003. A record minimum Arctic sea ice extent and area in 2002, *Geophys. Res. Lett.*, *30*, 1110-1113.
- Smith, S.D.; R.D. Muench and C.H. Pease, 1990. Polynyas and Leads: An Overview of Physical Processes and Environment. *J. Geophys. Res.* *95(C6)*: 9461-9479.
- Stroeve, J.C., M.C. Serreze, F. Fetterer, T. Arbetter, W. Meier, J. Maslanik, and K. Knowles, 2005. Tracking the Arctic's shrinking ice cover: Another extreme September minimum in 2004, *Geophys. Res. Lett.*, *32*, L04501, doi:10.1029/2004GL021810.
- Thorndike, A.S. and R. Colony, 1982. Sea ice motion in response to geostrophic winds, *J. Geophys. Res.*, *87(C8)*, 5845-5852.
- Thorndike, A.S., 1986. Kinematics of sea ice, in *The Geophysics of Sea Ice, NATO ASI Ser., Ser. B Phys.*, vol. 146, edited by N. Untersteiner, pp. 489-549, Plenum, New York.
- Torneby, L., 2006). A case study of northeasterly gales in Arctic waters, *Environment Canada cooperative program for operational meteorology, education and training*, 10 pages.
- Wadhams, P., 2000. *Ice in the ocean*, Gordon and Breach Publishers, London. 351 pages.
- Yu, Y., G.A. Maykut and D.A. Rothrock, 2004. Changes in the thickness distribution of Arctic sea ice between 1958-1970 and 1993-1997, *J. Geophys. Res.*, *109*, C08004 doi: 10.1029/2003JC001982.
- Zhang, J., D. Rothrock and M. Steele, 2000. Recent changes in the Arctic Sea Ice: The interplay between ice dynamics and thermodynamics, *J. Clim.*, *13*, 3099-3114.

CHAPTER SIX: A PHYSICAL EXPLANATION OF THE FORMATION OF THE CAPE BATHURST POLYNYA, NWT, CANADA

Galley, R.J., D.G. Barber, E. Key and S. Prinsenberg, 2009. A physical explanation of the formation of the Cape Bathurst Polynya, NWT, Canada. *Journal of Geophysical Research* – Submitted paper number 2009JC005572.

1. Introduction

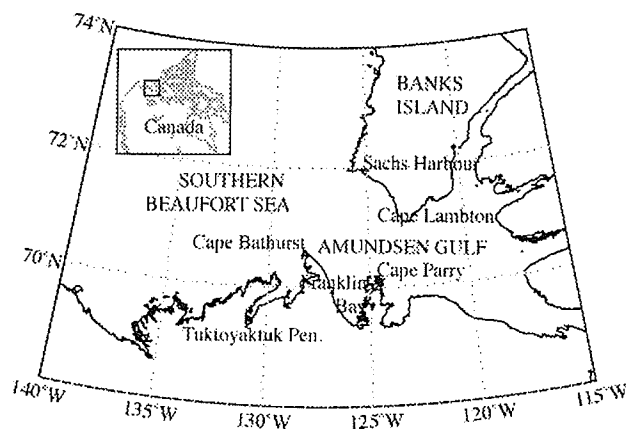
There are at least 61 different northern hemisphere polynyas, most of which are poorly understood (*Barber and Massom, 2007*) despite the fact that polynyas and flaw leads are integral components of the Arctic climate system and highly biologically productive regions. For much of the annual cycle Arctic sea ice extent and thickness is highly variable in polynya and lead areas, which determines the exchange of surface turbulent and radiative heat fluxes between the ocean and atmosphere (*Maykut, 1982; Ruffieux et al., 1995; Persson et al., 2002; Perovich, 2005*). The absence of a sea ice cover increases the turbulent fluxes to the atmosphere, which in turn feedback to the ocean surface positively enabling cloud formation, resulting in larger longwave fluxes to the surface thereby reducing sea ice cover (*Minnett and Key, 2007*). Leads and polynyas also reduce the albedo of the surface substantially, allowing the ocean to absorb much more shortwave radiation than in the presence of a sea ice cover. The positive sea ice-albedo feedback reduces or eliminates sea ice cover because it warms the ocean surface layer, making it more difficult to freeze. It also allows greater amounts of longwave radiation to be emitted to the atmosphere, which are trapped by clouds and re-emitted to the surface. Sea ice extent and thickness are also important variables in determining regional ice strength (*Andreas et al., 1993; Timco, 2008*). Sea ice extent and

thickness variability have an obvious influence on ice mass flux (*Aagaard and Carmack, 1989*) which combines the influence of ice presence thickness and strength.

Polynyas and leads are thought to be among the most biologically productive areas of the Arctic Ocean (*Dunbar, 1981; Smith, 1995; Tremblay et al., 2002; Arrigo and van Dijken, 2004*) due to the availability of light to the upper ocean as a result of reduced sea ice extent and/or thickness, due to comparatively high nutrient concentrations in the upper ocean resulting from wind-mixing, and/or due to advection of nutrients from less productive areas near the polynya or from upwelling of nutrients from below the pycnocline (*Arrigo, 2007*).

The Cape Bathurst polynya occurs each spring in the transition zone between the perennial sea ice pack of the southern Beaufort Sea and the seasonal sea ice of western Amundsen Gulf (*Smith et al. 1990; Galley et al., 2008*) (Figure 6.1).

Figure 6.1. The southern Beaufort Sea and Amundsen Gulf study area, (Inset) Amundsen Gulf's location in the Canadian Arctic



It is attended to by flaw leads radiating outward from the mouth of Amundsen Gulf northward along the west coast of Banks Island and westward along the continental coast which are maintained for much of the fall, winter and spring. The combination of a spring polynya and the flaw lead system which occurs in fall, winter and spring has been termed the Cape Bathurst polynya complex (e.g. *Smith et al.*, 1990; *Barber and Hanesiak*, 2000). Previous work in this region includes an overview the pertinent processes toward the understanding of the interaction of the physical environment with marine biota on the Canadian Shelf in the southeastern Beaufort Sea (*Carmack and Macdonald*, 2002). Drobot and Maslanik (2003) used the Barnett severity index to examine summer sea ice conditions in the Beaufort Sea north of Barrow, Alaska between 1953 and 2000 with respect to summer and winter atmospheric and surface variability. They found that light sea ice summers in the Beaufort Sea were preceded by winters when high pressure develops over Siberia, which leads to increased ice export across the transpolar drift stream while the Beaufort Gyre becomes less effective at moving old ice into the Beaufort Sea (Drobot and Maslanik, 2003). During light ice summers, the regional air temperature is higher than normal, and the Beaufort High over the Canadian Arctic Archipelago remains strong, effectively forcing sea ice out of the Beaufort Sea. Drobot and Maslanik (2003) go on to link these local/regional scale processes that create light ice summers with the positive phases of the Arctic Oscillation (AO) and North Atlantic oscillation (NAO) in winter and the negative phases of the AO and NAO in summer, giving first credit to the notion of winter pre-conditioning of summer sea ice conditions in the area. Barber and Hanesiak (2004) then explored the

meteorological forcing of sea ice concentration anomalies in the southern Beaufort Sea perennial pack between 1979 and 2000. A study of the annual cycles of sea ice concentration and phytoplankton abundance was conducted by *Arrigo and Van Dijken* (2004), using 5 years (1998-2002) of SSM/I and SeaWiFS data to relate the timing and intensity of phytoplankton blooms in the Cape Bathurst Polynya within the open water area. As part of the Canadian Arctic Shelf Exchange Study, 25 years of sea ice concentration data (1980-2004) in the southern Beaufort Sea and Amundsen Gulf was analyzed to determine the average summer and winter sea ice concentrations-by-type in the polynya region in each year and for the entire period. Each summer, a tongue of multiyear sea ice penetrates the mouth of Amundsen Gulf seeding new and young sea ice production each fall and creating a connection between the seasonal sea ice zone in Amundsen Gulf and the Beaufort Sea perennial pack (*Galley et al.*, 2008). Freeze-up began on average on the week of October 10th and was complete by the week of October 28th and varied little through the time series (*Galley et al.*, 2008), which compared well with earlier results from 1964-1974 by *Hammill* (1987). Flaw leads occurred on average throughout the winter west of Banks Island, north of the Tuktoyaktuk peninsula and within Amundsen Gulf along the coast of Banks Island, across the mouth of Franklin Bay and between Cape Lambton and Cape Parry (*Galley et al.*, 2008). In spring, break-up in western Amundsen Gulf began on average in mid-June and ended on average near the end of July, but was occasionally more variable than the duration of freeze-up; in 1991 and 2002 break-up in western Amundsen Gulf was not complete until the beginning of

October. Summer is characterized by periodic influxes of old ice to western Amundsen Gulf from the Beaufort Sea pack.

It was hypothesized in previous work that the connection made between the perennial pack and the seasonal sea ice zone of western Amundsen Gulf in the fall enables sea ice motion within western Amundsen Gulf throughout the winter, in part creating and maintaining flow leads along the west coast of Banks Island, the north coast of the Tuktoyaktuk Peninsula and within western Amundsen Gulf. It is also hypothesized that the winter flow leads in part allow the spring clearing of sea ice from western Amundsen Gulf to occur earlier than if the ice melted in place and that sea ice is cleared from western Amundsen Gulf in spring by south-easterly winds.

The Canadian Arctic Shelf Exchange Study (CASES) was conducted over an annual cycle in the Cape Bathurst polynya complex yielding a unique combination of oceanographic, sea ice and atmospheric data with which we explore the polynya complex's annual evolution and specifically the hypotheses noted above. This work will use elements of the CASES dataset in combination with remotely sensed data over the full annual cycle to explain the physical mechanisms which act in concert to operate the Cape Bathurst flow lead polynya complex. Understanding how the Cape Bathurst polynya complex is physically forced now is vital should we hope to understand how the polynya would operate in a future Arctic icescape responding to the observed change from perennial to seasonal sea ice.

The objective this work is to elucidate and describe in detail the contribution and timing of the important thermodynamic and dynamic processes over an annual sea ice cycle in the Cape Bathurst Polynya region that form the polynya.

2. Data and Methods

2.1. Canadian Ice Service digital archive and Radarsat-1

The Canadian Ice Service (CIS) digital ice chart archive data are used to describe the regional temporal sea ice evolution in the southern Beaufort Sea and Amundsen Gulf between September 2003 and August 2004. CIS digital data are based on manual interpretation of RADARSAT-1 (which has been the primary data source for the CIS digital archive since 1996), NOAA-AVHRR and Envisat ASAR, *in situ* observations, aerial and marine surveys (Fequet, 2002). The CIS dataset includes sea ice concentration by ice type, including new ice ($h_i < 10\text{cm}$), young ice ($h_i = 10\text{-}30\text{cm}$) and first-year ice ($h_i > 30\text{cm}$). Subsets of first year ice include thick ($h_i > 120\text{cm}$), medium ($70\text{cm} < h_i < 120\text{cm}$) and thin ($30\text{cm} < h_i < 70\text{cm}$). Old sea ice (including second year and multi-year) has survived a summer's melt. Total sea ice is the sum of all sea ice concentrations by type. The *Canadian Ice Service Archive Documentation Series* contains a substantial treatise on the observational and mapping accuracy of the CIS digital dataset including quality indices for each region through time (*Canadian Ice Service Archive Documentation Series*, 2006).

Sea ice concentration-by-type in the southern Beaufort Sea and western Amundsen Gulf (WAG) maps (Figure 6.2) were made by converting CIS digital charts to a four km² grid so that monthly medians could be calculated using weekly data.

CIS digital data in shapefile format were used to display the evolution of landfast and mobile sea ice extent from 1 December 2003 to 15 May 2004 (Figure 6.3). To illustrate spring break-up, four RADARSAT-1 ScanSAR images over Amundsen Gulf (24 May, 27 May, 3 June and 6 June 2004) were processed to normalized radar cross-section (σ°) where lighter tones indicate areas of high backscatter (Figure 6.11).

2.2. The sea ice thickness distribution of western Amundsen Gulf

Sea ice thickness measurements in western Amundsen Gulf were made using a helicopter-mounted electromagnetic (EM) induction system called IcePic to determine the thickness distribution within western Amundsen Gulf and the relative contribution of leads, ridges and level sea ice. The EM induction method for measurements of sea ice thickness over seawater is well established, as are its limitations (e.g. *Kovacs and Holladay, 1990; Prinsenberg and Holladay, 1993; Kovacs et al., 1996; Haas et al., 1997; Haas, 1998*). The IcePic system was hard-mounted on the nose of a BO105 helicopter flown from the *C.C.G.S. Amundsen* icebreaker. This system is an improvement upon helicopter-towed EM induction measurements, as the sensor is kept level near the ice surface throughout the flight, allowing its footprint to be smaller and more accurately accounted for. The near-circular footprint of the IcePic system is roughly 2.5 times the altitude (~2-4m) at which it is flown. Further details regarding technical information for the EM-induction system can be found in *Holladay (2006)*.

On 8 May 2004, a flight from *C.C.G.S. Amundsen* at her Franklin Bay overwintering station (70.05°N, 126.31°W) north to Sachs Harbour (71.83°N, 125.32°W) on Banks Island, then southwest to 128°W, and finally south-southeast back to *C.C.G.S. Amundsen* (Figure 6.7) was conducted, representing a sample of the sea ice thickness distribution in western Amundsen Gulf at near-maximum thickness. The northward flight from the *Amundsen* to Sachs Harbour contained six sections (numbered 1 to 6 from south to north), and the return flight contains six sections (numbered 7 to 12 from north to south) (Figure 6.7). Each point of thickness data was geo-located using a GPS. Leads were identified as continuous stretches of sea ice at least 5m long, where the thickness was less than 1m (after *Wadhams, 1987*) as sea ice less than 1m thick controls regional heat fluxes between the ocean and atmosphere (*Maykut, 1978*). Level sea ice was identified using a five point moving average and standard deviation (corresponding to a horizontal distance of about 25m) to select data points where the ice thickness was within 0.2 standard deviations of the mean for those five points (excluding leads). Finally, all remaining sea ice not already classified as a lead or level ice was classified as ridged/rubble sea ice. This methodology is not without its shortcomings, as ice less than 1m thick is classified as a lead regardless of whether it is composed of a thermodynamically grown slab of thin sea ice or two rafted slabs of relatively thin sea ice. Also, level sea ice could still consist of rafted slabs of sea ice thicker than 1m in total. However, visual inspection of the IcePic sea ice thickness data in cross-section found that it corresponded closely with the criteria used above.

2.3. Modeled thermodynamic sea ice growth in western Amundsen Gulf

The evolution of thermodynamic sea ice thickness was modeled between freeze-up in 2003 and break-up in 2004. This exercise was performed for two reasons: (1) to compare the evolution of the sea ice cover in the study area as observed by the CIS digital data to ice conditions as they would have occurred in the absence of dynamic processes and, (2) to compare the EM induction sea ice thickness measurements representing sea ice as it occurred on 8 May to what it would have looked like in the absence of dynamic processes. Our intention here is to tease apart the relative contributions of dynamic and thermodynamic growth to the overall sea ice environment of the polynya, while recognizing that these two processes are concomitant in reality.

The model (*Flato and Brown, 1996*) was forced using daily-averaged cloud amount, air temperature, wind speed, relative humidity and snowfall at sixty grid points of North American Regional Reanalysis (NARR) climate data in the region. Output included end-of-day snow and sea ice thickness, end-of-day eleven-layer snow and sea ice temperature profile (one snow layer and ten sea ice layers), and break-up and freeze-up dates for each location. NARR data (*Mesinger et al., 2004*) were used as they improve on the accuracy of temperature, winds and precipitation compared to the NCEP-DOE Global Reanalysis 2 products using the high resolution NCEP North American Model (which includes 45 layers and topography) together with the Regional Data Assimilation System which assimilates precipitation and other variables (*Mesinger et al., 2005*). When compared to Environment Canada station data at Cape Parry, the NARR data at the nearest ocean grid point were quite

similar over the period; the NARR air temperature was only 1.29°C warmer on average for the whole period, reasonable considering the Cape Parry station is on land, potentially leading to slightly cooler temperatures than at the nearest NARR ocean grid point. When compared to meteorological observations of air temperature on the *CCGS Amundsen* between 1 December 2003 and 1 June 2004 at her over-wintering site in Franklin Bay (70.05°N, 126.31°W), NARR air temperature data from the nearest ocean grid cell (70.2°N, 125.96°W) were slightly cooler than air temperature data from the *Amundsen* until the end of December 2003, then slightly warmer from then beginning of January onward. This could be due to the assimilation of air temperature data from land-based stations and radiosondes in snow and ice covered land areas which would be colder than the ocean in the fall and winter and warm up more quickly than ice-covered ocean in spring. Overall we are confident that these data are suitable as inputs to our thermodynamic modeling exercise.

2.4. Sea ice motion in the Southern Beaufort Sea and western Amundsen Gulf

A time series of sea ice motion data across Amundsen Gulf and the southern Beaufort Sea between 3 November 2003 and break-up (June 6) in 2004 were used to determine the timing, magnitude and direction of ice motion in the southern Beaufort Sea and western Amundsen Gulf. Eulerian data were produced on a 22km grid (see map in figure 6.4) by the Jet Propulsion Laboratory at the California Institute of Technology using the RADARSAT Geophysical Processor System (RGPS) employing 60 successive RADARSAT-1 ScanSAR images between 3 November 2003

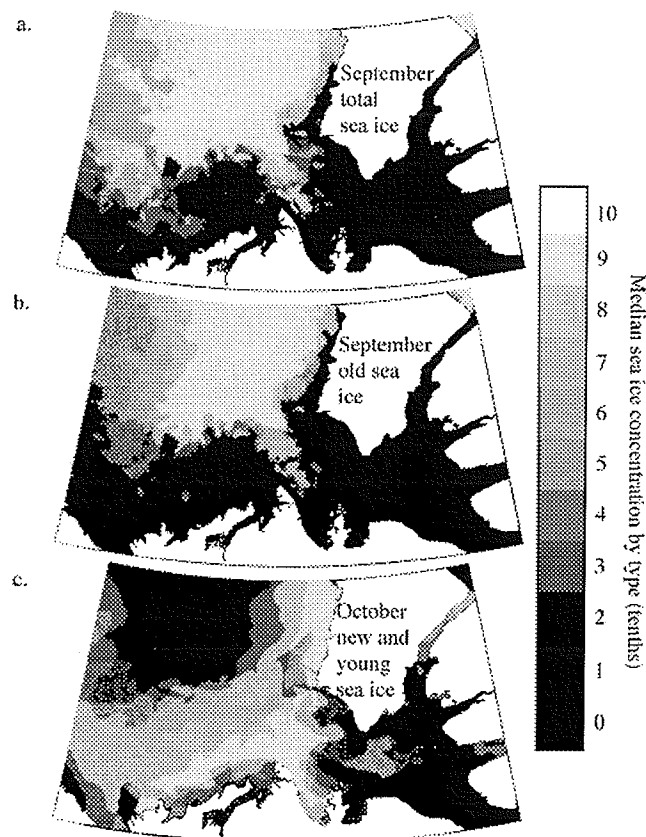
and 6 June 2004 at an average interval of 3 days. The magnitude and orientation of each Eulerian ice motion vector for each image pair were averaged for all the grid points in the southern Beaufort Sea and in Amundsen Gulf in order to compare the sea ice motion in Amundsen Gulf with sea ice motion in the southern Beaufort Sea (Figure 6.4). The processed scanSAR data provide high temporal and spatial resolution, allowing the identification of specific floes and the calculation of their speed and direction. Further details on the RGPS can be found in *Kwok* [1990]. Finally, daily NARR wind data averages for 60 points over the study region were made to compare with ice motion in the area to determine if and when it controls ice motion in the area (Figure 6.4).

3. Results

3.1. Evolution of the Cape Bathurst flaw lead polynya complex 2003-2004

In September 2003, sea ice concentrations were high in the Beaufort Sea west of Banks Island, consisting almost entirely of old sea ice making up the perennial Arctic pack (Figure 6.2). A tongue of sea ice consisting of about six tenths old ice and two-tenths thick first-year sea ice extending out from the Beaufort Sea perennial pack occurred in the mouth of western Amundsen Gulf (Figures 6.2a and b).

Figure 6.2. Sea ice concentration (tenths) over the study area:
 (a) median total sea ice concentration for September 2003, (b) median old sea ice concentration for September 2003 and (c) median new-and-young sea ice (<30cm thick) concentration for October 2003



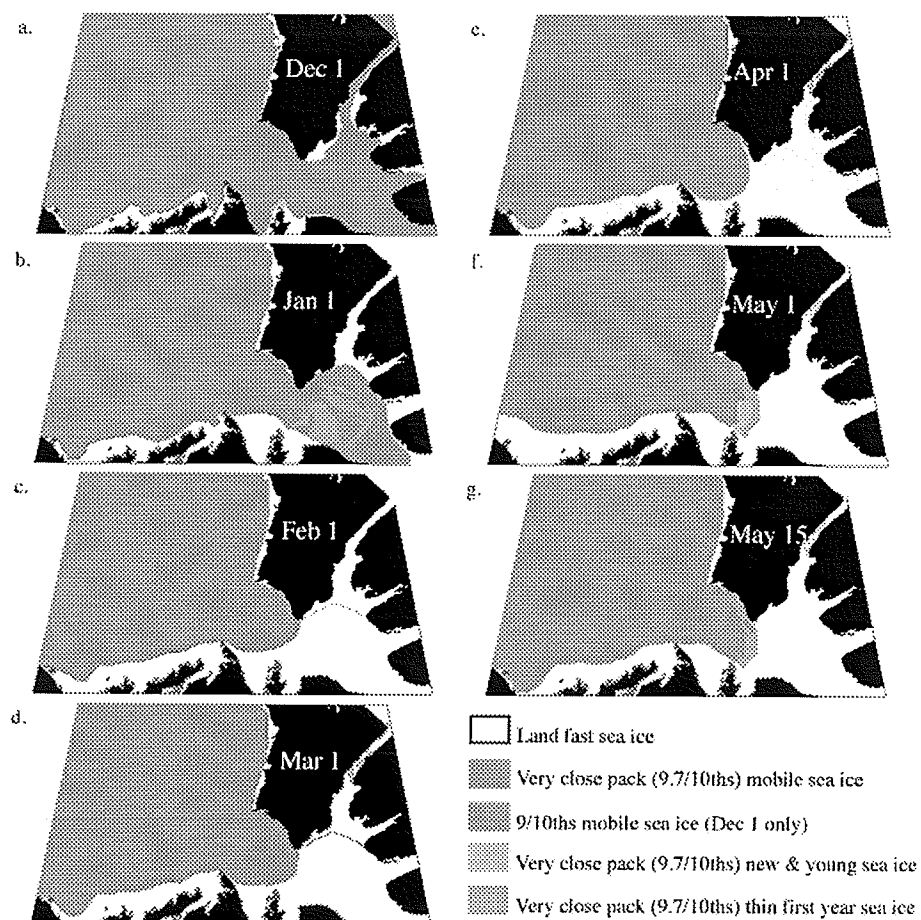
On average (1980-2004), a tongue of old and thick first year sea ice reached into the mouth of Amundsen Gulf from the southern Beaufort sea perennial ice pack prior to new and young ice formation, acting as an anchor point from which new and young ice growth radiates outward in fall (Galley *et al.*, 2009). Fall ice growth associated with this tongue of perennial ice is likely due to the reduction of the surface wind stress limiting mixing of warm surface mixed layer water to the surface, and to an enthalpy effect which reduces the local air temperature due to the presence of the

ice tongue. New and young sea ice formation in fall 2003 occurred first in the last week of September associated with an area of high old and thick first year ice concentrations. Freeze-up (when sea ice concentration increases from 20% to 80%) in the polynya region in 2003 occurred quickly, beginning at the end of September and ending mid-October, covering Amundsen Gulf in new and young sea ice within 1-2 weeks, consistent with the long-term average (*Galley et al., 2008*). Median new-and-young sea ice formation in October 2003 was associated with the periphery of thick first year and old sea ice in fall (Figure 6.2a-c). The formation of the winter flaw lead system and spring polynya is dependent upon this process; instead of sea ice formation occurring first in the shallower, more easily mixed shelf areas and growing outward from the coast as it does later in this area (and in other areas of the archipelago), sea ice formation begins in the middle of western Amundsen Gulf 'seeded' by the tongue of multi-year ice. This process makes a connection between the seasonal sea ice of western Amundsen Gulf and the perennial pack of the southern Beaufort Sea which we will show enables winter flaw lead and spring polynya formation.

The monthly evolution of sea ice concentration in the study area from CIS digital chart data shows that sea ice in western Amundsen Gulf maintains mobility throughout the winter and spring of 2003-2004 (Figure 6.3). Over the winter the spatial extent of landfast sea ice in Amundsen Gulf east of the southern tip of Banks Island becomes progressively larger until 1 February 2004 when the mobile sea ice area in western Amundsen Gulf reaches its typical winter shape (Figure 6.3c). February 1 shows that during January, the eastern half of Amundsen Gulf (covered

almost entirely by seasonal sea ice) became landfast. However, sea ice in western Amundsen Gulf composed of a mix of perennial and seasonal sea ice which began in the fall (Figure 6.2) was still mobile in spite of its high concentration (Figure 6.3c). At this point the mobile sea ice area in western Amundsen Gulf remained spatially the same until flaw leads began to form between it and the landfast ice of eastern Amundsen Gulf in May (Figure 6.3f, g).

Figure 6.3. The monthly evolution of the interface between mobile very close pack ice in the southern Beaufort Sea and western Amundsen Gulf and the landfast sea ice of Amundsen Gulf. Note the consist shape of the mobile sea ice tongue in western Amundsen Gulf beginning in February.



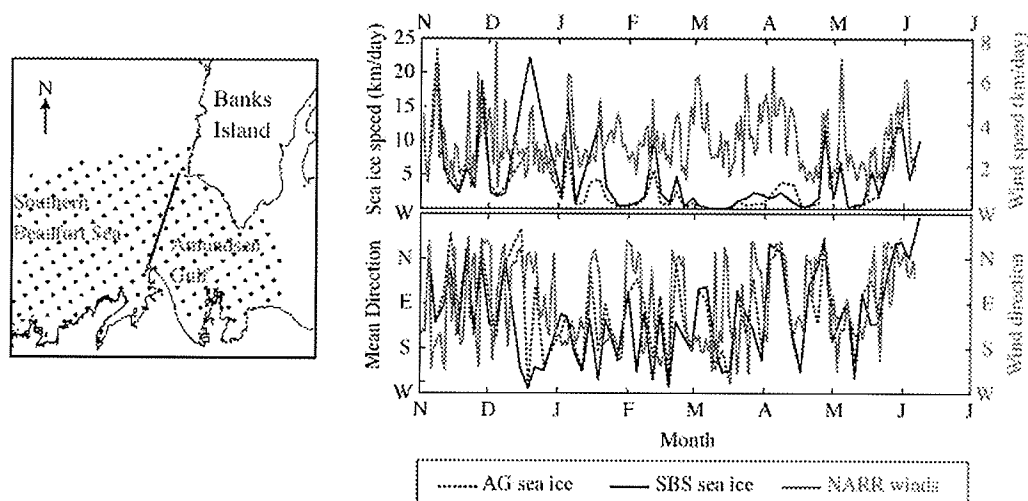
3.2. Sea ice motion in the Southern Beaufort Sea and western Amundsen Gulf

It should now be obvious from the previous section that sea ice in the southern Beaufort sea is mobile for the entire annual cycle, as is much of the sea ice in western Amundsen Gulf. Thus we examine sea ice motion data derived from successive Radarsat-1 scanSAR image pairs by the RGPS to determine if sea ice motion in western Amundsen Gulf (a transition zone between multi-year sea ice and seasonal sea ice), and the perennial pack ice of the southern Beaufort Sea occur in concert. The formation of the winter flaw lead system and spring polynya require that three conditions be met: (1) The sea ice in motion must have areas surrounding it that are physically weak (either thin or warm) enabling the ice cover to move despite high concentrations (2) the sea ice in motion must have somewhere to move to, (3) an external force (wind and/or ocean currents) must act on the sea ice cover to move it.

The connection made in fall by a tongue of old ice entering the mouth of Amundsen Gulf between the southern Beaufort Sea and Amundsen Gulf is vitally important to both the formation of the winter flaw lead system and the spring polynya. Without western Amundsen Gulf's connection to the Southern Beaufort Sea perennial pack, much of the mobile sea ice in the gulf would become landfast, disabling dynamic processes in winter and eliminating the ability of the wind in spring to clear western Amundsen Gulf forming the polynya. Instead the external force would only move the mobile sea ice toward the west away outside the mouth of Amundsen Gulf.

Sea ice speed (km/day) averaged over each RGPS time interval from 3 November 2003 to 6 June 2004 in the southern Beaufort Sea and western Amundsen Gulf followed each other quite closely throughout the observational period (Figure 6.4). The U- and V- components of average ice velocity vectors in the two regions were well correlated ($r^2 = 0.76$ and 0.75 respectively).

Figure 6.4. (Left) Study area map with RGPS grid position (black dots) bisected into the southern Beaufort Sea and Amundsen Gulf by black line. (Right) Mean sea ice speed and direction the ice is moving in the SBS and AG (black, dotted lines) overlaid with mean wind speed and direction the wind is going towards (blue lines) in the study area



In November and December 2003, sea ice speed and direction in western Amundsen Gulf was very similar to that in the southern Beaufort Sea (Figure 6.4). In November, predominantly thin (<30cm) sea ice in western Amundsen Gulf in combination with small concentrations of old sea ice (Figure 2) oscillated northwest and southeast along with sea ice in the southern Beaufort Sea (Figure 6.4). In

December, sea ice in the southern Beaufort Sea moved west-southwest and southwest (Figure 6.4), consistent with the anti-cyclonic rotation of the Beaufort gyre. At the same time, sea ice motion in Amundsen Gulf was most frequently towards the northwest and southeast, moving ice in and out of western Amundsen Gulf (Figure 6.4). Daily-averaged NARR winds for the area during November and December illustrate that during the fall, the direction of sea ice motion in Amundsen Gulf was similar to the direction the wind was blowing (Figure 6.4) (where wind direction plotted in Figure 6.4 shows the direction the wind is moving toward so they may be compared to ice motion direction data).

In January and February sea ice speed in Amundsen Gulf was much lower on average than in November and December, but sea ice speed in the southern Beaufort Sea continued similarly to November and December, alternating between west-southwest and southeast directions. The south-eastern edge of the Beaufort gyre typically moves south along the coast of Banks Island until it meets the continental coast near Cape Bathurst where it continues westerly (clockwise) along shelf towards Alaska. Sea ice motion results show that in January and February, ice motion in the southern Beaufort Sea outside the mouth of Amundsen Gulf compared well to ice motion in western Amundsen Gulf, which alternately moves toward the west and southwest or east-southeast (Figure 6.4). Sea ice speeds during this period are larger when sea ice is moving toward the west than when ice moves toward the southeast (Figure 6.4) for two reasons. First, sea ice in the southern Beaufort Sea moves most freely toward the west-southwest on its average anti-cyclonic rotation, and second because Amundsen Gulf is constrained by Victoria

Island, the continental coast and Banks Island to the east, south and north respectively. The direction that sea ice in Amundsen Gulf and the southern Beaufort Sea is moving during January and February still appears to be linked to the direction the wind is blowing toward (Figure 6.4: bottom panel at right). Interestingly, sea ice motion in January and February seemed to occur in three events (Figure 6.4: top panel at right), which coincided with periods of high wind speed. During January and February, much of Amundsen Gulf contained medium first year sea ice (0.7-1.2m thick) and was almost completely consolidated (nine-tenths concentration) (Figure 6.2) constraining sea ice motion but not eliminating it.

In March 2004 there was very little sea ice motion in both the southern Beaufort Sea and Amundsen Gulf. Near the end of March, sea ice motion in the southern Beaufort Sea began towards the east, coincident with ice motion in Amundsen Gulf and sustained high wind speeds (Figure 6.4: bottom panel at right).

At the beginning of April, ice motion toward the south in the southern Beaufort Sea and Amundsen Gulf occurred followed by a six day period of ice motion toward the northwest around 5 April 2004, which coincided with 6 days of strong winds toward the northwest which began on 3 April (Figure 6.4: bottom panel at right). Sea ice in western Amundsen Gulf moved southwest along with sea ice in the southern Beaufort Sea. As the wind switched towards the southeast on 10 April ice motion in Amundsen Gulf switched to the southeast starting on 12 April (Figure 6.4: bottom panel at right). Beginning on 23 April, sea ice in both western Amundsen Gulf and the southern Beaufort Sea moved northwest at comparatively high speed coincident with high wind speeds in that direction.

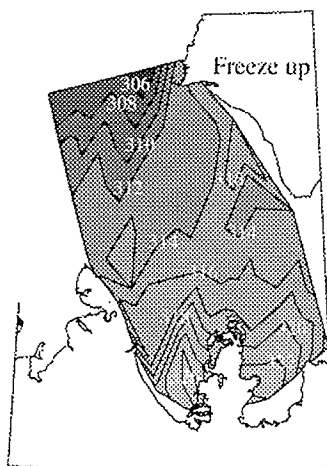
The sea ice in both western Amundsen Gulf and the southern Beaufort sea move in concert both in north-south and east-west directions throughout the winter maintaining the reverse-C shaped mobile sea ice zone in western Amundsen Gulf all winter and spring prior to the formation of the polynya.

3.3. Thermodynamic sea ice growth in western Amundsen Gulf

The annual evolution of sea ice thickness in WAG formed solely by thermodynamic processes between fall in 2003 and break-up in 2004 was modeled to determine if the thermodynamic sea ice growth alone over the annual cycle contributes in part to the formation and/or maintenance of the winter flaw lead system and therefore the spring polynya.

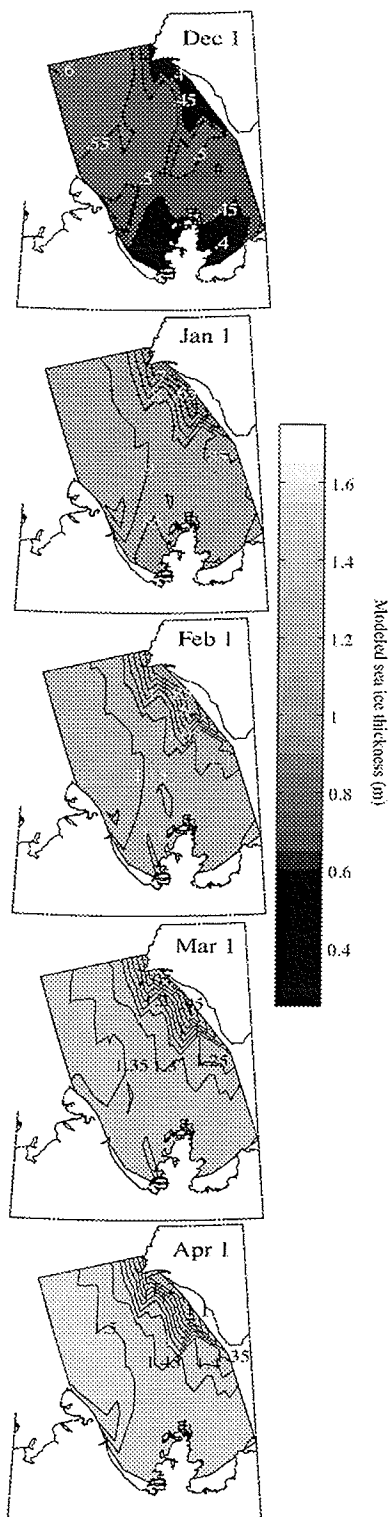
Modelled thermodynamic freeze-up occurred first in the southern Beaufort Sea outside the mouth of Amundsen Gulf in the fall around 01 November, followed by much of the middle of Amundsen Gulf about two weeks later (Figure 6.5) which was much later than observed in the CIS data above (Figure 6.2). Franklin Bay was the last area to freeze-up around the third week in November (Figure 6.5).

Figure 6.5. Modeled year-day of freeze-up in fall 2003 (YD306 = 2 Nov, YD326 = 22 Nov)



At the beginning of December, thermodynamically formed sea ice was thickest (0.60m) in the southern Beaufort Sea to the north and west of Amundsen Gulf, and relatively thick ice (0.55m) extended into the middle of western Amundsen Gulf (Figure 6.6), corresponding to the observed formation of new and young sea ice in that area in the fall (Figure 6.2c).

Figure 6.6. Modeled monthly sea ice thickness in the study area in winter 2004



Sea ice grew thinner moving north toward the coast of Banks Island in the north, and moving south into Franklin Bay. On 1 January 2004, sea ice in the middle of western Amundsen Gulf was still the thickest ($>0.90\text{m}$), while ice along the coast of Banks Island had grown considerably less thick (0.65m) (Figure 6.6). The ice in Franklin Bay was slightly thinner (0.85m thick) than the middle of Amundsen Gulf. As the winter progressed through February, March and April, the sea ice in the middle of the gulf grew thickest in the southern Beaufort Sea and in the middle of Amundsen Gulf (1.60m), with only slightly thinner (1.55m) sea ice in and around Franklin Bay. Sea ice in the north near the coast of Banks Island grew less thick (1.05 m) over the winter (Figure 6.6). We conclude (perhaps obviously) that thermodynamic sea ice growth probably does not contribute meaningfully to winter lead formation in the region as all the ice in the Gulf is greater than 1.0m in thickness by April.

3.4. Spring sea ice thickness distribution in western Amundsen Gulf

Fine scale thickness information from a helicopter-mounted EM induction system (IcePic) revealed that much the sea ice in WAG had been dynamically affected since its formation (Figures 6.7 and 6.8) which makes sense in light of the sea ice motion information presented above (Figure 6.4). The sea ice thickness data are presented in Figure 6.9 referenced against the sea ice thickness surface created by the thermodynamic model for the same day (8 May 2004). The proportion of level sea ice, leads, and ridged/rubble sea ice at the end of winter changed substantially dependent upon latitude and to a lesser extent longitude in our case

study (Figures 6.7 and 6.8). Summary statistics of each section in the map in Figure 6.7 are provided in Table 6.1. Moving from Franklin Bay to Sachs Harbour, semi-logarithmic probability distribution functions (PDF's) for each section are shown in Figure 6.7.

Figure 6.7. Map of western Amundsen Gulf (center panel) showing sea ice thickness sections flown by the IcePic system on May 8 2004 surrounded by semi-log probability distribution functions for sea ice thickness of each each section in the map

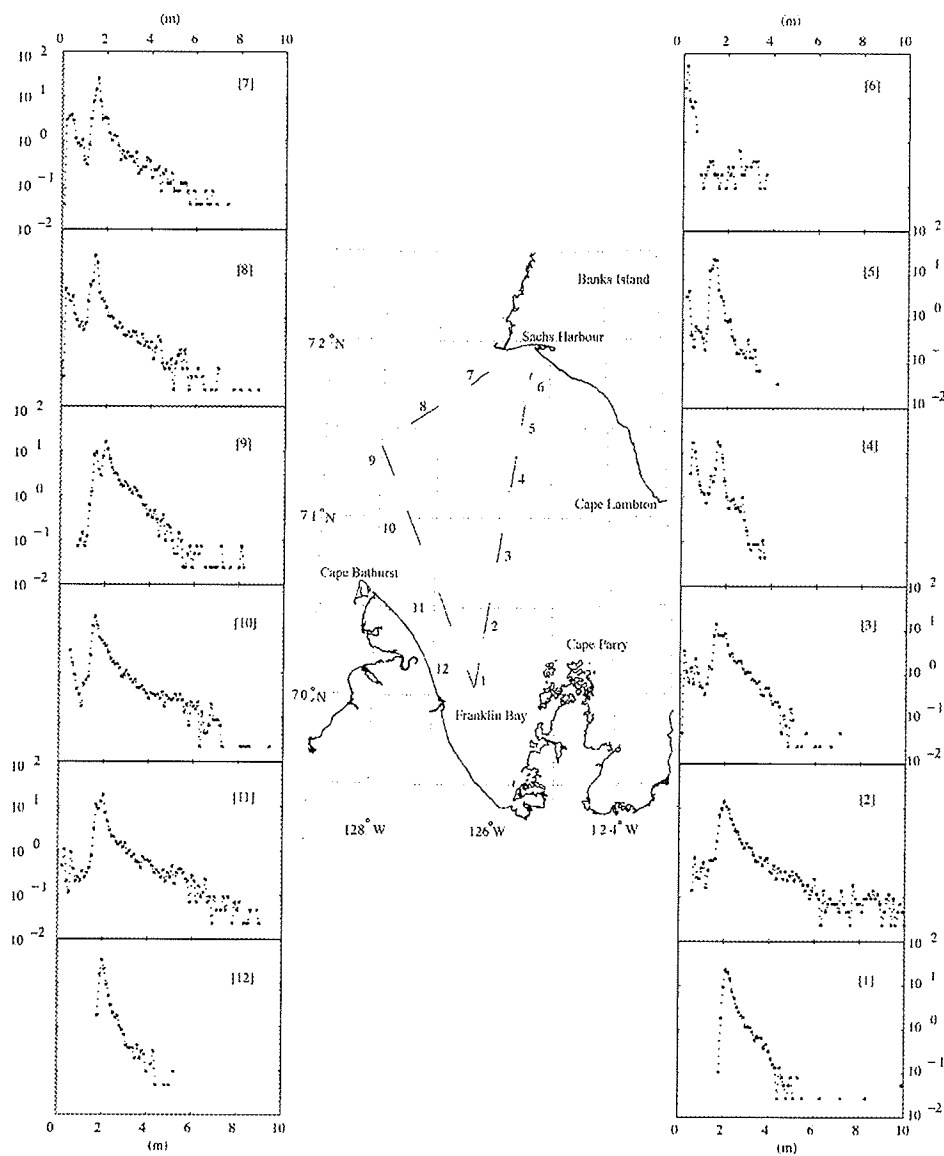
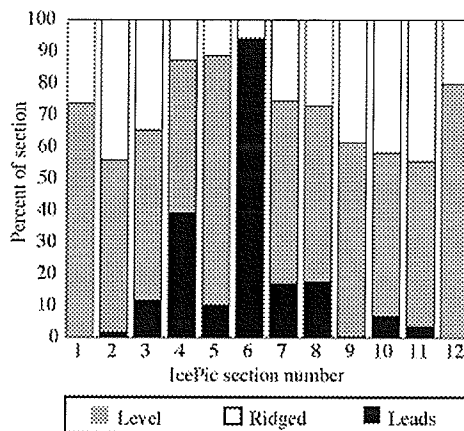


Figure 6.8. Percentage of level sea ice, leads and ridged/rubbed sea ice in each ice thickness section mapped in Figure 6.7



Section one occurred in Franklin Bay over landfast sea ice (Figure 6.7). Section two was the first mobile sea ice section and was substantially thicker and more affected by dynamic forcing than section one due mostly to shear ridging between the landfast ice edge and the mobile sea ice zone in WAG. Section three in the middle of WAG was also substantially dynamically affected, showing evidence of both convergence and divergence. Section four was generally thinner and the previous three sections (Table 6.1) and contained sea ice about 0.50m thick which was a result of sea ice growth in recently formed leads. Level sea ice in this section was interspersed with ridges. Sea ice in the fifth section was generally thinner again and had a smaller thickness range than the previous four sections. The PDF was bimodal with the peak at 0.25m (Figure 6.7) due to recent lead formation.

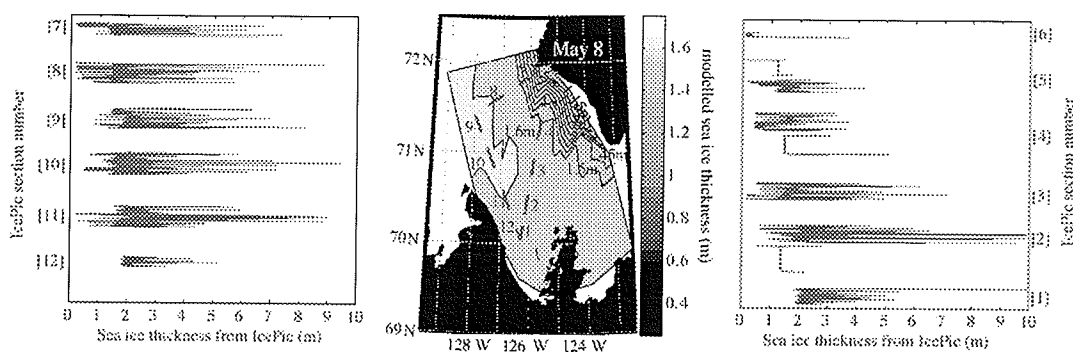
Table 6.1. Summary statistics for sea ice thickness (Z_i) sections 1 to 12 (for positions see the map in Figure 6.7)

Section Number	Section Length (km)	Latitude at mid-section ($^{\circ}$ N)	Mean Z_i (m)	Mode Z_i (m)	Mean Level Z_i (m)
1	17.4	70.1	2.37	2.29	2.21
2	20.0	70.45	2.55	2.01	2.06
3	19.1	70.85	1.88	1.82	1.79
4	20.1	71.25	1.27	2.70	1.66
5	13.3	71.6	1.35	0.25	1.42
6	4.9	71.8	0.36	1.52	NA
7	13.7	71.8	1.61	0.25	1.59
8	20.6	71.6	1.56	1.52	1.52
9	20.9	71.3	2.26	2.03	1.92
10	23.9	70.95	2.05	1.70	1.69
11	22.8	70.5	2.34	1.76	1.93
12	11.2	70.1	2.16	2.00	2.05

Ridges and rubble areas in this section were not as thick as in sections 1-4 due to the relative thinness of un-deformed sea ice in this area (Table 6.1). At the north end of section five, a wide re-frozen lead occurred which was 0.30m thick visible in the rightmost panel in Figure 6.9. The southern portion of this section was dominated by convergent motion while the northern portion was affected by divergence. Sea ice thickness at the south end of section six varied widely around 2m for half a kilometer then became thin (0.20m) and level over the rest of the section (Figure 6.9). Nearly all the ice in this near-shore area is relatively newly grown as a result of recent divergence from the south coast of Banks Island. Sections six and seven indicate the southwest coast of Banks Island was highly dynamic throughout the winter; ridging and new ice formation played a substantial role in the coastal sea ice thickness (Figures 6.7, 6.8, 6.9). The first four kilometers of section seven moving southwest were thin (0.30m thick) similar to the north end of section six, but were interrupted by a region of severe ridging with a maximum

thickness of 6.7m and followed by a second wide lead about 0.30m thick (Figure 6.9).

Figure 6.9. (Center) Modeled sea ice thickness on 8 May 2004 overlaid by the position of sea ice thickness sections on the same day. (Left and right panels) Ice thickness sections corresponding to the section positions at center (in blue)



The second lead zone was followed southward by ridging and then level sea ice about 1.65m thick interspersed with thick ridged sections. The north end of section eight began with a re-frozen lead approximately 0.22m thick within which dynamic processes had created ridged/rubble areas, followed by 1.60m thick level sea ice with a very thick ridge section exceeding 8.00m within it (Figure 6.9). The rest of section eight and nine indicated that dynamic processes dominated the volume, creating narrow leads and ridges throughout (Figures 6.8, 6.9). Sea ice less than 0.80m did not occur in section nine indicating this area was affected predominantly by convergence as ridge formation is clearly evident as more than 90% of the sea ice in this section fell into thickness classes larger than 1.50m (Figure 6.7). Section ten north of Cape Bathurst was dominated by dynamic processes, containing mostly ridge and rubble areas in combination with re-frozen leads. Three lead areas

occurred, one on the north end of the section approximately 0.80m thick, and two leads near the south end of the section slightly thinner than the north lead, approximately 0.50m thick (Figure 6.9). Section eleven east of Cape Bathurst covered two different sea ice zones separated by a lead. The sea ice at the north end was predominantly thermodynamically grown, about 2.05m thick and contained two ridge areas. The lead which divided section eleven latitudinally near 70.5°N was 0.20m thick, and the south end began with seven kilometers of thickly ridged/rubbed sea ice (6 to 8m) followed by ridges 3 and 4m thick. Section twelve ended near *C.C.G.S. Amundsen* where she over-wintered within landfast first-year sea ice in Franklin Bay (Figure 6.7). Landfast sea ice within Franklin Bay had grown to a thickness slightly greater than 2.00m, interspersed with some ridged areas. The magnitude of these ridges was comparatively small (Figure 6.9). The vast majority of sea ice (>70%) in the twelfth section was thermodynamically grown sea ice initiated during the fall freeze-up period, consisting of 1.90m, 2.00m and 2.10m thickness classes (Figure 6.7).

On 8 May 2004 modeled thermodynamic sea ice growth (coincident with EM sea ice thickness measurements), showed that the southern Beaufort Sea and the middle of the mouth of Amundsen Gulf would have grown thickest (>1.60m) (Figure 6.9: middle panel). Sea ice would have been steadily thinner moving east and north in western Amundsen Gulf toward Banks Island (Figure 6.9: middle panel). So, although the sea ice closest to Banks Island in western Amundsen Gulf would have grown to only 1.15m (Figure 6.9: middle panel), the ice thickness section data from the EM induction system (Figure 6.8, Figure 6.9: left and right panels) show that

dynamic forcing of sea ice thickness is ubiquitous in western Amundsen Gulf. Comparison of areas of relatively level sea ice such as section one (Figure 6.8) where the mean level sea ice thickness was 2.21m (Table 6.1) with modeled sea ice thickness on the same day (1.5m) indicate that even level sea ice areas have been dynamically thickened most likely early in their growth by rafting processes. Of note also is the area immediately south of Sachs Harbour off the coast of Banks Island, where sea ice thickness section six was observed to contain more than 90% lead ice with a mean thickness of 0.36m (Table 6.1, Figure 6.9: right panel). When compared to the modeled sea ice thickness in that area for the same day (1.15m) it is obvious that recent winter sea ice motion in western Amundsen Gulf is almost completely responsible for the sea ice thickness in that area prior to spring polynya formation. It is also apparent that a substantial shear zone denoted by huge ridging (near 10m thick in some cases) in sea ice thickness sections two and eleven (Figure 6.9: left and right panels), evidence of substantial sea ice motion throughout the winter are not accounted for by the modeled thermodynamic sea ice thickness for the same area (1.50m) (Figure 6.9: middle panel). Thermodynamics alone could never create/maintain the winter flaw lead system which in part enables the spring polynya to form; sea ice motion is almost completely responsible for the Cape Bathurst Polynya complex.

3.5. Spring formation of the Cape Bathurst Polynya

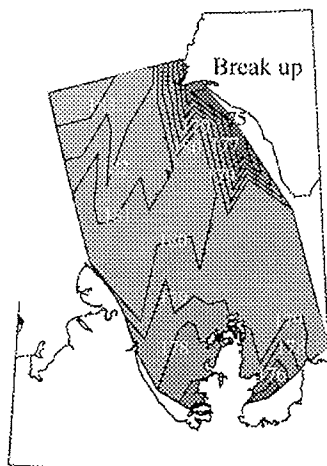
In May, mobile new and young sea ice as well as mobile thin first year sea ice were present at the interface between the mobile sea ice of WAG and the landfast

sea ice of eastern Amundsen Gulf (Figures 6.3f and g); evidence that the spring polynya had begun to form. On 3 May, sea ice in Amundsen Gulf and the southern Beaufort Sea moved southeast coincident with winds blowing in the same direction at the beginning of May (Figure 6.4: bottom panel at right). On 16 May, sea ice speed in the southern Beaufort Sea and then in Amundsen Gulf began to increase steadily in concert with increased and sustained wind speeds towards the northwest, then winds blowing toward the west (northwest and southwest) began on 23 May in western Amundsen Gulf and continued until 6 June (Figure 6.4: bottom panel at right) followed by northwest ice motion in western Amundsen Gulf beginning around 23 May which cleared western Amundsen Gulf of sea ice by 06 June 2004 (Figure 6.4: top and bottom panels at right). The sea ice thickness sections (Figures 6.7, 6.8, 6.9) reveal that there occurred a shear zone between the southern landfast sea ice edge in western Amundsen Gulf which disconnects mobile sea ice in the middle of the Gulf (Figure 6.3) as well as a large area of very thin (0.20m) sea ice adjacent to the southern coast of Banks Island disconnecting the mobile sea ice in the middle of the Gulf from the north landfast ice edge. It is apparent that sea ice motion prior to spring break-up had created areas of comparatively thin sea ice (grey reverse-'C' shaped feature on 24 May 2004 (Figures 6.3f, g) within the coastal areas of western Amundsen Gulf which enabled sea ice export from western Amundsen Gulf between 27 May and 6 June 2004.

In the absence of dynamics, the thermodynamic model melted sea ice in the polynya region in spring until zero sea ice thickness occurred (Figure 6.10). The

south coast of Banks Island would have been ice-free first on 20 June 2004, followed by Franklin Bay about a week later (Figure 6.10).

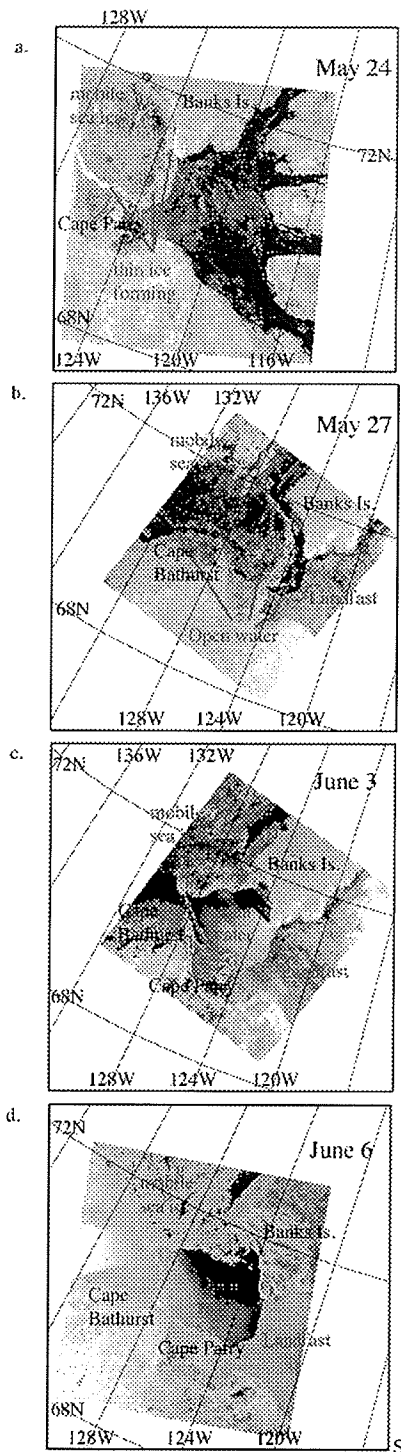
Figure 6.10. Modeled break-up (YD 175 = 23 Jun, YD183 = 1 Jul) in spring 2004



The middle of WAG would have been the next area to become ice-free at the end of June and the mouth of Amundsen Gulf was the last area to become ice-free around 03 July 2004 in the absence of dynamic processes. However, we know that this is not the case, as the Cape Bathurst spring polynya in western Amundsen Gulf formed dynamically between about 24 May and 6 June 2004 with the advection of mobile high concentration sea ice from the area (Figure 6.11) leaving behind landfast sea ice formed throughout the winter. The polynya formed slightly earlier than the historical average in 2004 (*Galley et al., 2008*). On May 24, the mobile sea ice in western Amundsen Gulf was delineated on RADARSAT-1 scanSAR imagery by a white-reverse-‘C’ shaped feature where thin sea ice was recently formed (Figure 6.11). This area appears white in the image denoting high backscatter to the radar

as a result of the high salinity of the surface of newly formed sea ice (Figure 6.11a). On May 27, the radar imagery clearly shows the sea ice in western Amundsen Gulf and the southern Beaufort Sea moving northwest leaving behind open water where the winter flaw lead system previously occurred (Figure 6.11b). On June 3 the winter mobile sea ice are had moved much further northwest almost completely clearing western Amundsen Gulf and opening the Cape Bathurst polynya (Figure 6.11c) which was opened further by June 6 (Figure 6.11d) leaving the landfast sea ice area of eastern Amundsen Gulf intact.

Figure 6.11. Radarsat-1 ScanSAR (σ^0) images of the advection of the mobile very close pack ice out of western Amundsen Gulf between May 24 and June 6 2004



4. Conclusions

The physical operation of the Cape Bathurst polynya has been investigated in detail over an annual cycle and explained as a case study of 2003-2004. In the fall, a tongue of old sea ice extended from the southern Beaufort Sea multi-year pack into western Amundsen Gulf between Franklin Bay and the southwest coast of Banks Island. This tongue provided an anchor point from which new and young sea ice growth radiated outward until it met landfast sea ice formed later connecting the Beaufort Gyre multi-year pack ice with seasonal sea ice in western Amundsen Gulf for the duration of the annual sea ice cycle. Thermodynamic modeling corroborated these observations.

Throughout December, anti-cyclonic sea ice motion in the southern Beaufort Sea enabled sea ice export from western Amundsen Gulf, which was continually reformed. Between January and the middle of May 2004, western Amundsen Gulf was near-completely covered by sea ice, but motion of the Beaufort Sea perennial pack in concert with ice motion in western Amundsen Gulf acted to maintain the winter flaw lead system (the reverse-'C' shaped feature in figures 6.3 and 6.11) which also showed up in the cross-section sea ice thickness results from the helicopter EM induction system.

From the beginning of May to 6 June 2004, when WAG was cleared of sea ice to form the spring polynya, sea ice speed in both the southern Beaufort Sea and western Amundsen Gulf increased and sea ice motion direction was very similar in both areas.

Sea ice in western Amundsen Gulf was moved out of the Gulf between 27 May and 6 June by two weeks of sustained winds toward the northwest, which drove ice in the southern Beaufort Sea north-northwest, taking the sea ice in Amundsen Gulf with it.

I conclude that the spring polynya in western Amundsen Gulf was formed by dynamic break-up, facilitated by several physical mechanisms occurring throughout the annual cycle in the region: (i) flaw leads maintained over winter by both sea ice motion in western Amundsen Gulf resulting from motion of the Beaufort Sea perennial pack due to its connection to seasonal sea ice in the Gulf formed in fall, and (ii) by the thermodynamic regime of the sea ice area directly south of Banks Island. These thinner, weaker leads disconnect sea ice in WAG from surrounding landfast ice, allowing it to be advected by wind forcing west into the southern Beaufort Sea in spring forming the Cape Bathurst polynya.

Results from our earlier work [*Galley et al., 2008*] show that summer sea ice concentrations in 2003 were close to long term average conditions save for a reduction in both total and old sea ice concentrations in the western portion of the southern Beaufort Sea; nearer Banks Island the total and old ice concentrations were high, consistent with the long term mean and the old ice tongue extended into WAG from the southern Beaufort Sea as it had done in 17 of the previous 23 years. Winter total and old sea ice in the study region in 2004 also resembled the long term mean and importantly, the winter new and young sea ice concentrations in the area (representing the flaw lead system in the transition zone between perennial ice in the southern Beaufort Sea and seasonal ice in Amundsen Gulf) were very close to

their long term average position and concentration. Finally, the polynya formed in the spring of 2004 a week later than the long-term mean (*Galley et al., 2008*).

Throughout our field and analytical work we recognized that dynamic and thermodynamic processes are concomitant variables. That said, we have attempted to tease apart the relative contributions of each with the thought that this will provide insights as to how the Cape Bathurst Polynya will operate in the decades ahead. The operation of the polynya is very important to how the marine ecosystem evolves within the polynya. We consider the results of this paper as a first-step in understanding how dynamic and thermodynamic processes act to form the Cape Bathurst polynya. Future work will link the processes governing this icescape with associated biological production, including the role of melt versus advection in controlling the light environment and stability of stratification of the ocean surface mixed layer.

Literature Cited

- Aagaard, K.L., L.K. Coachman and E. Carmack, (1981), On the halocline of the Arctic Ocean, *Deep Sea Res., Part A*, 28:529-545.
- Aagaard, K.L. and E.C. Carmack, (1989), The role of sea ice and other fresh water in the Arctic circulation, *J. Geophys. Res.*, 94(C10):14485-14498.
- Arbetter, T.E., J.A. Curry, M.M. Holland, and J.A. Maslanik, (1997), Response of sea-ice models to perturbations in surface heat flux, *Ann. Glaciol.*, 25: 193-197.
- Arrigo, K.R. and G.L. van Dijken, (2004), Annual cycles of sea ice and phytoplankton in Cape Bathurst polynya, southeastern Beaufort Sea, Canadian Arctic, *Geophys. Res. Lett.*, 31, doi:10.1029/2003GL018978.
- Arrigo, K.R., (2007), Chapter 7: Physical control of primary productivity in Arctic and Antarctic polynyas, In: Polynyas windows to the world, Smith, W.O. Jr. and D.G. Barber (eds.), Elsevier oceanographic series 74, Amsterdam.
- Barber, D.G. and J.M. Hanesiak, (2004), Meteorological forcing of sea ice concentrations in the southern Beaufort Sea over the period 1979-2000, *J. Geophys. Res.*, 109 doi:10.1029/2003JC002027.
- Barber, D.G. and R.A. Massom (2007), Chapter 1: The role of sea ice in Arctic and Antarctic polynyas, In: Polynyas windows to the world, Smith, W.O. Jr. and D.G. Barber (eds.), Elsevier oceanographic series 74, Amsterdam.
- Canadian Ice Service Archive Documentation Series (2006), Regional Charts: History, Accuracy, and Caveats, (http://ice.ec.gc.ca/IA_DOC/cisads_no_001_e.pdf) September 2006.
- Cavaliere, D.J. and S. Martin, (1994), The contribution of Alaskan, Siberian and Canadian coastal polynyas to the cold halocline layer of the Arctic Ocean, *J. Geophys. Res.*, 99(C9):18343-18362.
- Drobot, S.D. and J.A. Maslanik, (2003), Interannual variability in summer Beaufort Sea ice conditions: Relationship to winter and summer surface and atmospheric variability, *J. Geophys. Res.*, 108(C7), doi: 10.1029/2002JC001537.
- Dunbar, M.J., (1981), Physical causes and biological significance of polynyas and other open water in sea ice, In: Polynyas in the Canadian Arctic, Stirling, I. and H. Cleator (eds.), Canadian wildlife service occasional paper no. 45, Edmonton, AB.
- Flato, G.M. and R.D. Brown, 1996, Variability and climate sensitivity of landfast Arctic sea ice, *J. Geophys. Res.*, volume 101, number C10, pp. 25767 – 25777.

Fequet, D. (ed.) (2002), MANICE: Manual of standard procedures for observing and reporting ice conditions 9th edition, Canadian Ice Service – Environment Canada, Ottawa, ON.

Galley, R.J., E. Key, D.G. Barber, B.J. Hwang and J.K. Ehn, (2008), Spatial and temporal variability of sea ice in the southern Beaufort Sea and Amundsen Gulf: 1980-2004, *J. Geophys. Res.*, doi:10.1029/2007JC004553.

Golden, K.M., (2003), Critical behaviour of transport in sea ice, *Physica B* 338:274-83.

Haas, C., S. Gerland, H. Eicken, and H. Miller, (1997), Comparison of sea-ice thickness measurements under summer and winter conditions in the Arctic using a small electromagnetic induction device, *Geophysics*, 62(3): 749-757.

Haas, C., (1998), Evaluation of ship-based electromagnetic-inductive ice thickness measurements of summer sea-ice in the Bellinghausen and Amundsen Seas, Antarctica, *Cold Regions Sci. Tech.* 27:1-16.

Holladay, J.S., (2006), Application of airborne and surface-bases EM/Laser measurements to Ice/Water/Sediment models at Mackenzie Delta sites, Can.Tech.Rep.Hydrogr., *Ocean Sci.* 249: iv+47p.

Johnston, M., R. Frederking, and G. Timco, (2001), Decay-induced changes in the physical and mechanical properties of first year ice, *Proceedings of the 16th International Conference on Port and Ocean Engineering under Arctic Conditions*, August 2001, Ottawa, ON Canada.

Kovacs, A. and J.S. Holladay, (1990), Sea-ice thickness measurements using a small airborne electromagnetic sounding system, *Geophysics*, 55:1327-1337.

Kovacs, A., D. Diemand, and J.J. Bayer Jr., (1996), Electromagnetic induction sounding of sea ice thickness, *CRREL Report 96-6*, iii+9p.

Kwok, R., (1990), An ice-motion tracking system at the Alaska SAR facility, *IEEE Journal of Oceanic Engineering*, 15(1):44-54.

Maykut, G.A., (1978), Energy exchange over young sea ice in the central Arctic, *J. Geophys. Res.*, 83: 3646-3658.

Maykut, G.A., (1982), Large-scale heat exchange and ice production in the central Arctic, *J. Geophys. Res.*, 87(C10):7971-7984.

Mesinger, F., G. DiMego, E. Kalnay, K. Mitchell, P.C. Shafran, W. Ebisuzaki, D. Jovic, J. Woollen, E. Rogers, E.H. Berbery, M.B. Ek, Y. Fan, R. Grumbine, W. Higgins, H. Li, Y. Lin, G. Manikin, D. Parrish and W. Shi, (2004), North American Regional Reanalysis:

A long-term, consistent, high-resolution climate dataset for the North American domain, as a major improvement upon the earlier global reanalysis datasets in both resolution and accuracy, *Submitted to the Bulletin of the American Meteorological Society*, 7 November 2005,

(http://www.emc.ncep.noaa.gov/mmb/rreanl/narr_bams.pdf)

Mesinger, F., G. DiMego, E. Kalnay, P. Shafran, W. Ebisuzaki, D. Jovic, J. Woollen, K. Mitchell, E. Rogers, M. Ek, Y. Fan, R. Grumbine, W. Higgins, H. Li, Y. Lin, G. Manikin, D. Parrish and W. Shi (2005), NCEP Regional Reanalysis, *Presentation at the NARR Users Workshop*, San Diego, CA, 11 January 2005.

Minnett, P.J. and E.L. Key, (2007), Chapter 4: Meteorology and atmosphere-surface coupling in and around polynyas, In: *Polynyas windows to the world*, Smith, W.O. Jr. and D.G. Barber (eds.), Elsevier oceanographic series 74, Amsterdam.

Perovich, D.K., (2005), On the aggregate-scale partitioning of solar radiation in Arctic sea ice during the Surface Heat Budget of the Arctic Ocean (SHEBA) field experiment, *J. Geophys. Res.*, 110, doi:10.1029/2004JC002512.

Persson, P.O.G., C.W. Fairall, E.L. Andreas, P.S. Guest and D.K. Perovich, (2002), Measurements near the Atmospheric Surface Flux Group tower at SHEBA: Near-surface conditions and surface energy budget, *J. Geophys. Res.*, 107(C10), doi:10.1029/2000JC000705.

Prinsenberg, S.J. and J.S. Holladay, (1993), Using air-borne electromagnetic ice thickness sensor to validate remotely sensed marginal ice zone properties. In *Port and ocean engineering under arctic conditions (POAC 93)* HSVA(Ed.), 2:936-948.

Rothrock, D.A., Y. Yu and G.A. Maykut, (1999), Thinning of the Arctic sea-ice cover, *Geophys. Res. Lett.*, 26(23), 3469-3472.

Rudels, B., L.G. Anderson and E.P. Jones, (1996), Formation and evolution of the surface mixed layer and halocline of the Arctic Ocean, *J. Geophys. Res.*, 101(C4):8807-8821.

Ruffieux, D., P.O.G. Persson, C.W. Fairall and D. E. Wolfe, (1995), Ice pack and lead surface energy budgets during LEADDEX 1992, *J. Geophys. Res.*, 100(C3):4593-4612.

Smith, S.D., R.D. Muench, and C.H. Pease, (1990), Polynyas and leads: An overview of physical processes and environment, *J. Geophys. Res.*, 95(C6):9461-9479.

Smith, W.O. Jr., (1995), Primary productivity and new production in the Northeast Water (Greenland) polynya during summer-1992, *J. Geophys. Res.*, 100:4357-4370.

Steele, M., J.M. Morison, and T.B. Curtin, (1995), Halocline water formation in the Barents Sea, *J. Geophys. Res.*, 100:881-894.

Timco, G.W., (2008), Why does ice fail the way it does? *Proceedings of the 19th IAHR international symposium on ice*, Vancouver, B.C., Canada, 6-11 July, 2:557-577.

Tremblay, J.-E., Y. Gratton, J. Fauchot and N.M. Price, (2002), Climatic and oceanic forcing of new, net, and diatom production in the North Water, *Deep-Sea Res. II*, 49: 4927-4946.

Wadhams, P., (1987), Sea ice thickness distribution in the Greenland Sea and Eurasian Basin, May 1987, *J. Geophys. Res.* 97(C4):5331-5348.

WMO, (1970), World Meteorological Organization sea ice nomenclature, WMO Rep. 259., T.P.15, 147pp.+ 8 suppl., Geneva.

Zhang, J., D. Rothrock, and M. Steele, (2000), Recent changes in Arctic sea ice: the inter-play between ice dynamics and thermodynamics, *J. Clim.*, 13: 3099-3114..

CHAPTER SEVEN: CONCLUSIONS AND RECOMMENDATIONS

Summary and Contributions

Chapter one provides an introduction to this thesis and the rationale for performing the work contained herein.

Chapter two provides a review of the pertinent Arctic sea ice literature with special emphasis put on the thermodynamic and dynamic processes in snow covered sea ice on scales from one ice crystal to the regional and hemispheric interaction multi-year and seasonal sea ice in the Arctic climate system.

Chapter three presents physical measurements in a snow covered sea ice volume, using them to derive dielectric information at 250MHz and 1GHz for both the snow and ice thicknesses. This enabled the first measurements of separate snow and sea ice thickness at the same location to be remotely sensed using a ground penetrating radar system and further allowing for snow and sea ice thickness to be easily measured in time and space in future mass balance studies.

Moving to a larger spatial scale, Chapter four used a time series of synthetic aperture radar backscatter measurements over a landfast first-year sea ice volume to link the thermodynamic state of a snow-covered sea ice volume to the evolution of the upper ocean mixed layer in the adjacent water column; this is a new contribution in the field of sea ice-ocean interaction. This work is an important first step in the revealing how the physical oceanographic system of a polynya responds to melting of the surrounding landfast first-year sea ice.

In Chapter five, the interaction of different sea ice volumes was explored in time and space; the interaction of first-year sea ice with multi-year sea ice is explored spatially and temporally in the biologically significant Cape Bathurst Polynya. The interaction of first-year sea ice classes and multi-year sea ice was found to have changed over the 25-year period studied, implicating these processes in the potential alteration and/or extinction of the operation of the Cape Bathurst Polynya. This work is a distinct contribution to the field in the area of seasonal sea ice-multiyear sea ice interaction that maintains the biologically significant Cape Bathurst Polynya.

Following up on the historical context provided by the work in chapter five, chapter six investigated the dynamic and thermodynamic sea ice processes that create the interaction between the Arctic perennial sea ice pack and seasonal sea ice volumes regionally over an annual cycle. This work is a distinct contribution to the field as it describes the timing and relative contribution of thermodynamic and dynamic processes at the atmosphere-sea ice interface which create and maintain the interaction of different seasonal and multiyear sea ice volumes giving rise to the Cape Bathurst Polynya annually. It also concludes that if the interaction between multi-year and seasonal sea ice disappears as the extent of the Arctic pack continues to decline the Cape Bathurst Polynya may cease to operate as we know it; becoming most likely an area dominated by landfast first-year sea ice which would have to be melted out thermodynamically in spring.

Future Direction

(1) First, continued research into methods for accurate characterization of separate snow and sea ice thickness should be pursued. With continued ground penetrating radar work at multiple frequencies it should be possible to reveal information from within a snow or sea ice volume. It is possible that salinity and/or temperature horizons and their related brine volume differences or density differences could cause changes in the dielectric properties of the volume large enough to be detectable with a high enough frequency GPR system. I recommend moving to a frequency greater than 1GHz for this endeavor.

At a larger scale, the measurement of separate snow and sea ice thicknesses should proceed from the snow machine-based work on the scale of linear meters presented in chapter three, to helicopter-based ground penetrating radar surveys on the scale of linear kilometers in combination with electromagnetic induction equipment so that regions of particular biological an/or physical interest could be surveyed several times per year and over a number of years. Finally, this work could be conducted in combination with the acquisition of space-borne radar altimetry data which should be used to supplement current sea ice volume products like the Canadian Ice Service digital archive and sea ice extent products which are output by a number of space-borne sensors.

(2) With respect to large scale dynamic and thermodynamic sea ice processes, the work completed in chapters five and six should be enhanced by performing a similar study of the entire circumpolar flaw lead network in the Arctic using a combination of remotely sensed sea ice extent data and some type of re-

analysis climate data, be it the European Center for Medium-range Weather Forecast (ECMWF) re-analysis or the National Center for Environmental Prediction (NCEP) re-analysis data. It would be advantageous to supplement these data with sea ice volume data obtained as a result of recommendation (1).

(3) Finally, it would make sense to begin to model a polynya system in light of the conclusions of this thesis and the previous two recommendations, using a fully coupled atmosphere-sea ice-ocean model so that eventually sea ice processes at the regional scale which control the operation of polynyas at the ocean-sea ice-atmosphere interface could be projected into the future, similar to the way that hemispheric sea ice extent is now.

Conclusions

Chapter three begins the new research contained herein with the elucidation of a new method of separately measuring snow and sea ice thickness at the same location using ground penetrating radar. At the local scale, the physical and dielectric properties of snow-covered sea ice can be used in conjunction with ground penetrating radar reflection surveys at two frequencies to determine separate snow and ice thickness measurements at the same location. This method is effective over first-year sea ice covered by snow provided the snow layer is greater than 12cm thick. At that point the snow layer becomes indistinguishable from the sea ice volume to the properties of the frequency (1GHz) employed and the speed of the wave within the snow volume. Increasing the GPR frequency used could reduce the minimum detectable snow thickness.

Chapter four follows the snow and sea ice thickness measurements made in Chapter three by describing the relationship between a melting snow-covered sea ice volume and stratification of the adjacent upper ocean mixed layer. At local and regional scales, it was determined that the thermo-physical state of pond onset on a volume of melting landfast first-year sea ice as derived by synthetic aperture radar affects the timing of the evolution of the upper ocean mixed layer in the adjacent water column through the introduction of low salinity melt water which is vitally important to density-based stratification at the surface.

Chapter five explores the interaction of different sea ice volumes in time and space on the regional scale. Although the sea ice extent in an area may not change over time, the relative contributions of different seasonal sea ice thickness classes and sea ice age classes are concluded to have changed over time in the Cape Bathurst Polynya. The interaction between perennial Arctic sea ice and seasonal sea ice zones has been shown to be responsible for the trends toward thicker seasonal sea ice in the region during winter, and for trends toward more perennial sea ice in the region in summer; both processes could change the way the polynya operates in the future.

Finally, Chapter six builds on what was learned in chapter five regarding the interaction of different sea ice volumes by examining the effects of thermodynamic and dynamic processes on different volumes interacting over an annual cycle. A detailed annual study of the thermodynamic and dynamic processes that contribute to the operation of the Cape Bathurst Polynya concluded that as it occurs now, the Cape Bathurst Polynya is formed in spring as a result of a connection made the

previous fall between the perennial sea ice of the southern Beaufort Sea and the seasonal sea ice zone of western Amundsen Gulf. This connection allows for sea ice motion in the southern Beaufort Sea and western Amundsen Gulf in winter, keeping the ice in the polynya are mobile and giving it the ability to be advected out of the region in spring by persistent easterly and southeasterly winds much earlier than if it had melted out in place.

At this point my research into snow-covered sea ice volumes has come full-circle; I have moved from measuring volumes at the local scale, to their effect on the ocean column at the local and regional scale, to the interaction of different sea ice volumes in time and space, to finally the effect of thermodynamic and dynamic processes on the interaction of different sea ice volumes at the regional scale.

APPENDIX A: CONTRIBUTIONS OF COLLABORATING AUTHORS

Chapter Three

Alexandre Langlois and Michael Trachtenberg provided valuable discussion regarding the dielectric properties of the three media studied.

Chapter Four

David Barber contributed the basic idea for this analysis and provided valuable direction throughout the completion of the manuscript. John Yackel provided SAR data used in the analysis to determine pond onset date.

Chapter Five

Erica Key contributed valuable discussion regarding the trend analysis and both Byong Jun Hwang and Jens Ehn were helpful in helping me learn enough Matlab to write the code necessary for the historical and trend analyses.

Chapter Six

David Barber contributed his comments in several reviews of the manuscript. Simon Prinsenbergh provided me the EM induction sea ice thickness data within the manuscript. Erica Key provided valuable discussion regarding the organization of the presentation of such a process study.

APPENDIX B: ADDITIONAL CONTRIBUTIONS TO THE PEER-REVIEWED LITERATURE

In addition to the four peer-reviewed articles that compose this thesis, I also co-authored four articles during the course of my Ph.D. work :

Kuzyk, Z.Z., R.W. MacDonald, M.A. Granskog, R.K. Scharien, R.J. Galley, C. Michel, D. Barber, G. Stern, 2007. Sea ice, hydrological and biological processes in the Churchill River estuary region, Hudson Bay. *Estuarine, Coastal and Shelf Science*, 77(3): 369-384.

In *Kuzyk et al.*, (2007), I helped with the fieldwork required to perform the analysis. I also performed the thermodynamic sea ice modeling and wrote the section of text associated with the modeling work.

Ehn, J.K., B. Hwang, R. Galley and D. Barber, 2007. Investigations of newly formed sea ice in the Cape Bathurst Polynya: Part 1. Structural, physical and optical properties. *Journal of Geophysical Research – Oceans*, 112, C05002, doi:10.1029/2006JC003702.

In *Ehn et al.*, (2007) I helped with the field collection and analysis of the sea ice physical data and provided several thorough reviews of the finished manuscript.

Ehn, J.K., M.A. Granskog, T. Papakyriakou, R.J. Galley and D.G. Barber, 2005. Surface albedo observations of Hudson Bay land-fast sea ice during melt onset. *Annals of Glaciology*, 44.

In *Ehn et al.*, (2006) I helped with the field collection and analysis of the sea ice physical data and the optical data and provided several thorough reviews of the finished manuscript.

Hwang, B., D.G. Barber, J.K. Ehn, R.J. Galley and T. Grenfell, 2007. Investigations of newly formed sea ice in the Cape Bathurst Polynya: Part 2. Microwave emission. *Journal of Geophysical Research – Oceans*, volume 112, C05003. doi: 10.1029/2006JC003703.

In *Hwang et al.*, (2007) I helped with the field collection and analysis of the sea ice and snow physical data and provided several thorough reviews of the finished manuscript.